Evaluation of Passive Microwave-Based Sea Ice Edge and Marginal Ice Zone

by

Armina Soleymani

A thesis
presented to the University of Waterloo
in fulfillment of the
thesis requirement for the degree of
Doctor of Philosophy
in
Systems Design Engineering

Waterloo, Ontario, Canada, 2024

Examining Committee Membership

The following served on the examining committee for this thesis. The decision of the examining committee is by majority vote.

External Examiner:	Rasmus Tage Tonboe Associate Professor, Dept. of Space Research and Technology, Technical University of Denmark
Supervisor:	K. Andrea Scott Associate Professor, Dept. of Mechanical and Mechatronics Engineering, University of Waterloo
Internal Members:	Lisa Aultman-Hall Professor, Dept. of Systems Design Engineering, University of Waterloo
	Linlin Xu Research Assistant Professor, Dept. of Systems Design Engineering, University of Waterloo
Internal-External Member:	Chris Fletcher Associate Professor, Dept. of Geography and Environmental Management, University of Waterloo

Author's Declaration

This thesis consists of material all of which I authored or co-authored: see "Statement of Contributions" included in the thesis. This is a true copy of the thesis, including any required final revisions, as accepted by my examiners.

I understand that my thesis may be made electronically available to the public.

Statement of Contributions

Chapters 3, 4, and 5 encompass content derived from three papers, with minor modifications made for the sake of format consistency and clarification. These articles are distributed under the terms of the Creative Commons Attribution 4.0 license. As the primary author of these papers, I undertook the responsibility of conceptualizing the studies, programming, conducting key experiments, analyzing results, drafting, and submitting the manuscripts. Dr. Nastaran Saberi contributed to analyzing ice charts for Paper 1, while for Paper 3, Muhammed Patel facilitated running the model on Compute Canada and Prof. LinLin Xu provided feedback. Throughout this process, my supervisor, Prof. Andrea Scott, provided consistent guidance and offered valuable feedback on draft manuscripts. The references for the three papers are provided below.

1. Soleymani, A., Saberi, N. and Scott, K.A., 2023. Passive Microwave Sea Ice Edge Displacement Error over the Eastern Canadian Arctic 2013-2021. Canadian Journal of Remote Sensing (CJRS).

2. Soleymani, A. and Scott, A., 2023. Arctic Marginal Ice Zone Interannual Variability and Change Point Detection Using Two Definitions (1983-2022). Journal of Environmental Research Letters (ERL).

3. Soleymani, A., Patel, M., Xu, L., and Scott, A., 2024. On the definition of the marginal ice zone: A case study with SAR and passive microwave data in the Greenland Sea.

Additionally, during my doctoral studies, I authored and co-authored several papers within related fields, including

1. Soleymani, A. and Scott, K.A., 2021. Evaluation of a Neural Network on Sea Ice Concentration Estimation in MIZ Using Passive Microwave Data. IEEE Geoscience and Remote Sensing Symposium (IGARSS).

2. Soleymani, A. and Scott, A., 2022. Inter-Comparison of Passive Microwave Sea Ice Concentration and Sea Ice Edge Estimation with Operational Ice Charts in Baffin Bay, 2013-2021. In Fall Meeting 2022. American Geophysical Union (AGU).

3. Chen, X., Valencia, R., Soleymani, A. and Scott, K.A., 2023. Predicting Sea Ice Concentration with Uncertainty Quantification Using Passive Microwave and Reanalysis Data: A case study in Baffin Bay: A case study in Baffin Bay. IEEE Transactions on Geoscience and Remote Sensing (TGRS).

4. Chen, X., Valencia, R., Soleymani, A., Scott, K.A., Jiang, M., Xu, L., and Clausi, D., 2023. Uncertainty-Incorporated Arctic Sea Ice Concentration Estimation Using Heteroscedastic Bayesian Neural Networks. IEEE Geoscience and Remote Sensing Symposium (IGARSS).

5. Chen, X., Valencia, R., Soleymani, A., Scott, K.A., Xu, L., and Clausi, D., 2023. Calibration of Uncertainty in Sea Ice Concentration Retrieval with an Auxiliary Prediction Interval Estimator. IEEE Geoscience and Remote Sensing Letters (GRSL).

6. Andreas R. Stokholm, Jørgen Buus-Hinkler, Tore Wulf, Anton Korosov, Roberto Saldo, Leif T. Pedersen, David Arthurs, Ionut Dragan, Iacopo Modica, Juan Pedro, Annekatrien Debien, Xinwei Chen, Muhammed Patel, Fernando J. P. Cantu, Javier N. Turnes, Jinman Park, Linlin Xu, Andrea K. Scott, David A. Clausi, Yuan Fang, Mingzhe Jiang, Saeid Taleghanidoozdoozan, Neil C. Brubacher, Armina Soleymani, Zacharie Gousseau, Michał Smaczny, Patryk Kowalski, Jacek Komorowski, David Rijlaarsdam, Jan N. van Rijn, Jens Jakobsen, Martin S. J. Rogers, Nick Hughes, Tom Zagon, Rune Solberg, Nicolas Longépé, and Matilde B. Kreiner. "The AutoICE Challenge." The Cryosphere (TC).

Abstract

Sea ice is a vital factor in polar navigation, numerical weather prediction models, and climate change studies. It significantly influences the global climate, northern communities, and Earth's ecosystems. The sea ice edge and marginal ice zone are important areas for monitoring, as they affect ship navigation, human activities, and marine habitats. Passive microwave instruments offer valuable tools for monitoring the Earth's surface, regardless of solar illumination. This advantage is particularly prominent in polar regions, where harsh climate conditions, restricted accessibility, and polar darkness pose challenges to data collection. This thesis is dedicated to the analysis of the sea ice edge and the marginal ice zone obtained from passive microwave algorithms, with the aim of enhancing our understanding of these influential regions.

The first research compares the sea ice edge derived from three passive microwave algorithms against Canadian Ice Service charts over the Eastern Canadian Arctic. It also introduces a novel measurement for edge displacement error. The findings demonstrate differences in the performance of various algorithms across different seasons. During the freeze-up period, there is an increase in edge displacement error values, attributed to thin ice conditions. In April, the study observed the widest range of edge displacement error values, which were linked to fluctuations in wind speed and air temperature.

The second study focuses on a 40-year trend analysis of the Arctic marginal ice zone using the Bootstrap sea ice product, employing two definitions: one based on sea ice concentration and the other based on sea ice concentration anomaly. Comparative analysis shows consistent trends in marginal ice zone fraction, with the anomaly-based definition exhibiting higher values during transitional periods. Furthermore, change point detection analysis highlights an increase in marginal ice zone fraction after 2005 for the concentration-based definition and after 2007 for the anomaly-based definition, suggesting the influence of climate change on sea ice concentration and mobility.

In the third investigation, two sea ice products, passive microwave and synthetic aperture radar, are utilized to delineate the marginal ice zone in the Greenland Sea using two distinct definitions. The anomaly-based definition reveals a broader spatial marginal ice zone region, capturing the variability in sea ice concentration resulting from ice growth. This definition also maintains consistency across both sea ice products. Additionally, the study underscores the consistency of synthetic aperture radar in detecting the marginal ice zone (regardless of the definition) and its reduced sensitivity to the sea ice concentration anomaly standard deviation threshold, compared to passive microwave data.

Acknowledgements

I would like to express my deepest gratitude to my supervisor, Prof. K. Andrea Scott for her invaluable support and mentorship. I would also like to thank my committee members – Profs. Rasmus Tage Tonboe, Lisa Aultman-Hall, Linlin Xu, and Chris Fletcher for their valuable feedback.

Heartfelt thanks go to all my paper co-authors for their significant contributions. A special acknowledgment is reserved for the members of the Vision and Image Processing (VIP) research group at the University of Waterloo. Their camaraderie, support, and collaborative spirit have fostered a stimulating and productive laboratory environment.

My sincere gratitude is extended to all those who played a role in bringing this thesis to fruition. Whether your contribution was large or small, it has made a meaningful impact on my academic journey, and I am genuinely thankful.

Last but certainly not least, many thanks to my parents for their continuous and unconditional support and encouragement.

Dedication

This is dedicated to my family.

Table of Contents

List of Tables

List of Figures

List of Abbreviations

ASI ARTIST sea ice 12–15, 33, 34, 37, 39, 41, 46, 47, 49, 52, 53, 56, 59, 74

BT Bootstrap 12–14, 18, 20, 22, 33, 34, 39, 41, 46, 49, 52, 53, 55, 56, 59, 74, 80, 84, 86

MIZ Marginal ice zone 7, 8, 32, 33, 41, 49, 57–59, 61, 63, 67, 68, 71, 72, 79–85, 88–93, 95

NT2 NASA team 2 12, 13, 16, 17, 34, 39, 41, 46, 47, 52, 53, 56, 59, 74

PM Passive microwave xv, 6, 8–12, 18, 20, 21, 24, 28, 33–35, 41, 43, 44, 46, 47, 49, 52, 53, 55–57, 59, 74, 82–84, 86, 88, 90–95

SAR Synthetic aperture radar 9, 20, 24–26, 34, 47, 56, 82–85, 87, 88, 91–95

SIC Sea ice concentration 6, 8, 9, 11–18, 20–26, 28, 29, 32–37, 39, 41, 46, 47, 49, 52, 53, 55–61, 63, 67, 71, 73–75, 79, 80, 82–84, 87, 88, 90–92, 95

Chapter 1

Introduction

Sea ice is a major component of the cryosphere that plays a vital role in the Earth's climate system by reflecting a significant portion of the incoming solar radiation back into space and acting as a thermal barrier between the ocean and the atmosphere [5]. Although sea ice appears to be a thin blanket covering the ocean surface, it can affect heat, moisture, and momentum fluxes across the ocean-atmosphere interface [6]. Due to this complex interaction between sea ice and critical components of the Earth's climate system, sea ice has attracted increasing attention in climate-related research. Based on recent satellite observations, there has been a consistent decline in the extent of Arctic sea ice throughout the period from 1979 to 2023. The most substantial reduction occurred in the month of September, with a significant decrease of 12.2% or 4.67 million square kilometers, as reported by NASA [7]. The ongoing retreat of Arctic sea ice has drawn increased attention to the region, driven by its potential for economic and maritime development [8, 9, 10, 11]. Additionally, due to the retreat of Arctic ice, the "Northeast Passage" is expected to become navigable for open water ships in September from 2021 to 2025, and from August to October from 2025 to 2050 [12]. Another potential shipping route in the 21st century is the "Northwest Passage", the most direct shipping route between the Atlantic and Pacific Oceans, which provides companies with a shorter route and notable economic benefits [13, 14]. Another notable aspect of attention is the increasing interest in extending the shipping season for the transportation of goods and resources, such as iron ore from the Mary River Mine [15]. Additionally, the Inuit people residing in the northern region rely on the marine environment and Arctic marine mammals for their livelihoods [16], and they also utilize the sea ice cover for hunting and transportation purposes.

1.1 Motivation

Over recent decades, the Arctic sea ice cover has undergone substantial changes, impacting global climate, marine ecosystems, and human activities. The motivation behind this thesis arises from the importance of enhancing our comprehension of sea ice, specifically focusing on the sea ice edge and marginal ice zone, both experiencing rapid alteration. To elaborate further, this thesis is driven by the following motivations:

1. The first motivation revolves around the sea ice edge. Currently, there is a lack of recent studies regarding the performance of passive microwave sea ice edge estimation relative to ice charts, primarily in seasonal ice zones, which are becoming more prevalent in the Arctic regions. Recognizing the role of passive microwave sea ice concentration products [1] in the long-term planning of shipping routes, reanalysis data production, climate monitoring, and forecasting purposes, there is an interest in evaluating the extent to which the sea ice edge derived from different retrieval algorithms agree with those derived from the daily ice charts in a primarily seasonal ice zone. Moreover, there might be some scenarios in which two ice edges are situated at the same location but exhibit varying lengths, this can occur either with the ice edges from the same product at different times or with different products at the same time. To address these scenarios, we introduce a dimensionless measure that considers both edge length and displacement.

2. The second motivation shifts our focus to the Arctic marginal ice zone. The commonly used definition of this area relies on specific sea ice concentration thresholds. However, due to the diminishing extent of Arctic sea ice, the transition from thick multi-year ice to thinner first-year ice, increased fragmentation of the thinner sea ice, and the amplified influence of winds and waves, there is a possibility that sea ice concentration anomalies in the Arctic may be changing, directly impacting the boundaries and characteristics of the marginal ice zone. This prompts an investigation into whether a complementary definition for the Arctic marginal ice zone would be helpful. Moreover, given the susceptibility of the Arctic marginal ice zone to the impacts of climate change, it is important to examine whether significant shifts have occurred within the 40-year time series of the Arctic marginal ice zone fraction.

[1] Products refer to the data that are made publicly available by organizations for download or use.

3. The third motivation stems from the need to address a gap in comparing marginal ice zones derived from different sea ice products and various definitions as currently there is an absence of comparisons between marginal ice zone definitions across different sea ice products, such as passive microwave and synthetic aperture radar data. Recognizing the importance of the marginal ice zone fraction in offering insight into future climate conditions, there is an interest in assessing the capabilities of different sea ice products and methodologies to represent the marginal ice zone fraction. This assessment can serve as a helpful foundational basis for future studies.

1.2 Objectives

Based on the above motivations, this thesis aims to achieve the following three key objectives:

1. Evaluating the performance of different passive microwave sea ice concentration retrieval algorithms in estimating ice edge against daily ice charts, and also introducing a dimensionless measure to account for both edge length and displacement (see Chapter 3)

2. Investigating the Arctic marginal ice zone definition by incorporating two definitions, one based on sea ice concentration threshold and one based on sea ice concentration anomaly, and also analyzing the marginal ice zone interannual variability over the last 40 years using a passive microwave sea ice concentration retrieval algorithm (see Chapter 4)

3. Analyzing the impact of using different sea ice concentration products and varying marginal ice zone definitions on the estimation of the marginal ice zone fraction (see Chapter 5)

1.3 Thesis Structure

The rest of this thesis is organized as follows. Chapter 2 is divided into five main sections: sea ice, satellite remote sensing of sea ice, passive microwave radiometry, synthetic aper-

ture radar, and sea ice chart. The first section provides background information regarding sea ice and related parameters such as sea ice edge and marginal ice zone. The second section describes the remote sensing of sea ice using satellite observation. The subsequent sections delve into various methods for estimating sea ice, including passive microwave radiometry, synthetic aperture radar, and sea ice chart. Chapter 3, 4, and 5 provide detailed examinations of the first, second, and third objectives, respectively. Finally, a summary of contributions and conclusions as well as future works are described in Chapter 6.

Chapter 2

Background

This chapter begins by introducing fundamental concepts such as sea ice, ice edge, and the marginal ice zone. The second section delves into the remote sensing of sea ice through satellite observation, providing an overview of the methodology. The following part provides background information on passive microwave radiometry. Subsequently, various passive microwave sea ice concentration retrieval algorithms are discussed, outlining the different approaches used in estimating sea ice concentration. Additionally, this chapter covers the use of the synthetic aperture radar method for retrieving sea ice concentration. This section particularly emphasizes the utilization of convolutional neural networks for the estimation of ice concentration. Finally, the chapter explores another method for obtaining sea ice information, which is through the use of ice charts.

2.1 Sea Ice

When seawater freezes, sea ice forms, a process that expels salt into the water as ice crystals develop. This saline expulsion increases the underlying water salinity, causing it to become denser and sink within the ocean, thereby influencing ocean circulation patterns [17, 18]. Sea ice also plays a role in polar ecosystems; as it melts, the freshwater released is rich in nutrients, fostering the growth of phytoplankton, which serves as the foundation of marine food chains [19]. Additionally, sea ice has high albedo which means it absorbs less solar energy than open water, impacting global energy balance [20]. Human activities, particularly in the Arctic, rely on sea ice for hunting, transportation, and various commercial endeavors, including fishing, shipping, and tourism [21]. Sea ice has enormous

implications for various sectors such as the weather forecasting community [22]. One of the main parameters of sea ice is sea ice concentration (SIC) which is defined as the fraction of the surface of interest (e.g., a grid cell from a satellite image) that is covered by sea ice. SIC has a value between 0 and 1 (or 100%), where 0 indicates the open water (no sea ice) and values of 1 (or 100%) indicate an entirely ice-covered area. A typical grid cell used in such an analysis is 25 km × 25 km.

2.1.1 Sea Ice Edge

The sea ice edge is the boundary separating areas of open water from regions covered by sea ice. In other words, it represents the transition zone where the relatively ice-free ocean surface meets the sea ice or where ice begins to form. The position of the sea ice edge fluctuates throughout the year and varies annually, responding to changes in environmental factors such as temperature, wind patterns, and ocean currents [23]. This boundary holds significant importance across various domains. In climate-related studies, it serves as an indicator of the Earth's climate state and plays a key role in understanding climate variability and change. Additionally, the sea ice edge is vital for navigation, as it marks the boundary between navigable waters and hazardous icy conditions. Moreover, it is important in ecological research, as it delineates the interface between two distinct environments with different physical properties and ecosystems, influencing habitats, biodiversity, and species distribution in polar regions [24, 25, 26].

The precise location of the ice edge is crucial for ensuring safe navigation in ice-affected waters. Sea ice, with its typically higher albedo compared to ice-free ocean areas [27], plays a significant role in reflecting sunlight and influencing regional climate dynamics. Visible wavelength imagery obtained from satellites is a valuable tool for studying the sea ice edge. However, these sensors face limitations, as approximately 70% of the time, clouds and fog obstruct visibility, hindering the accurate detection of the ice edge [28]. Furthermore, visible imagery becomes impractical during the polar night due to the absence of sunlight. An alternative approach involves utilizing microwave sensors, both active and passive, operating within the microwave portion of the electromagnetic spectrum. These sensors are unaffected by polar darkness and possess the capability to penetrate through cloud cover, enabling the observation of the ice surface under almost all weather conditions.

The most common definition for the ice edge using passive microwave (PM) ice concentration products is defining the 15% SIC contour, which was found to be spatially sharp

[29] and, hence, a good proxy for the ice edge delineation. Ice edge displacement can refer to either the difference in the position of the ice edge between two products or the distance by which the edge of the sea ice pack has been estimated to shift over a given time, indicating retreat or growth. The assessment of the ice edge displacement often involves employing diverse metrics to measure the accuracy of the estimated ice edge location. One commonly used metric is the Integrated Ice Edge Error (IIEE) [30], designed to quantify the disparity between the estimated and true ice edge positions, expressed in area units. The IIEE is computed by summing the areas where discrepancies exist between the estimated and true ice edges regarding whether the ice concentration surpasses or falls below a specified threshold, typically set at 15%. Comprising two components, the IIEE is expressed as the sum of "O" and "U" (IIEE = O + U). Here, "O" denotes the region where the local sea ice extent is overestimated by the model estimation, while "U" represents the area where the local sea ice extent is underestimated by the model estimation. The schematic representation for defining IIEE is depicted in Figure 2.1.

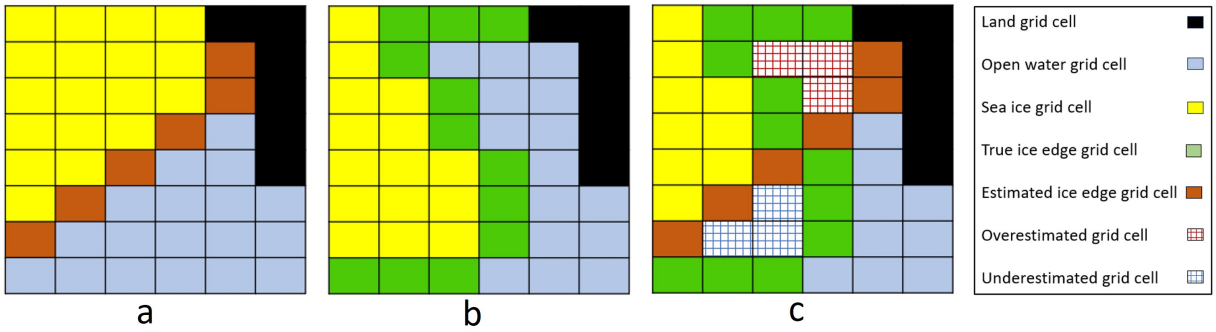

Figure 2.1: A schematic representation of defining the Integrated Ice Edge Error (IIEE) metric. Panel "a" shows the estimated ice edge in orange grid cells. Panel "b" shows the true ice edge in green grid cells. Panel "c" illustrates overestimated grid cells (hatched blue) and underestimated grid cells (hatched red). IIEE reflects the summation of the underestimated and overestimated grid cells.

2.1.2 Marginal Ice Zone

The MIZ is a transitional region between sea ice and open water, typically occurring at the boundary between the consolidated sea ice cover and the open ocean. The MIZ is a dynamic and ecologically important area, subject to seasonal and interannual variations.

The spatial extent, temporal variability, wave-ice interactions, floe size distribution, and ice dynamics within the MIZ are all important characteristics that are of interest for climate-related research (e.g., [31, 32, 33, 34, 35]). The ecosystems within the ice, ocean water, and seafloor are interconnected. Phytoplankton blooms in the MIZ spread a significant distance away from the ice edge, making MIZ region an important feeding area as well [36]. Recognizing that the characteristics of the MIZ can vary with the time of year, geographic location, and climatic conditions, understanding the characteristics of the MIZ is valuable for predicting changes in polar environments and their implications on global climate patterns.

The definition of the MIZ in studies varies depending on the specific aspects of interest. Definitions of the MIZ can be categorized based on (1) ice concentration: operationally, the MIZ is defined as the region within the sea ice where the SIC falls within the range of 15% to 80% [31]. Sea ice in this range is assumed to be mobile and can be influenced by ocean currents, (2) wave penetration: MIZ can be considered as the area where ocean waves interact with sea ice, penetrate ice cover [37], and impact the ice thickness [38]. This definition centers on the pivotal role of ocean waves in shaping the extent of the MIZ and determining the distribution of floe sizes. When the ice cover undergoes significant fragmentation, its behavior differs from pack ice, (3) ice concentration anomaly: exploring the question of whether subtle variations in grid cell concentration from passive microwave products provide a consistent indicator of changes in ice characteristics over the Antarctic sea ice, an alternative definition for the MIZ has been considered by applying a threshold on SIC anomaly [1] [39]. In this study, the focus will be on definitions based on ice concentration and ice concentration anomaly, as this research centers on MIZ derived from PM SIC retrieval algorithms.

2.2 Satellite Remote Sensing of Sea Ice

When it comes to monitoring sea ice, due to the polar harsh climate conditions and limited access, in-situ measurements are sparse and concerned with seasonality, as there are typically fewer measurements available during the winter [40]. Satellite remote sensing plays a significant role in monitoring sea ice [40]. In polar regions, satellite-borne data in the visible and infrared ranges are hampered by clouds, and in this regard, the low-frequency

[1] The deviation of SIC at a specific grid cell from its long-term average over a given time period.

microwave portion of the electromagnetic spectrum is particularly useful [41, 42, 5]. PM sensors can continuously observe the Earth's surface, regardless of weather conditions and solar illumination. Besides the frequent data acquisitions from PM sensors, they have a wide swath [2], enabling them to cover a large area which is advantageous in sea ice tasks due to the vast ice-covered areas [5]. Another means of estimating SIC using satellite imagery is synthetic aperture radar (SAR), an active remote sensing technique. Unlike traditional radar systems, which use a single antenna to transmit and receive radar signals, SAR employs a technique known as synthetic aperture to achieve high-resolution (3 m to 40 m) radar images with improved spatial detail and image quality. SAR systems are deployed on aircraft and satellites to observe and monitor the Earth's surface under various weather and lighting conditions. Ice charts represent another source of sea ice information, available at different temporal resolutions, such as daily, weekly, or monthly. These charts rely on a combination of data sources, including meteorological data, visual ship observations, airborne radar measurements, satellite images, and climatological information, to provide a comprehensive view of ice conditions. Additional information on each of the methods for retrieving SIC are provided separately in the following sections. These sections will explain each method in detail, providing a comprehensive understanding of how SIC is estimated using these approaches.

2.3 Passive Microwave Radiometry

According to Planck's theory [44], an object that absorbs all incident radiation and emits the same amount, according to its temperature, is a black body. Planck's law [45] expresses an equation in which the amount of radiation a black body emits is associated with its physical temperature and frequency. In microwave region, the simplified version of Planck's law [3], the Rayleigh-Jean's equation [46], can be written as

$$B_f = \frac{2 \times k \times T_{ph} \times f^2}{c^2}, \tag{2.1}$$

where B_f is the emitted radiation from a black body at a given frequency f ($\frac{W}{m^2.Hz}$). k is the Boltzmann's constant (1.38×10^{-23} J/K). c and T_{ph} stand for speed of light (m/s) and the temperature of the emitting layer (K), respectively. Emitting layer is a depth below

[2] A sensor sees a certain portion of the Earth's surface as the satellite revolves around the Earth. The area imaged on the surface is called a swath [43].

[3] Based on the fact that the frequency of the microwave signal is small and their wavelength is large [46]

the surface from where the emission comes. The depth of this layer in sea ice fluctuates between a few millimeters and decimeters, contingent upon its physical constitution and the microwave frequency. Typically, it is assumed that the radiating layer of the emitted microwave aligns with the penetration depth of the signal [5].

An object in nature radiates less energy than a black body at the same temperature. These objects are called gray bodies, and their emitted radiation at a given frequency is denoted as G_f, and their equivalent temperature is generally referred to as the brightness temperature (TB, in Kelvin). In other words [5]

$$G_f = \frac{2 \times k \times TB \times f^2}{c^2}. \tag{2.2}$$

At any given frequency, emissivity (ε) is defined as [5]

$$\varepsilon = \frac{G_f}{B_f}. \tag{2.3}$$

Combining Equation 2.1, 2.2, and 2.3 gives [5]

$$TB = \varepsilon T_{ph}. \tag{2.4}$$

2.3.1 Passive Microwave Sensors

The next topic is the history of PM sensors used for the Earth observation system (EOS). The first spaceborne microwave data was from the Nimbus-5 electrically scanning microwave radiometer (ESMR) in December 1972. With the Nimbus-7 scanning multichannel microwave radiometer (SMMR) launch in 1978, polar regions were first observed using multichannel passive microwave sensors. The SMMR was followed by a series of successive defense meteorological satellite program (DMSP) special sensor microwave/imager (SSM/I) and special sensor microwave imager/sounder (SSMIS) in 1987 and 2003, respectively. This relatively long history of polar remote sensing continues with the advanced microwave scanning radiometer (AMSR). AMSR has operated on three satellites: AMSR2 on JAXA's GCOM-W1 platform, advanced microwave scanning radiometer for EOS (AMSR-E) on NASA's Aqua platform, and AMSR on JAXA's ADEOS-II platform. The microwave radiation imager (MWRI) on the Chinese Feng-Yun satellite series was launched in 2008. An overview of commonly used satellite microwave sensors in sea ice is indicated in Table 2.1. Additionally, Table 2.2 includes the dimensions of the observation footprint from commonly used channels in sea ice applications, sourced from SSM/I, AMSR-E, and AMSR2

sensors.

Sensor	Satellite platform	Frequency (GHz)	Operation period (year)
SMMR	Nimbus7	6.6, 10.7, 18.0, 21.0, 37.0	1978-1987
SSM/I	DMSP	19.4, 22.2, 37.0, 85.5	1987-present
SSMIS	DMSP	19.4, 22.2, 37.0, 91.7	2003-present
AMSR-E	Aqua	6.9, 10.7, 18.7, 23.8, 36.5, 89.0	2002-2011
AMSR	ADEOS-II	6.9, 10.7, 18.7, 23.8, 36.5, 50.3, 52.8, 89.0	2002-2003
MWRI	FY-3 series	19.4, 22.2, 37.0, 91.7	2008-present
AMSR2	COM-W1	6.9, 7.3, 10.7, 18.7, 23.8, 36.5, 89.0	2012-present

Table 2.1: An overview of commonly used passive microwave sensors in sea ice studies.

Sensor	Frequency (GHz)	3-dB footprint size (km × km)
SSM/I	19.4	43 × 69
	22.2	50 × 40
	37.0	28 × 37
	85.5	13 × 15
AMSR-E	18.7	16 × 27
	23.8	31 × 18
	36.5	8 × 14
	89.0	6 × 4
AMSR2	18.7	14 × 22
	23.8	15 × 26
	36.5	7 × 12
	89.0	3 × 5

Table 2.2: An overview of 3-dB footprint size for each channel of commonly used passive microwave sensors in sea ice studies.

2.3.2 Passive Microwave SIC Retrieval Algorithms

For over 40 years, PM sensors have been used to retrieve SIC using different translators, called SIC retrieval algorithms, that translate the measured brightness temperatures to SICs. Open water exhibits significantly lower radiation emission in the horizontal polarization [4] (H-pol) compared to the vertical polarization (V-pol). This indicates that the polarization difference (denoted as $PD = TB_V - TB_H$) for open water is greater than that

[4]Polarization refers to the alignment of an electromagnetic signal.

observed for sea ice [47]. Most SIC retrieval algorithms rely on tie points, which are typical radiometric values corresponding to a given surface type. Tie points can vary both temporally and spatially, especially when dealing with thin ice. In addition to brightness temperature, polarization ratio (PR, Equation 2.5) and gradient ratio (GR, Equation 2.6) are two parameters that are commonly used in SIC retrieval algorithms. The PR at a given frequency (f) is defined as

$$PR(f) = \frac{TB_{fV} - TB_{fH}}{TB_{fV} + TB_{fH}}, \tag{2.5}$$

where V and H refer to V-pol and H-pol, respectively. The GR between two observations from two frequencies (f_1 and f_2) at the same polarization (p) is written as

$$GR(f_1 f_2 p) = \frac{TB_{f_1 p} - TB_{f_2 p}}{TB_{f_1 p} + TB_{f_2 p}}. \tag{2.6}$$

Emissivity represents a fundamental radiative characteristic of a material, while brightness temperature varies based on both emissivity and the temperature of the emitting layer. Consequently, using PR and GR are preferable over brightness temperature, given their greater independence from the physical temperature [5].

Several known sources of uncertainty associated with PM SIC retrieval algorithms are:

(1) Variability in sea ice emissivity: sensitivity to sea ice emissivity depends on the selection of input brightness temperatures at different frequencies and polarizations, as well as the specific retrieval algorithm utilized to estimate SIC. This variability introduces the potential for both underestimation and overestimation of SIC, depending on the algorithm selected [48]. It is also demonstrated that SIC algorithms fail to accurately capture the ice concentration variability, particularly in Arctic regions where SIC approaches 100% [49, 50].

(2) Melt ponds: the penetration depth of microwave radiation into liquid water is a few millimetres [46]. This shallow penetration depth makes it difficult for the sensor to distinguish between ocean water and meltwater on the ice surface. As a result, SIC algorithms may underestimate the actual ice concentration, particularly during the melt season when melt ponds are prevalent [51]. In a study by Rose *et al.* [52], a comparison of SIC derived from several PM retrieval algorithms, namely ARTIST sea ice (ASI), Enhanced NASA team or NASA team 2 (NT2), and Bootstrap (BT), and MODIS [5] over the Canadian archipelago on June 18, 2011, was undertaken. The study found that all PM retrieval algorithms underestimated the SIC by approximately 20 to 30% in regions with melt ponds.

[5] Moderate-resolution imaging spectroradiometer.

(3) Thin ice: in the presence of thin ice, SIC retrieval algorithms are known to underestimate the actual ice concentration [53, 54]. One possible explanation for this underestimation is the relationship between brightness temperature and sea ice thickness (SIT), which may be influenced by changes in the near-surface dielectric properties due to variations in brine salinity with thickness and temperature [55]. The effect of SIT on SIC bias over the areas of the Arctic that are known to have a 100% thin ice (using ENVISAT [6] ASAR [7] data) from 1 October to 12 December 2010 is carried out in a study by Ivanova *et al.* [56]. The ESA's [8] SMOS [9] observations were utilized to determine the thickness of thin ice. The study revealed that SIC is underestimated in thin ice and the bias is higher for the thinner ice.

(4) Atmospheric contributions: water vapor, cloud liquid water, and wind roughening of the ocean surface can lead to falsely increased observed brightness temperature (relative to the actual brightness temperature). This can lead to overestimation of the actual SIC. The effect of atmospheric contamination [10] is more pronounced over open water, than over consolidated sea ice [48]. To mitigate the effect of atmospheric contamination, weather filters are applied to the retrieved SICs. These threshold-based filters are empirically determined to remove weather effects over the open water. To correct for water vapor, the gradient ratios (Equation 2.6) of 19 and 22 GHz frequency are used [57]: GR(1922V) $\geq$ 0.04 [58], and to correct for cloud liquid water and wind roughening of the ocean surface, the gradient ratios of 19 and 37 GHz frequency are used [57]: GR(1937V) $\geq$ 0.045 [58]. According to these weather filters, SIC values for grid cells that meet either of the two criteria are deemed to be water (set to zero). Despite different types of weather filters being applied in SIC retrieval algorithms to mitigate atmospheric contamination, these filters may eliminate the low SIC values (up to 30%), resulting in an underestimation of ice concentration [48, 56]. Furthermore, a radiative transfer model can be employed to account for the impact of weather conditions on the measured brightness temperatures. This has also been used for lower frequency SIC retrieval algorithms [59]. Further elaboration on the radiative transfer model approach will be provided in the next section.

Focusing on several algorithms across different frequency channels, the ASI [60], NT2 [61] (using higher frequency channels), and BT [62] (using lower frequency channels) are

[6] Environmental satellite.
[7] Advanced SAR.
[8] European space agency.
[9] Soil moisture and ocean salinity
[10] Atmospheric contamination refers to the sum of the biases caused by water vapor, cloud liquid water, and wind roughening of the ocean surface [48].

selected for this research. These algorithms are commonly [63, 64] used retrieval algorithms in sea ice research studies [50, 65, 56, 66].

ARTIST Sea Ice (ASI) Algorithm

The Arctic Radiation and Turbulence Interaction STudy (ARTIST) sea ice (ASI) algorithm [67] uses the polarization difference (PD) of brightness temperatures at nearly 90 GHz. In the ASI algorithm, intermediate ice concentrations are calculated by interpolating the sea ice concentration values between open water and 100% ice cover. This interpolation is performed using a third-order polynomial equation, which is written as

$$SIC = 1.64 \times 10^{-5} PD^3 - 0.0016 PD^2 + 0.0192 PD + 0.9710. \tag{2.7}$$

In order to eliminate spurious SICs over open water, Spreen *et al.* [58] employed the lower-frequency channels as weather filters, a common method for compensating for the sensitivity to atmospheric contamination. In this method, the SIC values for grid cells that meet either of these below criteria are set to 0:

- GR(1922V) $\geq$ 0.040
- GR(1937V) $\geq$ 0.045
- SIC(BT $=$ 0 (If the corresponding SIC from BT algorithm is zero)

In a study by Lu *et al.* [68], a radiative transfer model [69] is used to correct for atmospheric contamination that occurs when employing the near 90 GHz frequency channel (the algorithm is called ASI2). The scheme evaluates the correction offsets, δTB, per each channel as

$$\delta TB = TB_{atm} - TB_{ref}, \tag{2.8}$$

$$TB_{corr} = TB_{obs} - \delta TB, \tag{2.9}$$

where TB_{atm} and TB_{ref} represent simulated brightness temperatures with and without atmospheric effects, respectively. TB_{corr} denotes the corrected brightness temperature, and TB_{obs} stands for the observed brightness temperature. TB_{atm} and TB_{ref} can be found as

$$TB_{atm} = TB(f, p, W, V, L = 0, SST, T_{ice}, SIC), \tag{2.10}$$

$$TB_{ref} = TB(f, p, W = 0, V = 0, L = 0, SST_{ref}, T_{ice,ref}, SIC), \tag{2.11}$$

where f is frequency, p is polarization, W is 10-m wind speed (m/s), V is water vapour (mm), L is cloud liquid water (mm), SST is sea surface temperature (K), T_{ice} is ice temperature (K). In order to calculate TB_{ref} , zero values were assigned to W, V, L, while $SST_{ref} = 271.5$ K and $T_{ice,ref} = 265$ K. Using this method improved accuracy in SIC measurement, particularly over open water, with negligible impact on areas with 100% SIC has been reported [68].

Despite the high spatial resolution of the 89 GHz channels of AMSR-E, these channels are sensitive to atmospheric effects [5], which can lead to ambiguous SIC estimation. Furthermore, since the polarization difference is in units of brightness temperature, this algorithm may be sensitive to ice temperature variability. The ASI algorithm, however, is known to have the least sensitivity to sea ice thickness compared to other SIC algorithms implemented in Heygster *et al.* [54], which is a key strength. The ASI SIC product is available from 2002 to 2011 (AMSR-E sensor) and from 2012 to 2022 (AMSR2 sensor) with different grid resolutions (~ 3 km and ~ 6 km).

NASA-Team (NT) Algorithm

The NASA-Team (NT) algorithm [60], uses two main Equations: PR (Equation 2.5), and GR (Equation 2.6). First, the algorithm calculates the PR(19) and plots it against the GR(1937V). A schematic diagram illustrating this method is provided in Figure 2.2. Based on the three brightness temperature clusters, tie points are derived to represent 100% concentrations of each surface type: first-year ice [11] (FYI), multi-year ice [12] (MYI), and open water (OW). The position of a point relative to these tie points determines its associated SIC value. For instance, points closer to OW correspond to lower SIC values, while points closer to the line connecting MYI and FYI represent higher SIC values. These three surfaces form the vertices of a triangle, and PR and GR values that fall between them indicate a mixture of surface types. In the Arctic, the observed brightness temperature

[11] The ice that has not survived a melt season.

[12] The ice that has survived at least one melt season.

is a composite measure derived from the weighted contributions of three main surface types: ice-free ocean, FYI, and MYI. Unique sets of tie points are established for each hemisphere and sensor used in the data product (see [70] for a list of tie points). The primary source of error in the NT algorithm can be attributed to ice surface effects such as glazing and layering [71], which can impact the 19 GHz brightness temperature, resulting in SIC underestimation. Lastly, the NT algorithm employs weather filters to remove spurious SIC estimates. These weather filters are based on the GR for the 37V and 19V channels and incorporate an additional GR using the 22V and 19V channels. The SIC values for grid cells that meet either of these below criteria are set to 0:

- GR(1922V) $\geq$ 0.045
- GR(1937V) $\geq$ 0.05

This product is available from 1978 to 1987 (SMMR sensor), from 1987 to 2007 (SSM/I sensor), and from 2008 to the present (SSMIS sensor) with a 25 km gridded resolution.

Enhanced NASA Team (NT2) Algorithm

The Enhanced NASA Team (NT2) algorithm [61] estimates SIC using lookup tables of rotated GRs and polarization ratios PRs calculated from brightness temperatures measured at 19, 37, and 85 GHz frequency channels. For each of the 12 representative atmospheric profiles [13], GRs and PRs are computed over all possible ranges of SIC using a radiative transfer model. These calculated GRs and PRs are arranged as look-up tables, with one table for each atmospheric profile. For the Arctic, this process is carried out separately for three different ice types: FYI, MYI, and thin ice. These different ice types exhibit different characteristic emissivities, influencing the surface emission component of the brightness temperatures used in calculating GRs and PRs. The ice concentration of a given grid cell is found by choosing the concentration value that best matches the actual and estimated PRs and GRs. A schematic diagram of this method is provided in Figure 2.3. This algorithm utilizes the near-90 GHz frequency channel, which makes it easier to distinguish between low ice concentrations and areas affected by surface effects associated with refreezing (snow layering and glazing). However, surface effects from melt processes have not been addressed in this algorithm [72].

[13] Atmospheric profiles refers to a set of simulated atmospheric conditions. These conditions are generated using various pre-defined atmospheric variables, including water vapor, cloud liquid water, wind speed.

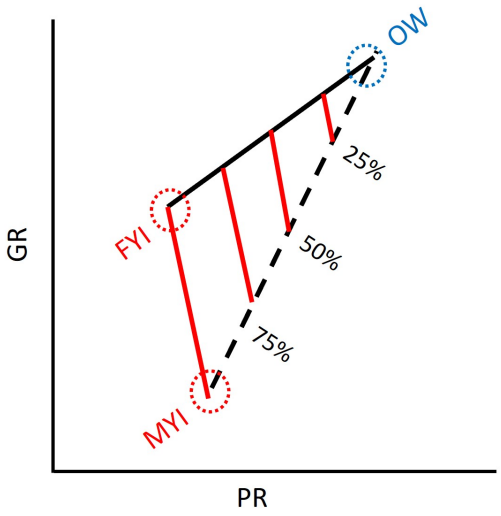

Figure 2.2: A schematic diagram of the technique used in NT algorithm over the Arctic. PR, GR, OW, FYI, and MYI denote the polarization ratio, gradient ratio, brightness temperature of open water, brightness temperature of first-year ice, and brightness temperature of multi-year ice, respectively.

Although the NT2 algorithm produces weather-corrected SIC, erroneous SIC estimates are still possible. Thus, the SIC values for grid cells that meet either of these below criteria are set to 0:

- GR(1922V) $\geq$ 0.045
- GR(1937V) $\geq$ 0.05

It is noted that this algorithm is susceptible to weather effects not represented by the 12 atmospheres [73]. This product is available from 2012 to 2022 (AMSR2 sensor) with a 12.5 km gridded resolution. Figure 2.4 and 2.5 are an illustration of how the weather filters work over the Arctic in the first day of January 2021 and June 2021, respectively. The AMSR2 brightness temperatures with a 12.5 km gridded resolution is obtained from the United States National Snow and Ice Data Center (NSIDC) [74]. In both Figures 2.4 and 2.5, the SIC value for points outside the range delineated by the black square are adjusted

to 0, representing open water, by the weather filters. It should noted that for both January 1 and June 1, there are some points (locations) near the boundary where the SIC values are high (around 50%). Moreover, there are some points (locations) outside of the defined box with nonzero SIC values (near 10 or 20%), however, they are ultimately set to zero in this scheme.

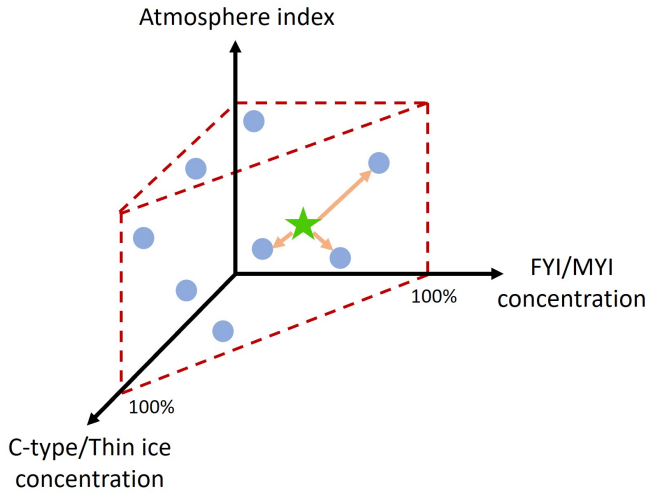

Figure 2.3: A schematic diagram of the technique used in NT2 algorithm over the Arctic. C-type, FYI, and MYI stand for ice with surface effects, first-year ice, and multi-year ice, respectively. The blue circle is an illustration of the modeled value and the green star is an illustration of the observed value.

Bootstrap (BT) Algorithm

The Bootstrap (BT) algorithm [71] estimates SIC using data from three PM channels of 19V, 37V, and 37H, which allows for the characterization and differentiation of two surface types: sea ice (SIC is near 100%) and ice-free (SIC is zero) regions. The algorithm relies on the clustering of 100% sea ice multichannel daily brightness temperatures to identify a suitable tie point for 100% and 0% SIC. A schematic diagram of this method is provided in Figure 2.6. By comparing the scatter plot of one passive microwave channel to another (37V vs. 37H and 37V vs. 19V), two clusters can be identified. One cluster comprises data points with a SIC of approximately 100% (forming a line AD), and the other comprises

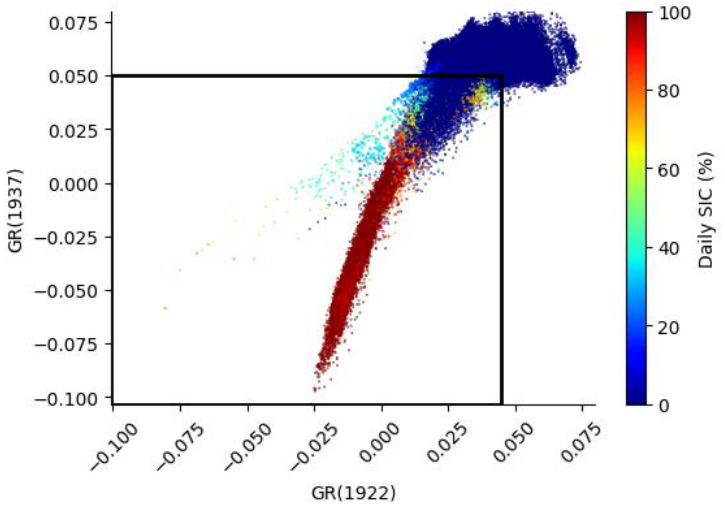

Figure 2.4: An example of GR(1922) vs. GR(1937) values (for AMSR2) for 01 January 2021 over the entire Arctic. By applying these weather filters, NT2 SIC values for points that lie outside the black box set to zero.

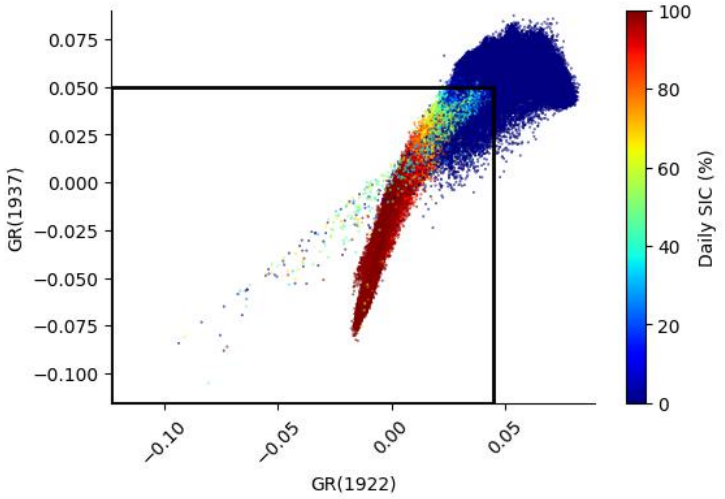

Figure 2.5: An example of GR(1922) vs. GR(1937) values (for AMSR2) for 01 June 2021 over the entire Arctic. By applying these weather filters, NT2 SIC values for points that lie outside the black box set to zero.

data points with a SIC of around 0% (OW). The algorithm uses the linearity of these clusters to estimate SIC for a given grid cell based on its brightness temperature values. For instance, the SIC for an arbitrary ice surface (represented by point B) can be determined by extending the line along OB until it intersects line AD, yielding point I, representing the brightness temperature of 100% ice concentration, and a location near O representing the brightness temperature of 0% ice concentration for this ice surface. The distance from B to I (or O) is a measure of the SIC. It is worth mentioning, for open water and low ice concentrations near the ice edge, the BT algorithm uses the 37V and 19V channels. This channel combination is more sensitive to the ice-water boundary and is able to distinguish low ice concentrations. For higher ice concentrations within the ice pack, away from the ice edge, the BT algorithm uses the 37H and 37V channels. This channel combination is suited for compact ice regions, as the scatter plot shows more distinct clustering of 100% ice tie points, enabling accurate retrieval of high concentrations through linear interpolation [75].

To filter out weather effects (mainly wind, water vapor, and cloud liquid water effects) over open water this algorithm applies a weather filter. In this scheme, SIC values are set to 0% if the difference between the brightness temperatures of the 19 and 22 GHz channels exceeds a predefined threshold. Also, a slanted line in the scatter plots of 37V and 19V shows the SIC value for points fall below this line are considered zero. This product is available from 1978 to 1987 (SMMR sensor), 1978 to 2007 (SSM/I sensor), and 2008 to the present (SSMIS) sensor with a 25 km gridded resolution. Figure 2.7 and 2.8 provide an illustration of how the weather filters operate over the Arctic in the first day of January 2021 and June 2021, respectively. The SSMIS brightness temperatures with a 25 km gridded resolution were obtained from the NSIDC [76]. Fot both Figures 2.7 and 2.8, in panel (a), a predefined threshold is depicted on the scatter plot of TB22-TB19V versus TB19V, typically represented by a vertical line at 16 K for the Arctic [77]. Consequently, SIC values for points with TB22-TB19V $>$ 16 K are set to zero. Additionally, panel (b) shows that SIC values for points lying below the slanted line (180 k $<$ TB19V $<$ 183 K) are set to zero. Panel (c) presents a scatter plot where both criteria (shown in panels a and b) are applied simultaneously.

SIC Uncertainty

Numerous algorithms and products have been developed utilizing the PM record. Validation studies (e.g., [56]) have been conducted over the years. These studies typically compare PM data with higher spatial resolution data from visible, infrared, or SAR prod-

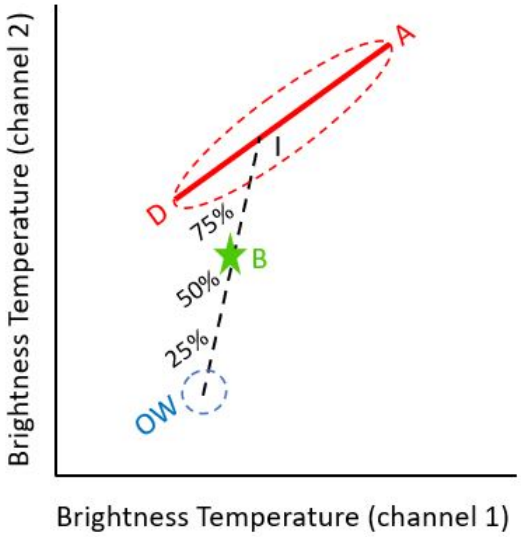

Figure 2.6: A schematic diagram of the technique used in BT algorithm. The line AD represents consolidated ice while OW represents open water. The black dashed line IO measures SIC for an arbitrary point B (represented by a green star).

ucts on various platforms, including satellites, aircraft, and occasionally ships. However, these validation efforts have often been limited to small regions and short time spans. Nevertheless, there has yet to be an effort to quantify the uncertainty in daily or monthly total sea ice extent estimates derived from PM instruments. The total SIC uncertainty (ε_{tot}) is given by two uncertainty components [78]

$$\varepsilon_{tot}^2 = \varepsilon_{alg}^2 + \varepsilon_{smear}^2, \tag{2.12}$$

where ε_{alg} is the inherent uncertainty of the SIC algorithm including residual geophysical noise [14], sensor noise, and ice surface emissivity variability and ε_{smear} is the uncertainty due to resampling from satellite swath to a grid (smearing uncertainty) and also the mismatch between footprints size at different channels (see Table 2.2).

The ε_{alg} is different for each algorithm as they employ different frequency channels, weather filters, brightness temperature corrections, and tie points, resulting in different sensitivities to geophysical noise. For example, the NT algorithm uses the unique tie points

[14]Geophysical parameters such as water vapour, cloud liquid water, surface temperature variability, and surface roughening by wind, all collectively referred to as geophysical noise.

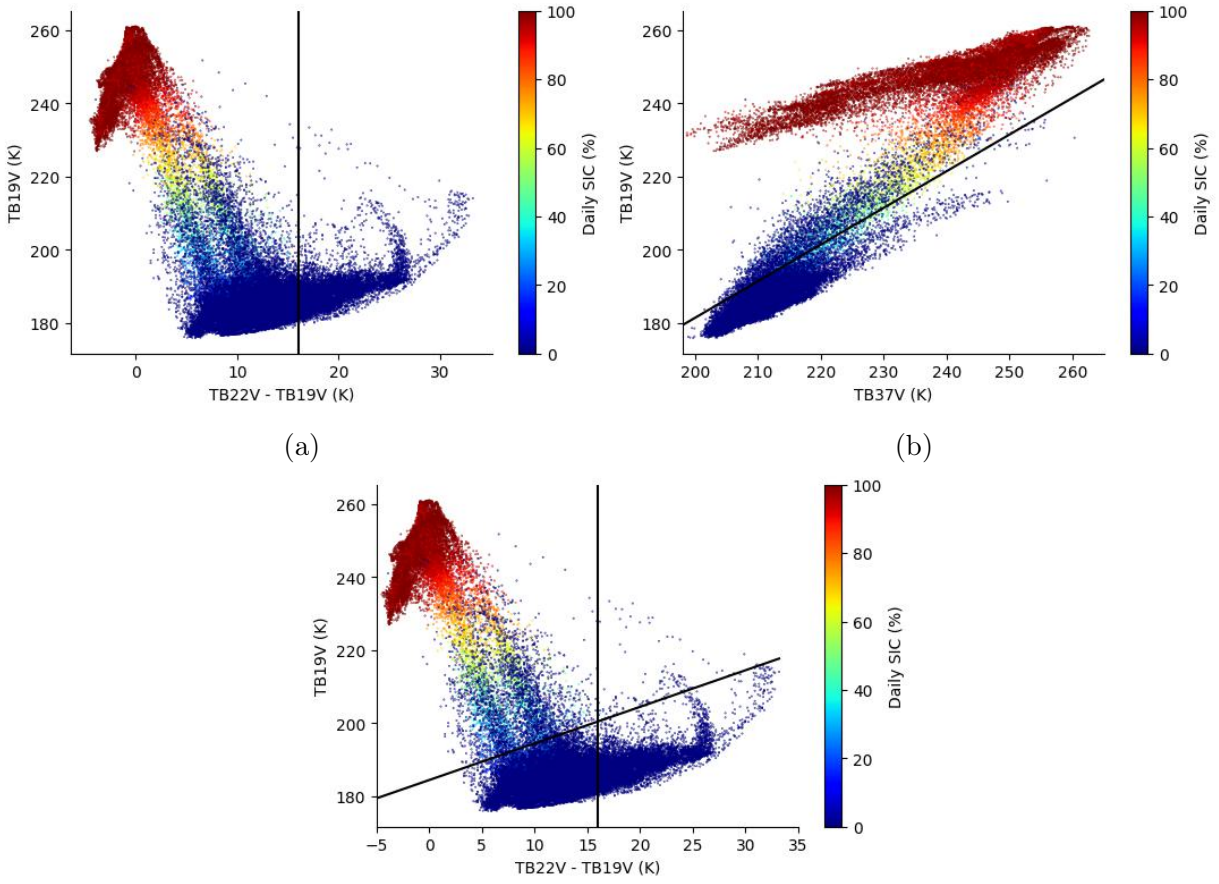

Figure 2.7: An example of TB22V-TB19V vs. TB19v scatter plot and TB37V vs. TB19v (for SSMIS) for 01 January 2021 over the entire Arctic. By applying these weather filters, BT SIC values for points exceeding the black vertical line or lying below the black slanted line are set to zero.

for each hemisphere, while in the BT algorithm, tie points change by date (dynamic) and hemisphere. In this context, employing regional (dynamic) tie points is recommended to optimize SIC algorithms for climate datasets. The dynamic approach ensures long-term stability in the sea ice climate record and mitigates sensitivity to noise parameters influenced by climatic trends. Dynamic tie points play an important role in accurately quantifying SIC uncertainties and inherently compensate for sensor drift or inter-sensor calibration differences. Thus, given that tie points are naturally changing geophysical pa-

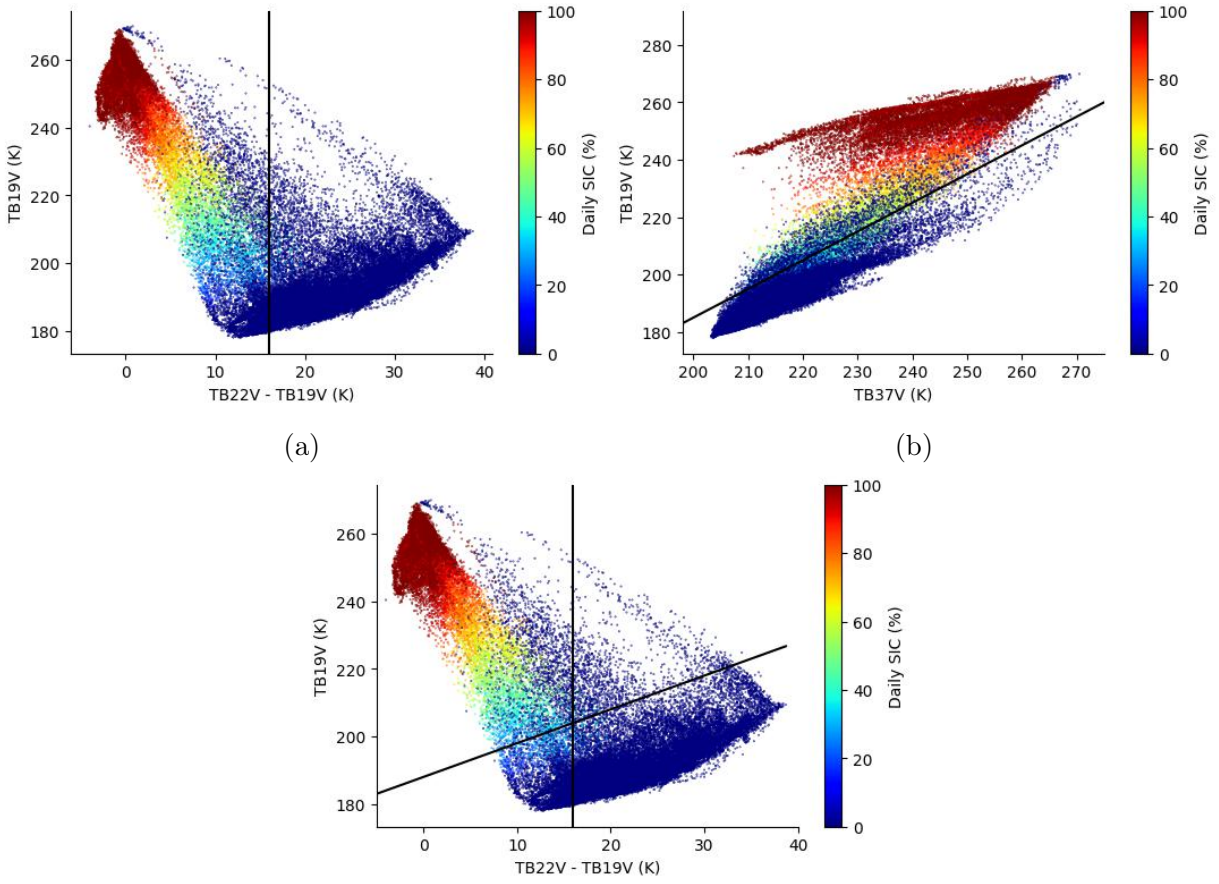

Figure 2.8: An example of TB22V-TB19V vs. TB19v scatter plot and TB37V vs. TB19v (for SSMIS) for 01 June 2021 over the entire Arctic. By applying these weather filters, BT SIC values for points exceeding the black vertical line or lying below the black slanted line are set to zero.

rameters, adopting a dynamic approach is preferable over the traditional static method [56]. Similarly the ε_{smear} can also be different for different algorithms, due to use of different frequency channels. The footprint size for the channels utilized for SIC mapping vary. For instance, for SSM/I the footprint size for the 19 GHz channels is 43 to 69 km and 28 to 37 km for the 37 GHz channels (see Table 2.2). Typically, the SIC data are depicted on a finer grid, usually 12.5 or 25 km, compared to the larger sensor footprint sizes (ranging from 28 to 69 km). This leads to an affect known as smearing. Furthermore,

when footprints of varying sizes are combined in the SIC retrieval algorithms (as inputs), an additional smearing effect occurs, termed the footprint mismatch error.

2.4 Synthetic Aperture Radar

Synthetic aperture radar (SAR) data serves as an alternative data source to obtain SIC information. SAR data can distinguish between different ice types and can provide high-resolution images of sea ice cover, aiding in the accurate determination of sea ice concentration. Furthermore, SAR data can be used to identify ice features such as leads, cracks, and ridges, which are paramount for navigation. This data is obtained from multiple sensors that send a microwave signal to the Earth and subsequently record the signal reflected back. This offers an advantage over PM data because it provides precise control over the amplitude and frequency of the transmitted signal. Hence, SAR data can achieve a superior spatial resolution compared to PM data. The interaction between the SAR signal and the Earth depends on the signal's wavelength, with the SAR signal having the strongest interaction with objects that are similar in size to its wavelength. For instance, C-band SAR data, characterized by a wavelength ranging from 7.5 to 3.8 centimetres (4-8 GHz), has been identified as the most appropriate choice for ocean and ice monitoring [79] which is used in this thesis. SAR signals with this wavelength remain unaltered by cloud cover and atmospheric interference, as these particles are significantly smaller than the wavelength of the SAR signal. The backscatter behaviour of the SAR signal relies on surface attributes like structure and roughness, the incidence angle, and the polarization of the SAR signal [80]. SAR sensors possess the capability to manage the orientation of the signal during transmission and reception, offering four distinct polarization options for SAR images, which are detailed below:

- HH Polarization corresponds to a signal oriented horizontally during both transmission and reception.
- HV Polarization signifies that the signal is horizontally oriented during transmission and vertically oriented during reception.
- VH Polarization denotes a signal that is vertically oriented during transmission and horizontally oriented during reception.
- VV Polarization designates a signal oriented vertically during both transmission and reception.

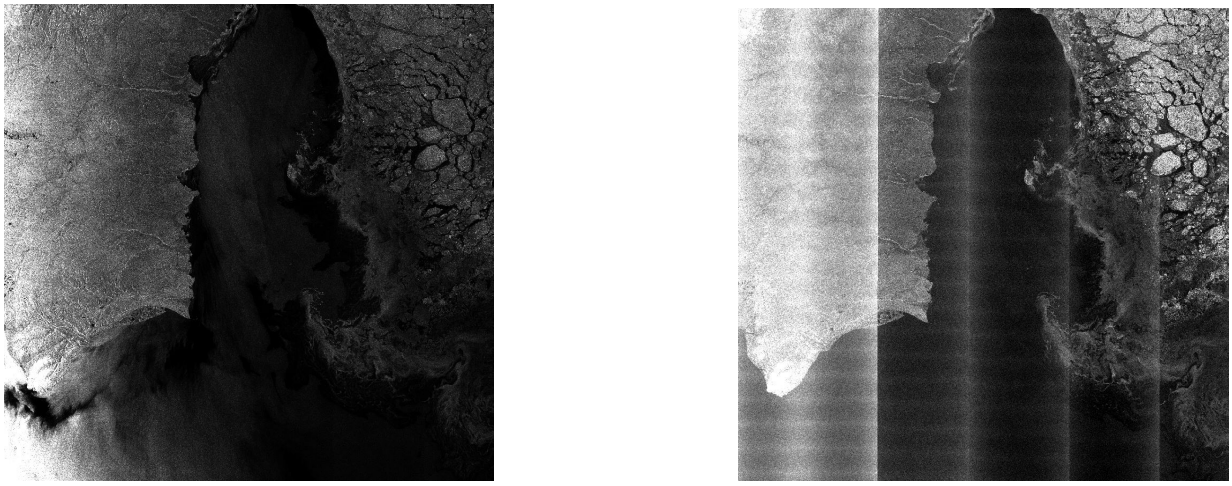

(a) HH (b) HV

Figure 2.9: Sentinel-1 SAR scenes captured on 2021/11/02, over the Beaufort Sea (a) HH Polarized, and (b) HV Polarized. These scenes are obtained from the Alaska Satellite Facility (ASF). The central grid cell coordinate is approximately 127.23° W, 72.12° N. The spatial resolution is 80 meter.

Figure 2.9 illustrates HH and HV polarized Sentinel-1 SAR images. It can be seen that the images of HH and HV polarization exhibit dissimilar appearances and convey distinct information due to their varying interactions with the Earth's surface. HH polarization was employed for its ability to capture a greater number of ice and water features in the images, aiding the model in ascertaining ice concentration. In contrast, HV polarization was chosen due to its relative insensitivity to variations in incidence angles when compared to HH polarization [81]. While SAR images offer numerous advantages for estimating ice concentration, they come with inherent limitations. Primarily, the interaction between the SAR signal and ice and water is highly complicated. The general notion that smooth water appears darker does not consistently hold true, as different incidence angles can cause smooth open water to appear bright in specific regions [82]. Additionally, SIC images are frequently susceptible to image noise, including speckle noise [15] and the presence of banding artifacts [16]. The banding effect is visible in the SAR image of HV polarization, as illustrated in Figure 2.9. Finally, extracting SIC from SAR images poses a challenge due to the limited information available from a single grid cell in a SAR image.

[15]Speckle noise refers to random variations in brightness or color that appear as grainy or speckled patterns in images.

[16]Banding artifacts are patterns of stripes or bands that appear in images.

2.4.1 Sea Ice Concentration Extraction

In the realm of SIC extraction from remote sensing imagery, deep learning has emerged as a transformative technology, significantly enhancing the ability to analyze and interpret vast amounts of data collected from SAR data [83, 84, 85, 86, 87]. This section delves into how deep learning is applied for SIC extraction from SAR imagery, its advantages, challenges, and future prospects. Deep learning algorithms, particularly convolutional neural networks (CNNs), have become instrumental in processing and analyzing remote sensing data. These algorithms excel in handling the high-dimensional data obtained from various sensors, enabling more accurate and efficient analysis than traditional methods. However, there are some challenges and limitations to this method; Data Availability and Quality: The effectiveness of deep learning models in remote sensing is heavily dependent on the availability of high-quality, labeled datasets. Computational Requirements: Training deep learning models requires significant computational resources, which can be a constraint for many researchers. Interpretability: Deep learning models in remote sensing, like in other fields, often act as "black boxes", making it challenging to understand how they derive their conclusions. In this study, we employed CNN model to extract SIC from SAR imagery.

Convolutional Neural Network

CNNs have become a cornerstone in the field of deep learning, particularly in the analysis of imagery. In remote sensing, CNNs are instrumental in processing and interpreting data obtained from aerial and satellite sensors, offering unparalleled capabilities in understanding spatial and temporal patterns on the Earth's surface. A CNN is a type of deep neural network designed to process data with a grid-like topology, such as images. It consists of several layers, each designed to perform specific operations that transform the input data into a more abstract and composite representation. The output of a convolutional layer is the convolution operation between the input and a user-specified number of filters.

The key components of CNNs are Convolutional Layers: These layers apply a set of learnable filters to the input. Each filter activates certain features at different spatial locations, capturing patterns like edges, textures, and shapes. Pooling Layers: Pooling

(usually max pooling) reduces the spatial size of the representation (depending on stride [17] number), decreasing the number of parameters and computation in the network, thereby controlling overfitting. Fully Connected Layers: Towards the end, CNNs have fully connected layers that use the features learned by the convolutional and pooling layers for classifying the input into various categories. Activation Functions: CNNs use activation functions like ReLU (Rectified Linear Unit) to introduce non-linear properties into the network, enabling it to learn more complex patterns in the data.

A fully convolutional network (FCN) is a type of deep learning model that shares similarities with a CNN due to its convolutional layers. However, it diverges from a traditional CNN in that it lacks fully connected layers at its conclusion [88]. FCNs are predominantly employed for tasks such as semantic segmentation, where each grid cell is assigned to a specific class. The ability of FCNs to process image patches in a single inference step renders them suitable for tasks like assigning ice concentration labels on a per-grid cell basis. The method being proposed utilizes an FCN that is structured on a U-net framework. The U-net architecture is a form of FCN that incorporates both encoding and decoding phases, supplemented by skip connections. The encoding phase of the U-net architecture represents a downsampling process, during which the initial input is subjected to feature extraction, yielding a condensed feature map. This dimensionality reduction is typically achieved through pooling operations. Conversely, the decoding phase involves upsampling, whereby the feature map produced during the encoding stage is reconstructed back to its original size.

2.5 Sea Ice Chart

Ice charts are based on a combination of all available data on ice conditions, including meteorological data, visual ship observations, airborne radar measurements, satellite images, and climatological information. These charts are generated at either the same spatial resolution as the data or slightly coarser [5]. To produce daily ice charts, trained analysts visually inspect all data available to estimate ice conditions. These conditions are used to identify spatial regions that have relatively similar ice attributes, which are indicated by drawing polygons on a map. In Figure 2.10 the Canadian Ice Service (CIS) daily ice chart on February 03, 2014, over the eastern Canadian Arctic is displayed as an illustration.

[17] The number of pixels by which we move the filter across the input image.

These daily ice charts are generated to facilitate operational activities such as shipping throughout the freeze-up to break-up periods. Since shipping activities are minimal during the consolidated ice season, the majority of charts generated during freeze-up and break-up period. Utilizing ice charts during this period offers two significant advantages: firstly, the freeze-up period is when PM SIC retrieval algorithms perform poorly due to the presence of thin ice (e.g., [53]); secondly, the break-up period is when PM SIC retrieval algorithms do not perform well due to the occurrence of surface melt (e.g., [89]). Daily ice charts (available at a different temporal frequency such as regional or weekly) are helpful in sea ice edge monitoring during periods when sea ice edge location and length fluctuate frequently (e.g., freeze-up period, a period during which the ice changes quickly in response to changing in air temperature and wind conditions). The daily ice charts can therefore provide insight into these fluctuations. The accuracy of these products is related to different factors such as the availability and resolution of source information as well as atmospheric conditions (e.g., cloud coverage or daylight), and surface conditions (e.g., covered with snow or rain) [90]. Details of the accuracy of a visually estimated ice concentration from these charts can be found in a study by Cheng *et al.* [91]. It is known that ice charts provide an accurate ice edge location [92, 93, 94]. The CIS daily ice charts (used in this study) are available from 2006 to the present. Prior to 2006, there was only the weekly regional ice chart available.

Egg Code

Each polygon within the ice chart is assigned an egg code (Figure 2.11), which follows the international standard set by the World Meteorological Organization (WMO) for coding ice-related information [2]. The egg code comprises details about the total ice concentration (C), the stage of ice development (S), and the predominant form of the ice floe (F), all encapsulated within an oval shape. At the highest level of the egg code, the total ice concentration (C_t) is specified, encompassing all stages of ice development. This total ice concentration is further divided into three partial ice concentrations: C_A, C_B, and C_C, forming the second row of the egg code. These partial concentrations reflect the presence of the first, second, and third thickest ice, along with their respective stages of development (S_A, S_B, and S_C). This breakdown into partial concentrations is utilized when multiple ice types coexist within the delineated polygon. Conversely, when only one type of ice is present, no partial concentration is reported. Within each of these three ice types (C_A, C_B, and C_C), the predominant form of the ice floe is denoted by F_A, F_B, and F_C, respectively. In ice charts, the concentration of ice is expressed as a tenth of the total concentration (1/10, 2/10, etc.). When the concentration falls below 1/10, it signifies open water, indi-

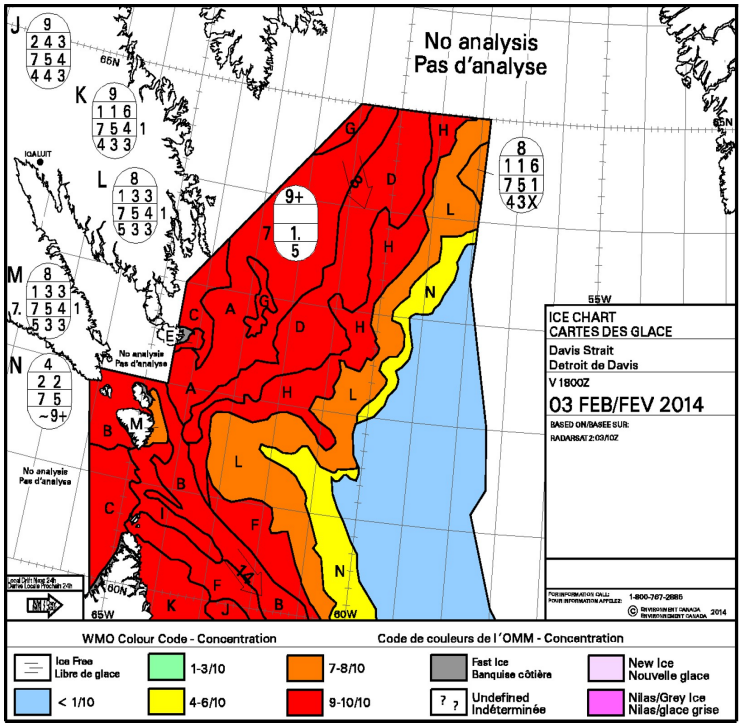

Figure 2.10: Daily ice chart from the Canadian Ice Service (CIS), showing ice conditions over the eastern Canadian Arctic on February 03, 2014.

cating that there is some ice present, although less than 1/10 of the area is covered by ice. This definition helps capture situations where ice is not completely absent but is present in very small quantities.

2.6 Other Available Products

In addition to the previously mentioned SIC products, various other offerings from distinct operational centers are also accessible for download. Specifically:

- **MODIS & AMSR2 SIC** [95]: Since October 2019, the University of Bremen has been generating SIC data at a 1 km grid resolution derived from both MODIS (Thermal infrared data) and ASI-AMSR2 (PM data) sources. Thermal infrared data offer high spatial resolution (1 km), but are limited to cloud-free conditions. In contrast,

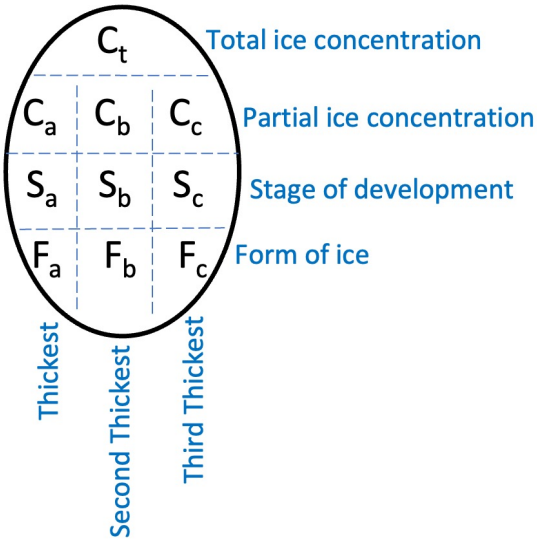

Figure 2.11: The World Meteorological Organization (WMO) standard egg code used for Canadian Ice Service (CIS) ice charting [2]. C_t is the total ice concentration value, C_A, C_B, and C_C are the first, second, and third thickest ice along with their respective stages of development (S_A, S_B, and S_C). F_A, F_B, and F_C show the predominant form of the ice floe in the mentioned three ice types.

AMSR2 data provide lower spatial resolution (5 km for the 89 GHz channels) but are available regardless of cloud cover. The thermal infrared SIC is determined based on local temperature anomaly [96] and enhancements detailed in Ludwig *et al.* [97]. The merging process involves selecting a 5 × 5 km box, roughly equivalent to one AMSR2 footprint. Within this box, the thermal infrared SIC is adjusted to match the mean of the PM SIC, while preserving their distribution. This ensures SIC consistency at the transition between cloud-free and cloudy pixels. Cloud-covered areas lacking thermal infrared SIC are filled with PM SIC, reducing the resolution to 5 km. Once merged, daily means are calculated, resulting in a spatially continuous SIC product at 1 km resolution (in some regions), five times finer than from AMSR2 PM observations [98].

- **NSIDC SIC CDR** [99]: The National Snow and Ice Data Center (NSIDC) is a repository for cryosphere and related geophysical data from various NASA Earth-observing satellite missions, airborne campaigns, and field observations. It offers a Climate Data Record (CDR) of SIC, available on a daily and monthly basis from 25

October 1978 to the present, with a spatial resolution of 25 km. This dataset covers both the Arctic and Antarctic regions. The CDR algorithm integrates SIC data from two established algorithms: the NASA Team (NT) algorithm and Bootstrap (BT) algorithm. It employs a rule-based approach to combine the outputs of these algorithms, capitalizing on their individual strengths. Widely utilized for climate model inputs, reanalyses, and environmental monitoring, the NSIDC CDR SIC dataset is valued for its long-term consistency and comprehensive monitoring of polar sea ice conditions (e.g., [100, 101, 66, 59]).

- **ESA SIC CDR** [102]: The Centre for Environmental Data Analysis (CEDA) is a UK-based organization that provides access to the European Space Agency (ESA) Sea Ice Climate Change Initiative (CCI) SIC product, which aims to provide long-term climate records from satellite data.It uses the measurements from the SSM/I and SSMIS over the polar regions (Arctic and Antarctic). This dataset is an enhanced-resolution version of the EUMETSAT (European Organisation for the Exploitation of Meteorological Satellites) Ocean and Sea Ice Satellite Application Facility Global Sea Ice Concentration Climate Data Record (OSI SAF OSI-450-a CDR) over the period 1991-2020.

- **EUMETSAT SIC CDR** [103]: The Ocean and Sea Ice Satellite Applications Facility (OSI SAF), operated by the European Organisation for the Exploitation of Meteorological Satellites (EUMETSAT), offers a range of SIC CDRs and interim CDRs (ICDRs) vital for climate research and model assessment. Among these, OSI-450-a is the most recent iteration of EUMETSAT OSI SAF Global SIC CDR, spanning from 1978 to 2020, derived from SMMR, SSM/I, and SSMIS satellite data. Complementing this, OSI-430-a serves as the ICDR extending OSI-450-a from 2021 onward. Both OSI-450-a and OSI-430-a furnish daily and monthly averaged SIC, alongside monthly sea ice extent. These values represent the fractional percentage of ice cover per grid cell, accompanied by corresponding per-cell uncertainty estimates. The reliability of OSI SAF SIC products is underscored by extensive validation efforts, including direct comparisons against meticulously curated 0% and 100% SIC reference datasets, as well as assessments against US National Ice Center charts and the NSIDC sea ice index. Widely adopted by climate modelers, numerical weather prediction, and ocean/ice reanalysis applications, these EUMETSAT OSI SAF SIC CDRs and ICDRs serve as key resources for understanding and forecasting climate dynamics.

- **C3 Sea Ice Edge** [104]: The Copernicus Climate Change Service (C3S) is a component of the European Union's Copernicus program, offering daily sea ice edge data with a 12.5 km gridded resolution. The sea ice edge categorizes the sea surface into

open water, open ice, and closed ice based on the amount of sea ice within each grid cell. This data is available for both the Northern and Southern Hemispheres. The SIC threshold of 30% is used to distinguish between open water and open ice, which is different from the 15% threshold commonly used for sea ice extent. The dataset relies on measurements from the series of SMMR, SSM/I, and SSMIS sensors. It combines CDRs, designed to offer sufficient length, consistency, and continuity for assessing climate variability and change, with ICDRs, providing regular temporal extensions to the CDRs, with expected consistency but not extensively verified. The CDRs of sea ice edge currently extend from 25 October 1978 to 31 December 2020.

- **USNIC MIZ** [105]: The U.S. National Ice Center (NIC) is a U.S. Navy, National Oceanic and Atmospheric Administration (NOAA), and U.S. Coast Guard partnership responsible for monitoring sea ice and providing operational ice analysis services. The daily MIZ product is defined by the World Meteorological Organization (WMO) as "the region of an ice cover which is affected by waves and swell penetrating into the ice from the open ocean". This data product is a U.S. National Ice Center (USNIC) rendering of the MIZ as the band of ice in concentrations between 1/10 and 8/10, or about 10% to 80% concentration. To define the MIZ the U.S. National Ice Center Arctic and Antarctic Sea Ice Charts are used. This MIZ product is vector-based and lack inherent resolution and is available from September 2004 for the Arctic.

The scarcity of the sea ice edge and MIZ products, compared to SIC products, is a key motivating factor for this research. Acknowledging this shortage, this thesis aims to generate sea ice edge and MIZ products to facilitate comprehensive analysis in climate studies focusing on polar regions.

Chapter 3

Sea Ice Edge Displacement Error

3.1 Introduction

The sea ice edge serves as the boundary between open water and sea ice, playing an important role in ship navigation as well as delineating the MIZ, a vital habitat for marine mammals and seabirds [106]. To determine the edge contour, a specific SIC threshold, typically set at 15%, is employed. The initial justification for this threshold stems from early validation studies, which observed that the 15% concentration contour exhibited the closest agreement with the 'true' ice edge in high-resolution airborne or satellite data [107]. Also, as a consequence of satellite orbit characteristics, PM instruments encounter a coverage gap, commonly referred to as the "pole hole", near the pole. The dimensions of this gap have varied among different sensors. It is generally assumed that the gap, present in all sensors, is ice-covered (>15% concentration). Consequently, the area of the pole hole is incorporated into the total extent measurement [108]. Another practical rationale for utilizing the 15% threshold is the implementation of post-processing "weather filters" by most algorithms. These filters are designed to mitigate weather-related artifacts, yet in practice, they may erroneously remove some low-concentration ice [56]. By adhering to the 15% threshold, the potential impact of the weather filter on extent estimates is minimized [108].

Accordingly, ice edges are defined as areas (e.g., grid cells) with a SIC of 15% or higher. In a prior investigation, the sea ice edge derived from PM data using ASI and BT algorithms was compared with pseudo-ship-observations based on the analysis of six moderate-resolution imaging spectroradiometer (MODIS) images over the Arctic region. The mean SIC at the edge determined from ship observations was found to be 10.5% for

ASI and 23.6% for BT. Notably, ASI exhibited similar SIC values at the ice edge in both summer and winter, while a significant difference was observed for the BT algorithm. This disparity suggests that the ASI ice edge location on cloud-free days is less variable than that determined by the BT algorithm, possibly indicating the latter's greater sensitivity to surface emissivity variations [109].

Microwave radiation emitted by the atmosphere has an impact on sea SIC retrieval algorithms, particularly near the ice edge [56]. The ASI algorithm assumes that atmospheric influence is a smooth function of the ice concentration and selects a third-order polynomial for the SIC between 0% and 100% ice cover. On the other hand, the BT algorithm adapts ice and water tie points seasonally (winter and summer) without regional specificity, employing one set of tie points for the northern hemisphere and another for the southern hemisphere. In contrast, the NT2 algorithm employs a radiative transfer model to address atmospheric effects, considering 12 sets of representative atmospheric conditions over both ice and open water. An evaluation of the NT2 SIC, utilizing synthetic aperture radar (SAR) data from RADARSAT-1 and MODIS images in the Bering Sea [92], revealed reasonable agreement between NT2 algorithm-derived ice edges and SAR ice edge locations under various wind range and temperature conditions. The study endorsed the use of manually derived ice edges from SAR for comparison with PM data and highlighted NT2's tendency to underestimate SIC for thin ice and overestimate it in frazil [1] ice conditions relative to SAR. Additionally, an assessment of the NT2 sea ice edge over the Arctic using the interactive multisensor snow and ice mapping system (IMS) indicated higher uncertainty associated with ice edge location during the melt season [110].

Currently, there is a lack of recent studies examining the performance of PM-based sea ice edge in comparison to ice charts, particularly in seasonal ice zones, which are becoming increasingly prevalent in Arctic regions [111]. Given the significance of PM sea ice concentration (SIC) products in long-term shipping route planning, reanalysis data production, climate monitoring, and forecasting, this study aims to quantify the agreement between sea ice edges derived from the ASI, NT2, and BT SIC retrieval algorithms and those obtained from daily Canadian Ice Service (CIS) charts in predominantly seasonal ice zones over the years 2013-2021. While the ASI algorithm offers finer spatial resolution compared to many PM sea ice products, the NT2 algorithm addresses weaknesses in the original NASA Team (NT) algorithm, particularly its sensitivity to emissivity variations, which is a key advantage of the NT2 algorithm. The BT algorithm, has been used in climate-related

[1] Frazil ice comprises loose, randomly oriented ice crystals that are typically millimeter and sub-millimeter in size with a variety of shapes.

studies to provide a long-term, consistent, and comprehensive SIC dataset. These characteristics lead us to choose these PM SIC retrieval algorithms to investigate the sea ice edge.

Regarding the evaluation of the ice edge displacement derived from two products, several metrics have been explored. Some of the metrics employed include the integrated ice-edge error [30], the root mean square ice edge displacement, the average ice edge displacement, the ice edge displacement bias, and the Hausdorff distance [112]. Notably, there is no agreement on the best measure [113] and these metrics focus solely on the displacement of two compared edges without accounting for their respective lengths. This becomes important when two ice edges are situated at the same location yet possess different lengths. Such situations can arise either when comparing ice edges from the same product at different times or when comparing different products at the same time. To address this limitation and consider both edge length and displacement, this research introduces an edge-length-based dimensionless measure called edge displacement error (EDE). This study aims to evaluate the performance of PM SIC products in sea ice edge estimation by using the EDE and the weighted average Hausdorff distance (δ_H^{wavg}), a recommended metric in previous research [112].

3.2 Experimental Design

3.2.1 Study Area

The study area covers sea ice along Baffin Island and the Davis Strait (Figure 3.1, panel a). This region has a high species richness of Arctic marine mammals, including narwhals, beluga whales, bowhead whales, ringed seals, and bearded seals [114]. Pikialasorsuaq, a large polynya in the northern part of Baffin Bay, serves as a critical breeding and feeding habitat for seabirds, attracting millions of them during the summer for feeding [115]. Thus, this region can play an essential role in polar ecosystems. Local Inuit depend on these Arctic marine mammals, and the marine environment for their livelihood [16], utilizing the ice cover as both a hunting platform and transportation route. At the same time, shipping traffic in this region is increasing [9], driven by the Mary River mine's demand to extend the shipping season [15]. Sea ice loss and increased ship traffic may increase noise pollution, and these trends may also threaten Arctic marine mammals' populations. This region corresponds to the eastern Canadian Arctic charting region for daily ice charts produced by CIS. It is important to note that over the study area, the coverage of the ice

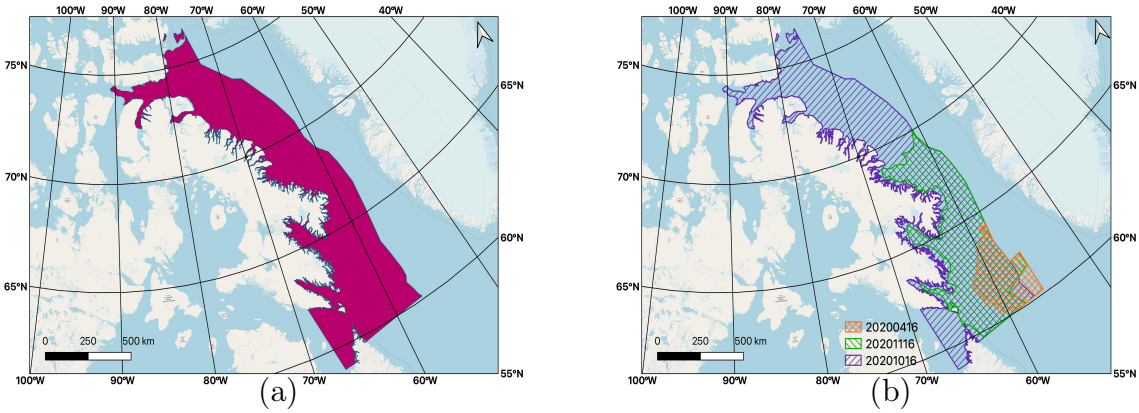

Figure 3.1: (a) The red outline shows the region of study, which is based on the maximum extent of all available daily ice charts during the study period. (b) An example of the data set coverage over the study area for a given day. Each date's coverage is indicated by a polygon with different colors. The study area's size changes daily and month to month due to changes in the area over which CIS is required to provide ice conditions, which depends on shipping and other activities in the region. Notice that the largest charted area in panel (b) is for October when the ice starts to freeze up, and there is still activity over a large region of Baffin Bay. Datum is the world geodetic system 1984 (WGS84), and the projection coordinate system is Lambert conformal conic.

chart data set varies, and therefore our study region varies daily, monthly, and annually. An example of how the charted region changes over time is demonstrated in Figure 3.1, panel b. Each date's coverage is indicated by a polygon with different colors. The study area's size changes daily and monthly due to changes in the area over which CIS is required to provide ice conditions, influenced by shipping and other regional activities. Notice the largest charted area in Figure 3.1, panel b is for October, which is when the ice is starting to freeze up, corresponding to heightened activity across a large expanse of Baffin Bay. In contrast, the smallest charted area is in April when there is limited shipping activity. The study period was selected as 2013-2021 to focus on recent changes. To evaluate the ice edge in this region, monthly SICs from October to June were utilized for sea ice edge calculations.

3.2.2 Dataset

Reanalysis Data

The climate variables required for this study are obtained from the European Centre for Medium-Range Weather Forecasts (ECMWF) Reanalysis 5th Generation (ERA5) dataset, accessible through the Copernicus climate data store [116]. ERA5 provides hourly data spanning 24 hours, with a spatial resolution of 30 km, covering the time period from 1940 to the present. To calculate the 10-meter wind speed in meters per second (m/s), we derive it by combining two original components: the 10-meter meridional component and the 10-meter zonal component of wind. The ERA5 dataset compiles in-situ data from the WMO Information System (WIS) Drifting Buoy dataset. The 10-meter meridional component represents the horizontal air movement speed toward the north, measured at a height of 10 meters above the Earth's surface. Conversely, the 10-meter zonal component of wind signifies the horizontal air movement speed toward the east. These two components are then combined to produce a unified measure of horizontal 10-meter wind speed by calculating the magnitude between the meridional and zonal components. The air temperature at a 2-meter height above the land or sea surface is measured in kelvin (K). ERA5 gathers and consolidates temperature data from the WIS as well. To ensure calculation consistency, the reanalysis data are re-gridded to the chart spatial resolution using bilinear interpolation.

PM SIC

In this study, the AMSR2 ASI SIC with a 6.25 km gridded resolution is obtained from the University of Bremen, Germany [58]. The AMSR2 NT2 SIC with a 12.5 km gridded resolution is acquired from the United States National Snow and Ice Data Center (NSIDC, [117]). The SSMIS BT SIC with a 25 km gridded resolution is obtained from the NSIDC [118]. To ensure calculation consistency, all SIC products are re-gridded to the chart spatial resolution using bilinear interpolation.

Chart SIC

CIS daily ice charts are obtained from Environment and Climate Change Canada (ECCC). The CIS daily ice charts are accessible in a format defined by the World Meteorological Organization (WMO) known as Sea Ice Grid (SIGRID). The SIGRID-3 format comprises

several files, including a shape file (.shp) accompanied by associated files (.dbf, .prj, .shx), and a metadata file (.xml). These files are bundled together into a zip file (.zip) for distribution. The shapefile serves as the central component, containing vector data that represents various aspects of ice information, including ice polygons and their associated attributes. To utilize this data effectively, vector files are initially converted into raster files. The Geospatial Data Abstraction Library (GDAL) in Python is employed to rasterize vector inputs. This procedure yields ice chart information at a grid cell level. The spatial resolution selected for this process is 5 km. As an illustrative example, Figure 3.2 displays the corresponding rasterized ice chart for February 03, 2014, covering the eastern Canadian Arctic.

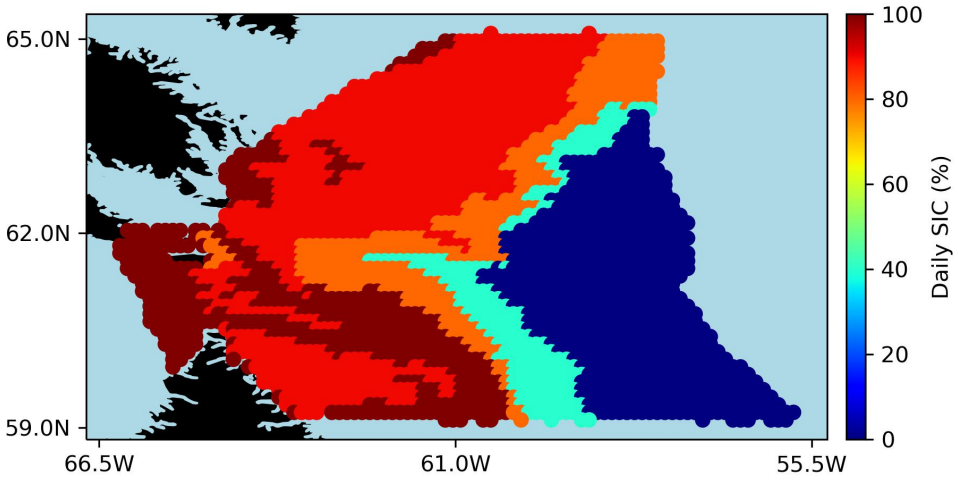

Figure 3.2: The rasterized CIS daily ice chart on February 03, 2014, over the eastern Canadian Arctic. Regions without data are shown in light blue, while land is shown in black.

Following the rasterization process [2], we updated the total ice concentration based on the code tables for SIGRID-3 variables (Appendix 5 given in [1]). We used SA, SB, SC, CA, CB, and CC to define the ice stage of development and the corresponding partial concentration for each grid cell. Consequently, each grid cell had three partial ice concentrations associated with three different stages of development in a single day. Lastly, we calculated the daily mean value of each partial ice concentration for each stage of development for

[2]The process of converting spatial data, typically in vector format, into a raster format which is made up of pixels.

the given grid cell. Based on the ice stage of development, we classified the ice type of the ice-covered grid cells (where SIC is not zero) into two categories:
1- thin ice: ice with thickness ≤ 30 cm (the thickness of more than 30 cm is not considered thin ice [56],
2 - thick ice: ice with thickness > 30 cm.
It is noted that the ice thickness range is assigned to each ice type based on the code tables for SIGRID-3 variables (Appendix 5 given in [1]). Table 3.1 outlines the stage of development associated with each ice category (thin and thick) considered for this study. It should be noted that these categories are less reliable after the ice growth season has been completed (according to our personal communication with CIS).
An illustration of SIC retrieved from the ASI, NT2, BT algorithms, rasterized ice chart, and CIS daily ice chart on February 03, 2014, over the study area is shown in Figure 3.3.

Table 3.1: Ice categories based on the ice stage of development included in the CIS ice charts. Adapted from the code tables for SIGRID-3 variables (Appendix 5 given in [1]).

Ice Category	Development Stage	Ice Thickness (cm)
Thin	New Ice Nilas and Ice Rind Young Ice Grey Ice Grey-White Ice	≤ 30
Thick	First Year Ice Thin First Year Ice Medium First Year Ice Thick First Year Ice Old Ice Second Year Ice Multi Year Ice Glacier Ice	> 30

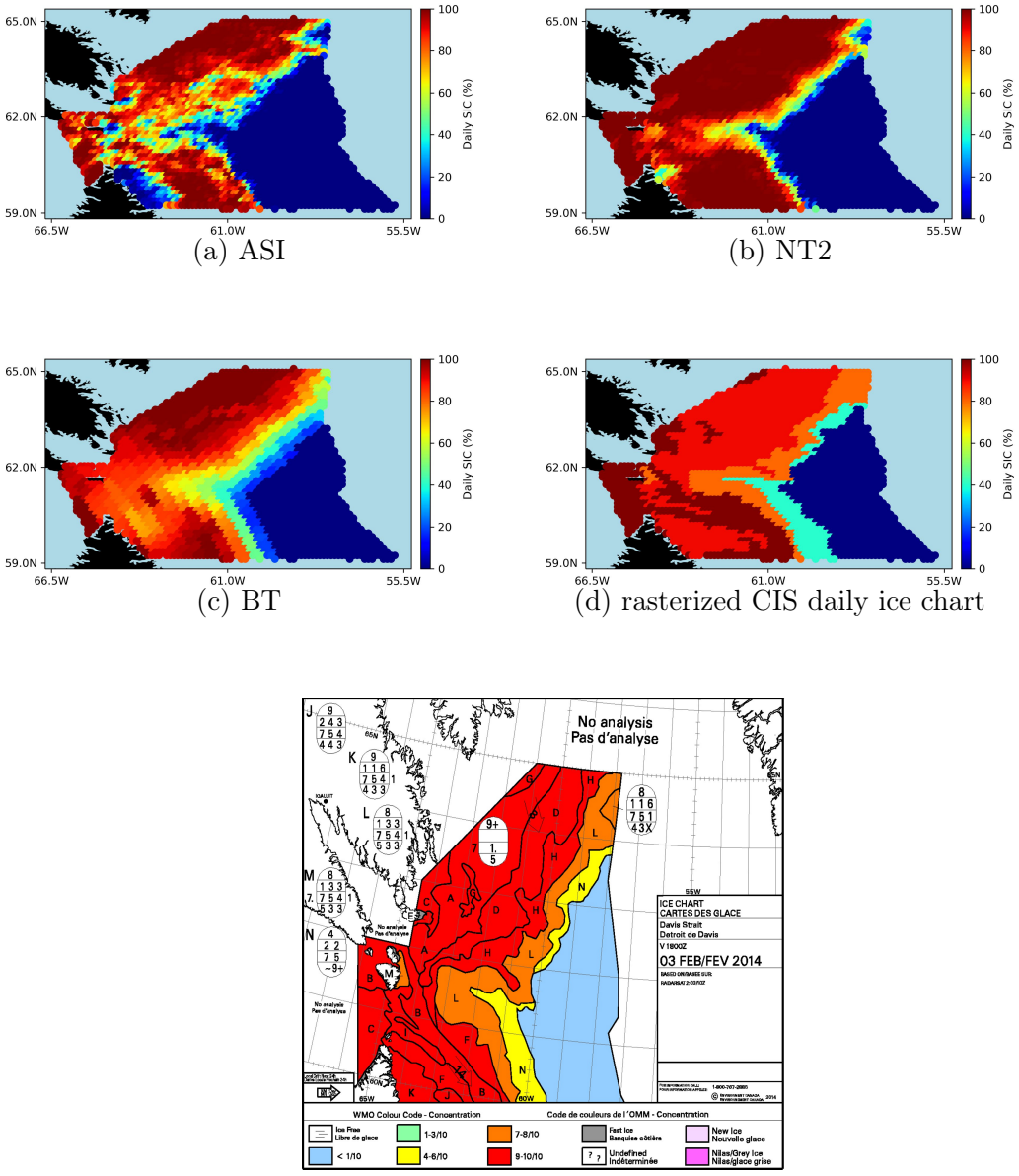

(a) ASI

(b) NT2

(c) BT

(d) rasterized CIS daily ice chart

(e) CIS daily ice chart

Figure 3.3: An illustration of SIC retrieved from the ASI (panel a), NT2 (panel b), BT (panel c) algorithms, rasterized CIS daily ice chart (panel d), and CIS daily ice chart (panel e) on February 03, 2014, over the study area. In panels a to d, regions without data are shown in light blue, while land is shown in black.

3.2.3 Sea Ice Edge Estimation

Following the calculation of the daily SIC value for each PM product, we generated the corresponding daily SIC based on the exact geolocation and date indicated on the CIS charts. A common method for estimating the ice edge location [112] for each product is to find grid cells with SICs exceeding 15% while their neighbours' SICs are below 15%. For a grid cell at i, j location and concentration of c, we consider it as the edge grid cell or e[i,j] if

$$c[i,j] \geq 15\% \quad \text{AND} \quad \min(c[i-1,j], c[i+1,j], c[i,j-1], c[i,j+1]) < 15\%. \tag{3.1}$$

After defining the edge grid cells using Equation 3.1, we applied the density-based spatial clustering of applications with noise (DBSCAN) method [119] to delineate the contour intersecting the MIZ. This is done to obtain a robust ice edge by eliminating the isolated ice patches. It is worth noting that the BT algorithm scarcely needed the clustering process, implying that the estimated edge is almost continuous due to its coarse spatial resolution and limited detail on SIC and sea ice edge. Figure 3.4 represents how the DBSCAN clustering method modifies the chart, ASI, NT2, and BT sea ice edges.

3.2.4 Edge Displacement Error

To assess the agreement between sea ice edge locations derived from the PM algorithms (ASI, NT2, BT) and those from the ice charts, we employed a recommended metric by Melsom *et al.* [112] known as the weighted average Hausdorff distance (δ_H^{wavg}, measured in kilometer)

$$\delta_H^{wavg} = \frac{1}{2}\left[\frac{1}{N_{ch}}\sum_{n=1}^{N_{ch}}\delta_{ch}^n + \frac{1}{N_{PM}}\sum_{n=1}^{N_{PM}}\delta_{PM}^n\right], \tag{3.2}$$

where N_{ch} and N_{PM} are the number of edge grid cells derived from the chart and PM product, respectively. δ_{ch} and δ_{PM} are the distance from the chart edge grid cell to the nearest edge grid cell derived from the PM product and the distance from the PM product edge grid cell to the nearest edge grid cell derived from the ice chart. A more detailed description, including a detailed comparison with other metrics, can be found in Melsom *et al.* [112]. By employing Equation 3.2, we can calculate the distance between two sea ice edges [112]. It is important to note that this approach only provides the distance between two sea ice edges [112]. The sea ice edges, however, may have different edge lengths while overlapping partially.

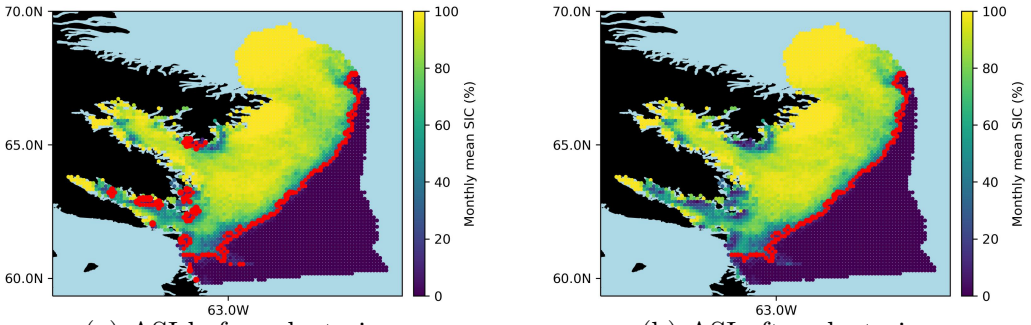

(a) ASI-before clustering (b) ASI-after clustering

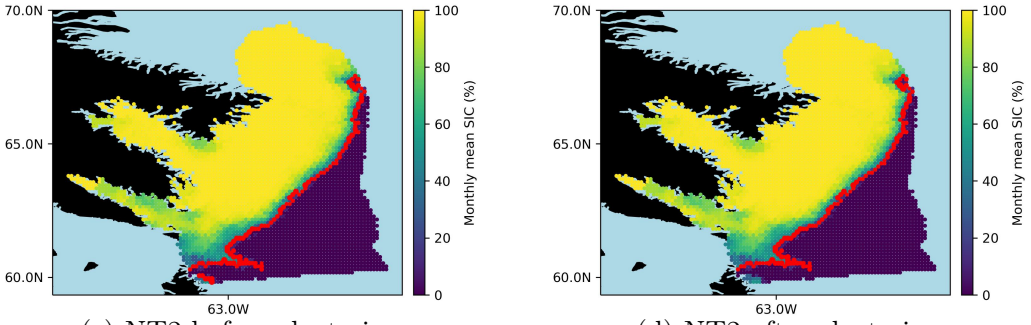

(c) NT2-before clustering (d) NT2-after clustering

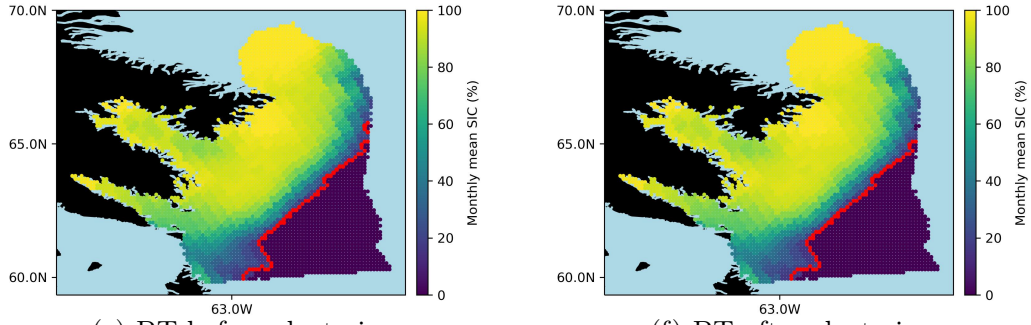

(e) BT-before clustering (f) BT-after clustering

Figure 3.4: An example of how the DBSCAN clustering method works for the ASI, NT2, and BT algorithms for the sea ice edge of December 2013 before clustering (panel a, c, e) and after clustering (panel b, d, e). The regions without data are shown in light blue, while land is shown in black.

Acknowledging the variability in both the location and length of the ice edge over time, we introduced the Edge Displacement Error (EDE). EDE is a dimensionless measure defined as

$$\text{EDE} = \frac{\delta_H^{wavg}}{L_{avg}}, \tag{3.3}$$

where L_{avg} is the average ice edge length (measured in kilometer) and can be expressed as

$$L_{avg} = \frac{L_{ch} + L_{PM}}{2}, \tag{3.4}$$

where L_{ch} and L_{PM} are the ice edge length from the chart and PM product, respectively. EDE can be any value equal to or greater than zero, where a zero EDE value indicates the ideal scenario where the location and length of the two ice edges are perfectly matched. In this study, the ice edge is defined as a grid cell set that satisfies the specified condition outlined above (Equation 3.1). To find the ice edge length derived from the chart and PM algorithm (L_{ch} and L_{PM}, respectively), it is necessary to consider the position of the ice edge grid cell derived from the chart and PM algorithm ($l_{ch}^{i,j}$ and $l_{PM}^{i,j}$, respectively), summing up the lengths of all grid cells [112]: $L_{ch} = \sum l_{ch}^{i,j}$, $L_{PM} = \sum l_{PM}^{i,j}$, where i, j are the position of ice edge grid cell derived from the chart and PM algorithm, respectively. For a detailed description of the computation of $l_{ch}^{i,j}$ and $l_{PM}^{i,j}$ refer to Melsom *et al.* [112].

Figure 3.5 represents how EDE and δ_H^{wavg} can be different in two scenarios, assuming the grid cell size is 10 km:
a) sea ice edges are in straight lines or with a few turns (EDE = 0.21, δ_H^{wavg} = 13.87 km),
b) sea ice edges are in meandering patterns with numerous turns (EDE = 0.12, δ_H^{wavg} = 15.90 km).
The EDE value in the first scenario (Figure 3.5, panel a) is higher than in the second scenario (Figure 3.5, panel b), while the δ_H^{wavg} in the first scenario is smaller than in the second scenario. The discrepancies can be explained by the fact that in the first scenario, the EDE and δ_H^{wavg} both can capture the edge displacement (regardless of the variation in edge lengths) since the edge lengths are approximately equal. In the second scenario, where sea ice edges meander, the edge lengths differ. Consequently, the δ_H^{wavg} (Equation 3.2) can only capture the distance between two edges. In this context, dividing δ_H^{wavg} by the average edge length (Equation 3.4) yields the normalized edge displacement (Equation 3.3). The EDE measurement, in this scenario, reflects the discrepancy in edge length and displacement.
Figure 3.6 illustrates the workflow of the described methodology.

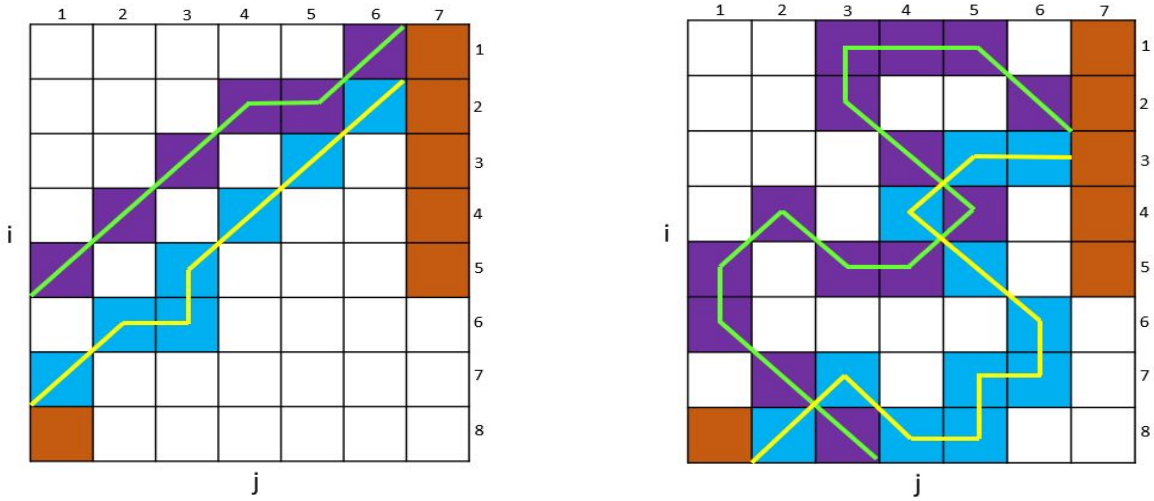

Figure 3.5: A schematic representation of the chart and PM algorithm ice edge lines (represented by green and yellow lines, respectively). Land grid cells are shown in brown. i and j show the position of grid cells. This figure represents how EDE and δ_H^{wavg} can be different in two scenarios, assuming the grid cell size is 10 km: a) sea ice edges are in straight lines or with a few turns (EDE = 0.21, δ_H^{wavg} = 13.87 km), b) sea ice edges are in meandering patterns with numerous turns (EDE = 0.12, δ_H^{wavg} = 15.90 km).

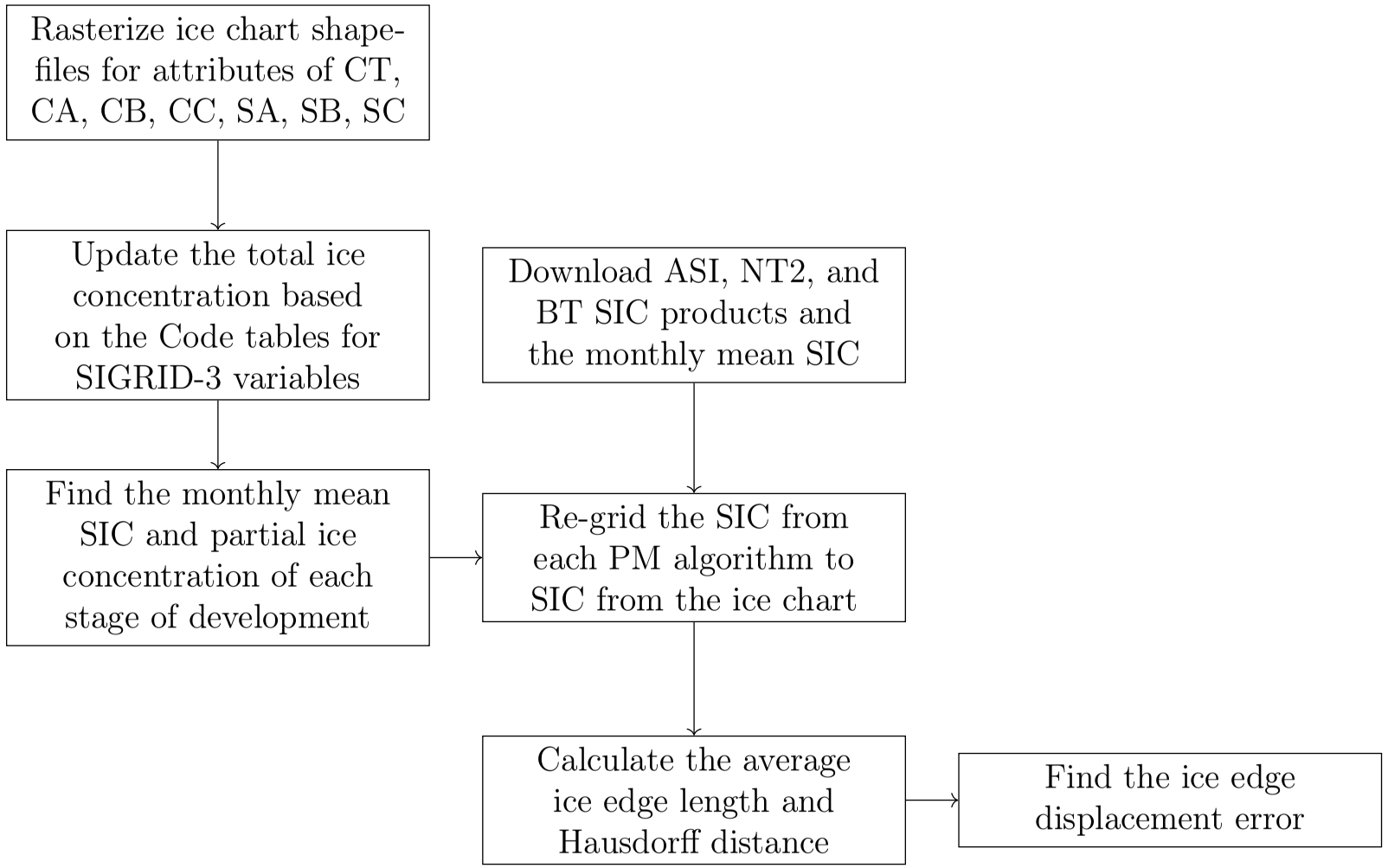

Figure 3.6: The flowchart outlining the steps of the methodology.

3.3 Results

3.3.1 Seasonal Ice Cover

The annual cycle of sea ice growth and decay from the years 2013 to 2021 over the study area is displayed in Figure 3.7. During these years, CIS daily ice charts provide coverage for all months, with the exception of September 2014 and 2021, as indicated by blue hatches in 3.7 as blue hatches. It is apparent that the ice grows and decays throughout the year. The freeze-up period begins in October when thin ice begins to emerge. A peak in the concentration of thin ice is observed at the end of the freeze-up period, just before the beginning of winter in January. Subsequently, this thin ice gradually transforms into thick ice, reaching a high concentration from January to March (winter season). During the melt season from April to June, the total ice concentration decreases, with the possibility of an increase in the relative concentration of thick ice. The summer season begins in July and extends through September. Following the determination of the ice condition over the study area, we calculated the corresponding daily sea ice edge for each PM product based on the exact location and day indicated on the CIS charts for the months of October to June over the years 2013-2021. On average, the chart SIC at the edge is 51.27%. Specifically, these values for winter, melt, and freeze-up seasons are 44.69%, 50.65%, and 58.47%, respectively. Since the 15% threshold was used in Equation 3.1 to estimate the sea ice edge, the chart mean SIC at the edge appears high, which is due to the polygonal nature of the ice chart data, In this format, the ice chart polygons adjacent to the ice edge may have total ice concentrations exceeding 15% (see Figure 3.3).

3.3.2 Chart and PM Sea Ice Edge

From the summary in Table 3.2, it is observed that the mean value of ASI SIC at the chart ice edge is 10.59%, well below the 15% SIC threshold. Specifically, this value for the winter season is 7.61% and increases to 16.16% and 8.00% in the melt season and freeze-up period, respectively. The mean value of NT2 SIC at the chart ice edge is 17.97%, close to the 15% threshold. This value for the winter season is 14.40% and increases to 24.27% and 15.26% in the melt season and freeze-up period, respectively. The mean value of BT SIC at the chart ice edge is 25.07, well above the 15% threshold. These values for winter, melt, and freeze-up seasons are 24.63%, 25.28%, and 25.29%, respectively. A possible explanation for these differences is due to the different spatial resolutions of the PM sensors. The SSMIS sensor has footprints of 28 to 70 kilometers for channels used in the BT algorithm. AMSR2

has a higher spatial resolution than SSMIS (3 to 26 km sensor footprints for channels used in the ASI and NT2 algorithms). Both sensor footprints are larger than the resolution of the data used to produce ice charts (e.g., primarily SAR). The mean SIC at the ice edge seems to be dependent on PM sensor spatial resolutions, with less variability across seasons for the larger footprint sensor.

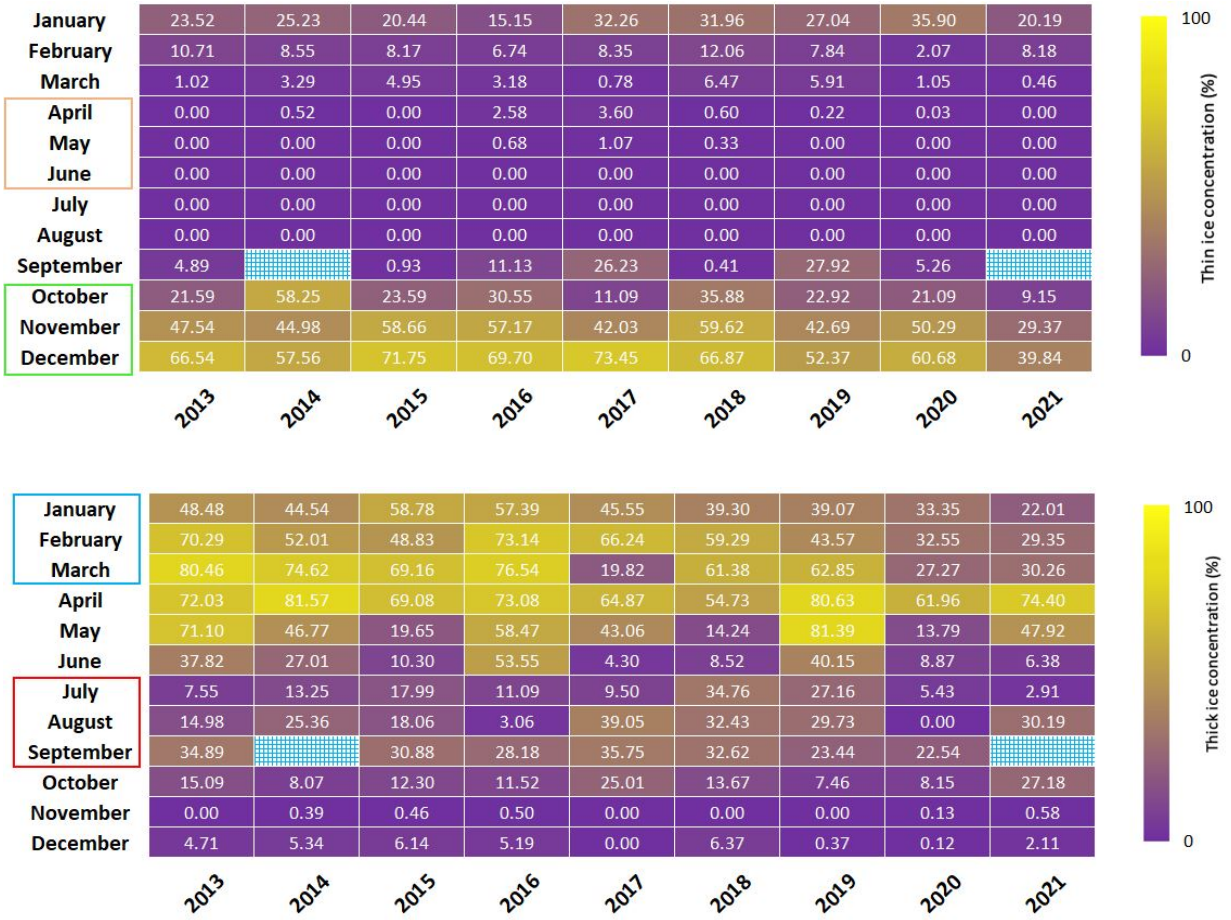

Figure 3.7: Annual partial concentration for thin (top) and thick (bottom) ice derived from the CIS ice charts in 2013-2021 over the ice-covered region of the study. The total ice concentration is the sum of the thin and thick ice. The blue hatches indicate no chart available for September 2014 and 2021 over the study area. The colors for seasons appear on the top: orange for melt and green for freeze-up. The colors for seasons appear on the bottom: blue for winter and red for summer.

Table 3.2: Statistics of sea ice edge derived from the ASI, NT2, and BT algorithms with respect to the CIS ice charts over the study area between 2013 and 2021. Standard deviation (SD) is taken over all data that are first averaged on a monthly basis. The Winter season includes January, February, and March. Melt season includes April, May, and June. The freeze-up season includes October, November, and December. Results are statistically significant at a 0.05 level. (*) sea ice concentration is calculated at the chart ice edge.

PM Product	Season	Mean SIC* (%)	SD SIC* (%)	Mean EDE	SD EDE	Mean δ_H^{wavg} (km)	SD δ_H^{wavg} (km)
AMSR2-ASI	all	10.59	6.48	0.19	0.09	98.93	36.21
	winter	7.61	5.73	0.17	0.06	62.67	16.82
	melt	16.16	10.83	0.18	0.13	86.06	49.50
	freeze-up	8.00	2.88	0.22	0.08	148.05	42.32
AMSR2-NT2	all	17.97	8.90	0.18	0.13	73.15	48.74
	winter	14.40	7.26	0.14	0.06	38.55	10.80
	melt	24.27	14.22	0.16	0.12	60.68	34.89
	freeze-up	15.26	5.24	0.23	0.22	120.23	100.53
SSMIS-BT	all	25.07	8.59	0.16	0.10	63.67	34.18
	winter	24.63	7.27	0.13	0.03	35.40	7.13
	melt	25.28	12.65	0.16	0.12	54.55	27.21
	freeze-up	25.29	5.86	0.20	0.15	101.07	68.20

These statistics suggest that the PM SIC products tend to have a lower SIC at the ice edge compared to the ice charts. These findings are consistent with the polygonal representation used in ice charts, as discussed previously, and underscore the operational nature of ice charts, which prioritize safety considerations. Accordingly, chart SIC values are expected to be higher than PM products at the edge [120]. Additionally, the ASI algorithm exhibits the lowest standard deviation (SD) SIC at the chart ice edge (6.48%), suggesting a consistent tendency for underestimation. The SD is calculated over all data, which are initially averaged on a monthly basis over the years 2013-2021. The ASI mean SIC value is well below 15%, suggesting that setting a SIC threshold of 10% may result in a sea ice edge location that aligns more closely with the ice charts. Conversely, the BT mean SIC value is well above 15% indicating that setting a SIC threshold of 20% could yield a sea ice edge location that aligns more closely with the ice charts.

A potential source of this disagreement between different products lies in the difference in resolution between PM SIC products and ice charts. A large sensor footprint limits the precision of the ice edge location estimation. For instance, within the large footprint of the SSMIS sensor, the observed brightness temperature may tend to blur the ice edge due to the mixture of ice and water. Consequently, the estimated edge location tends to extend outward. On the other hand, within the small footprint of the AMSR2 sensor, the ice edge may result in a concentration below the 15% threshold, leading to an underestimation of the edge location. Consequently, the estimated edge location tends to extend inward. Figure 3.8 provides an illustration of the monthly EDE and δ_H^{wavg} values over the study area in all months of 2017 (panels 1 to 27). It can be seen that the ASI ice edge appears closer to the consolidated ice region (inward); however, the BT ice edge often appears closer to open water (outward) for almost all months of the study period. Furthermore, differences in the algorithms also contribute to the disagreement between different products, with ASI being more sensitive to ice temperature and atmospheric moisture, leading to underestimating the ice edge location in the MIZ [94].

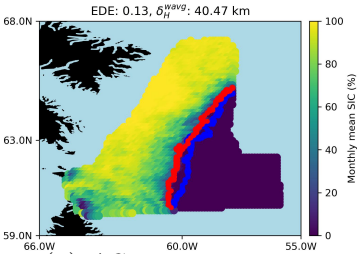

(1) ASI-January 2017

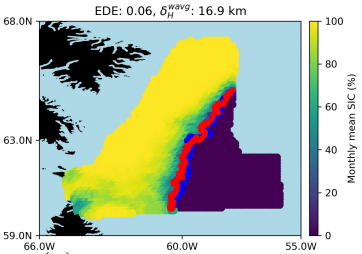

(2) NT2-January 2017

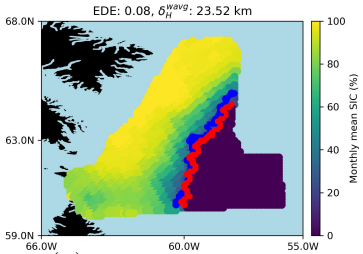

(3) BT-January 2017

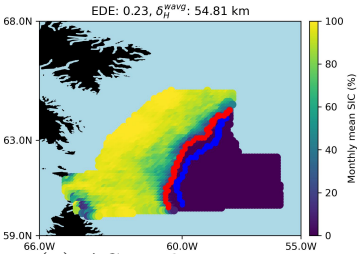

(4) ASI-February 2017

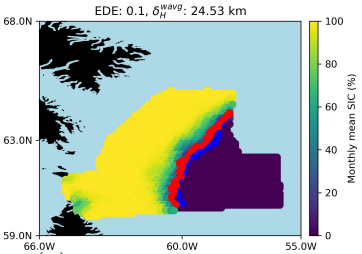

(5) NT2-February 2017

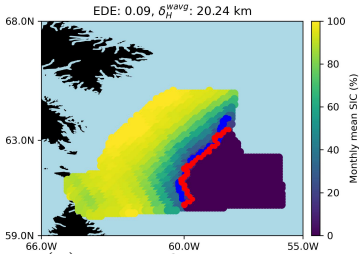

(6) BT-February 2017

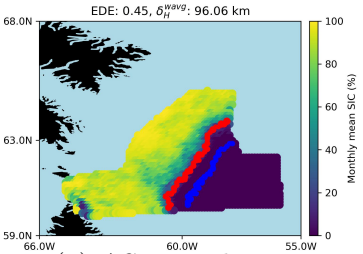

(7) ASI-March 2017

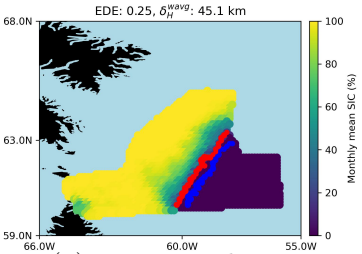

(8) NT2-March 2017

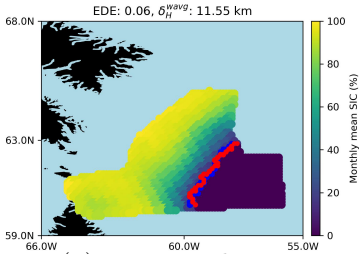

(9) BT-March 2017

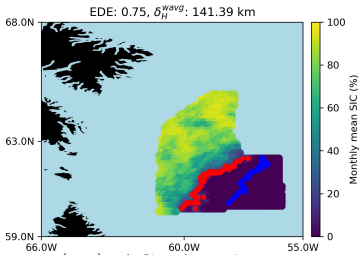

(10) ASI-April 2017

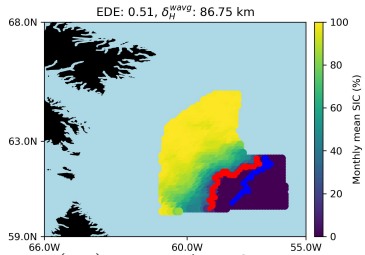

(11) NT2-April 2017

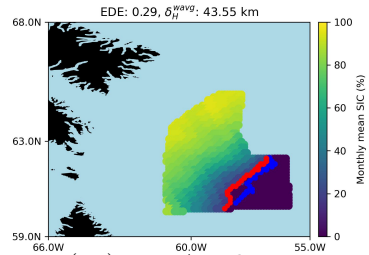

(12) BT-April 2017

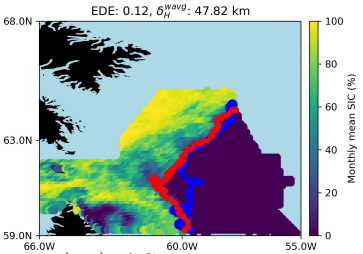

(13) ASI-May 2017

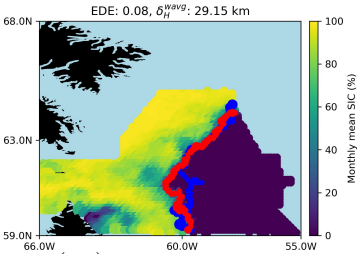

(14) NT2-May 2017

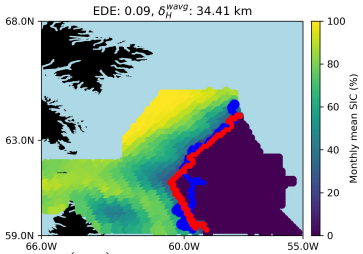

(15) BT-May 2017

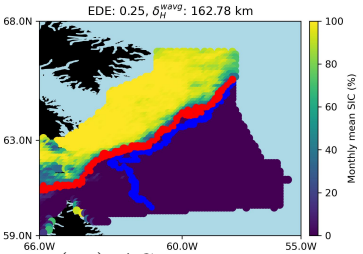

(16) ASI-June 2017

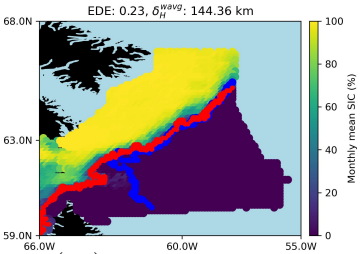

(17) NT2-June 2017

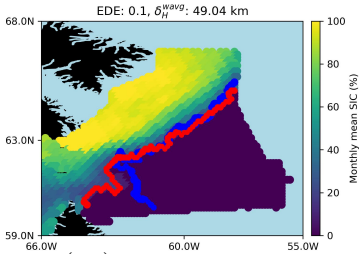

(18) BT-June 2017

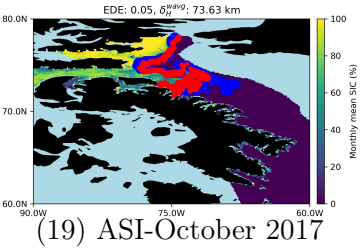

(19) ASI-October 2017

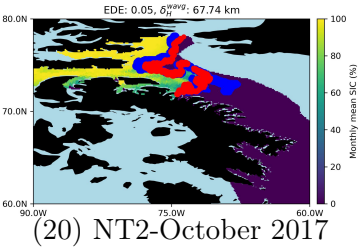

(20) NT2-October 2017

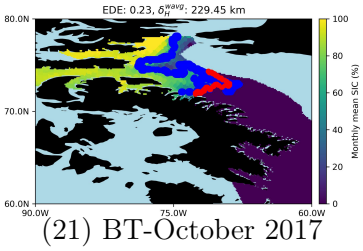

(21) BT-October 2017

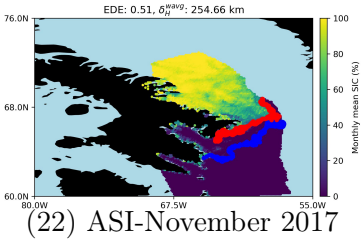

(22) ASI-November 2017

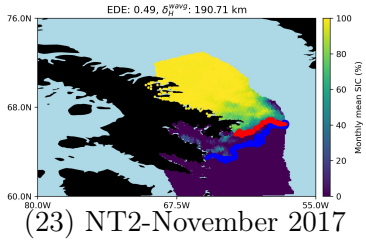

(23) NT2-November 2017

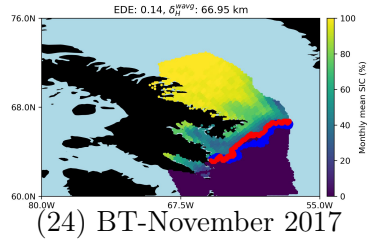

(24) BT-November 2017

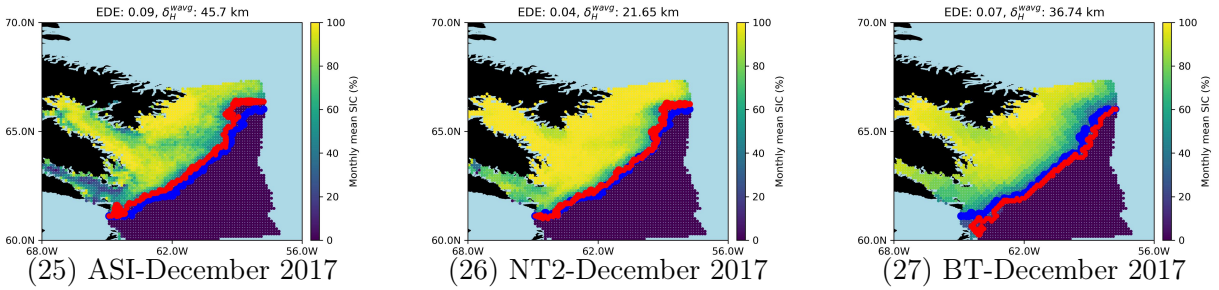

(25) ASI-December 2017 (26) NT2-December 2017 (27) BT-December 2017

Figure 3.8: An illustration of the monthly EDE and δ_H^{wavg} values over the study area in 2017 (panel 1-27). Ice edges determined by the CIS ice chart are in blue color contours, and those from the ASI, NT2, and BT algorithms are in red color contours. Edge determination is based on a 15% SIC threshold, and the ice edges are calculated based on the monthly SIC values. The regions without data are shown in light blue, while the lands are black.

3.3.3 Edge Displacement Error

Table 3.2 provides a comparison of sea ice edges derived from the PM products with those obtained from charts. Notably, the mean values of EDE and δ_H^{wavg} for the ASI, NT2, and BT algorithms exhibit higher values in the melt season and freeze-up period compared to the winter season. On average, the ASI algorithm shows the highest EDE and δ_H^{wavg}, while the BT algorithm demonstrates the lowest values. The spatial resolution limitation hinders precise ice edge location determination using PM SIC products. For instance, the accuracy of the ice edge location is constrained by the 25 km × 25 km spatial resolution of the SSMIS SIC product. The NT2 and BT algorithms exhibit more consistency with each other in terms of mean δH^{wavg} and L_{avg} than the NT2 and ASI algorithms, indicating a potential influence of sensor spatial resolution. The low EDE and δ_H^{wavg} standard deviation (SD) values in the BT algorithm (0.10 and 34.18 km, respectively) suggest low variability and close to the average values of EDE and δ_H^{wavg}. The winter season, characterized by a high concentration of thick ice, exhibits the lowest mean EDE and δ_H^{wavg} values for all three PM algorithms, reflecting a well-defined ice edge. Conversely, the freeze-up period, marked by the emergence of thin ice (see Figure 3.7), displays the highest mean EDE and δ_H^{wavg} values. In this period, small ice floes and filaments, combined with atmospheric and ocean forces, contribute to a diffuse ice edge. Additionally, during the melt season (which starts in April), waves and winds can break melting rotten ice, leading to a diffuse ice-water boundary, potentially causing erroneous SIC and sea ice edge estimation, consistent with findings in Pang *et al.* [109].

Figure 3.9 presents box-whisker plots that visually depict the variation of δ_H^{wavg}, L_{avg}, and EDE for the ASI, NT2, and BT algorithms across each month over the entire study period and study area. In each monthly box-whisker plot, the line across the box represents the median value, while a green triangle denotes the mean. The length of the box indicates the interquartile range (IQR) of the corresponding measurement. Notably, October exhibits the highest mean values of δ_H^{wavg}, L_{avg}, and EDE for all three PM algorithms. This observation aligns with October marking the onset of the freeze-up period, characterized by the appearance of thin ice in the study region (as discussed earlier). Additionally, monthly variations are evident in δ_H^{wavg}, L_{avg}, and EDE values, with the ASI and BT algorithms displaying the widest and narrowest spreads, respectively. Upon closer examination of the box-whisker plots, it is apparent that the mean EDE value for October falls outside the range represented by the box-whisker plots for both the NT2 and BT algorithms. This deviation suggests that the monthly EDE distributions are highly skewed during October.

The box-whisker plot for monthly EDE Figure 3.9 shows the range of EDE is high for April, indicating that normalizing δ_H^{wavg} with the total length provides an alternative measure for the difference between the ice edge locations that is less susceptible to changes in the charted area. In particular, the long positive whiskers observed in April indicate significant deviations toward higher values than the mean. This indicates a greater range of EDE values in April, reflecting the edge's highly dynamic nature this month. This observation is consistent with the fact that in April, the wind speed is relatively high, air temperature exhibits greater fluctuations compared to other months, and temperature is nearing the freezing point (Figure 3.10). Off-ice winds can propagate ice filaments into the ocean, creating a diffuse ice edge, which could lead to an erroneous SIC and sea ice edge, as also confirmed by Pang *et al.* [109]. To explore a possible explanation for the different behavior of April and October, observed in Figure 3.8, we examined Figure 3.9 panels 10 to 12 for April 2017 and panels 19 to 21 for October 2017. We noticed that in October (the beginning of the freeze-up period), the ice edge exhibits meandering behavior and extends further inward compared to April. Therefore, dividing δ_H^{wavg} by the ice edge length allows the meandering patterns to be captured.

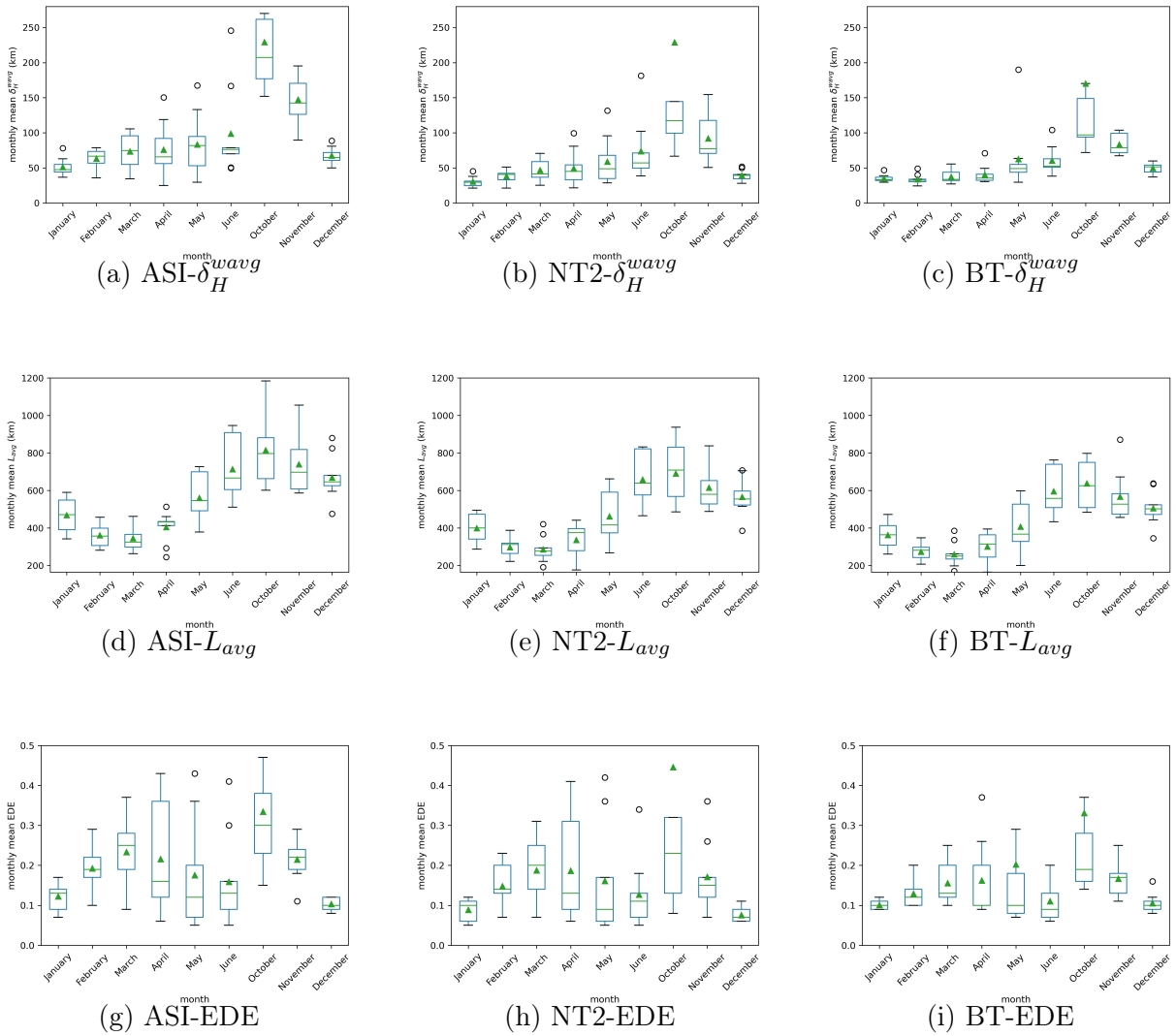

(a) ASI-δ_H^{wavg} (b) NT2-δ_H^{wavg} (c) BT-δ_H^{wavg}

(d) ASI-L_{avg} (e) NT2-L_{avg} (f) BT-L_{avg}

(g) ASI-EDE (h) NT2-EDE (i) BT-EDE

Figure 3.9: A box-whisker plot visualization of the δ_H^{wavg}: (a) ASI, (b) NT2, (c) BT, L_{avg}: (d) ASI, (e) NT2, (f) BT, and EDE (g) ASI, (h) NT2, (i) BT, in each month over the whole study period and study area. Each measurement's median and average values are indicated by a line across the box and a green triangle, respectively. The box length indicates the corresponding measurement's interquartile range (IQR). The circles outside the box indicate an outlier.

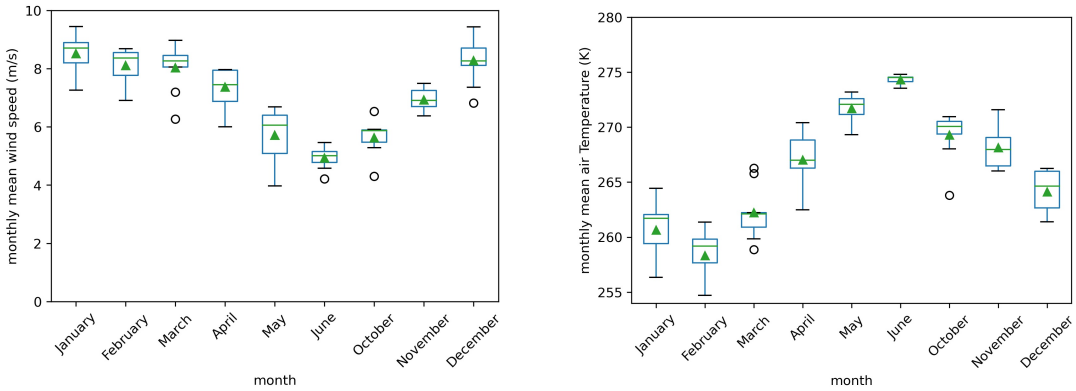

Figure 3.10: A box-whisker plot visualization of the monthly wind speed (m/s) and 2-meter air temperature over the whole study period and study area. Each measurement's median and average value are indicated by a line across the box and a green triangle, respectively. The box length indicates the corresponding measurement's interquartile range (IQR). The circle outside the box indicates an outlier.

3.4 Discussion

The determination of the ice edge derived from PM algorithms is a function of the spatial resolution of the sensor and the frequencies used by a given algorithm (because resolution varies with frequency). The smearing uncertainty, as described in Equation 2.12, can affect the presented results. For instance, in the case of BT algorithm, first, the footprint size of the 19 GHz channels of SSMIS instruments (see Table 2.2) exceeds the grid resolution used for presenting SIC product (25 × 25 km). Second, the BT algorithm combines 19 and 37 GHz frequency channels, with the footprint of the latter being smaller than that of the former (see Table 2.2). Consequently, the coverage area of the Earth's surface by these two frequencies entering the BT algorithm differs. In regions of homogeneous surfaces (fully sea ice covered or open water) these effects should have minimal impact. However, at the sea-ice edge where spatial gradients are sharp and the footprint covers a heterogeneous surfaces (mixture of open water and sea ice), these effects become more pronounced [59]. Lower resolution may cause the ice edge to appear blurred, potentially leading to an over-estimation. Conversely, the blurring effect may compensate for the challenges in detecting thin and melting ice near the ice edge, which is most prevalent near the ice edge [108]. It is worth noting that algorithms utilizing higher frequency channels (near-90 GHz) are more sensitive to geophysical noise but provide higher spatial resolution SIC products compared to those using lower frequency channels (up to 37 GHz) [121]. However, near-90 GHz data may be less sensitive to changes in physical properties in ice and snow due to their

shallower penetration depth compared to lower frequencies [56]. Ultimately, the choice of algorithms involves considerations of the trade-off between geophysical noise and spatial resolution.

3.5 Conclusion

This paper has assessed the performance of three PM SIC products (the ASI, NT2, and BT) in sea ice edge estimation with respect to the operational daily ice charts over the eastern Canadian Arctic for 2013-2021. In order to analyze the ice edge estimation in this region, the statistics are calculated from October to June, which corresponds to the ice-covered season. Key findings reveal that the PM algorithms underestimate the chart SIC at the edge. Our results indicate that normalizing the Hausdorff distance, δ_H^{wavg}, with the average length of the ice edge provides an alternative measure, EDE, that is less sensitive to changes in the charted area. The ASI algorithm exhibited the highest EDE on average, while the BT algorithm demonstrated the lowest EDE on average. These discrepancies in performance could be attributed to the difference in frequency, footprint size, and spatial resolution among the PM SIC products and ice charts. During the freeze-up period, all PM algorithms exhibited higher mean EDE values due to the presence of thin ice. Conversely, the lowest mean EDE values across all PM algorithms were observed during winter, characterized by a well-defined ice edge resulting from high concentrations of thick ice. A further observation was that the ASI ice edge appeared closer to ice than the chart ice edge. The BT ice edge, however, often appeared closer to open water than the chart ice edge due to the smear effect caused by the large sensor footprint. Considering the importance of PM SIC products, this study can assist in implementing bias-corrected PM product to be fused with ice charts or other SAR-based products.

Chapter 4

Marginal Ice Zone Interannual Variability

4.1 Introduction

The MIZ can be defined as the region between the consolidated ice cover and the open ocean. It is often considered the area where ocean waves interact with sea ice, penetrate ice cover [37], and impact the ice thickness [38]. A more practical definition of the MIZ is defined as the region where the SIC is between 0.15 and 0.80 [31], where SIC is often obtained using data from passive microwave sensors. Irrespective of the definition applied, investigating the MIZ is vital as it supports a diverse range of life, from sea ice algae and other primary producers to marine mammals and seabirds [106] and has implications for human access to the Arctic [122]. The MIZ is highly dynamic and responsive to fluctuations in cyclones [123], wind and ocean currents, making it a rapidly changing environment [124]. Due to its dynamic nature, the MIZ plays a significant role in modulating the exchange of heat and gases between the atmosphere and ocean [32]. Furthermore, MIZ can impact Arctic amplification, as it serves as a zone for Arctic cyclogenesis, which plays a big role in northward meridional heat transport [125]. Therefore, improving our understanding of Arctic climate change requires an enhanced understanding of MIZ spatial and temporal variability.

Strong and Rigor [31] used several PM SIC products across the Arctic (1979-2011) and indicated that the summer MIZ (July-September) expanded in width by 39%, while the winter MIZ (December-February) decreased in width by 15%. The observed widening of

the MIZ is reported to be closely associated with the decline of thick and multi-year sea ice. MIZ widening facilitates ship access to the Arctic [126]. Utilizing various passive microwave SIC products, another study in the Arctic (1978-2018) reported a constant MIZ extent trend that was attributed to a decrease in the perimeter as the MIZ moved north [32]. Several other studies tend to assume that the MIZ extent is increasing [127, 128, 129, 130]. Horvat [35] suggested using the marginal ice zone fraction (MIZF, the fraction of sea ice cover that is MIZ) as an alternative to solely relying on sea ice area for evaluating how changes in sea ice models affect past, present, and projected sea ice state. The strong correlation between sea ice area and global mean temperature (unlike the MIZF) makes it difficult to determine whether improvements in modeled sea ice are due to advancements in sea ice models or other components of climate models. This makes MIZF a more plausible method of assessing improvements in sea ice models. Considering the significance of passive microwave SIC products in activities such as long-term shipping route planning, reanalysis data production, climate monitoring, and forecasting, MIZF can potentially provide a realistic understanding of future climate conditions.

As an alternative approach to delineating the MIZ without relying on a fixed threshold ($0.15 \leq \text{SIC} < 0.80$), the study by Vichi [39] introduced an innovative method involving an indicator derived from the SIC anomaly. This indicator (denoted as σ^m_{SIA} and referred to as σ^a in our study) signifies the deviation of SIC at a specific grid cell from its long-term average over a given time period. Vichi concluded the indicator provides insight into the variability of the Antarctic MIZ, while the SIC threshold-based approach suffices for defining the Arctic MIZ; although this study did not explicitly examine the details of the anomaly-based approach in the Arctic. The decline of Arctic sea ice extent [131, 132], the replacement of thick and multi-year ice by thin and first-year ice [133, 134] and the more fragmented thinner sea ice, coupled with stronger winds and waves than in the past [126] highlight potential alteration in SIC anomaly. These observations, motivated us to explore the efficacy of the SIC anomaly-based MIZ definition in capturing meaningful insights, comparable to the established SIC threshold-based definitions, in the Arctic.

Given the vulnerability of the Arctic MIZ to the effects of climate change [135], there is a compelling need to investigate when (or if) significant shifts occur within the 40-year time series of the Arctic MIZF, which has not been examined previously. By understanding historical shifts, more accurate models for forecasting future sea ice conditions can be developed. This analysis affects not only human activities and ship navigation planning but also other sectors such as marine habitat life [136]. Knowledge of these shift points in the time series can provide data-driven insights into the timing and magnitude of envi-

ronmental changes, which can guide conservation efforts and policies aimed at mitigating climate change impacts. In this study, we used BT SIC, a long-term passive microwave SIC product, to investigate Arctic MIZ interannual and seasonal variability and possible change points over the last 40 years using two different MIZ definitions: SIC threshold-based, and SIC anomaly-based.

4.2 Experimental Design

4.2.1 Dataset

The BT SIC [137] was chosen as the primary sea ice product because it provides a long-term, consistent, and comprehensive SIC product. The BT ice edge also shows good agreement with the daily Canadian Ice Service (CIS) ice charts over the eastern Canadian Arctic, compared to other PM products [138]. To strengthen the observations, we incorporated several PM sea ice products namely ASI, NT2, Ocean and Sea Ice Satellite Application Facility-458 (OSI-458), covering the Arctic region from 2012 to 2020. This time frame was chosen to ensure consistency in the comparison, as it represents an overlapping period when all these products are available.

4.2.2 MIZ Fraction

The concept of marginal ice zone fraction (MIZF) is defined as [35]

$$\text{MIZF} = \frac{\text{MIZA}}{\text{SIA}}, \tag{4.1}$$

where MIZA represents the marginal ice zone area, which is the summation of each grid cell area multiplied by its SIC, provided it is MIZ. SIA denotes the sea ice area, which is the summation of each grid cell area multiplied by its SIC, provided it has at least 0.15 concentration.

4.2.3 SIC Threshold-based MIZ Fraction

To define the monthly MIZ_tF in each year, we first calculated the monthly mean SIC values for a particular grid cell for a given year. Next, we determined the MIZ using the

SIC criterion (MIZ_t) as $0.15 \leq SIC < 0.80$. Finally, we used Equation 4.1 to find the MIZ_tF.

4.2.4 SIC Anomaly-based MIZ Fraction

SIC Anomaly

The SIC anomaly refers to the deviation of SIC at a particular grid cell from its long-term average, which is taken over a given month for the years 1983-2022. To calculate the monthly SIC anomaly for a grid cell located at i, j ($a^m_{i,j,d}$), the following equation was used

$$a^m_{i,j,d} = SIC^m_{i,j,d} - SIC^m_{i,j}, \tag{4.2}$$

where $SIC^m_{i,j,d}$ is the SIC value at the grid cell with the location of i, j on each day d in a given month m, and $SIC^m_{i,j}$ is the long-term average SIC value for the same grid cell over the same month. Choosing a monthly time window for climatology reduces short-term fluctuations compared to daily process, providing a smoother dataset that can reflect long-term SIC patterns and trends.

SIC Anomaly Variability

The standard deviation of the monthly SIC anomaly (σ) captures the SIC variability of a given grid cell over a month. The monthly SIC anomaly for a given grid cell located at i, j or $\sigma^a_{i,j}$ over month m with n total days ($d = 1$ to n) can be calculated by taking the square root of the variance, which is the mean of the squared daily SIC anomalies or $a^m_{i,j,d}$ [39]. Mathematically, $\sigma^a_{i,j}$ can be expressed as

$$\sigma^a_{i,j} = \sqrt{\frac{1}{n}\sum_{d=1}^{n}(a^m_{i,j,d})^2}. \tag{4.3}$$

SIC Anomaly Distribution

Following defining the $\sigma^a_{i,j}$, we calculated the median value of each grid cell over the Arctic (1983-2022). Figure 4.1, panel a, shows the probability density function (PDF), empirical cumulative distribution functions (ECDF), and fitted Pareto distribution cumulative distribution function (fitted CDF) for the median of SIC anomaly standard deviation (σ^a).

To check the goodness-of-fit of the Pareto distribution, we used the Kolmogorov-Smirnov (K-S) test, and the resulting p-value was smaller than the chosen significance level of 0.05. Panel b and c in Figure 4.1 display the mean SIC and median σ^a spatial maps, respectively. The PDF plot displays two distinct peaks: peak 1 is centered approximately at 0.02, and peak 2 is situated around 0.15, with the trough between the peaks apparent around 0.11. Based on Figure 4.1, regions with mean SIC values close to 1 correspond to the median σ^a values below 0.11, hence these values correspond to regions of high ice concentration. Areas where the mean SIC values are less than 1 are associated with median σ^a values exceeding 0.11. Consequently, we established a threshold of 0.11 to identify significant anomalies in SIC for MIZ determination. To define the monthly MIZ_σF in each year, we first calculated the $\sigma^a_{i,j}$ (Equation 4.3). Then, we determined the MIZ using the SIC anomaly criterion (MIZ_σ) as $\sigma^a > 0.11$.

4.2.5 Change Point Detection

To investigate if there are change points within the 40-year time series of the Arctic MIZF, we employed the pruned exact linear time (PELT), a multiple change point detection method, introduced by Killick *et al.* [139] and used in sea-ice related studies [140, 141]. The PELT algorithm initiates with a single segment encompassing the entire time series. If the reduction in cost is less than a defined penalty value (>0), the penalized cost increases, and the year under consideration is not identified as a change point. Conversely, if the cost reduction surpasses the added penalty, the algorithm marks the year as a change point. Subsequently, the dataset is divided at this change point. Among the remaining candidate split points, PELT selects the one with the lowest cost, thus dividing the time series into two new segments. This process iterates for the two newly created datasets, both before and after the identified change point. If change points are detected in either of these new segments, they are further divided. This recursive procedure continues until no more change points are found within any part of the dataset. To implement the PELT algorithm, we utilized the "ruptures" Python library with a built-in cost function based on the radial basis function (RBF), which is a Gaussian kernel and is a good option when we have no information about the underlying data [142]. The RBF cost function quantifies the similarity between consecutive segments of the time series. If there is a shift or alteration in the data distribution, it is reflected in a noticeable change in the similarity scores between these segments. In contrast, when the data distribution remains stable, the similarity scores between consecutive segments remain relatively constant. A significant drop in similarity scores signals the presence of a potential change point. The statistical

significance of the change points is assessed using Welch's t-test (two-sided) with a significance level of 0.05.

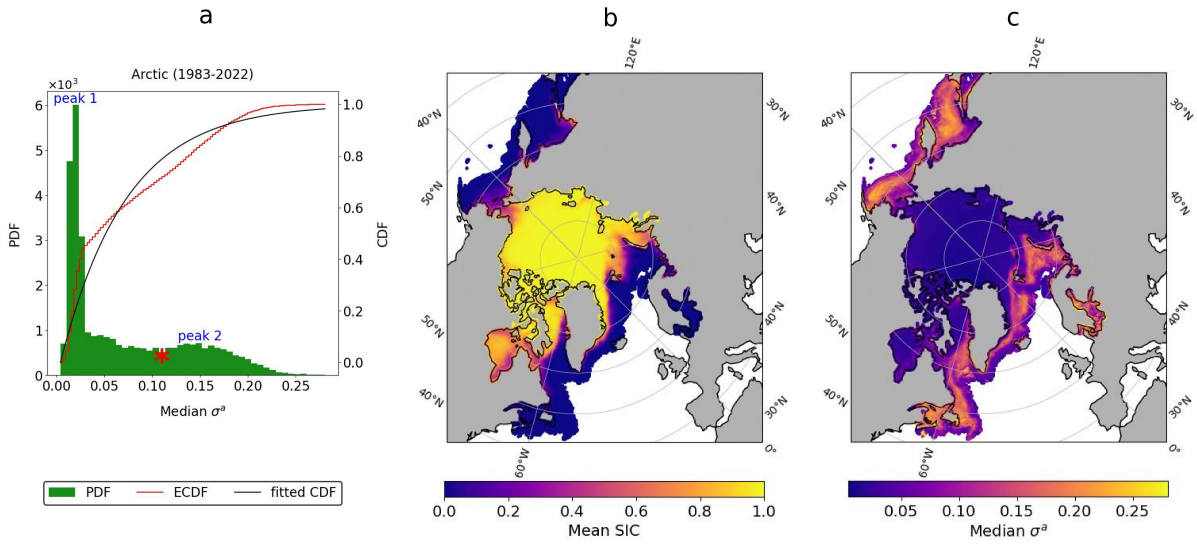

Figure 4.1: The PDF, ECDF, and fitted Pareto distribution CDF of the median of SIC anomaly standard deviation or σ^a (panel a), the mean SIC spatial map (panel b), and the median σ^a spatial map (panel c). In panel a, the trough between peak 1 and 2 is indicated by a red asterisk located at 0.11. The Bootstrap SIC data are over the Arctic (1983-2022). The Freedman-Diaconis rule is used to find the number of histogram bins for the PDF distribution. The outliers (defined by the interquartile range method [3]) and grid cells with $\sigma^a = 0$ are excluded from the median σ^a spatial map. These regions are shown in white, while the land is grey.

4.3 Results

4.3.1 MIZ Interannual Variability

The trend, mean, and standard deviation (SD) for the Arctic sea ice extent, MIZ_tF, and $MIZ_\sigma F$ are presented in Table 4.1. Also, the time series of the Arctic sea ice extent over 1983-2022 is shown in Figure 4.2. A declining trend has been observed in sea ice extent over the last 40 years. For sea ice extent, September shows the fastest rate of decline (consistent with other studies, e.g., [143, 144, 145]), the lowest mean and the highest SD values. The trend of MIZ_tF in January, March, and April, is slightly negative, other months have a positive trend, except for February where there is no trend. October shows the fastest rate of increase in MIZ_tF. July and August show the highest mean values for MIZ_tF. August and October show the highest SD values for MIZ_tF. The trend of $MIZ_\sigma F$ from January to April is slightly negative with the remaining months showing a positive trend. August shows the fastest rate of increase in $MIZ_\sigma F$. July and October show the highest mean values for $MIZ_\sigma F$. November shows the highest SD values for $MIZ_\sigma F$. It is noted that the $MIZ_\sigma F$ SD value in November is three times greater than the MIZ_tF SD value (shows the largest SD difference). The time series of the Arctic MIZ_tF and $MIZ_\sigma F$ over 1983-2022 is shown in Figure 4.3 and 4.4, respectively. The green line shows the linear regression trend over 40 years. The MIZ_tF reached its maximum and minimum values in August 2012 (0.34) and December 1987 (0.06), respectively. While the $MIZ_\sigma F$ reached its maximum and minimum values in November 2021 (0.45) and December 1987 (0.01), respectively.

Focusing on the interannual variations of MIZF using the SIC threshold-based definition (Figure 4.3) and the SIC anomaly-based definition (Figure 4.4) we noticed some months with significantly different behaviour for these two MIZ definitions. We focused on two noticeable ones: July (from 2011 to 2013) and November (from 2020 to 2022). For the month of July, from 2011 to 2012, the MIZ_tF value shows a sharp increase, followed by a sharp decrease from 2012 to 2013. This behaviour is the opposite for the $MIZ_\sigma F$. The year 2012 was an anomalously low year for sea ice extent in the Arctic (see July panel in Figure 4.2), which could lead to low SIC fluctuations for months and regions with ice-free conditions. To gain deeper insights into this, MIZ spatial maps are presented in Figure 4.6. Figure 4.5 presents the sub-regions of the Arctic. For the MIZ_t, in July 2012 the East Siberian, Chukchi, and the Beaufort Seas, were flagged as MIZ, but were not flagged in July 2011 and 2013. In contrast, MIZ_σ shows a more fragmented MIZ region in the Beaufort, Chukchi, and East Siberian Seas compared to MIZ_t in July 2012. For MIZ_σ, the primary sub-regions contributing to the negative shift in July 2012 are Hudson Bay, Baffin

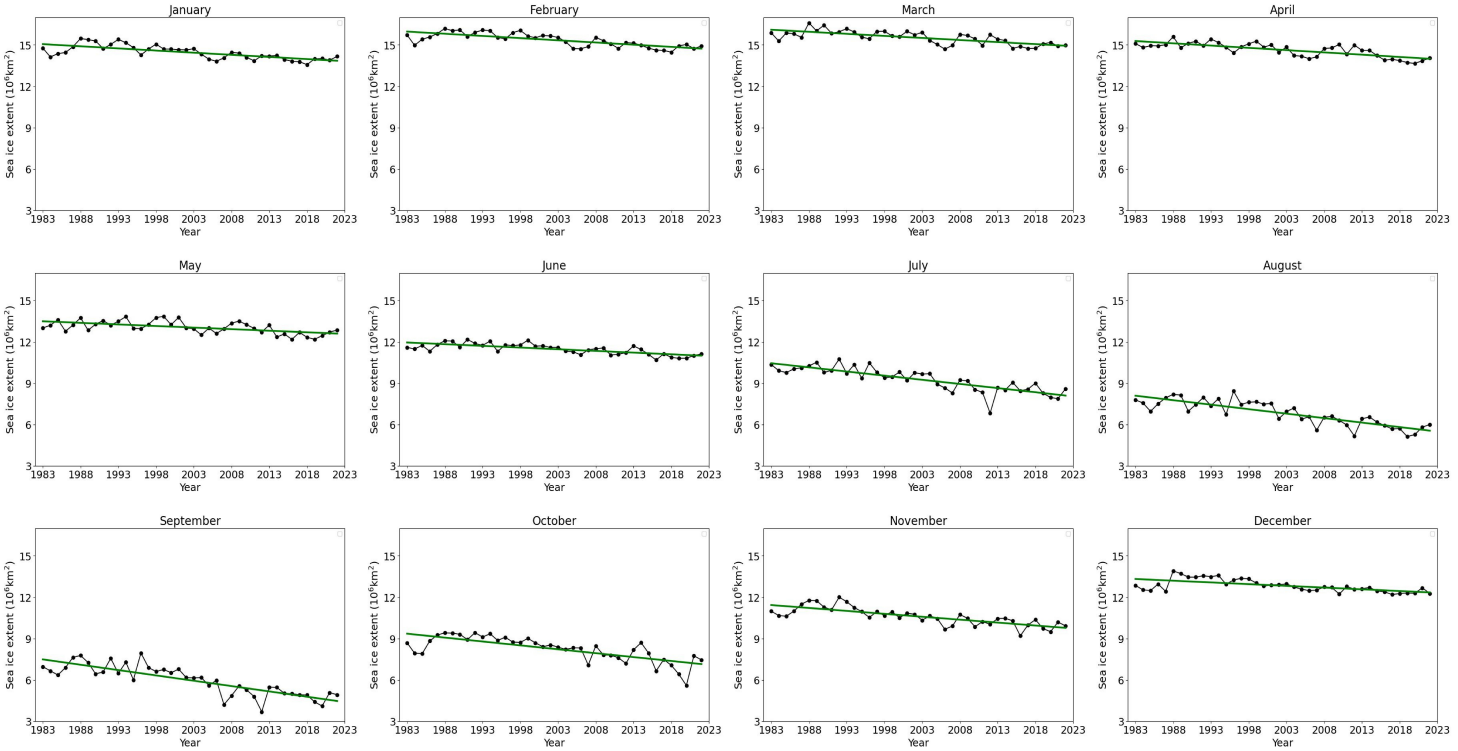

Figure 4.2: Temporal variability of the Arctic sea ice extent over 1983-2022. Sea ice extent is the area of grid cells with SIC ≥ 0.15. The green line shows the linear regression trend over 40 years, which was statistically significant at a 0.05 level using Student's t-test.

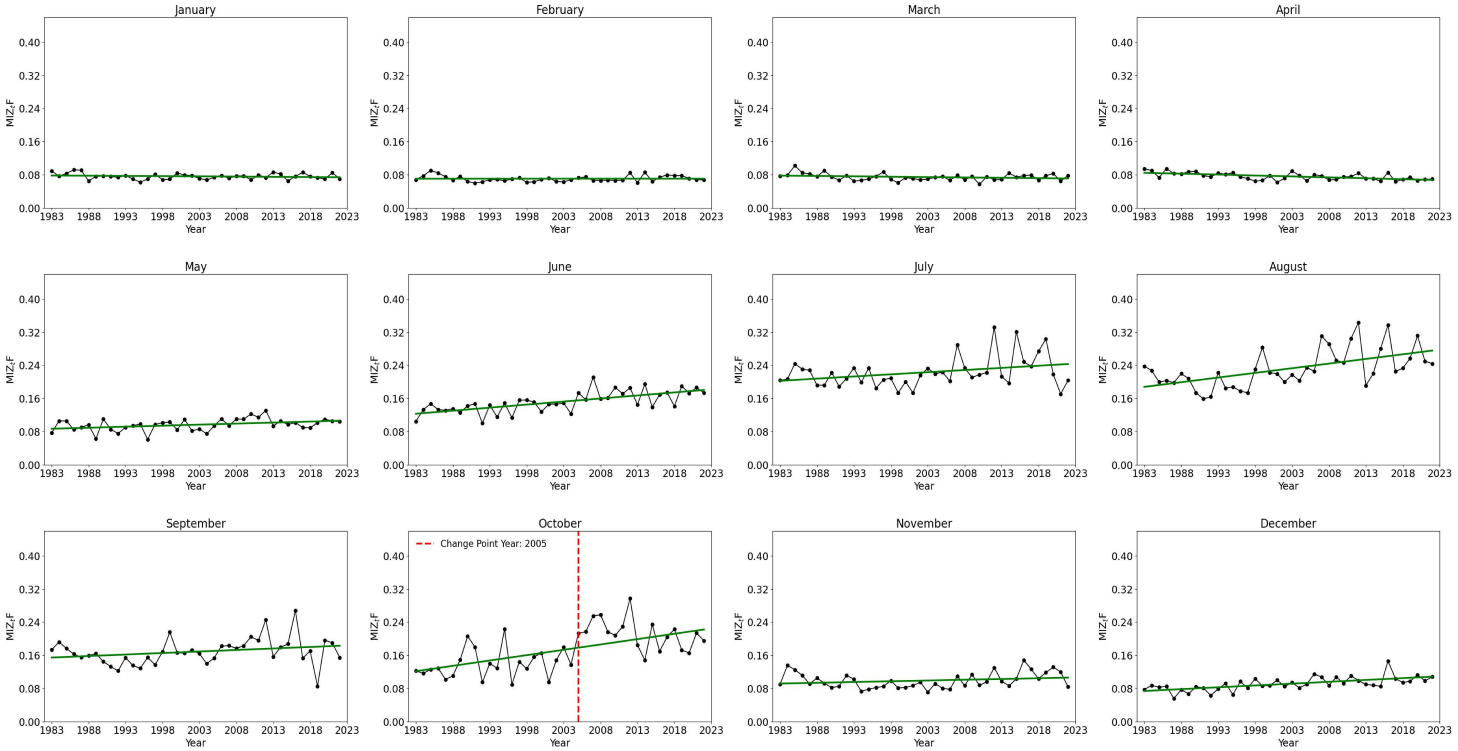

Figure 4.3: Temporal variability of the Arctic marginal ice zone fraction using the SIC threshold-based definition (MIZ_tF) over 1983-2022. The MIZ_t grid cells are defined using the criterion of $0.15 \leq \text{SIC} < 0.80$. A PELT test is used to detect the change point in each time series (shown with a dashed line in red) which was statistically significant at a 0.05 level using Welch's t-test. The green line shows the linear regression trend over 40 years which was statistically significant at a 0.05 level using Student's t-test.

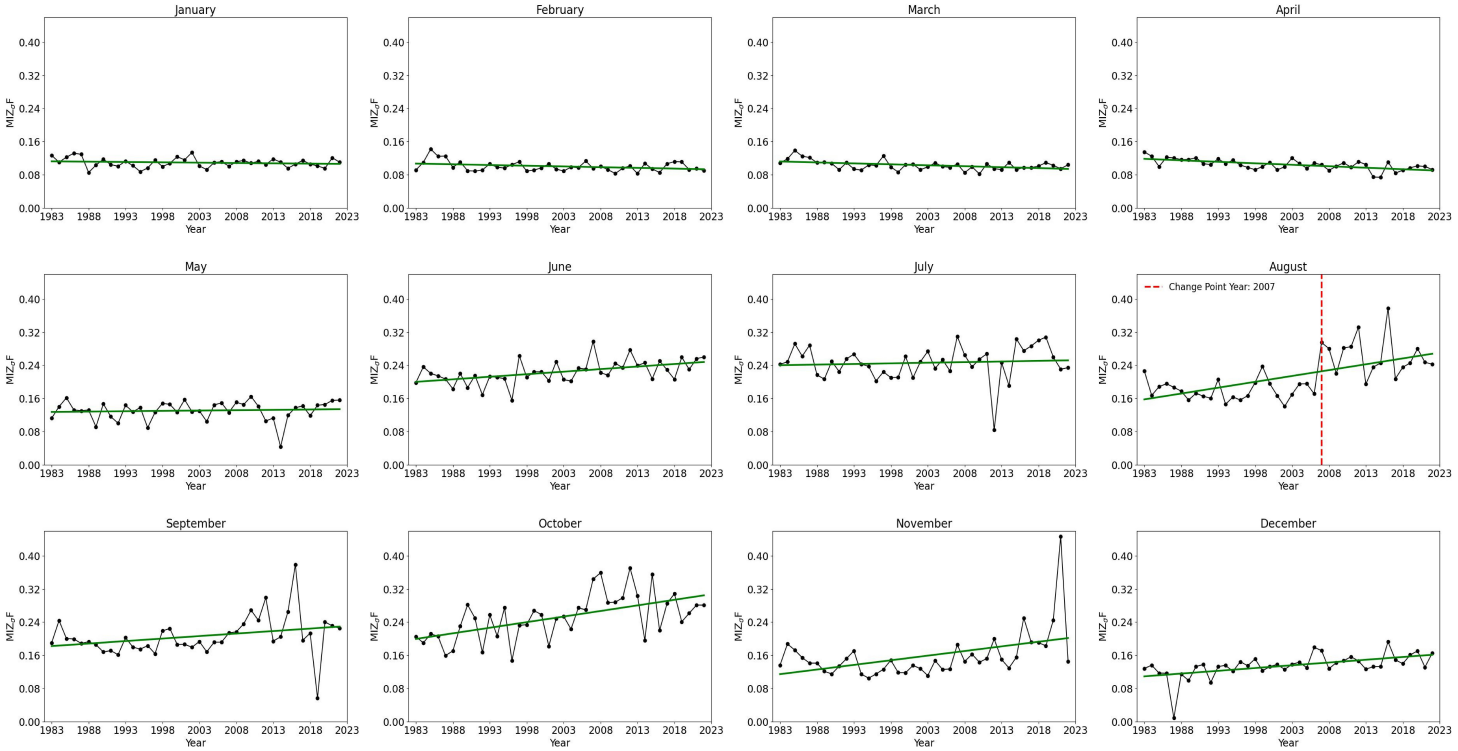

Figure 4.4: Temporal variability of the Arctic marginal ice zone fraction using the SIC anomaly-based definition ($\text{MIZ}_\sigma\text{F}$) over 1983-2022. The MIZ_σ grid cells are defined using the criterion of $\sigma^a > 0.11$. A PELT test is used to detect the change point in each time series (shown with a dashed line in red) which was statistically significant at a 0.05 level using Welch's t-test. The green line shows the linear regression trend over 40 years which was statistically significant at a 0.05 level using Student's t-test.

Bay, Greenland and Barents Seas, which are flagged as MIZ and in July 2011 and 2013 (not in July 2012). These observed differences between MIZ_tF and $MIZ_\sigma F$ align with the fact that the sea ice in the East Siberian, Beaufort, and Chukchi Seas is thicker than that in Hudson Bay, Baffin Bay, Greenland, and Barents Seas, which is thinner and more seasonal [143]. Differences between MIZ_t and MIZ_σ can also be seen in the Canadian Archipelago, which has experienced a transition to thinner ice and more mobile ice, due to ongoing warming [146]. These results should be further investigated in relation to ice charts. Melt conditions lead to fluctuations in brightness temperatures, in particular during melt onset, which occurs in June and July in this region [147, 111]. These fluctuations are reflected in SIC estimates from passive microwave sensors.

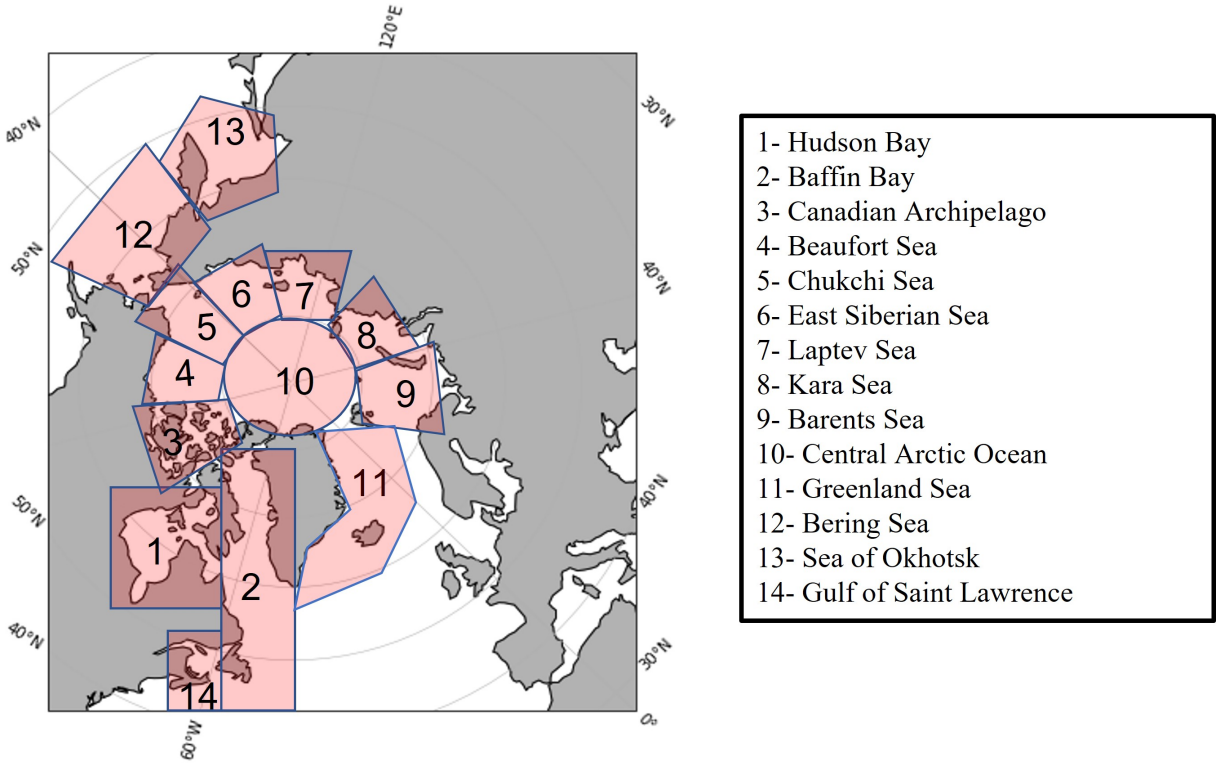

Figure 4.5: Sub-regions of the Arctic (based on the National Snow and Ice Data Center). The projection coordinate system is Polar Stereographic. The land is shown in grey.

For November, the MIZ_tF value, shows a slight decrease from 2020 to 2021 and a decline from 2021 to 2022. While the $MIZ_\sigma F$ value shows a significant increase from November 2020 to 2021, followed by a steep decline from 2021 to 2022. To better understand this,

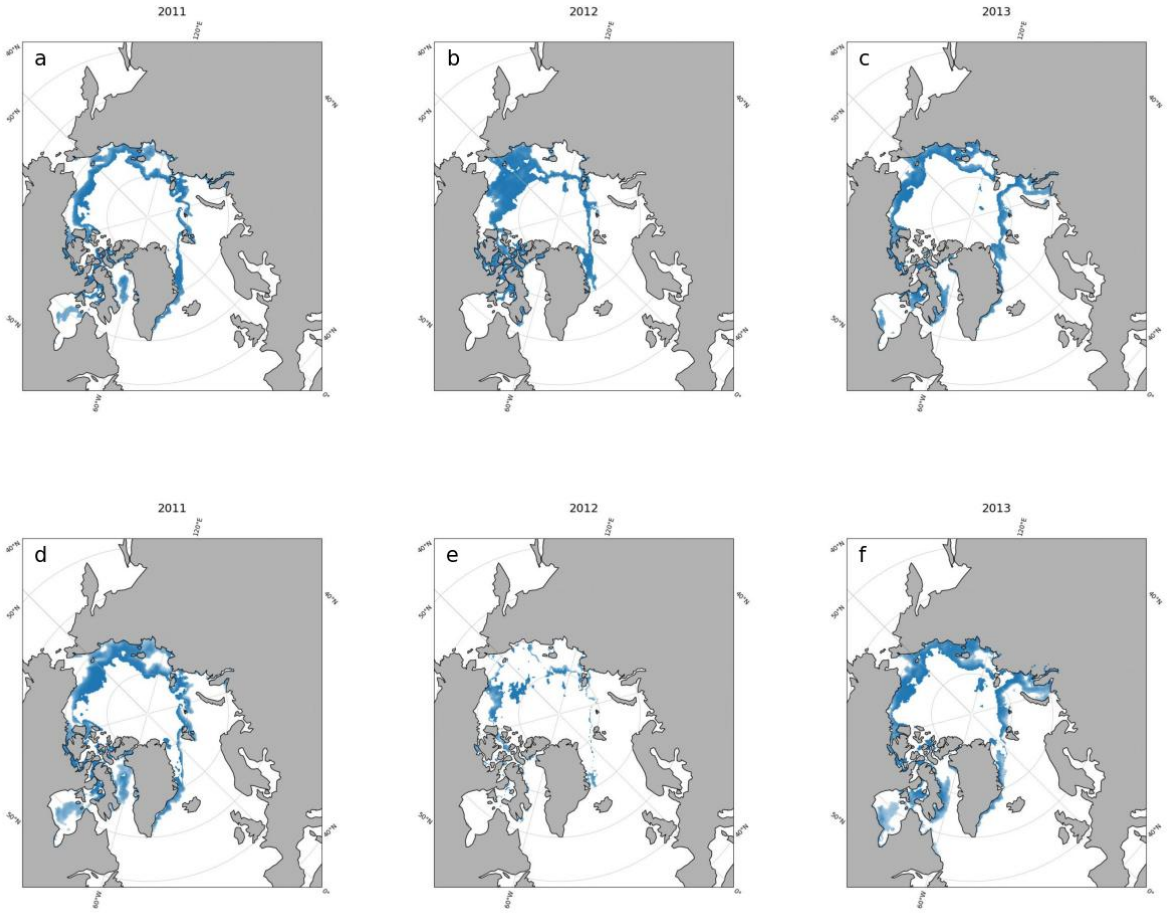

Figure 4.6: MIZ_t spatial map in July 2011 (panel a), 2012 (panel b), and 2013 (panel c) and MIZ_σ spatial map in July 2011 (panel d), 2012 (panel e), and 2013 (panel f). The MIZ_t grid cells are defined using the criterion of $0.15 \leq \text{SIC} < 0.80$. The MIZ_σ grid cells are defined using the criterion of $\sigma^a > 0.11$. The land is shown in grey.

we examined the MIZ spatial maps, presented in Figure 4.7. For MIZ_t, there is a slight difference between the region identified as MIZ from 2020-2022 mainly associated with the Chukchi Sea, Baffin Bay and part of Hudson Bay. For MIZ_σ, the primary sub-regions varying across these three years include the Beaufort, Chukchi, East Siberian and Laptev Seas, Baffin, and Hudson Bay. Significant differences between the two MIZ definitions are found in 2021 across the East Siberian, Laptev, Kara and Barents Seas. The observed disparities

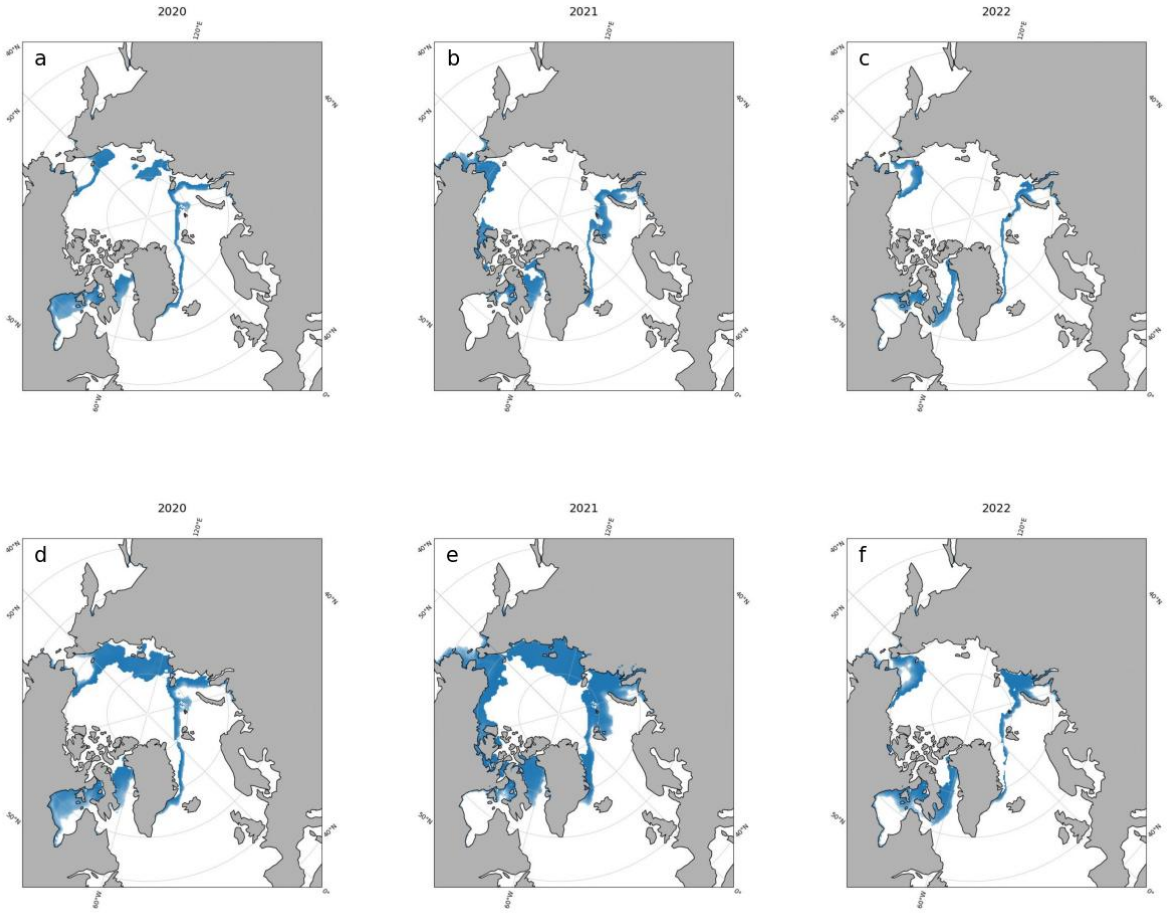

Figure 4.7: MIZ_t mean SIC spatial map (first row) and MIZ_σ mean SIC spatial map (second row) in November 2020 (left panel), 2021 (middle panel), and 2022 (right panel). The MIZ_t grid cells are defined using the criterion of $0.15 \leq SIC < 0.80$. The MIZ_σ grid cells are defined using the criterion of $\sigma^a > 0.11$. The land is shown in grey.

between MIZ_t and MIZ_σ align with the findings reported in the Sea Ice Outlook, stating that in 2021, the Chukchi and Barents Seas underwent an early freeze-up in November, with the Chukchi Sea reaching its largest sea ice extent in 20 years and in November 2021. While in 2021, Hudson Bay exhibited significantly delayed freeze-up events compared to the average [148].

Table 4.1: Trend, mean, and standard deviation (SD) values for the Arctic sea ice extent, MIZ_tF, and $MIZ_\sigma F$ over 1983-2022. Sea ice extent is the area of grid cells with SIC ≥ 0.15. The MIZ_t grid cells are defined using the criterion of $0.15 \leq$ SIC < 0.80. The MIZ_σ grid cells are defined using the criterion of $\sigma^a > 0.11$. The results are statistically significant at a 0.05 level using Student's t-test.

Month	sea ice extent (10^6 km^2)			MIZ_tF			$MIZ_\sigma F$		
	Trend (per year)	Mean	SD	Trend (per year)	Mean	SD	Trend (per year)	mean	SD
January	-0.03	14.45	0.50	-0.0001	0.08	0.01	-0.0002	0.11	0.01
February	-0.03	15.35	0.50	0.0000	0.07	0.01	-0.0003	0.10	0.01
March	-0.03	15.52	0.49	-0.0002	0.07	0.01	-0.0005	0.10	0.01
April	-0.03	14.64	0.51	-0.0004	0.08	0.01	-0.0007	0.10	0.01
May	-0.02	13.04	0.46	0.0005	0.10	0.01	0.0002	0.13	0.02
June	-0.02	11.47	0.39	0.0015	0.15	0.03	0.0012	0.22	0.03
July	-0.06	9.27	0.86	0.0010	0.22	0.04	0.0003	0.25	0.04
August	-0.07	6.82	0.91	0.0022	0.23	0.05	0.0028	0.21	0.05
September	-0.08	5.98	1.09	0.0007	0.17	0.03	0.0012	0.21	0.05
October	-0.06	8.25	0.9	0.0026	0.17	0.05	0.0027	0.25	0.05
November	-0.04	10.60	0.64	0.0004	0.10	0.02	0.0022	0.16	0.06
December	-0.03	12.84	0.46	0.0009	0.09	0.02	0.0013	0.14	0.03

To explore the seasonal and regional disparities between the two MIZ definitions, we analyzed the MIZ_t and MIZ_σ spatial maps for the Arctic in all months over 40 years. The corresponding figures have been included in the Appendix (Figures 1 to 40). Our analysis reveals that during the break-up (July and August) there is an increase in regions identified as MIZ using the SIC threshold-based definition than the anomaly-based definition, which may be attributed to the sensitivity of the threshold definition to the melting process. Whereas during the freeze-up (October and November) there is an increase in areas classified as MIZ based on SIC anomaly definition, particularly near the ice edge. This discrepancy is particularly marked in regions such as the Beaufort Sea, East Siberian Sea, Laptev Sea, and Greenland Sea.

4.3.2 MIZ Change Point Analysis

The change points in the monthly MIZ_t and MIZ_σ time series are detected using the PELT test. For MIZ_tF (Figure 4.3), a change point was detected in October corresponding to the year 2005. Other months did not show a significant change point year. To investigate this observation, Figure 4.8 illustrates the MIZ_t map in October before and after the change point (panel a and b, respectively). The most noticeable change after 2005 is an increase in the regions flagged as MIZ for the Amundsen Gulf, Beaufort, Chukchi, East Siberian and Laptev Seas. According to a recent study (over the period of 1990-2019), there was a shift in SIC in 2005 over the East Siberian and Laptev Seas [136]. This can result in a large sea ice-covered area with intermediate SIC leading to an increase in the MIZ_t in this year.

For the MIZ_σF (Figure 4.4), the change point year for August was detected in the year 2007. Other months did not show a change point year. To investigate this observation, Figure 4.9 illustrates the MIZ_σ map in June before and after the change point (panel a and b, respectively). The most noticeable change after 2007 is an increase in the regions flagged as MIZ for the Beaufort, Chukchi, and East Siberian seas. A shift in SIC in the Beaufort and Chukchi Seas and a strong increase in ice velocity with the strengthening of the rotation of the Beaufort Gyre have been noted for 2007, along with a decrease in sea ice residence time for the East Siberian Sea (study over the period of 1990-2019 [136]). These events, in particular a more mobile ice pack, can result in a large sea ice anomaly leading to an increase in the MIZ_σ in this year.

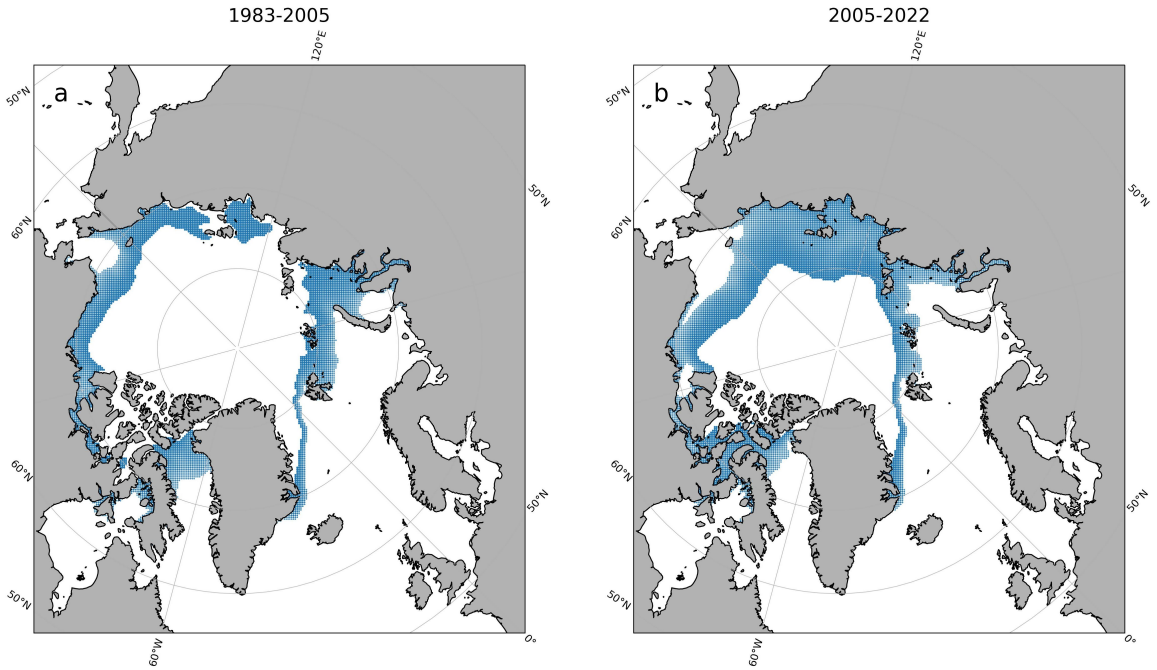

Figure 4.8: MIZ_t map in October before the change point year (panel a) and after the change point (panel b). The change point year (2005) is detected using the PELT method which was statistically significant at a 0.05 level using Welch's t-test. The MIZ_t grid cells are defined using the criterion of $0.15 \leq SIC < 0.80$. The land is shown in grey.

4.3.3 MIZ Seasonal Cycle

To visualize the MIZ seasonal cycle, a box-whisker plot of MIZF over the Arctic (1983-2022) is shown in Figure 4.10. August shows the highest mean value for MIZ_tF (0.23). While for $MIZ_\sigma F$, July and October show the highest mean value. A consistent MIZF trend is observed for both definitions from January to May. Possibly because, as the ice grows, both the SIA and the MIZA increase, and this results in a constant MIZF (Equation 4.1). Subsequent to May, MIZ_tF experiences growth, peaking in August (consistent with a study by Rolph *et al.* [32]). The MIZ_tF retreats in September and stays almost the same in October. Thereafter, MIZ_tF decreases until December. However, the $MIZ_\sigma F$ displays a substantial increase from May to July, reaching its first peak, and then gradually recedes until December, with the exception of an increase in October where it reaches its second peak. The most notable difference in mean MIZF values between MIZ_tF and $MIZ_\sigma F$ is

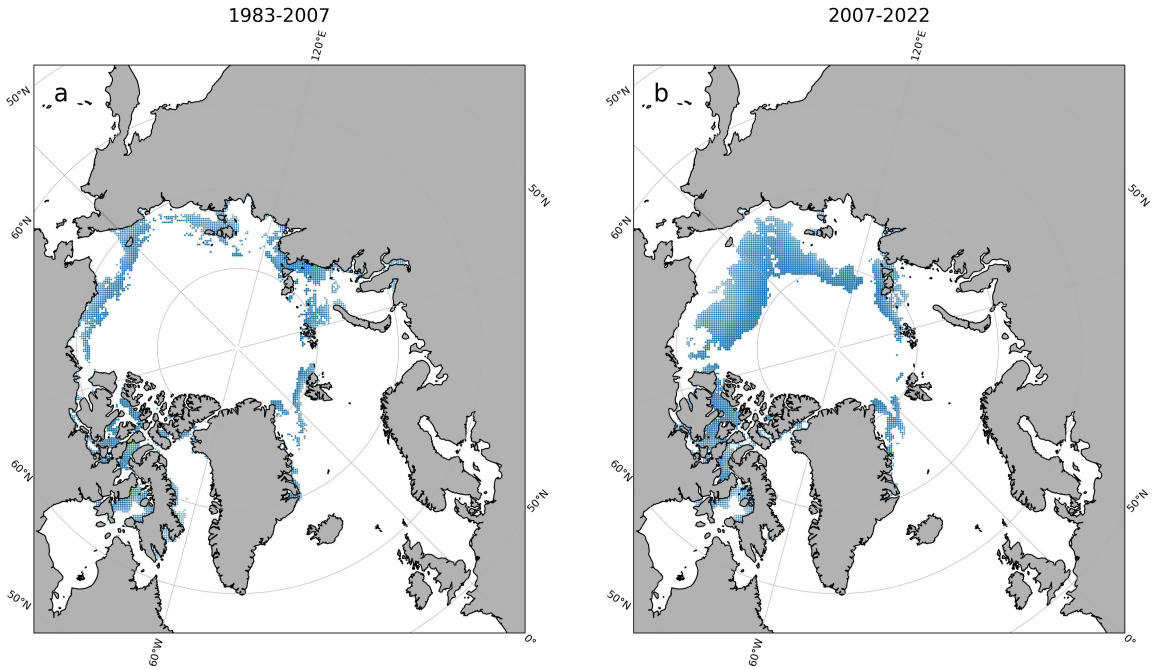

Figure 4.9: MIZ_σ map in August before the change point year (panel a) and after the change point (panel b). The change point year (2007) is detected using the PELT method which was statistically significant at a 0.05 level using Welch's t-test. The MIZ_σ grid cells are defined using the criterion of $\sigma^a > 0.11$. The land is shown in grey.

evident in October. Given that October is within the freeze-up period, the associated SIC fluctuations linked to ice growth and consolidation can be captured by the MIZ_σ. Indeed, the average value of MIZ_tF remained constant in October when compared to September. This indicates that both MIZA and SIA (Equation 4.1) were changing at a consistent rate in October. On the other hand, for MIZ_σF, the variations in SIC could result in a change in MIZA that exceeds the change in SIA (Equation 4.1). Consequently, this can result in an increase in the mean value of MIZ_σF in October. Additionally, for several months (July, August and November), the interquartile range (box length) is larger for the MIZ_σF than the MIZ_tF, which demonstrates the capability of MIZ_σ in capturing transition periods characterized by substantial fluctuations in SIC.

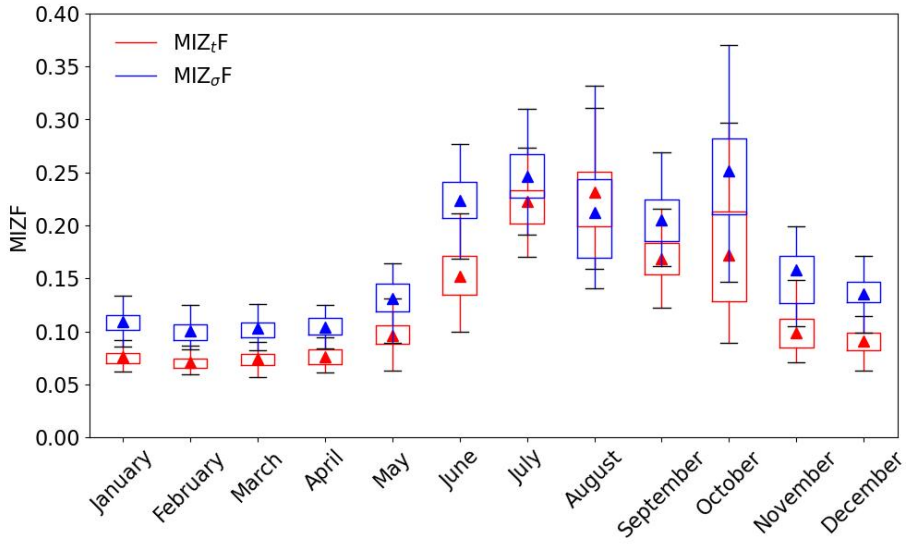

Figure 4.10: A box-whisker plot visualization of the seasonal cycle of MIZ$_t$F (red box) and MIZ$_\sigma$F (blue box) over the Arctic (1983-2022). The MIZ$_t$ grid cells are defined using the criterion of $0.15 \leq \text{SIC} < 0.80$. The MIZ$_\sigma$ grid cells are defined using the criterion of $\sigma^a > 0.11$. The MIZF average values are indicated by a triangle. The box length indicates the MIZF interquartile range.

4.3.4 Effect of PM Products on MIZ$_\sigma$

In order to investigate the influence of the choice of PM SIC product on the MIZ$_\sigma$F values, we provided the PDF, ECDF, and fitted Pareto distribution CDF of the median of SIC anomaly standard deviation or σ^a (panel a), the mean SIC spatial map (panel b), and the median σ^a spatial map (panel c) for SIC estimated from the ASI, NT2, OSI-458, and BT algorithms over the Arctic (2012-2020) are displayed in Figures 4.11, 4.12, 4.13, and 4.14, respectively. The ASI product's multiple peaks suggest a different range of SIC variability within the data. In contrast, the NT2 and BT products display two distinct peaks, possibly representing the boundary between ice-covered and open water areas. OSI-458's less pronounced second peak could suggest a more gradual transition from ice to open water. These differences highlight the inherent differences in the PM SIC retrieval algorithms which stem from the use of different frequencies, weather filters, corrections for brightness temperature, or dynamic tie points, all contributing to the estimated SIC variations. Additionally, the choice of spatial resolution for calculating SIC can lead to further discrepancies among the products. Consequently, different SIC products produce

distinct MIZ_tF values, mainly due to the variations in SIC. These discrepancies also lead to different $\text{MIZ}_\sigma\text{F}$ values, mainly due to the difference in SIC anomaly, which in turn gives distinct PDF distributions characterized by differing thresholds of σ^a.

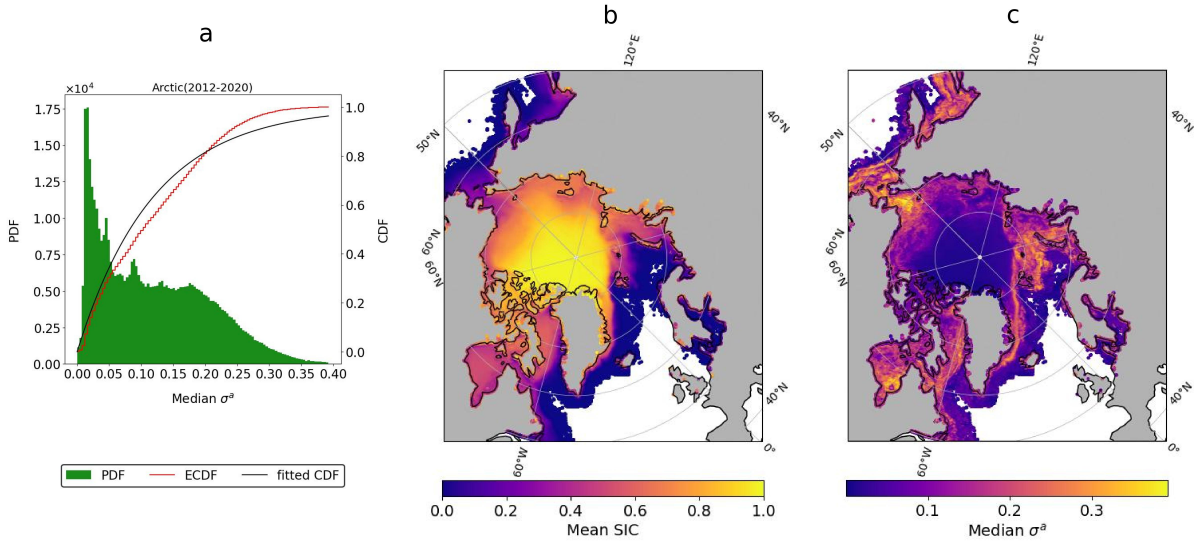

Figure 4.11: The PDF, ECDF, and fitted Pareto distribution CDF of the median of SIC anomaly standard deviation or σ^a (panel a), the mean SIC spatial map (panel b), and the median σ^a spatial map (panel c). The Arctic Radiation and Turbulence Interaction Study (ASI) sea ice SIC data are over the Arctic (2012-2020). The Freedman-Diaconis rule is used to find the number of histogram bins for the PDF distribution. The outliers (defined by the interquartile range method [3]) and grid cells with $\sigma^a = 0$ are excluded from the median σ^a spatial map. The corresponding grid cells are also excluded from the mean SIC spatial map. These regions are shown in white, while the land is grey.

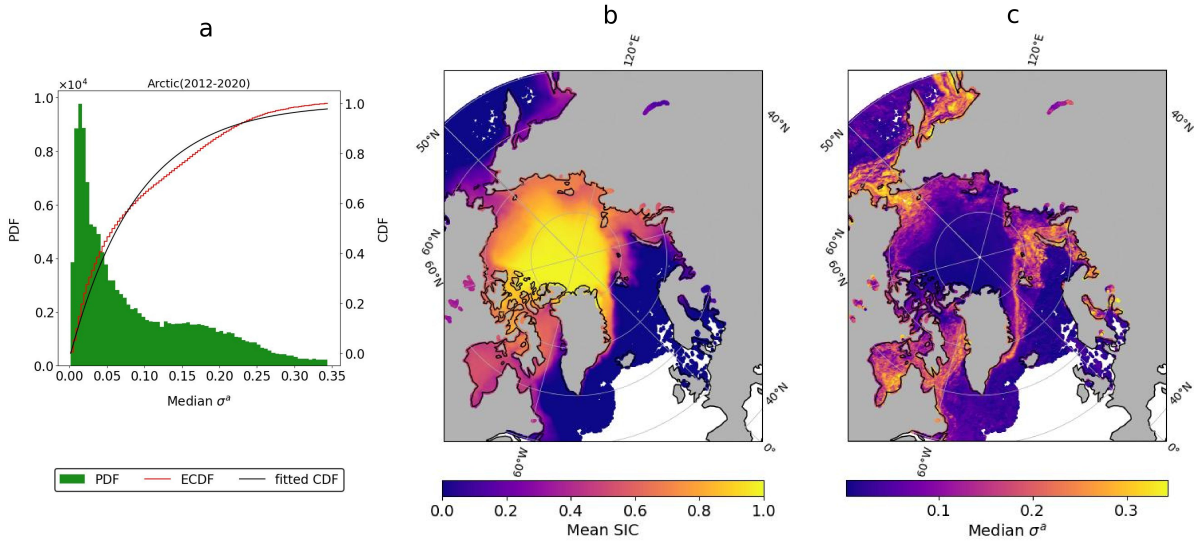

Figure 4.12: The PDF, ECDF, and fitted Pareto distribution CDF of the median of SIC anomaly standard deviation or σ^a (panel a), the mean SIC spatial map (panel b), and the median σ^a spatial map (panel c). The enhanced NASA Team 2 (NT2) SIC data are over the Arctic (2012-2020). The Freedman-Diaconis rule is used to find the number of histogram bins for the PDF distribution. The outliers (defined by the interquartile range method [3]) and grid cells with $\sigma^a = 0$ are excluded from the median σ^a spatial map. The corresponding grid cells are also excluded from the mean SIC spatial map. These regions are shown in white, while the land is grey.

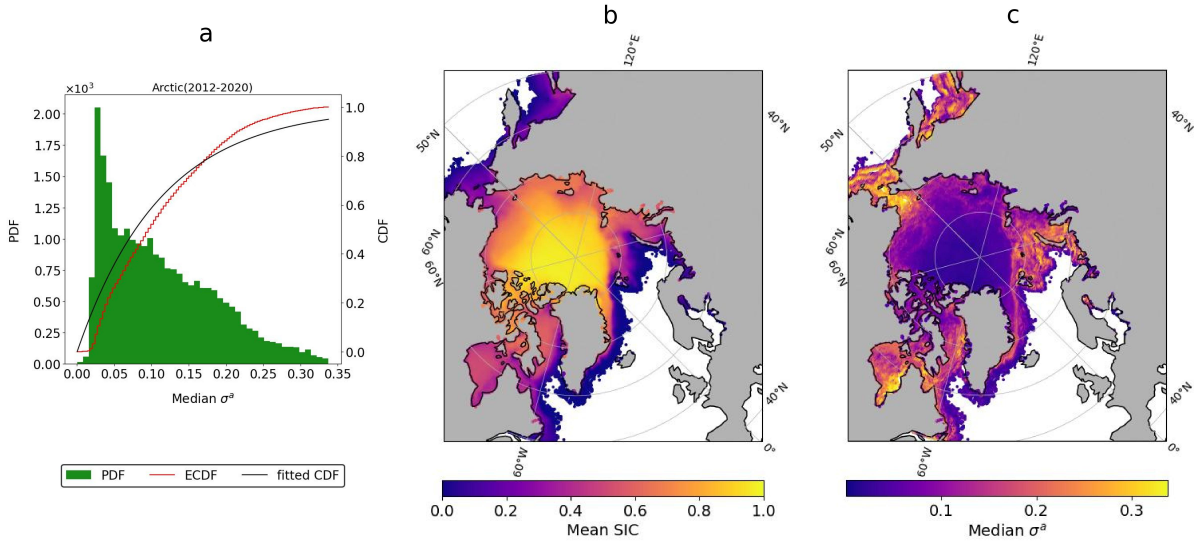

Figure 4.13: The PDF, ECDF, and fitted Pareto distribution CDF of the median of SIC anomaly standard deviation or σ^a (panel a), the mean SIC spatial map (panel b), and the median σ^a spatial map (panel c). The Ocean and Sea Ice Satellite Application Facility-458 (OSI-458) SIC data are over the Arctic (2012-2020). The Freedman-Diaconis rule is used to find the number of histogram bins for the PDF distribution. The outliers (defined by the interquartile range method [3]) and grid cells with $\sigma^a = 0$ are excluded from the median σ^a spatial map. The corresponding grid cells are also excluded from the mean SIC spatial map. These regions are shown in white, while the land is grey.

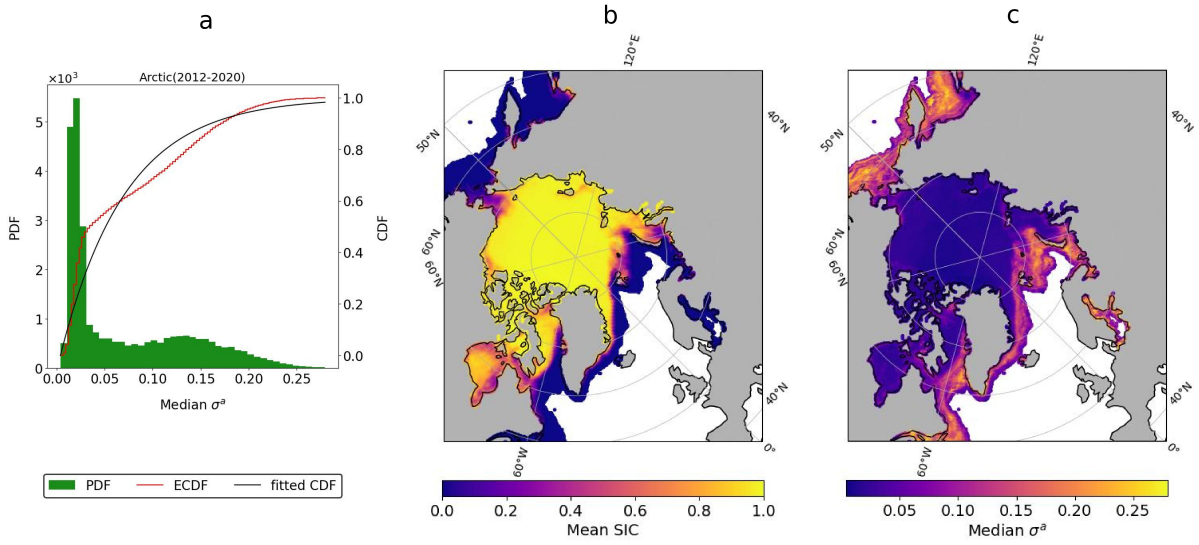

Figure 4.14: The PDF, ECDF, and fitted Pareto distribution CDF of the median of SIC anomaly standard deviation or σ^a (panel a), the mean SIC spatial map (panel b), and the median σ^a spatial map (panel c). The Bootstrap (BT) SIC data are over the Arctic (2012-2020). The Freedman-Diaconis rule is used to find the number of histogram bins for the PDF distribution. The outliers (defined by the interquartile range method [3]) and grid cells with $\sigma^a = 0$ are excluded from the median σ^a spatial map. The corresponding grid cells are also excluded from the mean SIC spatial map. These regions are shown in white, while the land is grey.

4.4 Discussion

In contrast to the consistent downward trend observed in Arctic sea ice extent across all months from 1983 to 2022, the trends in MIZ_tF and $MIZ_\sigma F$ are more variable. Over the study period, the Arctic MIZ_t reached its maximum fraction in July 2012, while its minimum fraction was recorded in March 2010. On the other hand, the Arctic MIZ_σ attained its highest fraction in August 2016, contrasting with its lowest fraction observed in December 1987. August also showed the fastest rate of increase of $MIZ_\sigma F$. Concerning monitoring Arctic sea ice extent, September stands out as a pivotal month, given that it consistently displays the lowest annual sea ice extent. For a comprehensive analysis of MIZ, however, July, August and October can offer information about the changes in ice-covered areas that cannot be obtained solely by focusing on the month with the minimum sea ice extent.

The SIC threshold-based definition of MIZ provides a practical means of identifying the transition between consolidated ice and open water. This definition proves useful in many applications, for example, SIC serves as an input in higher-level geophysical products, such as Level 4 sea surface temperature, and ice velocity drift products. However, there might be merit in the MIZ_σ use of the SIC anomaly in these products as well. MIZF can also be used to study habitat changes for marine mammals and seabirds, which could be more sensitive to fluctuations in SIC than the SIC value. Moreover, the SIC anomaly-based definition captures unusual or extreme fluctuations (e.g., rapid ice retreat/advance, cyclones) more effectively than absolute SIC values. For example, there was a strong Arctic cyclone recorded in August 2016 [4], the impact of which was captured in MIZ_σ (Figure 4.15). The impact of a particular cyclone on sea ice cover depends on the location of the event (e.g., proximity to the coast, ice edge) in addition to the characteristics of the sea ice [149]. Monitoring the location of these and similar events that lead to fluctuations in SIC is necessary, especially for planning safe navigation routes in the Arctic region.

Although the two MIZ definitions yield comparable seasonal trends in MIZF, MIZ_σ captures transition periods, such as freeze-up and break-up seasons. These periods are characterized by heightened SIC fluctuations, for example, owing to the presence of thin or fragmented ice, and fluctuations in other variables such as air temperature and solar radiation. As observed, the regions exhibiting significant contrast between the two MIZ definitions are those dominated by thin seasonal ice, in comparison to regions dominated by thick multi-year ice. With the Arctic sea ice thinning [150], the associated increased SIC variability, the strengthening effect of air temperature on sea ice [151], greater sensitivity of the pack ice to wind forcing [152], and the extension of melt season [153], tracking

SIC anomaly becomes increasingly pertinent. Thin ice and its variable concentration values could lead to a different PDF distribution for the median σ^a, necessitating updates to the σ^a threshold. In light of the Arctic's increasingly dynamic ice conditions, the SIC anomaly-based MIZ definition offers an additional approach to characterizing a climatically key region beyond the sea ice extent or the SIC threshold-based MIZ definition.

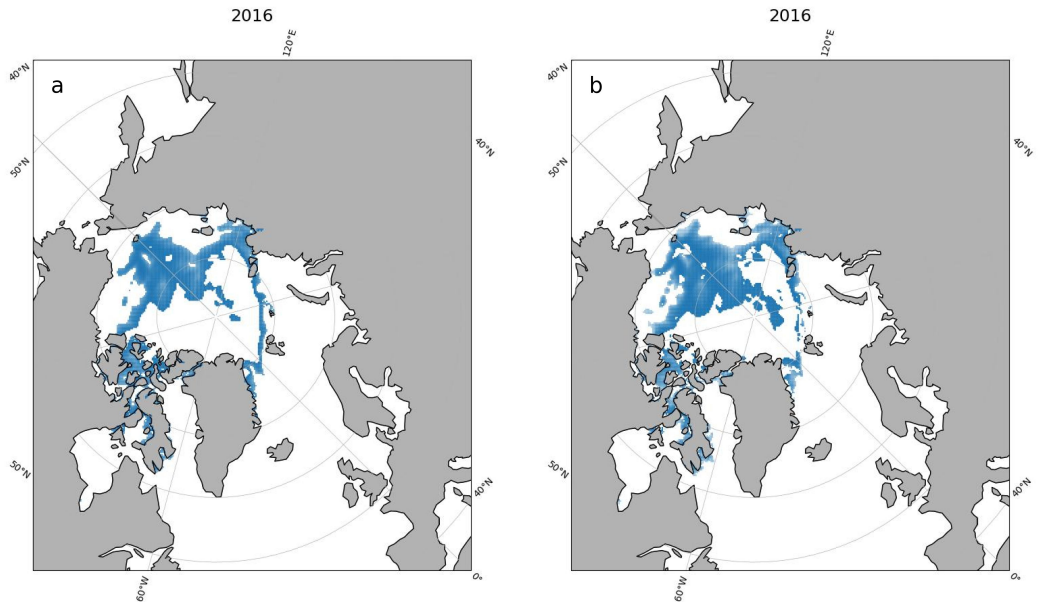

Figure 4.15: MIZ_t spatial map (panel a) and MIZ_σ map (panel b) in August 2016. The MIZ_t grid cells are defined using the criterion of $0.15 \leq SIC < 0.80$. The MIZ_σ grid cells are defined using the criterion of $\sigma^a > 0.11$. The strong Arctic cyclone affected sea ice in the Laptev Sea and Central Arctic Ocean [4]. The land is shown in grey.

4.5 Conclusion

In this study, we used BT SIC product to detect the trend and change point of the Arctic MIZ (1983-2022) using two MIZ definitions: MIZ_t and MIZ_σ. Our observations indicate that over the last 40 years, the Arctic MIZ_t reached its maximum fraction in August 2012, while its minimum fraction was recorded in December 1987. The Arctic MIZ_σ attained

its highest fraction in November 2021, contrasting with its lowest fraction observed in December 1987. While the two MIZ definitions yield comparable seasonal trends in MIZF, $MIZ_\sigma F$ values are highest in transition periods (e.g., freeze-up and break-up) in comparison with MIZ_t, which peaks in August. We also observed consistently higher MIZF values for the MIZ_σ than for MIZ_t across all seasons. Remarkably, October and August show the fastest rate of increase in MIZ_tF and $MIZ_\sigma F$, mirroring the accelerated decline in sea ice extent during the same months. Using the PELT change point method, we observed that for MIZ_tF in October, the change point year happened in 2005. For $MIZ_\sigma F$ in August, the change point year occurred in 2007. For both MIZ definitions, the MIZ region is increased for the period after the change point year and other months did not show a significant change point year. These change point years might be linked with shifts in sea ice concentration and sea ice velocity [136] for MIZ_t and MIZ_σ, respectively. This knowledge aids in the improvement of seasonal ice forecasts, safer navigation, resilient coastal communities, and marine habitat protection. In a forthcoming study, we will compare these two MIZ definitions using synthetic aperture radar imagery and provide information on the advantages and disadvantages of each definition.

Chapter 5

Marginal Ice Zone Comparison With SAR Data

5.1 Introduction

Building upon the insights from the previous study (Chapter 4), our interest led us to further explore the utilization of the anomaly-based definition of the MIZ rather than relying on a predetermined SIC threshold. To this end, an alternative source of SIC is required to evaluate the consistency of these definitions. Utilizing SAR data, which employs an active remote sensing technique, is suitable for this assessment. SAR data offers advantages such as fine resolution (in contrast to PM data) and the ability to penetrate cloud cover (unlike optical and thermal infrared data), making it a viable option. The deployment of SAR data for deriving SIC estimates presents notable benefits, yet the process is inherently challenging due to complex interactions among the SAR signal, water, and ice. The backscatter of SAR signals is influenced by various factors, including imaging geometry, surface conditions, and the presence of different ice types. Recent studies have underscored the effectiveness of convolutional neural networks (CNNs) in estimating SIC from SAR data.

The use of CNN for SIC estimation from SAR images was pioneered in a study by Wang *et al.* [154], where the need for separate feature extraction or post-segmentation processing was eliminated by their methodology. This approach yielded SIC maps with an absolute average error of under 10% in comparison to ice charts interpreted manually. Following this, further research employing a fully convolutional network specifically de-

signed for SIC estimation from SAR imagery demonstrated a slight increase in accuracy and computational efficiency over the traditional CNN methods [83]. To overcome the limited availability of training data, particularly for infrequently observed conditions, a study explored the importance of including samples of intermediate SIC, specifically from the MIZ, in the training dataset. Despite potential inaccuracies in MIZ data, the results indicated that incorporating these samples enhances the performance of the CNN. Further experiments involved increasing the number of MIZ samples, demonstrating that better representation in the test data is achieved when more samples from similar regions are included (an improvement in the classification accuracy of the MIZ from 0.66 to 0.74) [155]. In a recent investigation, a U-net model was employed to predict SIC across various sub-regions in the Arctic. This model utilized Sentinel-1 SAR data (HH and HV), Dual-pol Advanced Microwave Scanning Radiometer 2 brightness temperature data at 18.7 and 36.5 GHz, atmospheric variables (10-m wind speed, 2-m air temperature, total column water vapor, total column cloud liquid water), geolocation information (latitude and longitude) for each grid cell, scene acquisition month, and ice chart-derived label maps. The findings demonstrated a promising accuracy of 92% for the predicted SIC [156].

Emphasizing the superior performance of CNNs in SIC estimation and recognizing the importance of establishing a robust criterion for identifying the MIZ, this study marks the exploration of MIZ comparisons utilizing SAR data and deep learning methods. Our methodology involves the application of a CNN-based model to extract SAR SIC. The comparison is made between two MIZ definitions: SIC threshold-based and SIC anomaly-based, with each derived from both PM and SAR data. In the previous study investigating the Arctic MIZ over the last 40 years (see Chapter 4), it was observed that the SIC anomaly-based MIZF values peak during the transition periods such as freeze-up (due to the SIC fluctuations linked to ice growth) and this can be captured by the MIZ anomaly definition. A disparity in the MIZ over the Greenland Sea during November 2021 based on the two MIZ definitions was reported in this study. However, this observation was not compared with an alternative SIC data source. By focusing on this specific month and region and applying SAR data alongside that from PM, we aimed to gain insights into the capability of different SIC products and methodologies to represent the rapidly evolving state of the MIZ during freeze-up.

5.2 Experimental Design

5.2.1 Dataset

PM Data

Following the MIZ analysis in Chapter 4, which revealed significant differences in MIZ obtained from two different definitions, in particular in November 2020 to 2022 (see Figure 5.1), we chose here to focus on a more in-depth analysis of November 2021. With the objective of detecting MIZ using SAR data, our attention is directed towards the Greenland Sea for the month of November 2021. The Greenland Sea is frequently observed using Sentinel-1 data and has been studied by Strong and Rigor [31], who used several PM SIC products in the Arctic (1979–2011) and indicated that the Arctic summer MIZ expanded in width by 39%, while the Arctic winter MIZ decreased in width by 15%. The observed widening of the MIZ is reported to be closely associated with the decline of thick and multi-year sea ice. In the present study, we used BT SIC in our analysis, with a 25 km gridded resolution from the United States National Snow and Ice Data Center [157].

Sentinel-1 SAR Data

To extract SIC from SAR data we follow the well-established approach of using a convolutional neural network. For model training, we employed the publicly available AI4Arctic Sea Ice Challenge dataset [158]. The SAR data used in this study corresponds to two-channel dual-polarized (HH and HV) Sentinel-1 (C-band, 5.410 GHz), Ground Range Detected Medium spatial resolution images acquired in the Extra-Wide mode. Thermal noise correction and calibration (for σ_0) for the Sentinel-1 SAR scenes in the dataset was performed using the NERSC algorithm [159]. The total number of scenes was 533, where the available scenes covering the Greenland Sea were 110. To enhance data handling efficiency, the original SAR data with a 40 m grid cell spacing (~ 10,000 × 10,000 grid cells) has undergone downsampling to 80 m (~ 5,000 × 5,000 grid cells) using a 2×2 averaging kernel. Each scene is normalized based on the statistical information for the entire dataset. The corresponding rasterized ice charts SIC used for the labels during the training were produced by the Greenland Ice Service at the Danish Meteorological Institute [158]. To execute the inference process, we acquired Sentinel-1 SAR scenes from the Alaska Satellite Facility (ASF, [160]), with specifications identical to those of the training scenes. For November 2021 there were 270 scenes available for the Greenland Sea. Subsequently, we

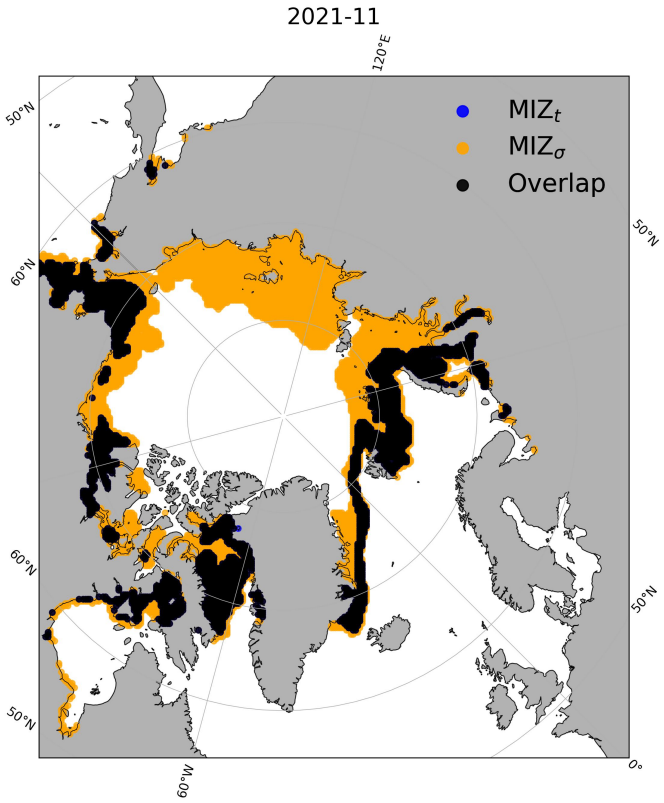

Figure 5.1: MIZ$_t$ and MIZ$_\sigma$ spatial map over the Arctic in November 2021. The MIZ$_t$ grid cells are defined using the criterion of $0.15 \leq \text{SIC} < 0.80$. The MIZ$_\sigma$ grid cells are defined using the criterion of $\sigma^a > 0.11$. The land is shown in grey.

performed pre-processing using the same procedures applied to the training scenes. A map illustrating the number of days for which SAR scenes are available for each grid cell over the region is shown in Figure 5.2. Notably, this map indicates that in the region under investigation for MIZ occurrences, SAR data is available for well over three-quarters of the days in a month. This extensive coverage can contribute to ensuring the reliability of the results and the validity of the interpretation.

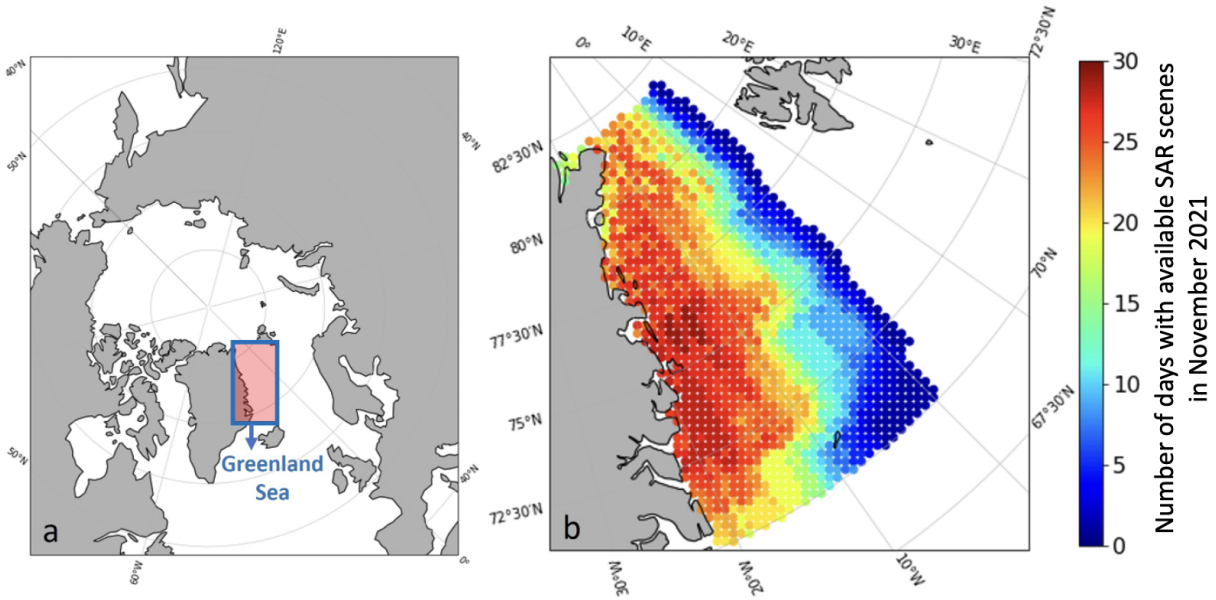

Figure 5.2: (a) The study region consists of the Greenland Sea, (b) Number of days Sentinel-1 SAR data (obtained from the Alaska Satellite Facility) is available over the Greenland Sea in November 2021 at each geographic location. The land is shown in grey.

SMOS Sea Ice Thickness

For the purpose of strengthening the observations, we employed the soil moisture and ocean salinity (SMOS) sea ice thickness (SIT) data, with a 12.5 km gridded resolution from the ESA [1] [161]. To maintain calculation consistency, the SMOS SIT is re-gridded to the BT spatial resolution using bilinear interpolation. The microwave imaging radiometer using aperture synthesis (MIRAS) instrument is a PM radiometer (L-Band, 1.4 GHz) onboard the SMOS satellite which can capture sea ice thickness. SMOS data have been accessible since 2010, with the mission's operational timeline extended until at least the end of 2025. The maximum retrievable ice thickness is contingent on sea ice salinity and temperature, exhibiting variability across regions and seasons. Consequently, it is useful to complement the SIT data with its associated uncertainty. Data with an uncertainty exceeding 1 meter should be utilized cautiously [162]. Notably, SMOS SIT is not available for latitudes south of 50°N and during the months of May to September.

[1] European Space Agency.

5.2.2 Model Architecture

In this research, we employed a U-net model [163] for the estimation of SAR SIC. The baseline architecture of the U-net model is depicted in Figure 5.3. In this study, we modified the architecture by incorporating 32 filters in the first two blocks and 64 filters for the remaining blocks. The U-net incorporated a rectified linear unit (ReLU) activation function to introduce nonlinearity between layers. Image upsampling was achieved through a transpose convolution operation with a stride rate of 1 and a zero value. Stochastic gradient descent served as the chosen optimizer for the U-net, trained with a starting learning rate of 0.001. Following the initial setup, a cosine learning rate schedule with restarts [164] was employed to adjust the learning rate during training. This model architecture was selected for its efficiency and the quality of predictions for SIC [156] and has been trained from scratch using two inputs (HH and HV SAR channels). The "Kaiming He initialization" method [165] was employed to initialize the weights of the network. Following the AI4Arctic Sea Ice Challenge protocol [158], we used 495 scenes for training, 18 scenes for validation (which were randomly chosen from the 513 total scenes), and 20 scenes for testing. The model was trained until it reached convergence, meaning the training loss stabilized and showed minimal changes. The training process required approximately six hours to complete. The R-squared values at convergence (at epoch 85) were 0.91 for the training set and 0.89 for the test set, respectively. All experiments are conducted on the Narval cluster of Compute Canada [166] using an NVIDIA A100-SXM4-40GB GPU and 128GB of memory, with the PyTorch 1.12 library. An illustration of the model output is presented in Figure 5.4.

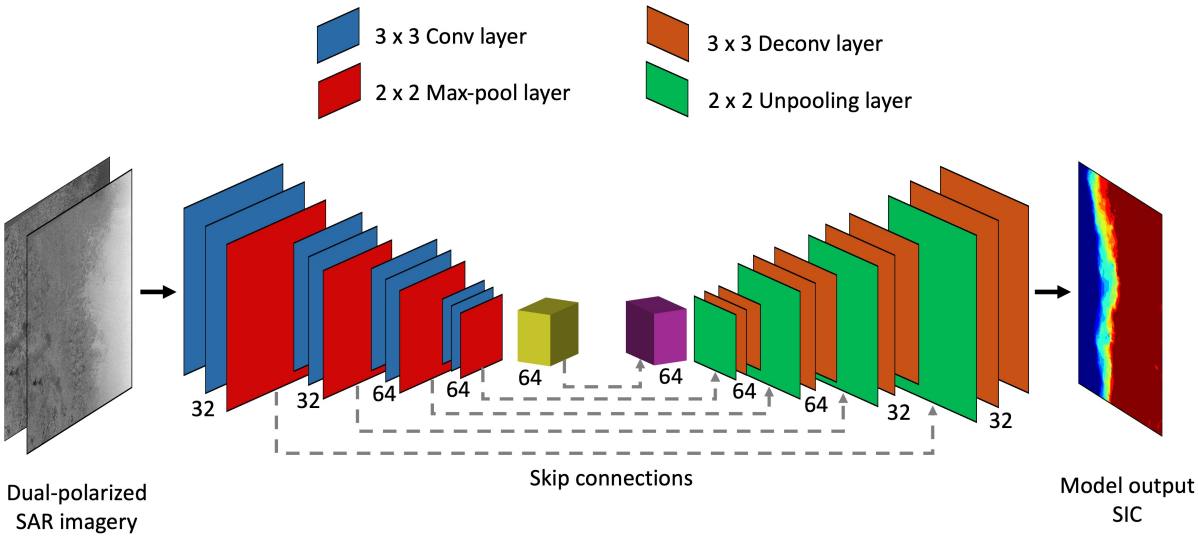

Figure 5.3: The U-net model architecture employed for extracting SIC from SAR data.

5.2.3 Spatial and Temporal Mapping of SAR SIC

To address the spatial resolution disparity between the SIC from PM and SIC from SAR, we matched them by presenting them at the same spatial resolution prior to conducting calculations. This involved averaging the SAR SIC over an area equivalent to the PM footprint and that can be modeled as an ellipse with a minor axis of 28 km and a major axis of 70 km, approximating a circular shape with a diameter of 49 km. Subsequently, we determined the average SIC for all grid cells within this spatial resolution. Finally, to ensure calculation consistency, SAR SIC is re-gridded to the PM spatial resolution using bilinear interpolation. Figure 5.5 illustrates the daily SIC map for PM, SAR (averaged over the PM footprint before land-masking), and SAR (re-gridded to PM spatial resolution).

5.2.4 MIZ Definitions

SIC Threshold-based MIZ Fraction (MIZ_tF)

To define the monthly MIZ_t, we first calculated the monthly mean SIC values for a particular grid cell over a month. Next, we determined the MIZ using the SIC criterion (MIZ_t) as $0.15 \leq SIC < 0.80$. The SIC threshold-based MIZ Fraction (MIZ_tF) can be obtained by

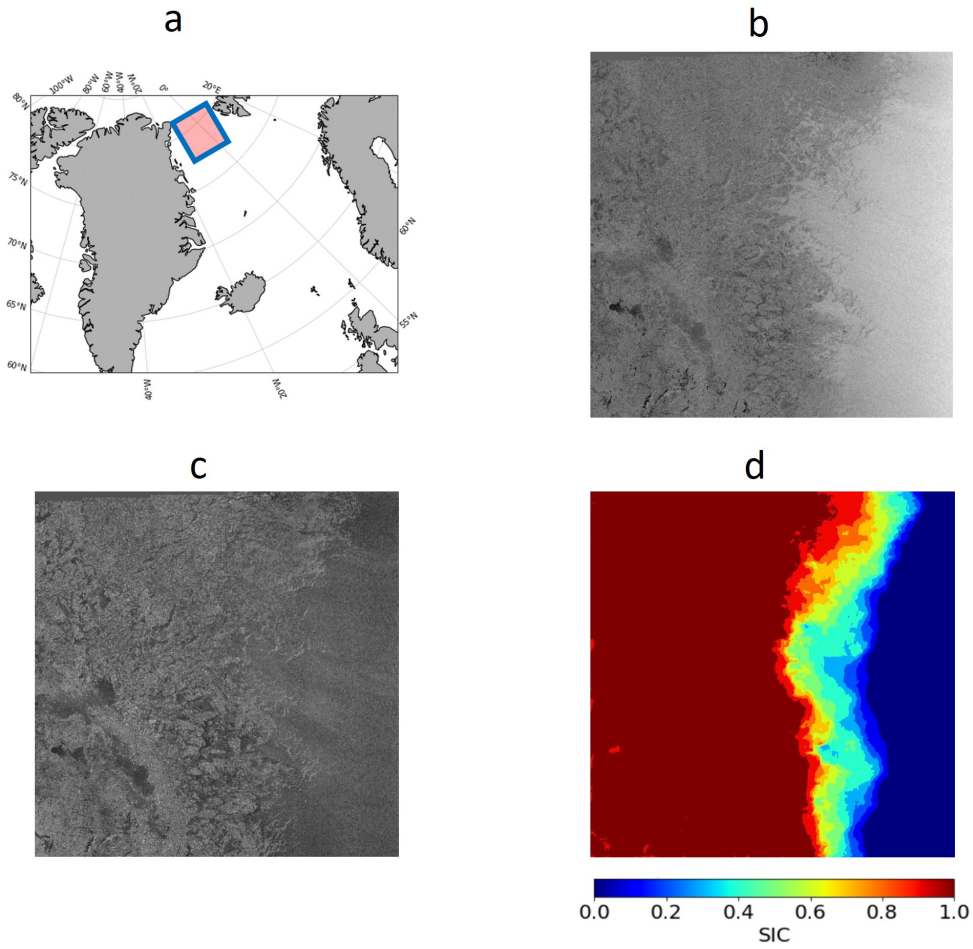

Figure 5.4: (a) Schematic representation of Sentinel-1 SAR scene geographic location, (b) HH Polarized Sentinel-1 SAR scene acquired 2021/11/03 over the Greenland Sea, (c) HV Polarized Sentinel-1 SAR scene acquired 2021/11/03 over the Greenland Sea, and (d) model output SIC for the corresponding Greenland Sea Sentinel-1 SAR scene.

dividing the MIZ area (considering MIZ_t) by the sea ice area.

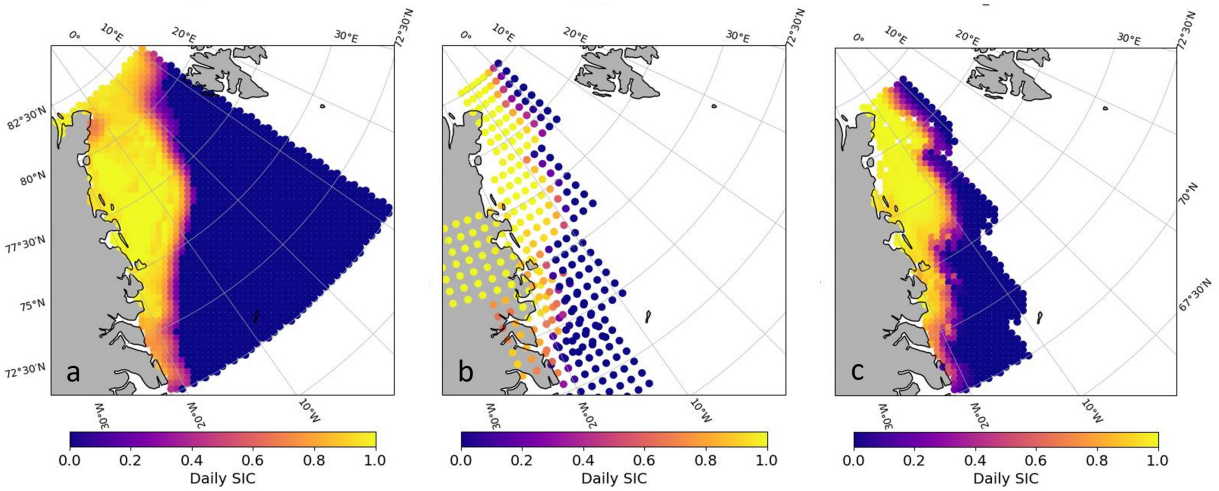

Figure 5.5: (a) Bootstrap daily SIC map, (b) SAR daily SIC map (averaged over the Bootstrap footprint before land-masking), and (c) SAR daily SIC map (re-gridded to Bootstrap spatial resolution) over the Greenland Sea on 2021/11/03. The land is shown in grey.

SIC Anomaly-based MIZ Fraction ($MIZ_{\sigma}F$)

SIC anomaly is defined as the deviation of SIC at a particular grid cell from its long-term average taken over November 2021. The monthly SIC anomaly for a grid cell located at i, j, is calculated as $a^m_{i,j,d} = SIC^m_{i,j,d} - SIC^m_{i,j}$ [167], where $SIC^m_{i,j,d}$ is the SIC value at the grid cell with the location of i, j on each day d in a given month m (in this study November 2021), and $SIC^m_{i,j}$ is the average SIC value for the same grid cell over November 2021. The standard deviation of the monthly SIC anomaly (σ) captures the SIC variability of a given grid cell over a month. The monthly SIC anomaly for a given grid cell located at i, j or $\sigma^a_{i,j}$ over month m with n total days ($d = 1$ to n) can be calculated by taking the square root of the variance, which is the mean of the squared daily SIC anomalies or $a^m_{i,j,d}$ [39]. $\sigma^a_{i,j}$ can be defined as $\sigma^a_{i,j} = \sqrt{\frac{1}{n}\sum_{d=1}^{n}(a^m_{i,j,d})^2}$ [167]. Following defining the $\sigma^a_{i,j}$, one can compute the median value of each grid cell over November 2021 for both sub-regions. Plotting the probability density function (PDF) allows for the identification of distinct regions based on the median σ^a behaviour. Subsequently, a threshold can be applied to delineate these regions. Drawing inspiration from the methodology of [167], who established a threshold of 0.11 from the PM SIC PDF plot covering the entire Arctic over 40 years, we have opted to apply the same threshold of 0.11 to the standard deviation of SIC anomaly (alternative thresholds are considered in Section 5.3.3). The SIC anomaly-based MIZ fraction ($MIZ_{\sigma}F$)

can then be obtained by dividing the MIZ area (considering MIZ_σ) by the sea ice area.

5.3 Results

5.3.1 Difference in SIC Products

For PM product, the monthly SIC map (Figure 5.6 panel a) shows a clear delineation of open water and consolidated ice in regions where the SIC varies from low to intermediate SIC (at the ice edge boundary). The median σ^a map (Figure 5.6 panel b) signifies areas with variable SIC, likely to be experiencing transitional states associated with freeze-up (ice growth). The fact that MIZ_tF has a lower value (0.16) than $\text{MIZ}_\sigma\text{F}$ (0.59) suggests that the former is less sensitive to the ice condition (over the transition period), potentially excluding regions that the latter would classify as MIZ (Figure 5.6 panel c). For SAR product, the monthly SIC map (Figure 5.7 panel a) reveals a less pronounced distinction between open water and consolidated ice regions when compared to the PM SIC map. Additionally, looking at the SAR median σ^a maps (Figure 5.7 panel b), we observe that a central region is not consistently identified with high values, unlike the PM product. Upon examining SMOS sea ice thickness data, we deduce that this discrepancy likely arises from the presence of thin ice in early November, as ice begins to form. The PM data might inaccurately classify this area as open water [53, 54], whereas SAR data can discern thin ice, which typically exhibits regions with features such as ice filaments and ice eddies, which can be identified with a CNN. In Figure 5.8, daily SMOS SIT and SIT uncertainty maps for several days in November 2021 are presented. The visuals illustrate the growth and formation of ice in the specified region, with noticeable thickening towards the end of the month. The SIT uncertainty maps demonstrate areas where SIT data might be less reliable due to various factors that affect the precision of satellite measurements, such as changes in ice temperature, salinity, or the transition from thin to thicker ice. These factors can introduce complexities in the signal received by the SMOS satellite, thus increasing the uncertainty in SIT estimates [168].

Comparing SAR product, processing with CNNs, to PM algorithms highlights key distinctions. SAR SIC leverages machine learning, trained on diverse ice condition datasets, allowing it to detect intricate patterns and features in SAR data. This approach contrasts with the PM algorithm's empirical method, which relies on physical microwave emissions and brightness temperature to estimate SIC. While SAR-CNN can discern a

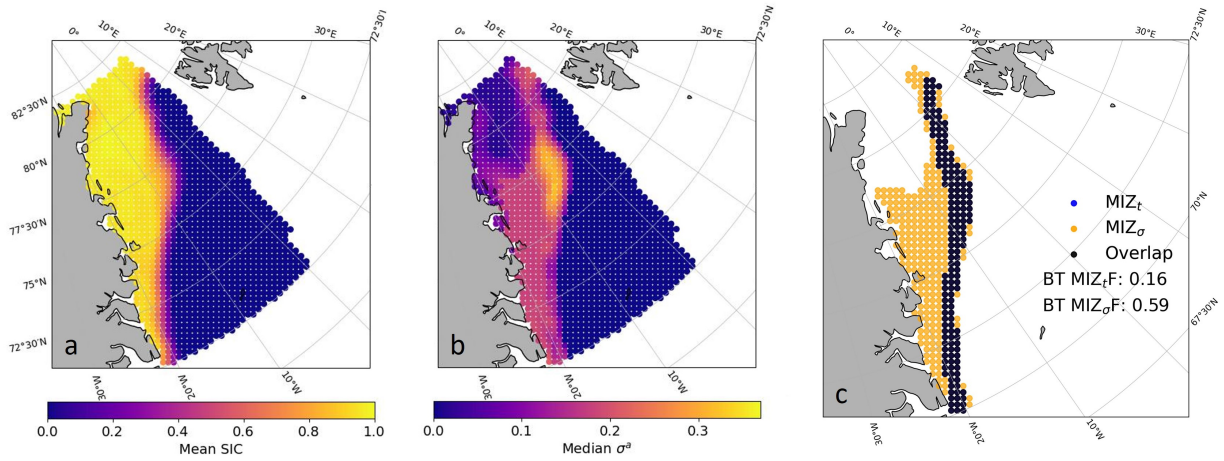

Figure 5.6: (a) BT mean SIC map, (b) BT median σ^a map, and (c) MIZ_t and MIZ_σ spatial map for BT over the Greenland Sea in November 2021. The MIZ_t grid cells (denoted by orange circles) are defined using the criterion of $0.15 \leq SIC < 0.80$. The MIZ_σ grid cells (denoted by blue circles) are defined using the criterion of $\sigma^a > 0.11$. Overlapping areas between both MIZ definitions are depicted as black circles. The land is shown in grey.

broader range of ice conditions and provide detailed MIZ delineation, the PM algorithm, being less parameter-intensive, might not adapt as well to varied ice scenarios, especially in mixed or thin ice areas. Thus, the SAR-CNN's data-driven model offers more complexity in detection than the faster PM approach, illustrating the fundamental difference between machine learning and empirical methodologies in ice detection. At the same time, in many regions, the SAR image acquisition frequency from SAR is not sufficient to use the anomaly definition.

5.3.2 Difference in MIZ Definitions

Figure 5.9 highlights the disparities in MIZF values derived from the two different definitions of the MIZ. The comparison indicates that regions identified by the SIC threshold-based definition from two distinct products have minimal overlap. Conversely, MIZ regions determined by the anomaly-based definition show a significant overlap. The anomaly-based definition typically yields higher MIZF values, identifying a broader spatial distribution of SIC anomalies. On the other hand, the threshold-based definition tends to outline a more

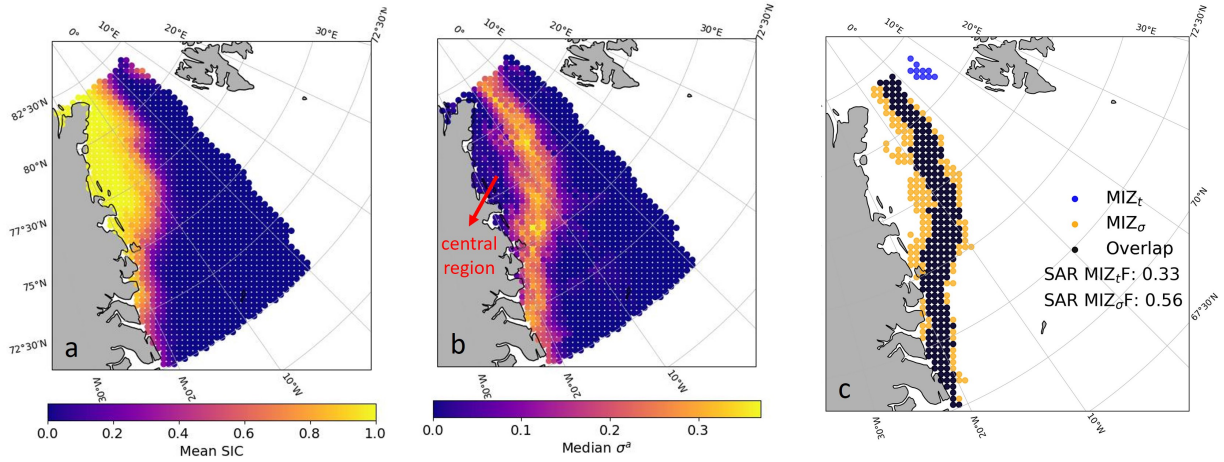

Figure 5.7: (a) SAR mean SIC map, (b) SAR median σ^a map, and (c) MIZ$_t$ and MIZ$_\sigma$ spatial map for SAR over the Greenland Sea in November 2021. The MIZ$_t$ grid cells (denoted by orange circles) are defined using the criterion of $0.15 \leq \text{SIC} < 0.80$. The MIZ$_\sigma$ grid cells (denoted by blue circles) are defined using the criterion of $\sigma^a > 0.11$. Overlapping areas between both MIZ definitions are depicted as black circles. The land is shown in grey.

narrowly defined MIZ, beneficial for pinpointing the precise transitional area from open water to pack ice. However, an anomaly-based threshold could potentially broaden the MIZ boundary, encompassing areas with highly variable ice conditions and possibly reflecting zones of ice formation. This approach captures the MIZ's variability and dynamics more comprehensively, including in regions where the ice is forming or changing.

5.3.3 Difference in σ^a Threshold

To investigate the impact of varying threshold levels of σ^a on MIZ$_\sigma$F determined by the anomaly-based approach, Figure 5.10 showcases the analysis across three distinct σ^a thresholds: 0.15, 0.18, and 0.22. These thresholds were utilized to delineate the MIZ$_\sigma$ using data from both PM and SAR products. It can be seen that at a threshold of 0.15 (panel a), both PM and SAR products show a significant amount of overlap in the identification of the MIZ$_\sigma$. The MIZ$_\sigma$F values are relatively close, with PM MIZ$_\sigma$F at 0.49 and SAR MIZ$_\sigma$F at 0.47. This suggests that both products are in relatively good agreement when the threshold

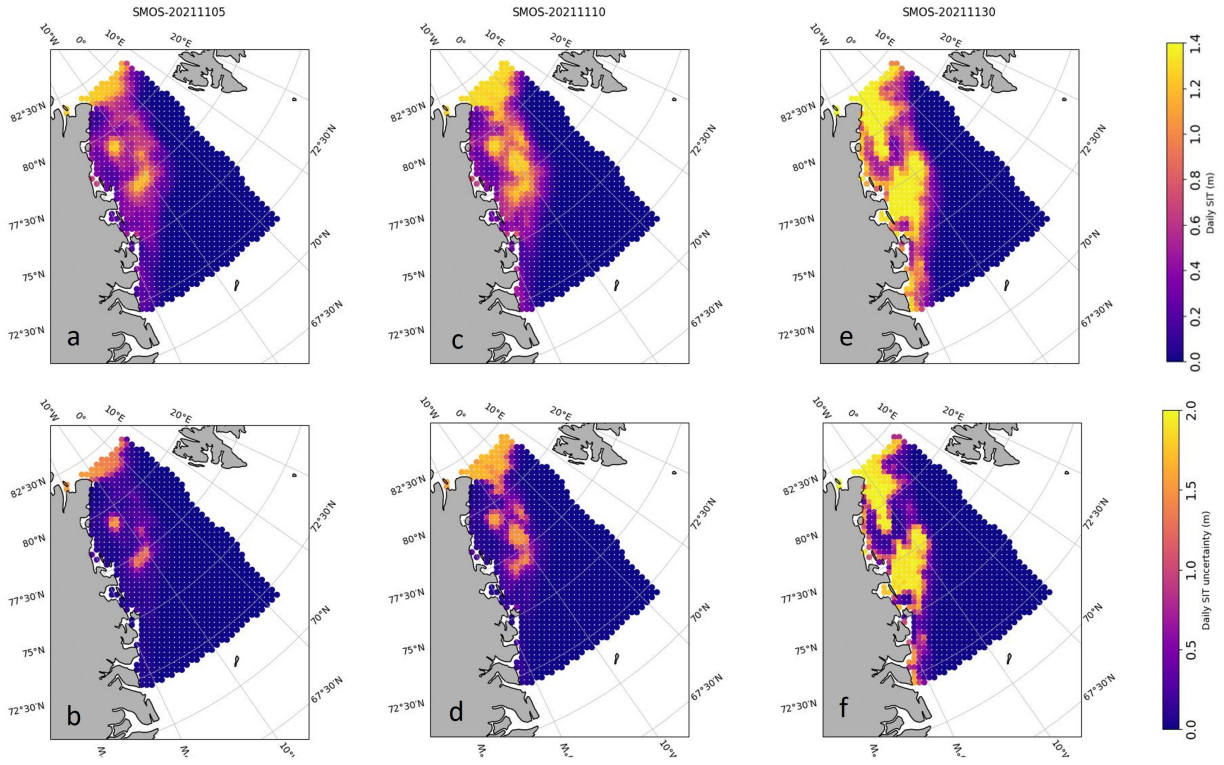

Figure 5.8: Daily SMOS sea ice thickness (SIT) and SIT uncertainty maps for 2021-11-05 (panel a and b), 2021-11-10 (panel c and d), and 2021-11-30 (panel e and f) over the Greenland Sea. The land is shown in grey.

is set to 0.15. As the threshold increases to 0.18, there is still a notable overlap between PM $MIZ_\sigma F$ and SAR $MIZ_\sigma F$, but the $MIZ_\sigma F$ values start to diverge more significantly, with PM $MIZ_\sigma F$ decreasing to 0.33 and SAR $MIZ_\sigma F$ slightly decreasing to 0.42. This indicates that the PM product is beginning to exclude some areas from the MIZ_σ that the SAR product still includes. With the highest threshold of 0.22, the difference between these two products becomes more pronounced. The PM $MIZ_\sigma F$ drops remarkably to 0.07, indicating that many areas previously identified as MIZ_σ by the PM product at lower thresholds are no longer included. In contrast, the SAR $MIZ_\sigma F$ remains higher at 0.29, suggesting that the SAR data continues to identify a larger area as MIZ_σ at this higher threshold.

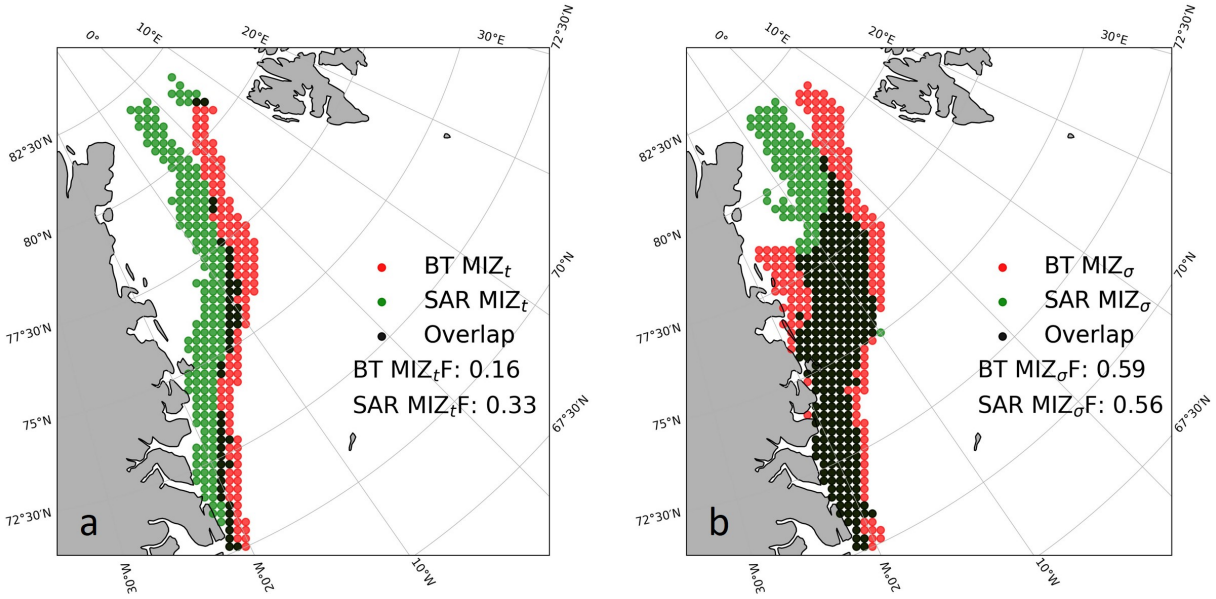

Figure 5.9: MIZ_t (panel a) and MIZ_σ (panel b) spatial map for BT and SAR over the Greenland Sea in November 2021. The MIZ_t grid cells (denoted by red circles) are defined using the criterion of $0.15 \leq \text{SIC} < 0.80$. The MIZ_σ grid cells (denoted by green circles) are defined using the criterion of $\sigma^a > 0.11$. Overlapping areas between both MIZ definitions are depicted as black circles. The land is shown in grey.

5.4 Conclusion

In this study, two MIZ definitions using PM and SAR SIC products, are investigated for November 2021 over the Greenland Sea. Our discussion has shed light on the factors contributing to variations in the MIZF. These variations are influenced by two key factors: the choice of SIC products and the selection of MIZ definitions. The anomaly-based definition of MIZ tends to yield a spatially extensive MIZ region, capturing more of the sea ice concentration variability due to ice growth. The anomaly-based definition of MIZ is also more consistent over the two products. We also found that when the threshold for the standard deviation of SIC anomaly increases, the MIZ_σF derived from PM product decreases more dramatically than the MIZ_σF from the SAR product. This could imply that the PM product's sensitivity to changes in SIC anomalies decreases as the threshold is raised, whereas the SAR product consistently detects the MIZ_σ over a large spatial area, showing less susceptibility to the chosen thresholds in comparison to the PM data. The implications of this study suggest that the selection of MIZ definition should be carefully

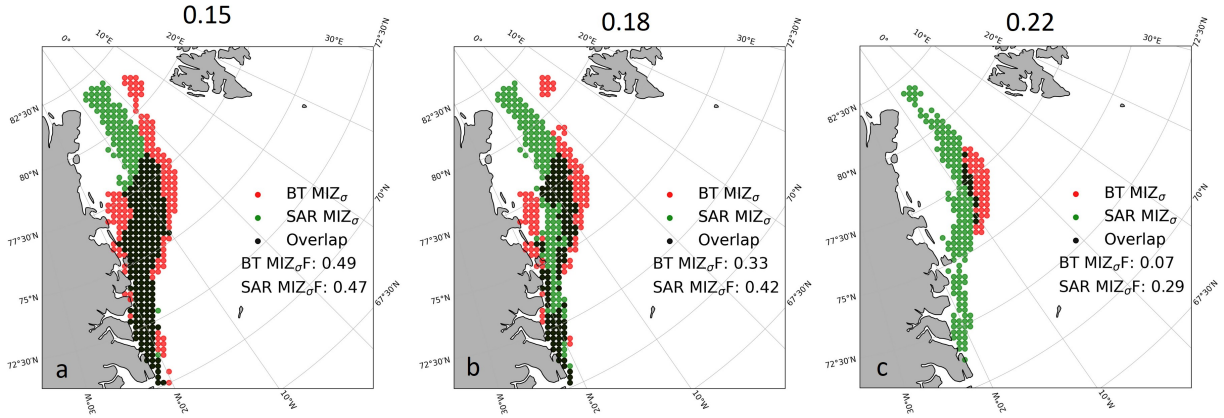

Figure 5.10: MIZ$_\sigma$ spatial map for BT and SAR over the Greenland Sea in November 2021. The MIZ$_\sigma$ grid cells are defined using the criterion of $\sigma^a > 0.15$ (panel a), $\sigma^a > 0.18$ (panel b), and $\sigma^a > 0.22$ (panel c). The land is shown in grey.

considered based on the intended practical or research application. The insights obtained from this analysis offer a valuable reference point for future explorations and can serve as a guide for operational applications, scientific inquiry, and environmental monitoring within polar regions.

Chapter 6

Conclusions

In Chapter 3, three passive microwave algorithms (ASI, NT2, BT) were compared in the eastern Canadian Arctic to examine sea ice edge displacement error (EDE), which is a dimensionless measure used to assess the difference between the PM-based ice edge and the chart-based ice edge locations and lengths of sea ice edges over time. ASI had the highest EDE, while BT had the lowest. Ice edge in October (beginning of freeze-up period) exhibits significant meandering. April showed the highest EDE variability due to fluctuating winds and temperatures. In Chapter 4, a 40-year analysis of the MIZ using two definitions was investigated, one based on SIC threshold (MIZ_t) and the other based on a SIC anomaly (MIZ_σ). The $MIZ_\sigma F$ consistently peaked during freeze-up and break-up, reflecting higher values across all seasons. Post mid-2000s, both $MIZ_t F$ and $MIZ_\sigma F$ significantly increased, suggesting potential climate change impacts in the Arctic. In Chapter 5, the investigation into MIZ detection in the Greenland Sea using PM and SAR SIC data revealed the spatially extensive delineation of the MIZ through the anomaly-based definition. Furthermore, this delineation exhibited consistency across different data products. Higher SIC anomaly thresholds showed a sharper decrease in PM data's $MIZ_\sigma F$ compared to SAR data, highlighting SAR's spatially broad MIZ detection and its reduced susceptibility to changes in thresholds. In conclusion, this thesis enhances our understanding of Arctic sea ice conditions through a comparative analysis of sea ice edge displacement error, shedding light on PM algorithm performance. The 40-year trend and change point analysis using BT SIC data broadens our knowledge on MIZ fluctuations and climate change impacts. Additionally, the comparison of different definitions for the MIZ serves as a guide for future scientific investigation.

6.1 Concluding Remarks

The primary contributions of this work are as follows

- In Chapter 3, sea ice edge derived from three PM algorithms, ASI, NT2, and BT, are compared to those derived from the daily Canadian Ice Service charts over a primarily seasonal ice zone in the eastern Canadian Arctic for 2013-2021. In order to determine the ice edge error, we introduced an edge-length-based displacement measure called the EDE, a dimensionless measurement obtained by dividing the weighted average Hausdorff distance by the ice edge length, where the weighted average Hausdorff distance is derived from a given PM product and the ice chart, while the ice edge length is determined by the average of the ice edge lengths from both the chart and the PM algorithm. We found that the ASI algorithm has the highest EDE on average, while the BT algorithm has the lowest one. In the freeze-up period, the PM algorithms have the highest mean EDE value relative to other months due to the appearance of thin ice. A greater range of EDE values was observed in April than in other months. It is concluded that EDE, with less sensitivity to changes in the charted area, is a reliable method for assessing the ice edge from PM SIC algorithms relative to the ice charts, as it is not affected by the fluctuations in the coverage area of the ice chart. The EDE helps to provide a consistent and meaningful comparison of edge displacement across various scenarios and products.

- In Chapter 4, we used BT SIC to detect the trend and change point of the Arctic MIZ over 40 years (1983-2022) using two different MIZ definitions: SIC threshold-based (MIZ_t) and SIC anomaly-based (MIZ_σ). This study marks the first examination of an anomaly based MIZ definition in the Arctic, to assess its potential usefulness as a complementary definition to existing definitions. While the two MIZ definitions yield comparable seasonal trends in MIZF, the MIZ_σF values peak during the transition periods (e.g., freeze-up and break-up), while the MIZ_tF values peak in August. The analysis also uncovers consistently higher MIZF values for the MIZ_σ than for MIZ_t across all seasons. Moreover, October and August show the fastest rate of increase in MIZ_tF and MIZ_σF, reflecting the coinciding rapid decrease in sea ice extent during those particular months. Employing the PELT, a multiple change point detection method, highlights a significant increase in the MIZ_tF in October (after 2005) and MIZ_σF in August (after 2007). This can be indicative of the recent climate change impacts in the Arctic region that may be linked with shifts in SIC and sea ice mobility for MIZ_t and MIZ_σ, respectively. It is concluded that the SIC anomaly-based

definition can be considered as a complementary definition to delineate the MIZ over the Arctic.

- In Chapter 5, we used PM and SAR SIC in the Greenland Sea in November 2021 to detect the MIZ using two different MIZ definitions: SIC threshold-based (MIZ_t) and SIC anomaly-based (MIZ_σ). This study marks the comparison of two sea ice products employing the SIC anomaly-based definition of the MIZ. Our findings reveal that the SIC anomaly-based definition delineates an extensive MIZ region, capturing the variation in SIC attributed to the sea ice growth. This definition also demonstrated greater consistency across the two different SIC data products. We also found that increasing the threshold for the SIC anomaly standard deviation results in a steeper decline in $MIZ_\sigma F$ from PM data than from SAR data, suggesting SAR's more consistent MIZ_σ detection and less sensitivity to varying thresholds, compared to PM data. We concluded that the SIC anomaly-based definition of MIZ effectively identifies areas where SIC fluctuates during transitional periods like freeze-up due to the emergence of thin ice. This method proves efficient in detecting spatially (characterized by high SIC anomaly) and temporally (represented by shifts in ice transition times) significant regions, thereby showcasing its utility as a complementary approach alongside the traditional SIC threshold-based definition.

6.2 Research Impacts

In light of the upcoming Copernicus imaging microwave radiometer (CIMR) mission, proposed to launch as early as 2028, the findings of this study hold significant relevance to the mission's anticipated outcomes. CIMR, designed as a multi-frequency mission, will measure 1.4 GHz at 55 km, 6.9 and 10.6 GHz at ~ 15 km and 18.7 GHz at ~ 5 km spatial resolution [169]. This capability promises to furnish users with sea ice parameters at a notably high spatial resolution of about 5 km, surpassing the limitations posed by near-90 GHz solutions affected by atmospheric conditions. Leveraging these SIC products, alongside the methodology discussed for EDE measurement and MIZ analysis, presents an intriguing avenue for comparison and potential advancement in operational applications. Furthermore, such endeavors could potentially contribute to the refinement of operational products and methodologies at operational centers (see Section 2.6 for a discussion) through data fusion techniques, such as integrating PM data with SAR-based products like ice charts. Such fusion efforts could aid in bias correction of PM products, as well as the evaluation and

initialization of climate model outputs.

Considering the anomaly-based definition of the MIZ, its applications extend to the initialization and validation of sea ice models. Notably, Posey et al. [170] utilized MIZ contours to assess the performance of the US Navy ice forecast model. Additionally, given the association between MIZ boundaries and the ice edge boundary, defining the MIZ could directly impact the ice edge identification purposes. For instance, the "Argo float program" in 2016 utilized Antarctic MIZ products to investigate instances where floats ceased reporting, presumably encountering the ice edge [171]. Beyond its immediate applications, employing the anomaly-based definition allows for a broader characterization of climatically crucial regions beyond the sea ice extent or SIC. This expanded perspective could be of interest to researchers in various fields. Moreover, the temporal variability captured by this definition, with different ice transition periods exhibiting varying SIC anomalies (e.g., higher anomalies during break-up and freeze-up periods), suggests its capability to serve in temporal classification tasks (e.g., [172]).

Furthermore, in reference to the forthcoming SAR mission NISAR (NASA-Indian Space Research Organisation (ISRO) Synthetic Aperture Radar), planned to launch in early 2024 [173], a recent study has highlighted the enhanced capability of detecting newly formed ice at L-band NISAR compared to C-band SAR [174]. Hence, there is potential for this study to be expanded to explore MIZ incorporating data from this mission in the future. Our findings also underscore discrepancies in MIZ delineation between SAR and PM data, even when employing the traditional threshold-based definition. These disparities hold significance for various downstream applications reliant on MIZ extent monitoring (e.g., sea ice thickness estimation, sea ice velocity determination, and the Argo float program). These applications depend on the accurate identification of MIZ in their screening processes to determine the necessity of data retrieval at specific locations.

6.3 Research Limitations

Several limitations were encountered during this research. The first contribution (Chapter 3) faced challenges in reference data for the ice edge due to data variability. For instance, ice charts, utilized as reference data, lack daily availability over a long time series and for the entire Arctic region. Moreover, alternative data sources like SAR products pose challenges due to their re-visit time, potentially failing to cover the same locations daily. Furthermore,

lack of spatial autocorrelation across different SIC products posed another limitation in this study. The disparity in spatial resolution directly influenced the methodology, requiring the use of clustering methods to remove isolated ice patches for high-resolution products. Conversely, coarse spatial resolution products offered limited detail on SIC, affecting the sea ice edge estimation. In the second contribution (Chapter 4), leveraging the extensive data availability of PM data was useful. However, a significant challenge emerged in accessing data for analyzing long-term trends using atmospheric variables from reanalysis data. This challenge arises from the dependency of reanalysis data (like ERA5) on SIC from PM data as a lower boundary condition, complicating the examination of long-term trends in atmospheric variables.

For the third contribution (Chapter 5), the methodology employed was based on the definition of SIC anomaly, which necessitates daily SIC values for specific grid cells over a defined period (e.g., a month). However, finding an independent source of SIC data with PM SIC products presented challenges. In this research, SAR products were utilized as an alternative SIC products. The constraint lies in the revisit time associated with SAR products, making it difficult to find regions consistently covered on a daily basis for an entire month. Consequently, the question arise regarding the adequacy of the number of observation days needed to capture meaningful anomalies. This dilemma is compounded by the spatio-temporal nature of the problem, as anomalies can manifest on various time scales (from short-term fluctuations to longer-term trends) and some regions might show higher anomaly. Note that the grid cells exhibiting higher variability may necessitate more frequent observations to accurately capture meaningful anomalies. Moreover, no dataset is immune to noise or errors, further complicating the analysis. Increasing the number of observation days can help alleviate the impact of noise and yield a more robust anomaly estimate. However, in scenarios where data availability is limited for the region of study, conducting sensitivity analyses by varying the number of observation days and assessing their impact on the results becomes important. This approach aids in identifying the optimal balance between the required number of observation days per grid cell over a given time frame and the reliability of the results, all while considering computational efficiency. This aspect was not investigated in the study since data availability for the study region was not constrained.

6.4 Future Works

The research conducted in this work has contributed to the evaluation of the sea ice edge as identified by various passive microwave retrieval algorithms and has introduced a measurement approach for estimating ice edge displacement. Additionally, in this thesis, two definitions of MIZ were investigated for SIC measured from two different sensors. There are several areas that warrant further investigation and can be explored in future work:

- **Incorporating Additional Data Sources for Ice Edge Comparison:** Within Chapter 3, incorporating the ice edge data obtained from different products (discussed in Section 2.6) can help in assessing the accuracy and reliability of ice edge delineation from different remote-sensing sea ice products. This approach facilitates the identification of which product is best suited for sea ice-related assessments.
- **Comprehensive Ice Edge Displacement Analysis:** In Chapter 3, future investigations could concentrate on implementing the suggested ice edge displacement measurement in other regions where the ice edge holds significance, such as the Beaufort Sea. This analysis would serve to validate the feasibility of the new measurement approach, potentially yielding a comprehensive sea ice edge displacement analysis.
- **Long-Term Trend Analysis:** Regarding chapter 3, extending the temporal coverage of the study might enable the examination of long-term trends in ice edge variation. This would be particularly valuable in the context of climate change and its impact on sea ice variability over time.
- **Utilizing Different PM SIC Products:** In Chapter 4, an alternative PM SIC products such as OSISAF (commonly referred to as a hybrid algorithm) or those products discussed in Section 2.6 could be incorporated. Such inclusion has the potential to yield divergent conclusions and illuminate additional facets of PM algorithm utilization.
- **Analyze Underlying Variables:** Concerning Chapter 4, future research can look into the long term time series of the geophysical variables such as wind speed over the ocean that affect the MIZ variability. This would provide a more solid foundation for evaluating the effectiveness of the MIZ definitions used in this thesis.
- **Expand the Region of Study:** In the examination of MIZ definitions for the comparative study outlined in Chapter 5, the focus of the research was limited to a specific Arctic sub-region. Enhancing the scope of the study to encompass a more

diverse array of locations has the potential to offer a more thorough understanding of the MIZ and its variations across various Arctic regions.

- **Consider Seasonal Variability:** Within Chapter 5, investigating how the MIZ, derived from different definitions, varies with the seasons can lead to more accurate predictions and understanding of the ice variability. This could also involve examining the impact of seasonal changes on marine ecosystems and human activities in the Arctic.

References

[1] WI. Joint. SIGRID-3: A vector archive format for sea ice charts: developed by the International Ice Charting Working Group's Ad Hoc Format Team for the WMO Global Digital Sea Ice Data Bank Project. *Commission for Oceanography and Marine Meteorology Technical Report, No. 23*, 2004.

[2] JCOMM Expert Team on Sea Ice. Sea-Ice Nomenclature: snapshot of the WMO Sea Ice Nomenclature. *JCOMM Technical Report- No. 23*, 1(259):121, 2014.

[3] Steven Walfish. A review of statistical outlier methods. *Pharmaceutical technology*, 30(11):82, 2006.

[4] Akio Yamagami, Mio Matsueda, and Hiroshi L Tanaka. Extreme arctic cyclone in August 2016. *Atmospheric Science Letters*, 18(7):307–314, 2017.

[5] Mohammed Shokr and Nirmal Sinha. *Sea ice: physics and remote sensing*. John Wiley & Sons, 2015.

[6] David N Thomas and Gerhard Dieckmann. *Sea ice: an introduction to its physics, chemistry, biology and geology*. John Wiley & Sons, 2008.

[7] NASA Global Climate Change and Global Warming: Vital Signs of the Planet. Global Climate Change: Evidence. https://climate.nasa.gov/vital-signs/arctic-sea-ice/, 2003. [Accessed February 2024].

[8] Walter N Meier, Greta K Hovelsrud, Bob EH Van Oort, Jeffrey R Key, Kit M Kovacs, Christine Michel, Christian Haas, Mats A Granskog, Sebastian Gerland, Donald K Perovich, et al. Arctic sea ice in transformation: A review of recent observed changes and impacts on biology and human activity. *Reviews of Geophysics*, 52(3):185–217, 2014.

[9] Jackie Dawson, Larissa Pizzolato, Stephen EL Howell, Luke Copland, and Margaret E Johnston. Temporal and spatial patterns of ship traffic in the Canadian Arctic from 1990 to 2015. *Arctic*, 71(1):15–26, 2018.

[10] Alexandra N Stocker, Angelika HH Renner, and Maaike Knol-Kauffman. Sea ice variability and maritime activity around Svalbard in the period 2012–2019. *Scientific reports*, 10(1):1–12, 2020.

[11] Hyangsun Han, Sungjae Lee, Hyun-Cheol Kim, and Miae Kim. Retrieval of Summer Sea Ice Concentration in the Pacific Arctic Ocean from AMSR2 Observations and Numerical Weather Data Using Random Forest Regression. *Remote Sensing*, 13(12):2283, 2021.

[12] Jinlei Chen, Shichang Kang, Changsheng Chen, Qinglong You, Wentao Du, Min Xu, Xinyue Zhong, Wei Zhang, and Jizu Chen. Changes in sea ice and future accessibility along the Arctic Northeast Passage. *Global and Planetary Change*, 195:103319, 2020.

[13] Scott R Stephenson, Laurence C Smith, Lawson W Brigham, and John A Agnew. Projected 21st-century changes to Arctic marine access. *Climatic Change*, 118:885–899, 2013.

[14] Jin-Lei Chen, Shi-Chang Kang, Jun-Ming Guo, Min Xu, and Zhi-Min Zhang. Variation of sea ice and perspectives of the Northwest Passage in the Arctic Ocean. *Advances in Climate Change Research*, 12(4):447–455, 2021.

[15] Katherine Wilson, Andrew Arreak, Trevor Bell, Gita Ljubicic, Sikumiut Committee, et al. The mittimatalik siku asijjipallianinga (sea ice climate atlas): How inuit knowledge, earth observations, and sea ice charts can fill ipcc climate knowledge gaps. *Frontiers in Climate*, page 117, 2021.

[16] Jackie Dawson, Natalie Carter, Nicolien van Luijk, Colleen Parker, Melissa Weber, Alison Cook, Kayla Grey, and Jennifer Provencher. Infusing Inuit and local knowledge into the Low Impact Shipping Corridors: An adaptation to increased shipping activity and climate change in Arctic Canada. *Environmental Science & Policy*, 105:19–36, 2020.

[17] Wilford F Weeks and Stephen F Ackley. The growth, structure, and properties of sea ice. In *The geophysics of sea ice*, pages 9–164. Springer, 1986.

[18] Kenneth O Bennington. Desalination features in natural sea ice. *Journal of Glaciology*, 6(48):845–857, 1967.

[19] a WALKER O Smith Jr. Phytoplankton dynamics in marginal ice zones. *Oceanography and Marine Biology*, 25:11–38, 1987.

[20] National Snow and Ice Data Center. Why Sea Ice Matters. https://nsidc.org/learn/parts-cryosphere/sea-ice/why-sea-ice-matters. [Accessed April 2024].

[21] Marco Tedesco. *Remote sensing of the cryosphere*. John Wiley & Sons, 2014.

[22] Jonathan J Day, Sarah Keeley, Gabriele Arduini, Linus Magnusson, Kristian Mogensen, Mark Rodwell, Irina Sandu, and Steffen Tietsche. Benefits and challenges of dynamic sea ice for weather forecasts. *Weather and Climate Dynamics*, 3(3):713–731, 2022.

[23] Robin D Muench. The sea ice margins: a summary of physical phenomena. 1989.

[24] Michael SW Bradstreet. Occurrence, habitat use, and behavior of seabirds, marine mammals, and Arctic cod at the Pond Inlet ice edge. *Arctic*, pages 28–40, 1982.

[25] CJ Mundy, Michel Gosselin, Jens Ehn, Yves Gratton, Andrea Rossnagel, David G Barber, Johannie Martin, Jean-Éric Tremblay, Molly Palmer, Kevin R Arrigo, et al. Contribution of under-ice primary production to an ice-edge upwelling phytoplankton bloom in the Canadian Beaufort Sea. *Geophysical Research Letters*, 36(17), 2009.

[26] Mathieu LeBlanc, Stéphane Gauthier, Svend Erik Garbus, Anders Mosbech, and Louis Fortier. The co-distribution of Arctic cod and its seabird predators across the marginal ice zone in Baffin Bay. *Elementa: Science of the Anthropocene*, 7:1, 2019.

[27] Dorothy Hall. *Remote sensing of ice and snow*. Springer Science & Business Media, 2012.

[28] William G Pichel, Pablo Clement-Colon, Cheryl Bertoia, Michael Van Woert, Christopher C Wakerman, Frank Monaldo, Donald R Thompson, Karen S Friedman, and Xiaofeng Li. Routine production of SAR-derived ice and ocean products in the United States. *ESA Special Publication*, 565:19, 2004.

[29] JC Comiso and HJ Zwally. Concentration gradients and growth/decay characteristics of the seasonal sea ice cover. *Journal of Geophysical Research: Oceans*, 89(C5):8081–8103, 1984.

[30] Helge F Goessling, Steffen Tietsche, Jonathan J Day, Ed Hawkins, and Thomas Jung. Predictability of the Arctic sea ice edge. *Geophysical Research Letters*, 43(4):1642–1650, 2016.

[31] Courtenay Strong and Ignatius G Rigor. Arctic marginal ice zone trending wider in summer and narrower in winter. *Geophysical Research Letters*, 40(18):4864–4868, 2013.

[32] Rebecca J Rolph, Daniel L Feltham, and David Schröder. Changes of the Arctic marginal ice zone during the satellite era. *The Cryosphere*, 14(6):1971–1984, 2020.

[33] Vernon A Squire. Marginal ice zone dynamics. *Philosophical Transactions of the Royal Society A*, 380(2235):20210266, 2022.

[34] Jim Thomson. Wave propagation in the marginal ice zone: connections and feedback mechanisms within the air–ice–ocean system. *Philosophical Transactions of the Royal Society A*, 380(2235):20210251, 2022.

[35] Christopher Horvat. Marginal ice zone fraction benchmarks sea ice and climate model skill. *Nature Communications*, 12(1):2221, 2021.

[36] Norwegian Polar Institute . The marginal ice zone. https://www.npolar.no/en/themes/the-marginal-ice-zone/. [Accessed April 2024].

[37] D Dumont, A Kohout, and L Bertino. A wave-based model for the marginal ice zone including a floe breaking parameterization. *Journal of Geophysical Research: Oceans*, 116(C4), 2011.

[38] Peter Sutherland and Dany Dumont. Marginal ice zone thickness and extent due to wave radiation stress. *Journal of Physical Oceanography*, 48(8):1885–1901, 2018.

[39] Marcello Vichi. An indicator of sea ice variability for the Antarctic marginal ice zone. *The Cryosphere*, 16(10):4087–4106, 2022.

[40] Tom Carrieres, Mark Buehner, Jean-Francois Lemieux, and Leif Toudal Pedersen. *Sea ice analysis and forecasting: Towards an increased reliance on automated prediction systems*. Cambridge University Press, 2017.

[41] DR Thomas. Arctic sea ice signatures for passive microwave algorithms. *Journal of Geophysical Research: Oceans*, 98(C6):10037–10052, 1993.

[42] Laura C Brown, Stephen EL Howell, Jonas Mortin, and Chris Derksen. Evaluation of the Interactive Multisensor Snow and Ice Mapping System (IMS) for monitoring sea ice phenology. *Remote sensing of environment*, 147:65–78, 2014.

[43] Government of Canada. Satellite Characteristics: Orbits and Swaths. https://www.nrcan.gc.ca/maps-tools-and-publications/satellite-imagery-and-air-photos/tutorial-fundamentals-remote-sensing/satellites-and-sensors/satellite-characteristics-orbits-and-swaths/9283, 2015. [Accessed January 2022].

[44] Max Planck. *The theory of heat radiation*. Blakiston, 1914.

[45] Max Planck. On the law of distribution of energy in the normal spectrum. *Annalen der physik*, 4(553):1, 1901.

[46] Fawaz T Ulaby, Richard K Moore, and Adrian K Fung. Microwave Remote Sensing Fundamentals and Radiometry. Vol. 1, Microwave Remote Sensing: Active and Passive. *Remote Sensing*, 2, 1981.

[47] Duane T Eppler, L Dennis Farmer, Alan W Lohanick, Mark R Anderson, Donald J Cavalieri, Josefino Comiso, Per Gloersen, Caren Garrity, Thomas C Grenfell, Martti Hallikainen, et al. Passive microwave signatures of sea ice. In *Microwave remote sensing of sea ice*, volume 68, pages 47–71. Amer. Geophys. Union, 1992.

[48] Søren Andersen, Rasmus Tonboe, Stefan Kern, and Harald Schyberg. Improved retrieval of sea ice total concentration from spaceborne passive microwave observations using numerical weather prediction model fields: An intercomparison of nine algorithms. *Remote Sensing of Environment*, 104(4):374–392, 2006.

[49] Ron Kwok. sea ice concentration estimates from satellite passive microwave radiometry and openings from SAR ice motion. *Geophysical Research Letters*, 29(9):25–1, 2002.

[50] Søren Andersen, Rasmus Tonboe, Lars Kaleschke, Georg Heygster, and Leif Toudal Pedersen. Intercomparison of passive microwave sea ice concentration retrievals over the high-concentration Arctic sea ice. *Journal of Geophysical Research: Oceans*, 112(C8):C08004, 2007.

[51] Anja Rösel and Lars Kaleschke. Influence of melt ponds on microwave sensors' sea ice concentration retrieval algorithms. In *2012 IEEE International Geoscience and Remote Sensing Symposium*, pages 3261–3264. IEEE, 2012.

[52] Anja Rösel, Lars Kaleschke, and Gerit Birnbaum. Melt ponds on Arctic sea ice determined from MODIS satellite data using an artificial neural network. *The Cryosphere*, 6(2):431–446, 2012.

[53] Ronald Kwok, Josefino C Comiso, S Martin, and R Drucker. Ross Sea polynyas: Response of ice concentration retrievals to large areas of thin ice. *Journal of Geophysical Research: Oceans*, 112(C12), 2007.

[54] Georg Heygster, Marcus Huntemann, Natalia Ivanova, Roberto Saldo, and Leif Toudal Pedersen. Response of passive microwave sea ice concentration algorithms to thin ice. In *2014 IEEE geoscience and remote sensing symposium*, pages 3618–3621. IEEE, 2014.

[55] Kazuhiro Naoki, Jinro Ukita, Fumihiko Nishio, Masashige Nakayama, Josefino C Comiso, and Al Gasiewski. Thin sea ice thickness as inferred from passive microwave and in situ observations. *Journal of Geophysical Research: Oceans*, 113(C2), 2008.

[56] Natalia Ivanova, LT Pedersen, RT Tonboe, Stefan Kern, G Heygster, T Lavergne, A Sørensen, Roberto Saldo, G Dybkjær, L Brucker, et al. Inter-comparison and evaluation of sea ice algorithms: towards further identification of challenges and optimal approach using passive microwave observations. *The Cryosphere*, 9:1797–1817, 2015.

[57] Donald J Cavalieri, Karen M St Germain, and Calvin T Swift. Reduction of weather effects in the calculation of sea-ice concentration with the DMSP SSM/I. *Journal of Glaciology*, 41(139):455–464, 1995.

[58] Gunnar Spreen, Lars Kaleschke, and Georg Heygster. Sea ice remote sensing using AMSR-E 89-GHz channels. *Journal of Geophysical Research: Oceans*, 113(C2), 2008.

[59] Thomas Lavergne, Atle Macdonald Sørensen, Stefan Kern, Rasmus Tonboe, Dirk Notz, Signe Aaboe, Louisa Bell, Gorm Dybkjær, Steinar Eastwood, Carolina Gabarro, et al. Version 2 of the EUMETSAT OSI SAF and ESA CCI sea-ice concentration climate data records. *The Cryosphere*, 13(1):49–78, 2019.

[60] Donald J Cavalieri, Per Gloersen, and William J Campbell. Determination of sea ice parameters with the Nimbus 7 SMMR. *Journal of Geophysical Research: Atmospheres*, 89(D4):5355–5369, 1984.

[61] Thorsten Markus and Donald J Cavalieri. An enhancement of the NASA Team sea ice algorithm. *IEEE Transactions on Geoscience and Remote Sensing*, 38(3):1387–1398, 2000.

[62] Josefino C Comiso and Fumihiko Nishio. Trends in the sea ice cover using enhanced and compatible AMSR-E, SSM/I, and SMMR data. *Journal of Geophysical Research: Oceans*, 113(C2), 2008.

[63] Yuanren Xiu, Zhijun Li, Ruibo Lei, Qingkai Wang, Peng Lu, and Matti Leppäranta. Comparisons of passive microwave remote sensing sea ice concentrations with ship-based visual observations during the CHINARE Arctic summer cruises of 2010–2018. *Acta Oceanologica Sinica*, 39(9):38–49, 2020.

[64] Shuang Liang, Jiangyuan Zeng, Zhen Li, Dejing Qiao, Ping Zhang, and Haiyun Bi. Consistent Comparison of Remotely Sensed Sea Ice Concentration Products with ERA-Interim Reanalysis Data in Polar Regions. *Remote Sensing*, 12(18):2880, 2020.

[65] Hyangsun Han and Hyun-cheol Kim. Evaluation of summer passive microwave sea ice concentrations in the Chukchi Sea based on KOMPSAT-5 SAR and numerical weather prediction data. *Remote Sensing of Environment*, 209:343–362, 2018.

[66] Stefan Kern, Thomas Lavergne, Dirk Notz, Leif Toudal Pedersen, Rasmus Tage Tonboe, Roberto Saldo, and Atle MacDonald Sørensen. Satellite passive microwave sea-ice concentration data set intercomparison: closed ice and ship-based observations. *The Cryosphere*, 13(12):3261–3307, 2019.

[67] Einar Svendsen, Christian Matzler, and Thomas C Grenfell. A model for retrieving total sea ice concentration from a spaceborne dual-polarized passive microwave instrument operating near 90 GHz. *International Journal of Remote Sensing*, 8(10):1479–1487, 1987.

[68] Junshen Lu, Georg Heygster, and Gunnar Spreen. Atmospheric correction of sea ice concentration retrieval for 89 GHz AMSR-E observations. *IEEE Journal of Selected Topics in Applied Earth Observations and Remote Sensing*, 11(5):1442–1457, 2018.

[69] FJ Wentz and T Meissner. AMSR Ocean Algorithm, Algorithm Theoretical Basis Document. *Remote Sensing Systems*, 59, 2000.

[70] Donald J Cavalieri, Claire L Parkinson, Per Gloersen, and H Jay Zwally. Arctic and Antarctic Sea Ice Concentrations from Multichannel Passive-Microwave Satellite Data Sets: October 1978-September 1995 User's Guide. Technical report, 1997.

[71] Josefino C Comiso, Donald J Cavalieri, Claire L Parkinson, and Per Gloersen. Passive microwave algorithms for sea ice concentration: A comparison of two techniques. *Remote sensing of Environment*, 60(3):357–384, 1997.

[72] WN Meier, T Markus, J Comiso, A Ivanoff, and J Miller. AMSR2 sea ice algorithm theoretical basis document. *NASA Goddard Space Flight Center: Greenbelt, MD, USA*, 2017.

[73] K Andrea Scott, Mark Buehner, Alain Caya, and Tom Carrieres. Direct assimilation of AMSR-E brightness temperatures for estimating sea ice concentration. *Monthly weather review*, 140(3):997–1013, 2012.

[74] W. N. Meier, T. Markus, and J. C. Comiso. AMSR-E/AMSR2 Unified L3 Daily 12.5 km Brightness Temperatures, Sea Ice Concentration, Motion & Snow Depth Polar Grids, Version 1. https://nsidc.org/data/AU_SI12/versions/1, 2018.

[75] National Snow and Ice Data Center. Descriptions and differences between NASA team and bootstrap algorithms. https://nsidc.org/data/user-resources/help-center/descriptions-and-differences-between-nasa-team-and-bootstrap-algorithms, 2024.

[76] W. N. Meier, J. S. Stewart, H. Wilcox, D. J. Scott, and M. A. Hardman. DMSP SSM/I-SSMIS Daily Polar Gridded Brightness Temperatures, Version 6. https://nsidc.org/data/NSIDC-0001/versions/6, 2021.

[77] Josefino C Comiso and CW Sullivan. Satellite microwave and in situ observations of the weddell sea ice cover and its marginal ice zone. *Journal of geophysical research: Oceans*, 91(C8):9663–9681, 1986.

[78] Rasmus T Tonboe, Steinar Eastwood, Thomas Lavergne, Atle M Sørensen, Nicholas Rathmann, Gorm Dybkjær, Leif Toudal Pedersen, Jacob L Høyer, and Stefan Kern. The EUMETSAT sea ice concentration climate data record. *The Cryosphere*, 10(5):2275–2290, 2016.

[79] NASA Earth Science Data Systems. What is synthetic aperture radar?, 2020. [Accessed October 2023].

[80] Alberto Moreira, Pau Prats-Iraola, Marwan Younis, Gerhard Krieger, Irena Hajnsek, and Konstantinos P. Papathanassiou. A Tutorial on Synthetic Aperture Radar. *IEEE Geoscience and Remote Sensing Magazine*, 1(1):6–43, 2013.

[81] Keerthijan Radhakrishnan. Sea ice concentration estimation: Using passive microwave and SAR data with fully convolutional networks. Master's thesis, University of Waterloo, 2020.

[82] Matt Arkett, Dean Flett, Roger De Abreu, and Cameron Gillespie. Sea Ice Type and Open Water Discrimination for Operational Ice Monitoring with RADARSAT-2. In *2006 IEEE International Symposium on Geoscience and Remote Sensing*, pages 1631–1634. IEEE, 2006.

[83] Lei Wang, K Andrea Scott, David A Clausi, and Yan Xu. Ice concentration estimation in the gulf of St. Lawrence using fully convolutional neural network. In *2017 IEEE International Geoscience and Remote Sensing Symposium (IGARSS)*, pages 4991–4994. IEEE, 2017.

[84] David Malmgren-Hansen, Leif Toudal Pedersen, Allan Aasbjerg Nielsen, Matilde Brandt Kreiner, Roberto Saldo, Henning Skriver, John Lavelle, Jørgen Buus-Hinkler, and Klaus Harnvig Krane. A convolutional neural network architecture for sentinel-1 and AMSR2 data fusion. *IEEE Transactions on Geoscience and Remote Sensing*, 59(3):1890–1902, 2020.

[85] Juha Karvonen. Baltic sea ice concentration estimation from c-band dual-polarized sar imagery by image segmentation and convolutional neural networks. *IEEE Transactions on Geoscience and Remote Sensing*, 60:1–11, 2021.

[86] Keerthijan Radhakrishnan, K Andrea Scott, and David A Clausi. Sea ice concentration estimation: Using passive microwave and SAR data with a U-net and curriculum learning. *IEEE Journal of Selected Topics in Applied Earth Observations and Remote Sensing*, 14:5339–5351, 2021.

[87] Iris De Gelis, Aurélien Colin, and Nicolas Longépé. Prediction of categorized Sea Ice Concentration from Sentinel-1 SAR images based on a Fully Convolutional Network. *IEEE Journal of Selected Topics in Applied Earth Observations and Remote Sensing*, 2021.

[88] Jonathan Long, Evan Shelhamer, and Trevor Darrell. Fully convolutional networks for semantic segmentation. In *2015 IEEE Conference on Computer Vision and Pattern Recognition (CVPR)*, pages 3431–3440, 2015.

[89] Stefan Kern, Thomas Lavergne, Dirk Notz, Leif Toudal Pedersen, and Rasmus Tonboe. Satellite passive microwave sea-ice concentration data set inter-comparison for Arctic summer conditions. *The Cryosphere*, 14(7):2469–2493, 2020.

[90] CIS MANICE. Manual of standard procedures for observing and reporting ice conditions, 2005.

[91] Angela Cheng, Barbara Casati, Adrienne Tivy, Tom Zagon, Jean-François Lemieux, and L Bruno Tremblay. Accuracy and inter-analyst agreement of visually estimated sea ice concentrations in Canadian Ice Service ice charts using single-polarization RADARSAT-2. *The Cryosphere*, 14(4):1289–1310, 2020.

[92] John F Heinrichs, Donald J Cavalieri, and Thorsten Markus. Assessment of the AMSR-E Sea Ice-Concentration product at the ice edge using RADARSAT-1 and MODIS imagery. *IEEE transactions on Geoscience and Remote Sensing*, 44(11):3070–3080, 2006.

[93] B Ozsoy-Cicek, H Xie, SF Ackley, and K Ye. Antarctic summer sea ice concentration and extent: comparison of ODEN 2006 ship observations, satellite passive microwave and NIC sea ice charts. *The Cryosphere*, 3(1):1–9, 2009.

[94] Jiange Liu, K Andrea Scott, Ahmed Gawish, and Paul Fieguth. Automatic detection of the ice edge in SAR imagery using curvelet transform and active contour. *Remote Sensing*, 8(6):480, 2016.

[95] Institute of Environmental Physics, University of Bremen. 1 KM resolution sea ice concentration from MODIS & AMSR2. https://data.seaice.uni-bremen.de/modis_amsr2. [Accessed April 2024].

[96] Clemens Drüe and Günther Heinemann. High-resolution maps of the sea-ice concentration from MODIS satellite data. *Geophysical research letters*, 31(20), 2004.

[97] Valentin Ludwig, Gunnar Spreen, Christian Haas, Larysa Istomina, Frank Kauker, and Dmitrii Murashkin. The 2018 North Greenland polynya observed by a newly introduced merged optical and passive microwave sea-ice concentration dataset. *The Cryosphere*, 13(7):2051–2073, 2019.

[98] University of Bremen. MODIS/AMSR2 DESCRIPTION. https://seaice.uni-bremen.de/sea-ice-concentration/modis-amsr2/. [Accessed April 2024].

[99] NOAA/NSIDC Climate Data Record of Passive Microwave Sea Ice Concentration, Version 4. https://nsidc.org/data/g02202/versions/4. [Accessed April 2024].

[100] Angela C Bliss and Mark R Anderson. Arctic sea ice melt onset timing from passive microwave-based and surface air temperature-based methods. *Journal of Geophysical Research: Atmospheres*, 123(17):9063–9080, 2018.

[101] Ge Peng, Anthony Arguez, Walter N Meier, Freja Vamborg, Jake Crouch, and Philip Jones. Sea ice climate normals for seasonal ice monitoring of arctic and sub-regions. *Data*, 4(3):122, 2019.

[102] Lavergne, T. and Sørensen, A. and Tonboe, R.T. and Kreiner, M. and Saldo, R. and Birkedal, A. and Baordo, F. and Aspenes, T. and Eastwood, S. ESA Sea Ice Climate Change Initiative (Sea_Ice_cci): High(er) Resolution Sea Ice Concentration Climate Data Record Version 3 (SSM/I and SSMIS). https://catalogue.ceda.ac.uk/uuid/eade27004395466aaa006135e1b2ad1a. [Accessed April 2024].

[103] EUMETSAT SAF on Ocean and Sea Ice. OSI SAF (2022): Global Sea Ice Concentration Climate Data Record v3.0 - Multimission. http://doi.org/10.15770/EUM_SAF_OSI_0013, 2022. [Accessed April 2024].

[104] Copernicus Climate Change Service, Climate Data Store. Sea ice edge and type daily gridded data from 1978 to present derived from satellite observations. https://cds.climate.copernicus.eu/cdsapp#!/dataset/satellite-sea-ice-edge-type?tab=form. [Accessed April 2024].

[105] U.S. National Ice Center. U.S. National Ice Center Daily Marginal Ice Zone Products, Version 1. https://nsidc.org/data/g10017/versions/1, 2020. [Accessed April 2024].

[106] Mathieu LeBlanc, Stéphane Gauthier, Svend Erik Garbus, Anders Mosbech, and Louis Fortier. The co-distribution of Arctic cod and its seabird predators across the marginal ice zone in Baffin Bay. *Elementa: Science of the Anthropocene*, 7, 01 2019.

[107] DJ Cavalieri, JP Crawford, MR Drinkwater, DT Eppler, LD Farmer, RR Jentz, and CC Wackerman. Aircraft active and passive microwave validation of sea ice concentration from the Defense Meteorological Satellite Program Special Sensor Microwave Imager. *Journal of Geophysical Research: Oceans*, 96(C12):21989–22008, 1991.

[108] Walter N Meier and J Scott Stewart. Assessing uncertainties in sea ice extent climate indicators. *Environmental Research Letters*, 14(3):035005, 2019.

[109] Xiaoping Pang, Jian Pu, Xi Zhao, Qing Ji, Meng Qu, and Zian Cheng. Comparison between AMSR2 sea ice concentration products and pseudo-ship observations of the Arctic and Antarctic sea ice edge on cloud-free days. *Remote Sensing*, 10(2):317, 2018.

[110] Yinghui Liu, Sean Helfrich, Walter N Meier, and Richard Dworak. Assessment of AMSR2 ice extent and ice edge in the Arctic using IMS. *Remote Sensing*, 12(10):1582, 2020.

[111] Angela C Bliss, Michael Steele, Ge Peng, Walter N Meier, and Suzanne Dickinson. Regional variability of Arctic sea ice seasonal change climate indicators from a passive microwave climate data record. *Environmental Research Letters*, 14(4):045003, 2019.

[112] Arne Melsom, Cyril Palerme, and Malte Müller. Validation metrics for ice edge position forecasts. *Ocean Science*, 15(3):615–630, 2019.

[113] Cyril Palerme, Malte Müller, and Arne Melsom. An intercomparison of verification scores for evaluating the sea ice edge position in seasonal forecasts. *Geophysical Research Letters*, 46(9):4757–4763, 2019.

[114] Kristin L Laidre, Harry Stern, Kit M Kovacs, Lloyd Lowry, Sue E Moore, Eric V Regehr, Steven H Ferguson, Øystein Wiig, Peter Boveng, Robyn P Angliss, et al. Arctic marine mammal population status, sea ice habitat loss, and conservation recommendations for the 21st century. *Conservation Biology*, 29(3):724–737, 2015.

[115] Mads Peter Heide-Jørgensen, Louise M Burt, Rikke Guldborg Hansen, Nynne Hjort Nielsen, Marianne Rasmussen, Sabrina Fossette, and Harry Stern. The significance of the North Water polynya to Arctic top predators. *Environment and Society (AMBIO)*, 42(5):596–610, 2013.

[116] H. Hersbach, B. Bell, P. Berrisford, G. Biavati, A. Horányi, J. Muñoz Sabater, J. Nicolas, C. Peubey, I. Radu, R. amd Rozum, D. Schepers, A. Simmons, C. Soci, D. Dee, and J-N. Thépaut. *ERA5 hourly data on single levels from 1979 to present*. Copernicus Climate Change Service (C3S) Climate Data Store (CDS), 2018.

[117] W Meier, T Markus, and J Comiso. AMSR-E/AMSR2 Unified L3 Daily 12.5 km Brightness Temperatures, Sea Ice Concentration, Motion & Snow Depth Polar Grids, Version 1. 2018.

[118] J Comiso. Bootstrap Sea Ice Concentrations from Nimbus-7 SMMR and DMSP SSM/I-SSMIS, Version 3. 2017.

[119] Martin Ester, Hans-Peter Kriegel, Jörg Sander, Xiaowei Xu, et al. A density-based algorithm for discovering clusters in large spatial databases with noise. In *Conference on Knowledge Discovery and Data Mining (KDD)*, volume 96, pages 226–231, 1996.

[120] Lei Wang, K Andrea Scott, and David A Clausi. Sea ice concentration estimation during freeze-up from SAR imagery using a convolutional neural network. *Remote Sensing*, 9(5):408, 2017.

[121] Thomas C Grenfell, David G Barber, Adrian K Fung, Anthony J Gow, Kenneth C Jezek, EJ Knapp, Son V Nghiem, Robert G Onstott, Donald K Perovich, Collin S Roesler, et al. Evolution of electromagnetic signatures of sea ice from initial formation to the establishment of thick first-year ice. *IEEE Transactions on geoscience and remote sensing*, 36(5):1642–1654, 1998.

[122] TS Rogers, JE Walsh, TS Rupp, LW Brigham, and M Sfraga. Future Arctic marine access: analysis and evaluation of observations, models, and projections of sea ice. *The Cryosphere*, 7(1):321–332, 2013.

[123] Peter M Finocchio, James D Doyle, Daniel P Stern, and Matthew G Fearon. Short-term impacts of Arctic summer cyclones on sea ice extent in the marginal ice zone. *Geophysical Research Letters*, 47(13):e2020GL088338, 2020.

[124] Dirk Notz. Challenges in simulating sea ice in Earth System Models. *Wiley Interdisciplinary Reviews: Climate Change*, 3(6):509–526, 2012.

[125] Jun Inoue and Masatake E Hori. Arctic cyclogenesis at the marginal ice zone: A contributory mechanism for the temperature amplification? *Geophysical Research Letters*, 38(12), 2011.

[126] Yevgeny Aksenov, Ekaterina E Popova, Andrew Yool, AJ George Nurser, Timothy D Williams, Laurent Bertino, and Jon Bergh. On the future navigability of Arctic sea routes: High-resolution projections of the Arctic Ocean and sea ice. *Marine Policy*, 75:300–317, 2017.

[127] Christopher Horvat and Eli Tziperman. A prognostic model of the sea-ice floe size and thickness distribution. *The Cryosphere*, 9(6):2119–2134, 2015.

[128] Michel Tsamados, Daniel Feltham, Alek Petty, David Schroeder, and Daniela Flocco. Processes controlling surface, bottom and lateral melt of Arctic sea ice in a state of the art sea ice model. *Philosophical Transactions of the Royal Society A: Mathematical, Physical and Engineering Sciences*, 373(2052):20140167, 2015.

[129] Courtenay Strong, Dallas Foster, Elena Cherkaev, Ian Eisenman, and Kenneth M Golden. On the definition of marginal ice zone width. *Journal of Atmospheric and Oceanic Technology*, 34(7):1565–1584, 2017.

[130] Guillaume Boutin, Camille Lique, Fabrice Ardhuin, Clément Rousset, Claude Talandier, Mickael Accensi, and Fanny Girard-Ardhuin. Towards a coupled model to investigate wave–sea ice interactions in the Arctic marginal ice zone. *The Cryosphere*, 14(2):709–735, 2020.

[131] Julienne Stroeve, Marika M Holland, Walt Meier, Ted Scambos, and Mark Serreze. Arctic sea ice decline: Faster than forecast. *Geophysical research letters*, 34(9), 2007.

[132] Donald J Cavalieri and Claire L Parkinson. Arctic sea ice variability and trends, 1979–2010. *The Cryosphere*, 6(4):881–889, 2012.

[133] JA Maslanik, C Fowler, J Stroeve, S Drobot, J Zwally, D Yi, and W Emery. A younger, thinner Arctic ice cover: Increased potential for rapid, extensive sea-ice loss. *Geophysical Research Letters*, 34(24), 2007.

[134] James Maslanik, Julienne Stroeve, Charles Fowler, and William Emery. Distribution and trends in Arctic sea ice age through spring 2011. *Geophysical Research Letters*, 38(13), 2011.

[135] David Palma, Alix Varnajot, Kari Dalen, Ilker K Basaran, Charles Brunette, Marta Bystrowska, Anastasia D Korablina, Robynne C Nowicki, and Thomas A Ronge. Cruising the marginal ice zone: Climate change and Arctic tourism. *Polar Geography*, 42(4):215–235, 2019.

[136] Hiroshi Sumata, Laura de Steur, Dmitry V Divine, Mats A Granskog, and Sebastian Gerland. Regime shift in Arctic Ocean sea ice thickness. *Nature*, 615(7952):443–449, 2023.

[137] Josefino Comiso. Enhanced sea ice concentrations from passive microwave data. *NASA Goddard Space Flight Center, Greenbelt, Maryland*, 20, 2007.

[138] Armina Soleymani, Nastaran Saberi, and K. Andrea Scott. Passive microwave sea ice edge displacement error over the eastern Canadian Arctic 2013-2021. *Canadian Journal of Remote sensing*, 92(1), 2023.

[139] Rebecca Killick, Paul Fearnhead, and Idris A Eckley. Optimal detection of changepoints with a linear computational cost. *Journal of the American Statistical Association*, 107(500):1590–1598, 2012.

[140] Luis Gimeno-Sotelo, Raquel Nieto, Marta Vázquez, and Luis Gimeno. A new pattern of the moisture transport for precipitation related to the drastic decline in Arctic sea ice extent. *Earth System Dynamics*, 9(2):611–625, 2018.

[141] Ariaan Purich and Edward W Doddridge. Record low Antarctic sea ice coverage indicates a new sea ice state. *Communications Earth & Environment*, 4(1):314, 2023.

[142] Kevin Feasel. Change Point Detection. In *Finding Ghosts in Your Data: Anomaly Detection Techniques with Examples in Python*, pages 247–261. Springer, 2022.

[143] Ingrid H Onarheim, Tor Eldevik, Lars H Smedsrud, and Julienne C Stroeve. Seasonal and regional manifestation of Arctic sea ice loss. *Journal of Climate*, 31(12):4917–4932, 2018.

[144] Yunhe Wang, Haibo Bi, Haijun Huang, Yanxia Liu, Yilin Liu, Xi Liang, Min Fu, and Zehua Zhang. Satellite-observed trends in the Arctic sea ice concentration for the period 1979–2016. *Journal of Oceanology and Limnology*, 37(1):18–37, 2019.

[145] Walter N Meier and Julienne Stroeve. An updated assessment of the changing Arctic sea ice cover. *Oceanography*, 35(3/4):10–19, 2022.

[146] Stephen EL Howell and Mike Brady. The dynamic response of sea ice to warming in the Canadian Arctic Archipelago. *Geophysical Research Letters*, 46(22):13119–13125, 2019.

[147] Stephen Marshall, K. Andrea Scott, and Randall K. Scharien. Passive microwave melt onset retrieval based on a variable threshold: Assessment in the canadian arctic archipelago. *Remote Sensing*, 11(11), 2019.

[148] U. S. Bhatt, W. Meier, E. Blanchard-Wrigglesworth, F. Massonnet, H. Goessling, V. Ludwig, P. Bieniek, H. Eicken, M. Fisher, L. C. Hamilton, J. Little, J. E. Overland, M. Serreze, M. Steele, J. Stroeve, J. Walsh, M. Wang, and H. V. Wiggins. Sea ice outlook: 2022 post season report, December 2022.

[149] Peter M Finocchio and James D Doyle. Summer cyclones and their association with short-term sea ice variability in the Pacific sector of the Arctic. *Frontiers in Earth Science*, 9:738497, 2021.

[150] Ron Kwok. Arctic sea ice thickness, volume, and multiyear ice coverage: losses and coupled variability (1958–2018). *Environmental Research Letters*, 13(10):105005, 2018.

[151] Miao Yu, Peng Lu, Zhiyuan Li, Zhijun Li, Qingkai Wang, Xiaowei Cao, and Xiaodong Chen. Sea ice conditions and navigability through the Northeast Passage in the past 40 years based on remote-sensing data. *International Journal of Digital Earth*, 14(5):555–574, 2021.

[152] MC Serreze, JA Maslanik, TA Scambos, F Fetterer, J Stroeve, K Knowles, C Fowler, S Drobot, RG Barry, and TM Haran. A record minimum arctic sea ice extent and area in 2002. *Geophysical Research Letters*, 30(3), 2003.

[153] JC Stroeve, Thorsten Markus, Linette Boisvert, J Miller, and A Barrett. Changes in Arctic melt season and implications for sea ice loss. *Geophysical Research Letters*, 41(4):1216–1225, 2014.

[154] Lei Wang, K Andrea Scott, Linlin Xu, and David A Clausi. Sea ice concentration estimation during melt from dual-pol SAR scenes using deep convolutional neural networks: A case study. *IEEE Transactions on Geoscience and Remote Sensing*, 54(8):4524–4533, 2016.

[155] Yan Xu and K Andrea Scott. Impact of intermediate ice concentration training data on sea ice concentration estimates from a convolutional neural network. *International Journal of Remote Sensing*, 40(15):5799–5811, 2019.

[156] Xinwei Chen, Muhammed Patel, Fernando Pena Cantu, Jinman Park, Javier Noa Turnes, Linlin Xu, K Andrea Scott, and David A Clausi. MMSeaIce: Multi-task Mapping of Sea Ice Parameters from AI4Arctic Sea Ice Challenge Dataset. *EGUsphere*, 2023:1–17, 2023.

[157] JC Comiso. Bootstrap Sea Ice Concentrations from Nimbus-7 SMMR and DMSP SSM/I-SSMIS, Version 3, boulder, Colorado USA. NASA National Snow and Ice Data Center Distributed Active Archive Center, 2017.

[158] J. Buus-Hinkler, T. Wulf, A. R. Stokholm, A. Korosov, R. Saldo, L. T. Pedersen, et al. AI4Arctic Sea Ice Challenge Dataset. https://doi.org/10.11583/DTU.c.6244065.v2, 2022.

[159] Anton Korosov, Denis Demchev, Nuno Miranda, Niccolò Franceschi, and Jeong-Won Park. Thermal denoising of cross-polarized Sentinel-1 data in interferometric and extra wide swath modes. *IEEE Transactions on Geoscience and Remote Sensing*, 60:1–11, 2021.

[160] Alaska Satellite Facility. Alaska satellite facility search. https://search.asf.alaska.edu/, 2023.

[161] European Space Agency. Smos l3 sea ice thickness, version 3.3. https://doi.org/10.57780/sm1-5ebe10b, 2023.

[162] European Space Agency. SMOS ESL 2019-2024: ESL for Geophysical (L3 & 4) data over land ice and sea ice. SMOS L3 Sea Ice Thickness ATBD, 2021.

[163] Olaf Ronneberger, Philipp Fischer, and Thomas Brox. U-net: Convolutional networks for biomedical image segmentation. In *Medical Image Computing and Computer-Assisted Intervention–MICCAI 2015: 18th International Conference, Munich, Germany, October 5-9, 2015, Proceedings, Part III 18*, pages 234–241. Springer, 2015.

[164] Ilya Loshchilov and Frank Hutter. SGDR: Stochastic gradient descent with warm restarts. *arXiv preprint arXiv:1608.03983*, 2016.

[165] Kaiming He, Xiangyu Zhang, Shaoqing Ren, and Jian Sun. Delving deep into rectifiers: Surpassing human-level performance on imagenet classification. In *Proceedings of the IEEE international conference on computer vision*, pages 1026–1034, 2015.

[166] Susan Baldwin. Compute Canada: advancing computational research. In *Journal of Physics: Conference Series*, volume 341, page 012001. IOP Publishing, 2012.

[167] Armina Soleymani and K Andrea Scott. Arctic marginal ice zone interannual variability and change point detection using two definitions (1983–2022). *Environmental Research Letters*, 18(12):124002, 2023.

[168] Lars Kaleschke, Xiangshan Tian-Kunze, Stefan Hendricks, and Robert Ricker. SMOS-derived Antarctic thin sea-ice thickness: data description and validation in the Weddell Sea. *Earth System Science Data Discussions*, 2023:1–30, 2023.

[169] Raul Cristian Scarlat, Gunnar Spreen, Georg Heygster, Marcus Huntemann, Cătălin Paţilea, Leif Toudal Pedersen, and Roberto Saldo. Sea ice and atmospheric parameter retrieval from satellite microwave radiometers: Synergy of AMSR2 and SMOS compared with the CIMR candidate mission. *Journal of Geophysical Research: Oceans*, 125(3):e2019JC015749, 2020.

[170] Pamela G Posey, EJ Metzger, AJ Wallcraft, DA Hebert, RA Allard, OM Smedstad, MW Phelps, F Fetterer, JS Stewart, WN Meier, et al. Improving Arctic sea ice edge forecasts by assimilating high horizontal resolution sea ice concentration data into the US Navy's ice forecast systems. *The Cryosphere*, 9(4):1735–1745, 2015.

[171] U.S. National Ice Center. updated daily. U.S. National Ice Center Daily Marginal Ice Zone Products, Version 1. https://doi.org/10.7265/ggcq-1m67. [Accessed April 2024].

[172] Ge Peng, Michael Steele, Angela C Bliss, Walter N Meier, and Suzanne Dickinson. Temporal means and variability of Arctic sea ice melt and freeze season climate indicators using a satellite climate data record. *Remote Sensing*, 10(9):1328, 2018.

[173] NASA. NISAR. https://nisar.jpl.nasa.gov/mission/quick-facts/. [Accessed April 2024].

[174] Mallik S Mahmud, Vishnu Nandan, Suman Singha, Stephen EL Howell, Torsten Geldsetzer, John Yackel, and Benoit Montpetit. C-and L-band SAR signatures of Arctic sea ice during freeze-up. *Remote Sensing of Environment*, 279:113129, 2022.

APPENDICES

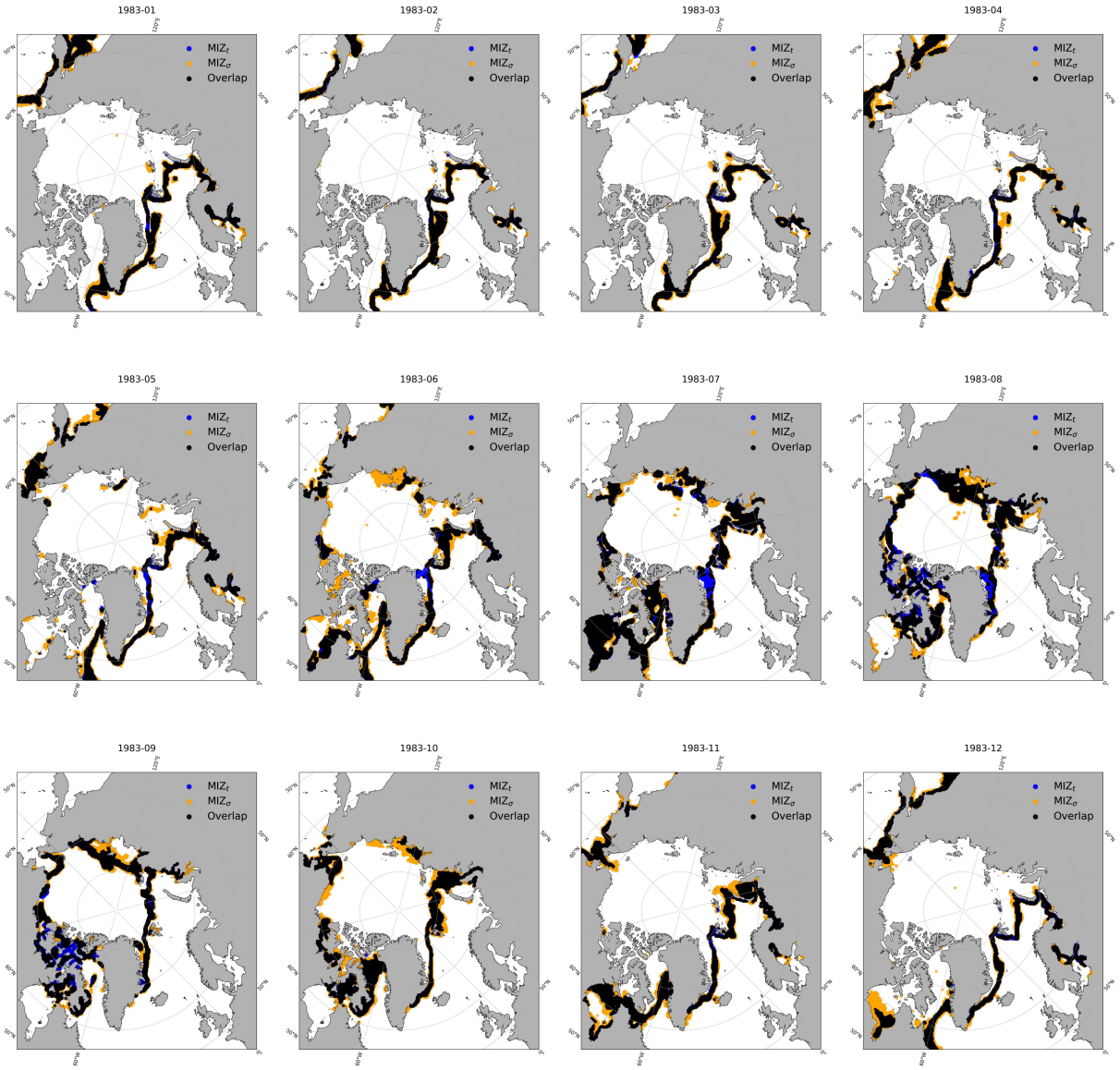

Figure 1: MIZ$_t$ and MIZ$_\sigma$ spatial map for all months in 1983. The MIZ$_t$ grid cells are defined using the criterion of $0.15 \leq \text{SIC} < 0.80$. The MIZ$_\sigma$ grid cells are defined using the criterion of $\sigma^a > 0.11$. The land is shown in grey.

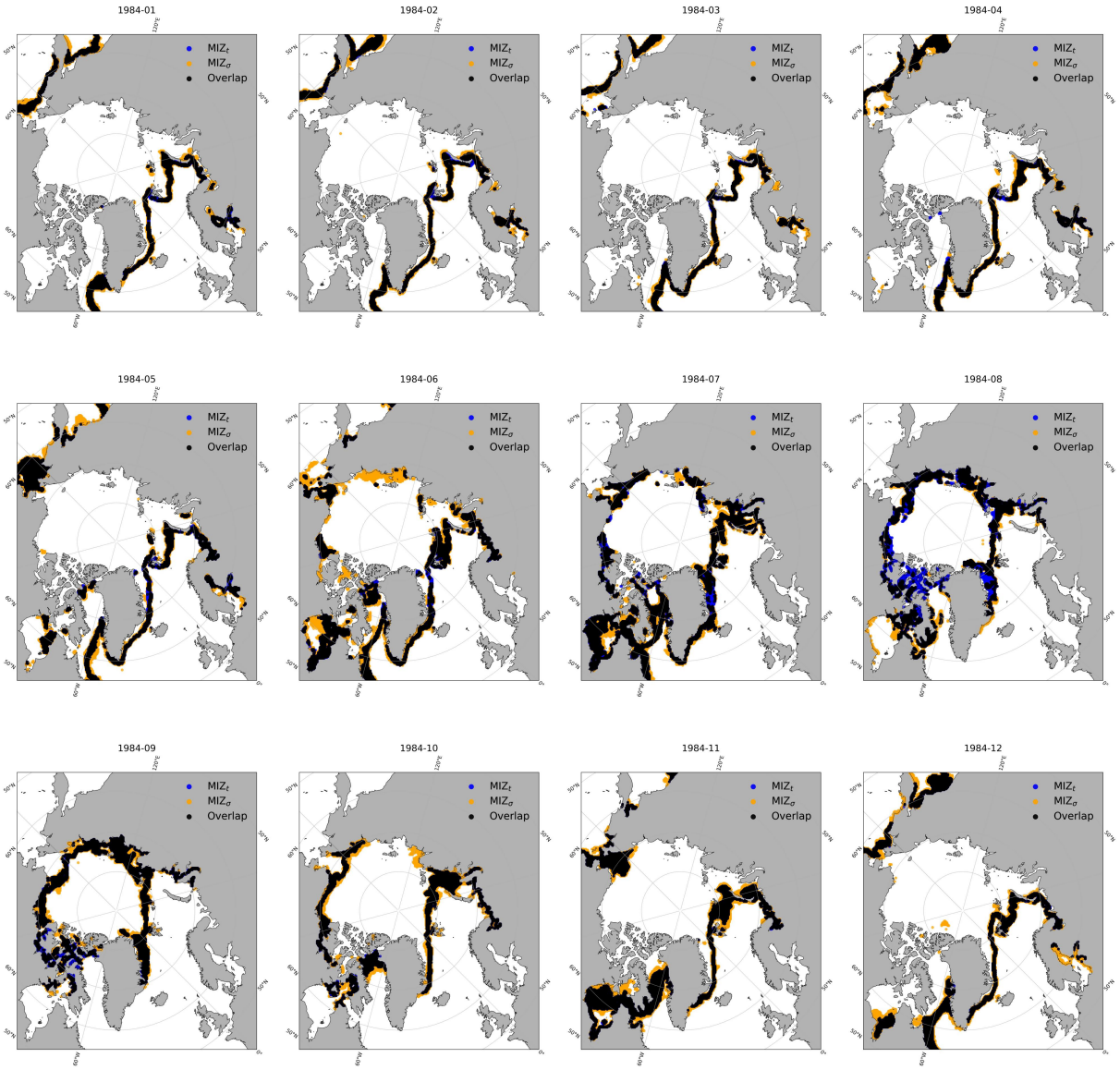

Figure 2: MIZ$_t$ and MIZ$_\sigma$ spatial map for all months in 1984. The MIZ$_t$ grid cells are defined using the criterion of $0.15 \leq \text{SIC} < 0.80$. The MIZ$_\sigma$ grid cells are defined using the criterion of $\sigma^a > 0.11$. The land is shown in grey.

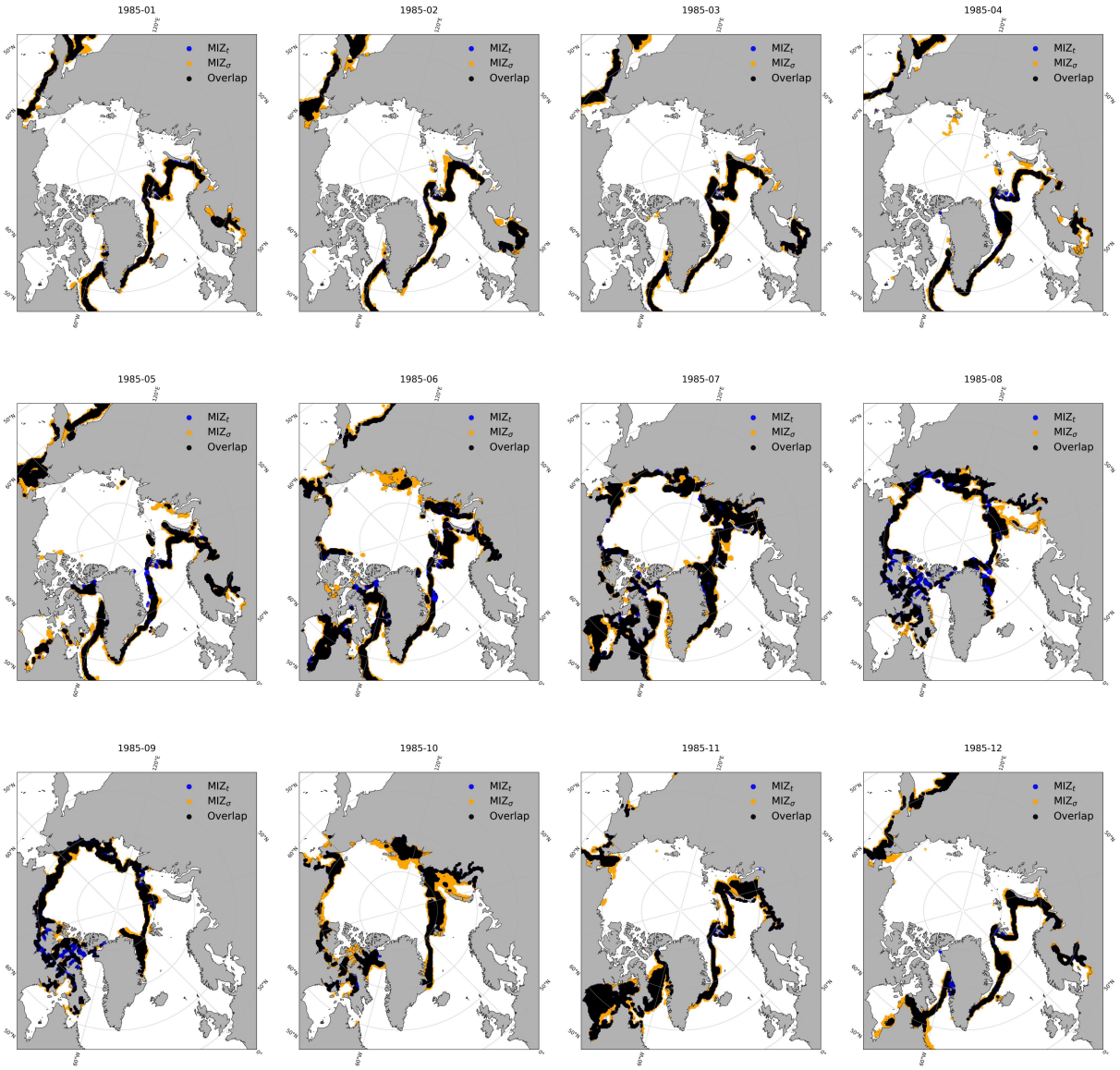

Figure 3: MIZ$_t$ and MIZ$_\sigma$ spatial map for all months in 1985. The MIZ$_t$ grid cells are defined using the criterion of $0.15 \leq \text{SIC} < 0.80$. The MIZ$_\sigma$ grid cells are defined using the criterion of $\sigma^a > 0.11$. The land is shown in grey.

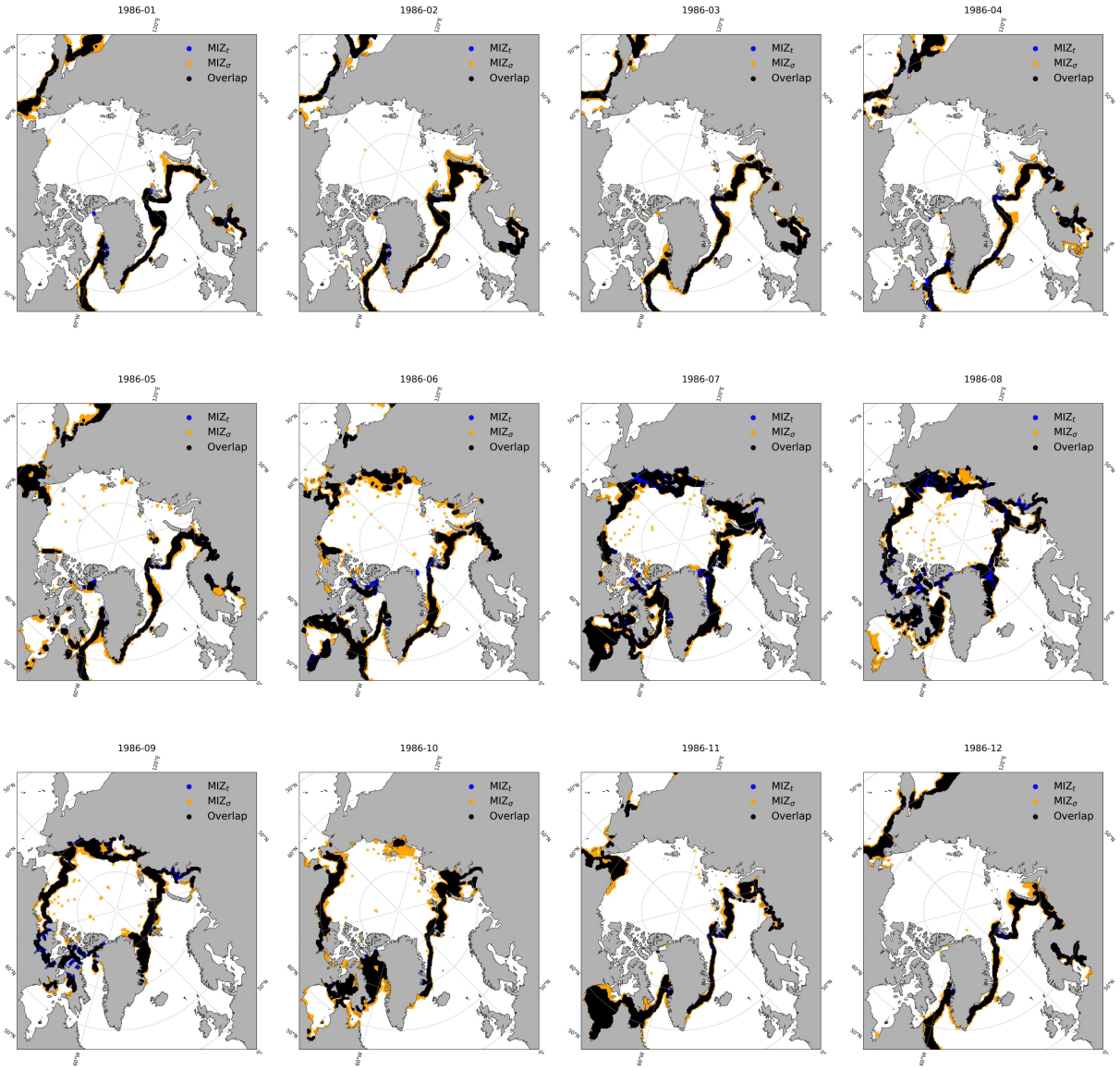

Figure 4: MIZ$_t$ and MIZ$_\sigma$ spatial map for all months in 1986. The MIZ$_t$ grid cells are defined using the criterion of $0.15 \leq \text{SIC} < 0.80$. The MIZ$_\sigma$ grid cells are defined using the criterion of $\sigma^a > 0.11$. The land is shown in grey.

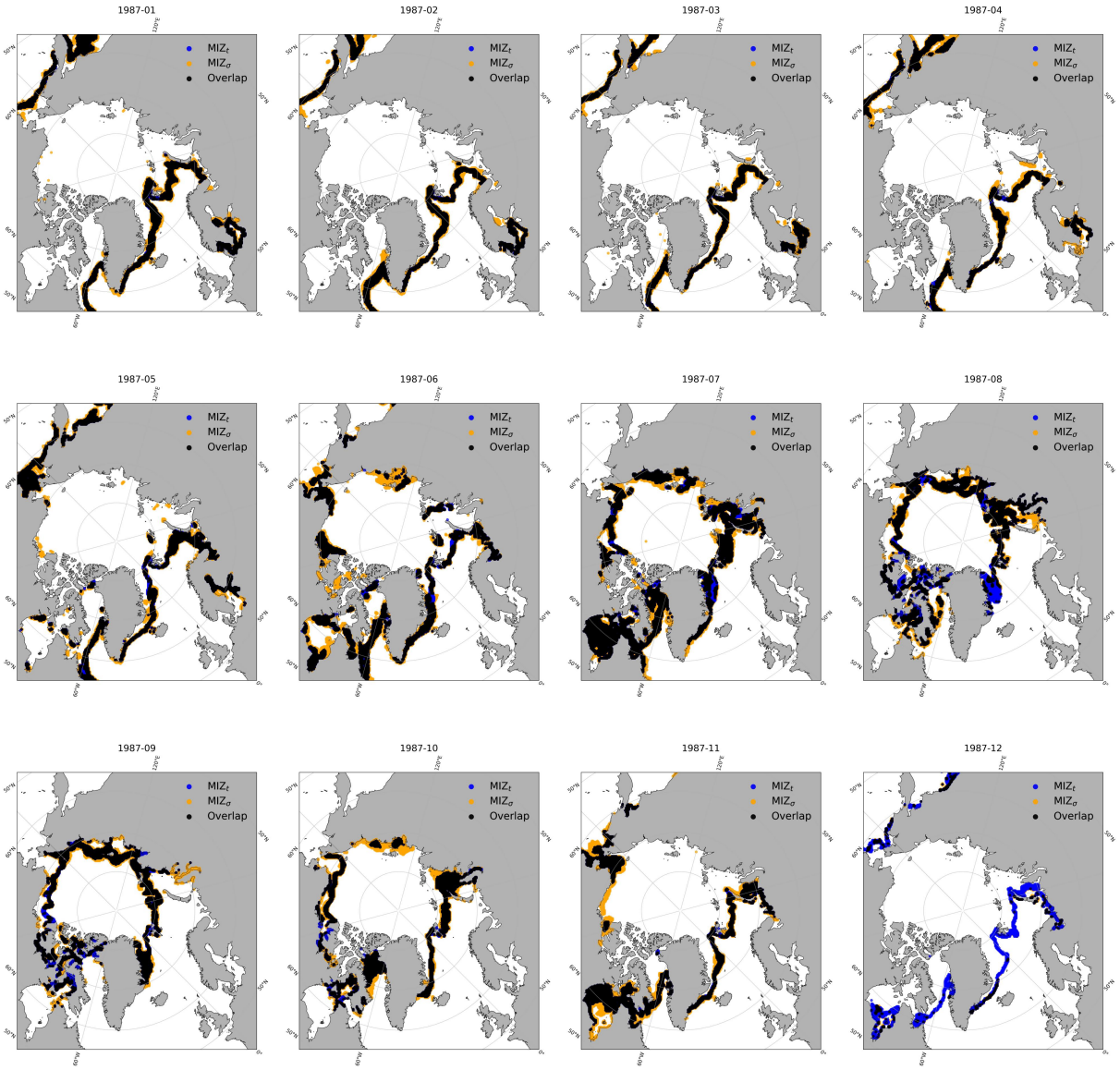

Figure 5: MIZ$_t$ and MIZ$_\sigma$ spatial map for all months in 1987. The MIZ$_t$ grid cells are defined using the criterion of $0.15 \leq \text{SIC} < 0.80$. The MIZ$_\sigma$ grid cells are defined using the criterion of $\sigma^a > 0.11$. The land is shown in grey.

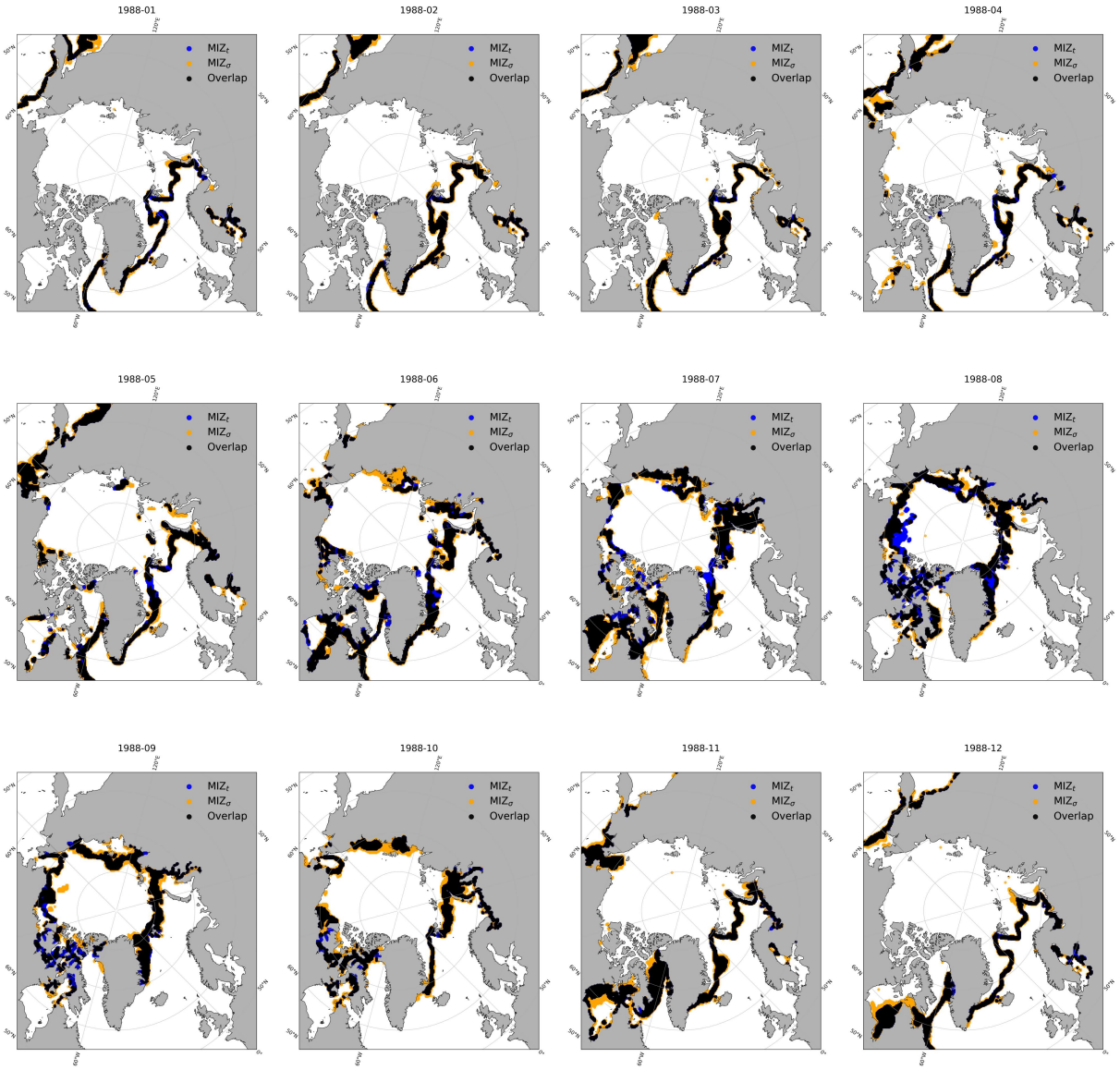

Figure 6: MIZ$_t$ and MIZ$_\sigma$ spatial map for all months in 1988. The MIZ$_t$ grid cells are defined using the criterion of $0.15 \leq \text{SIC} < 0.80$. The MIZ$_\sigma$ grid cells are defined using the criterion of $\sigma^a > 0.11$. The land is shown in grey.

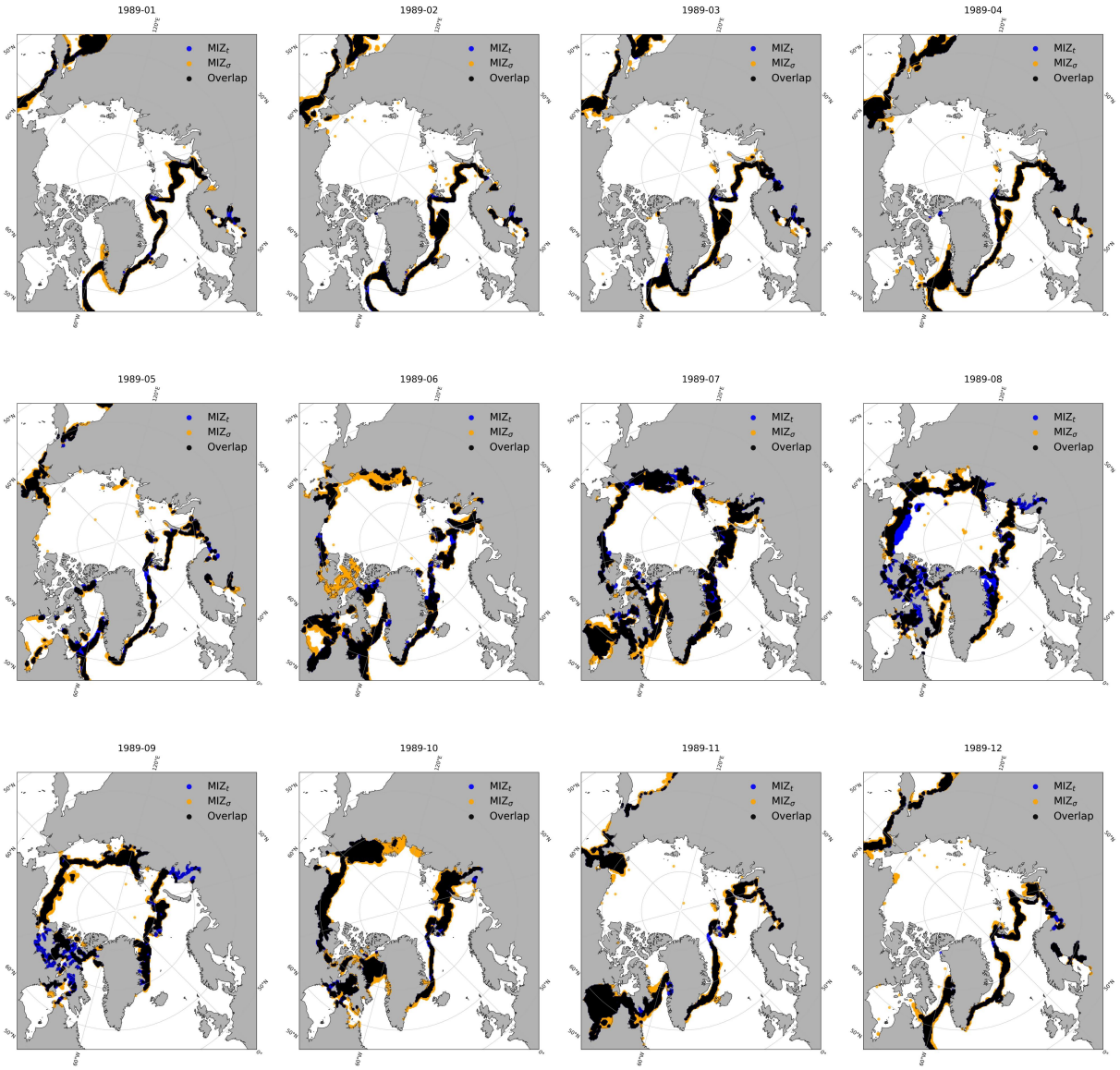

Figure 7: MIZ$_t$ and MIZ$_\sigma$ spatial map for all months in 1989. The MIZ$_t$ grid cells are defined using the criterion of $0.15 \leq \text{SIC} < 0.80$. The MIZ$_\sigma$ grid cells are defined using the criterion of $\sigma^a > 0.11$. The land is shown in grey.

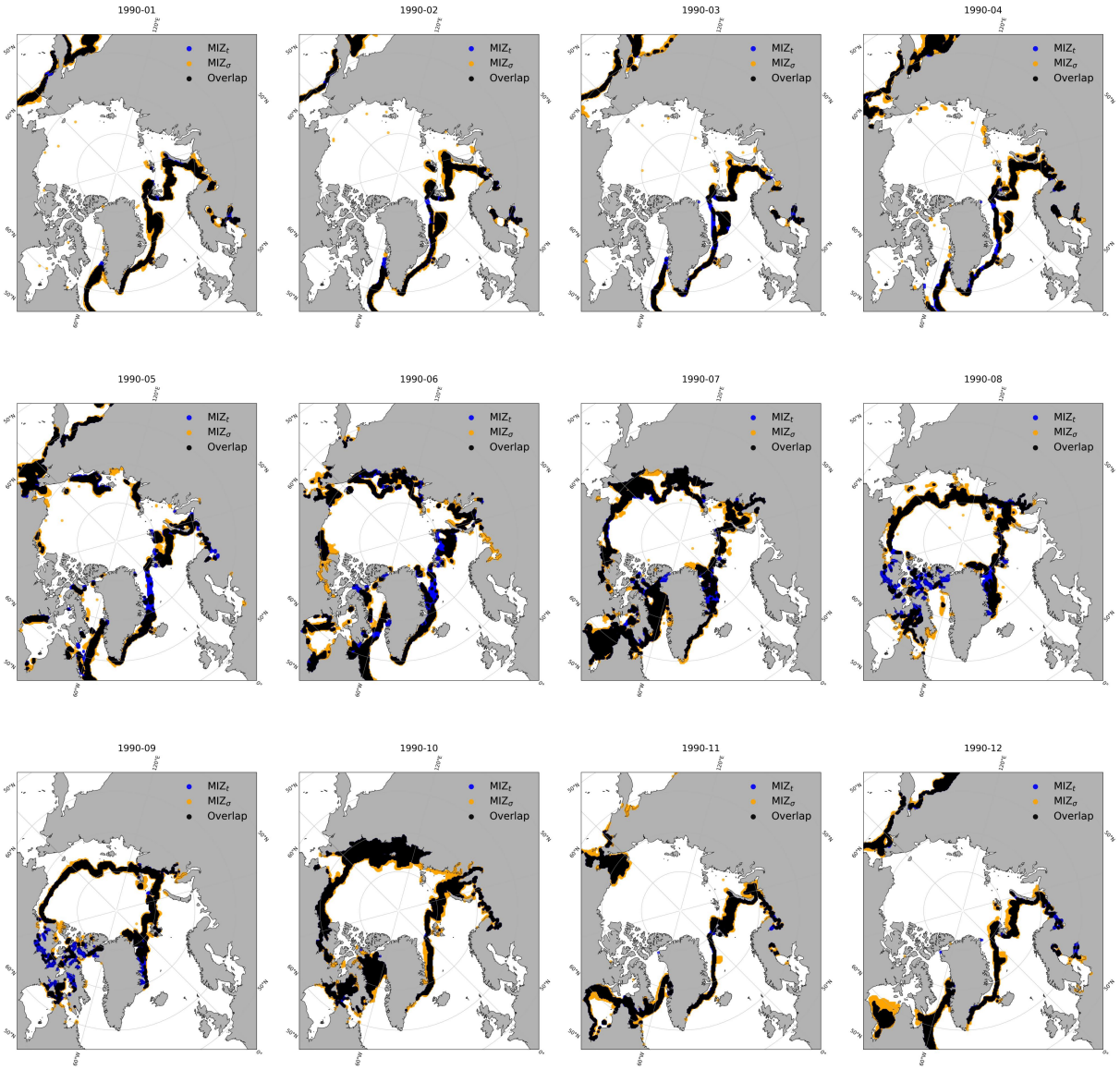

Figure 8: MIZ$_t$ and MIZ$_\sigma$ spatial map for all months in 1990. The MIZ$_t$ grid cells are defined using the criterion of $0.15 \leq \text{SIC} < 0.80$. The MIZ$_\sigma$ grid cells are defined using the criterion of $\sigma^a > 0.11$. The land is shown in grey.

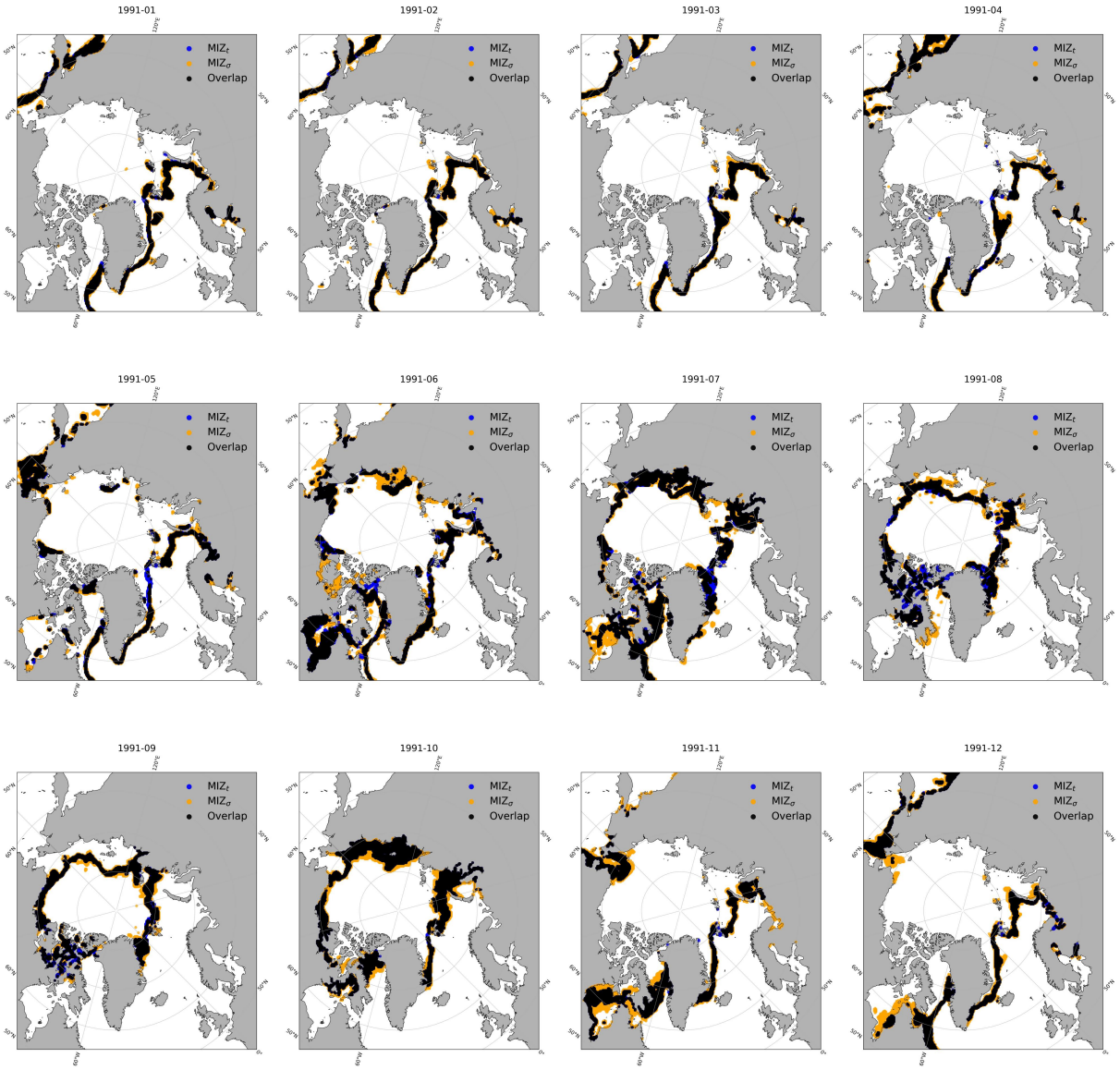

Figure 9: MIZ$_t$ and MIZ$_\sigma$ spatial map for all months in 1991. The MIZ$_t$ grid cells are defined using the criterion of $0.15 \leq \text{SIC} < 0.80$. The MIZ$_\sigma$ grid cells are defined using the criterion of $\sigma^a > 0.11$. The land is shown in grey.

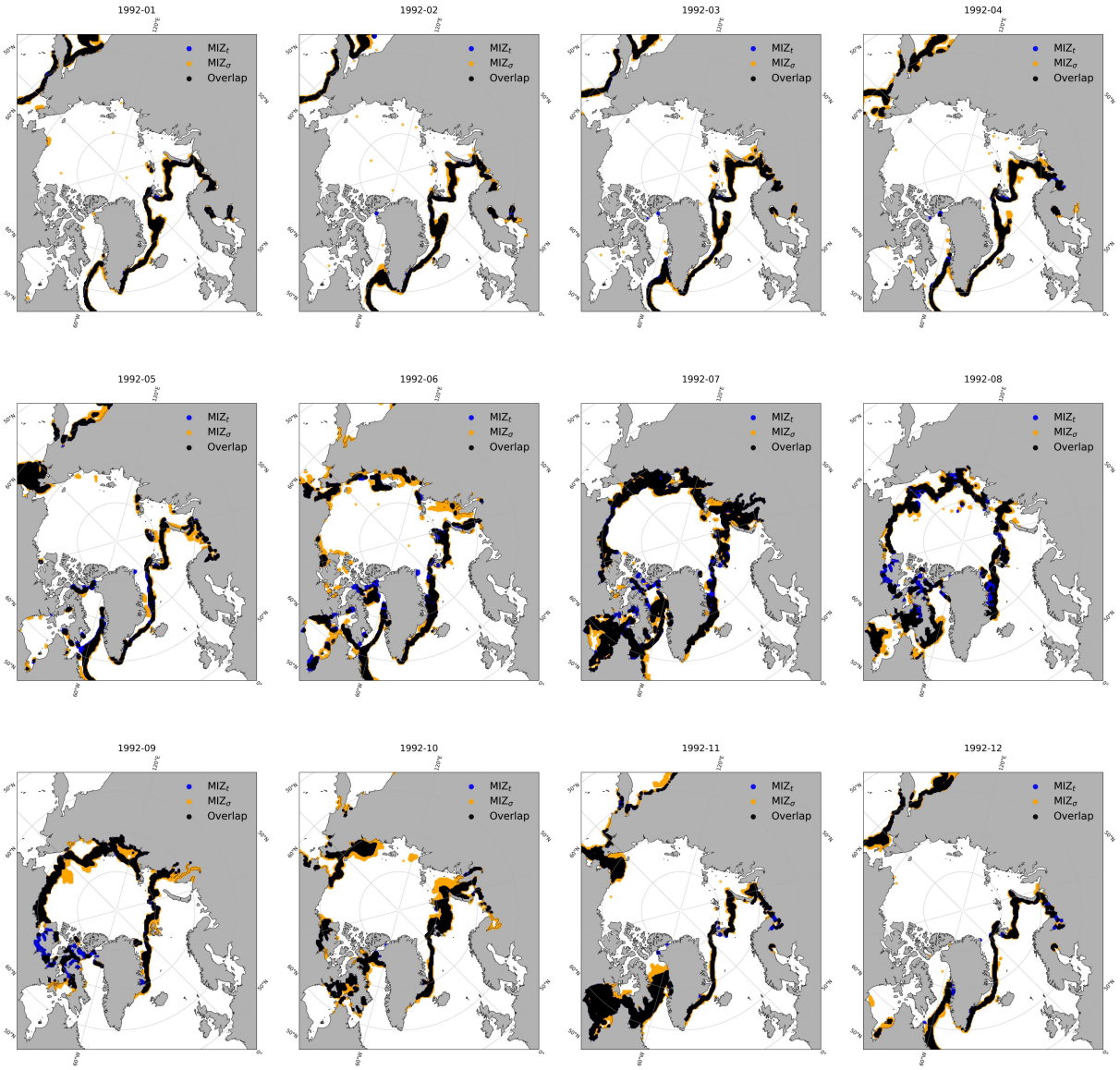

Figure 10: MIZ$_t$ and MIZ$_\sigma$ spatial map for all months in 1992. The MIZ$_t$ grid cells are defined using the criterion of $0.15 \leq \text{SIC} < 0.80$. The MIZ$_\sigma$ grid cells are defined using the criterion of $\sigma^a > 0.11$. The land is shown in grey.

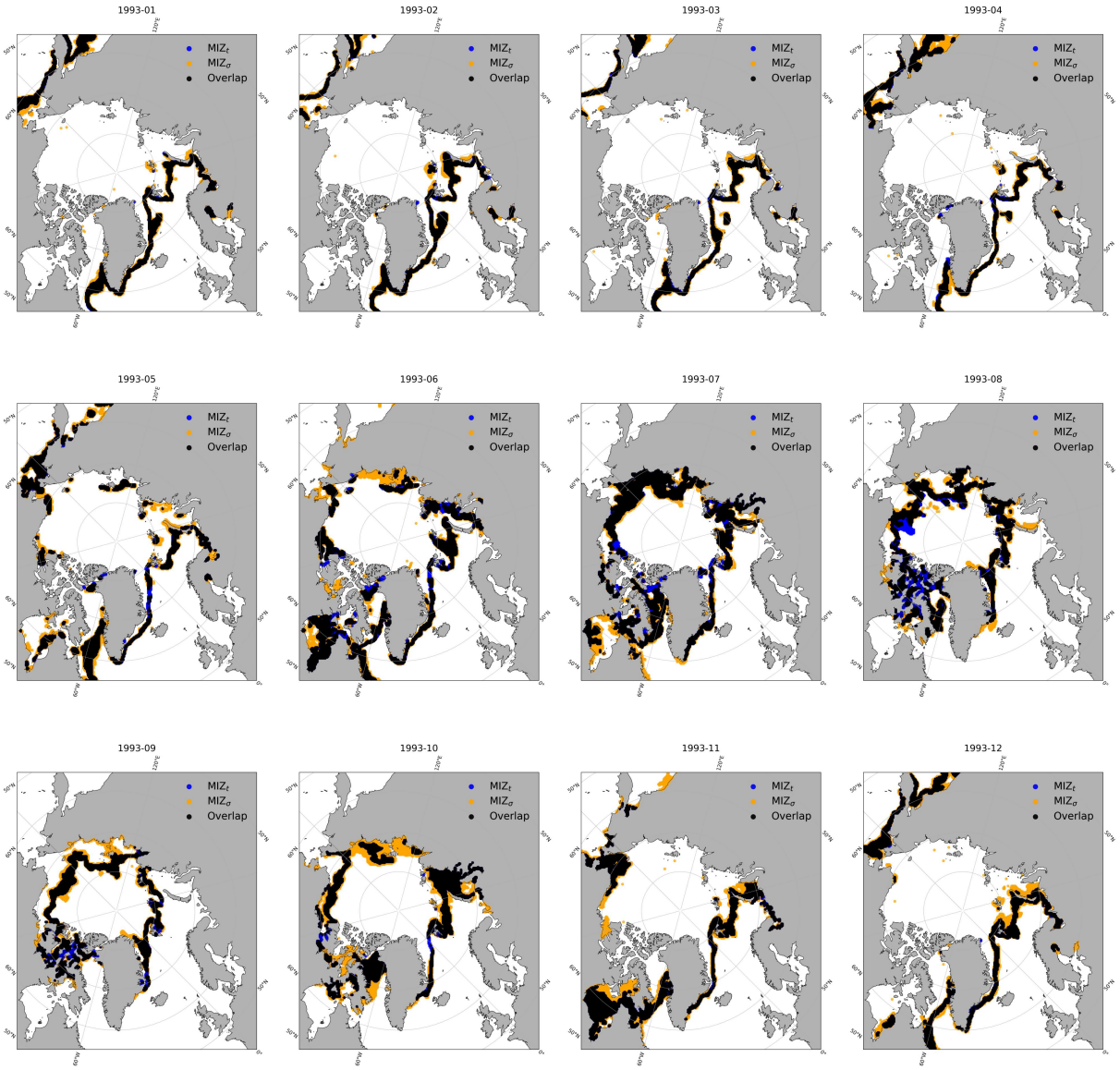

Figure 11: MIZ$_t$ and MIZ$_\sigma$ spatial map for all months in 1993. The MIZ$_t$ grid cells are defined using the criterion of $0.15 \leq \text{SIC} < 0.80$. The MIZ$_\sigma$ grid cells are defined using the criterion of $\sigma^a > 0.11$. The land is shown in grey.

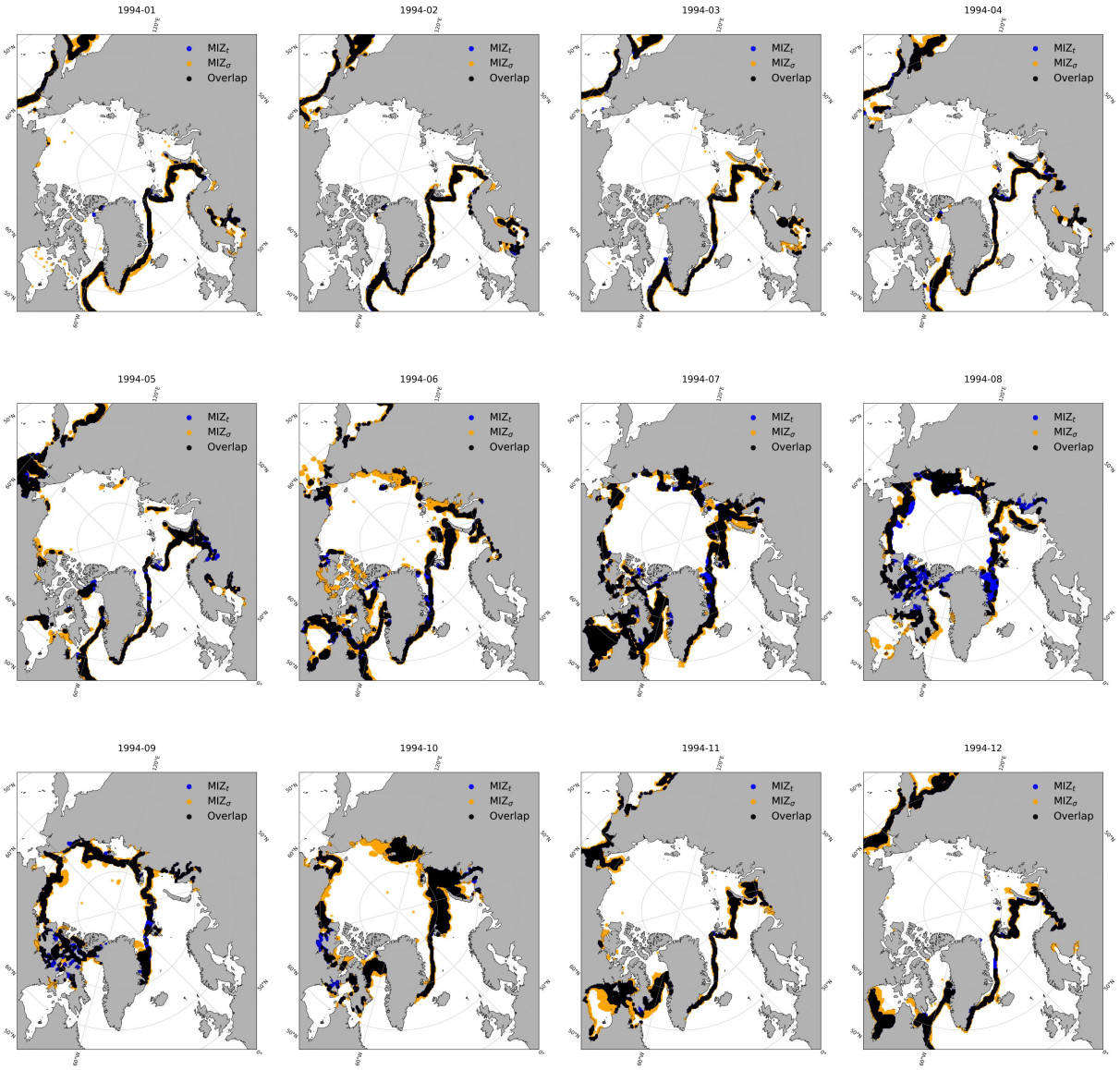

Figure 12: MIZ$_t$ and MIZ$_\sigma$ spatial map for all months in 1994. The MIZ$_t$ grid cells are defined using the criterion of $0.15 \leq \text{SIC} < 0.80$. The MIZ$_\sigma$ grid cells are defined using the criterion of $\sigma^a > 0.11$. The land is shown in grey.

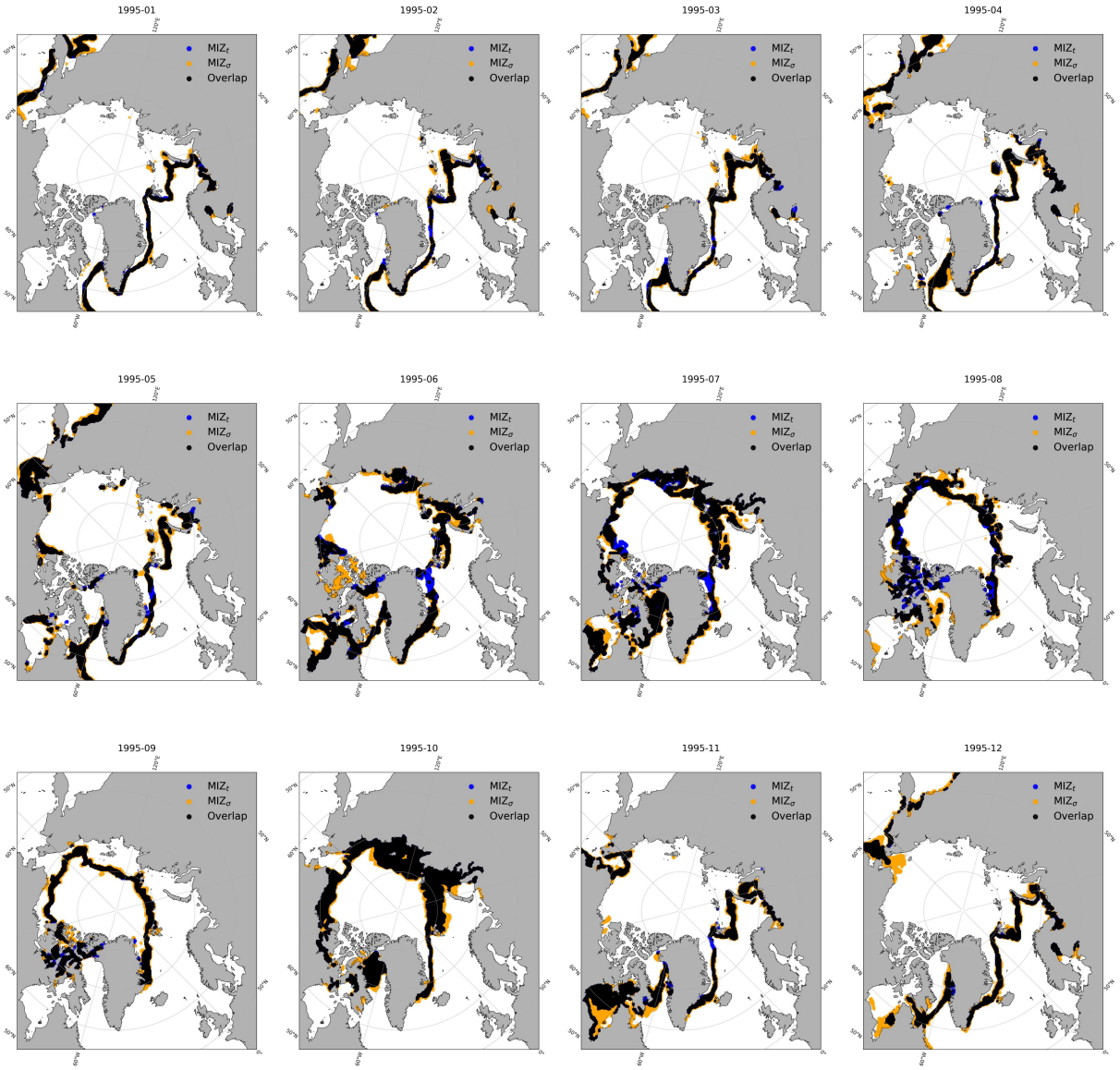

Figure 13: MIZ$_t$ and MIZ$_\sigma$ spatial map for all months in 1995. The MIZ$_t$ grid cells are defined using the criterion of $0.15 \leq \text{SIC} < 0.80$. The MIZ$_\sigma$ grid cells are defined using the criterion of $\sigma^a > 0.11$. The land is shown in grey.

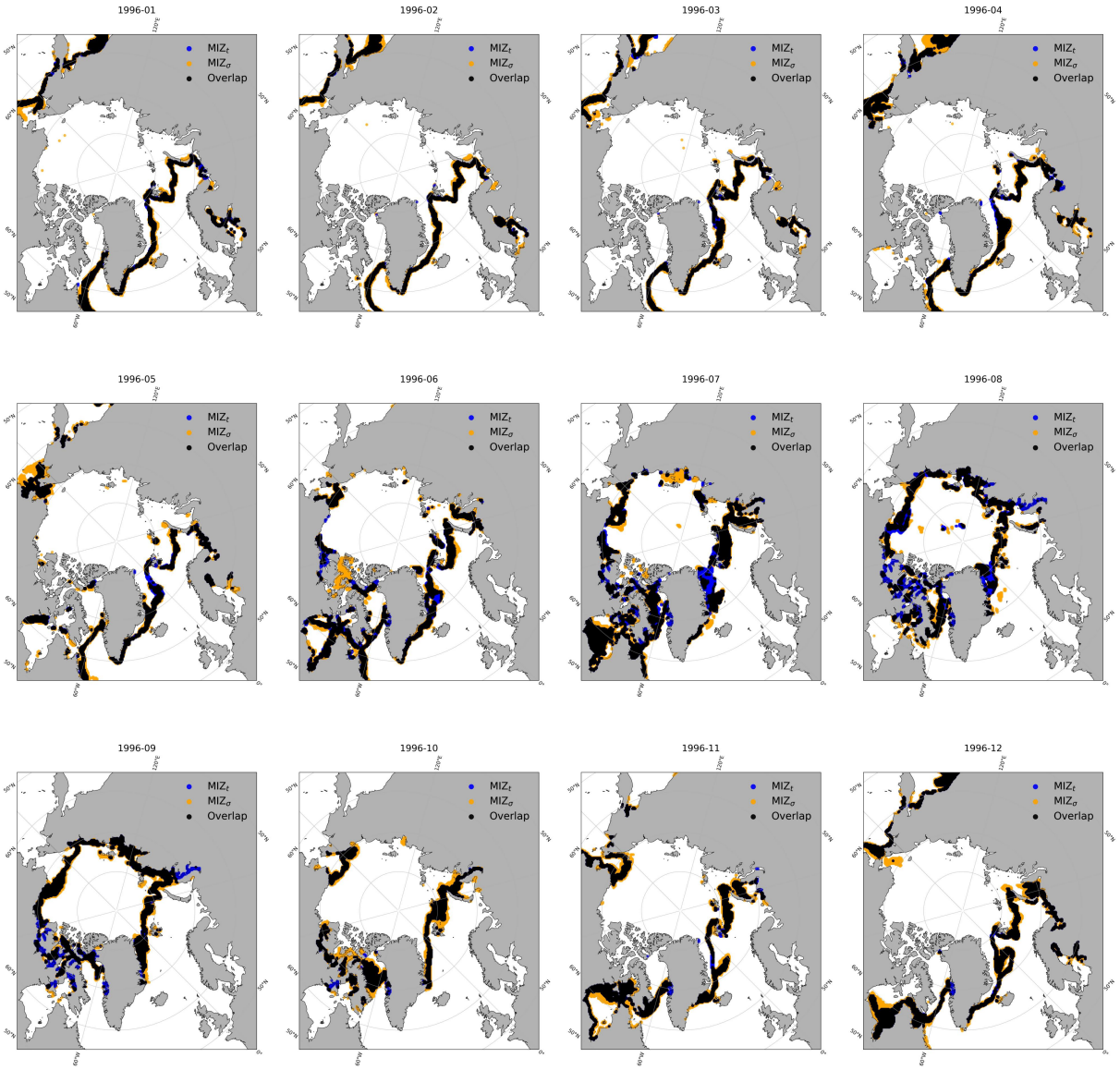

Figure 14: MIZ$_t$ and MIZ$_\sigma$ spatial map for all months in 1996. The MIZ$_t$ grid cells are defined using the criterion of $0.15 \leq \text{SIC} < 0.80$. The MIZ$_\sigma$ grid cells are defined using the criterion of $\sigma^a > 0.11$. The land is shown in grey.

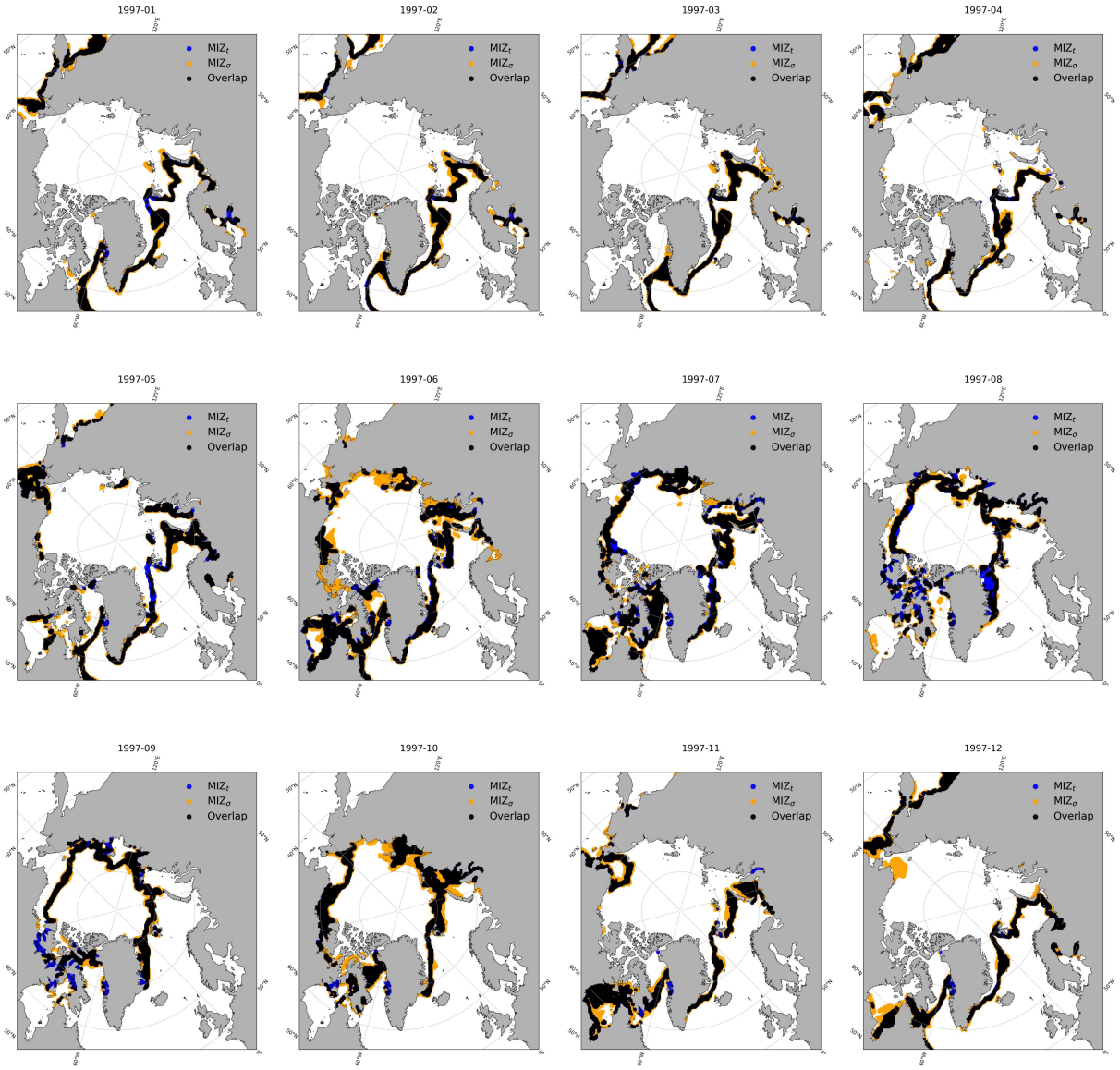

Figure 15: MIZ$_t$ and MIZ$_\sigma$ spatial map for all months in 1997. The MIZ$_t$ grid cells are defined using the criterion of $0.15 \leq \text{SIC} < 0.80$. The MIZ$_\sigma$ grid cells are defined using the criterion of $\sigma^a > 0.11$. The land is shown in grey.

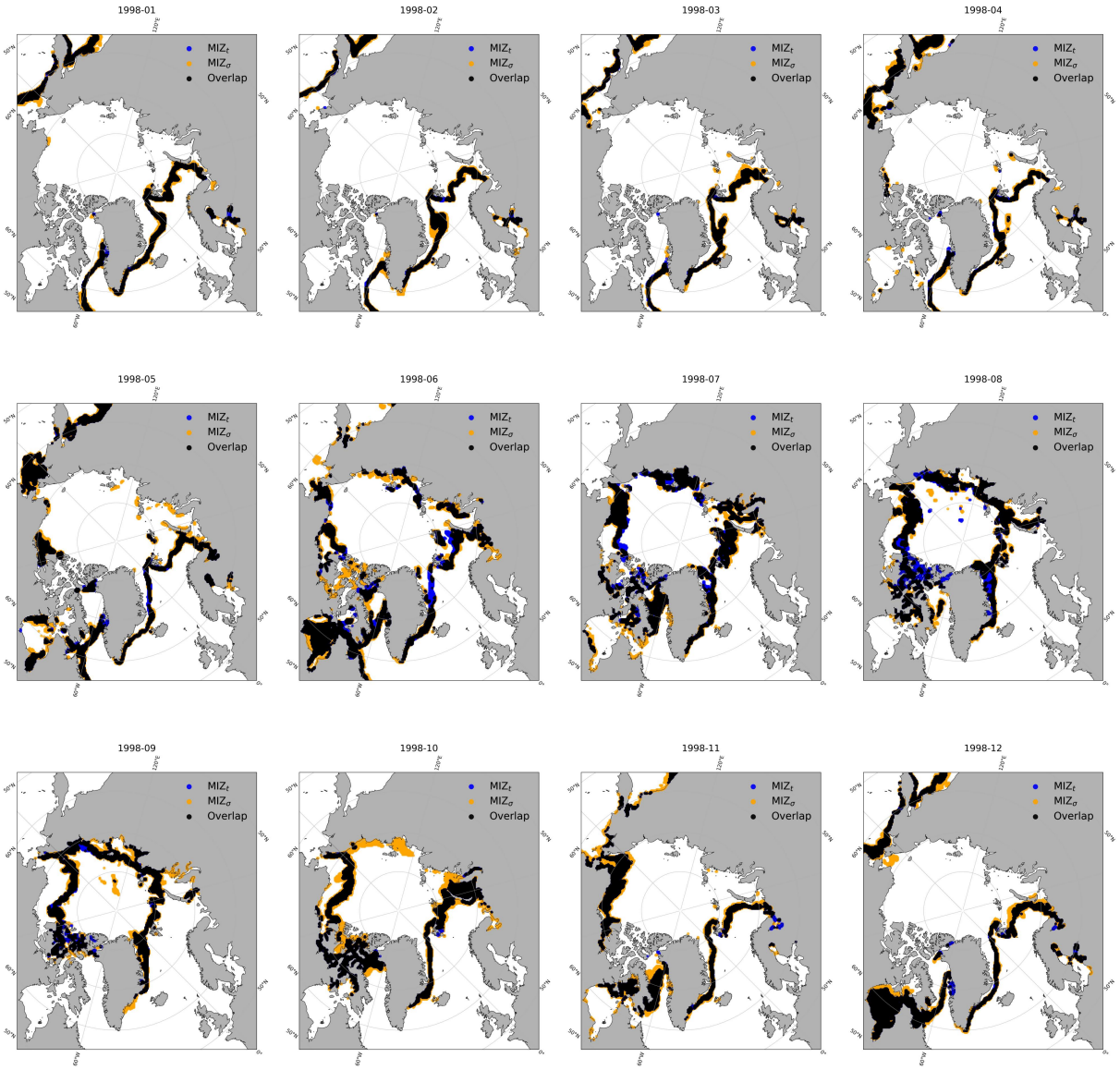

Figure 16: MIZ$_t$ and MIZ$_\sigma$ spatial map for all months in 1998. The MIZ$_t$ grid cells are defined using the criterion of $0.15 \leq \text{SIC} < 0.80$. The MIZ$_\sigma$ grid cells are defined using the criterion of $\sigma^a > 0.11$. The land is shown in grey.

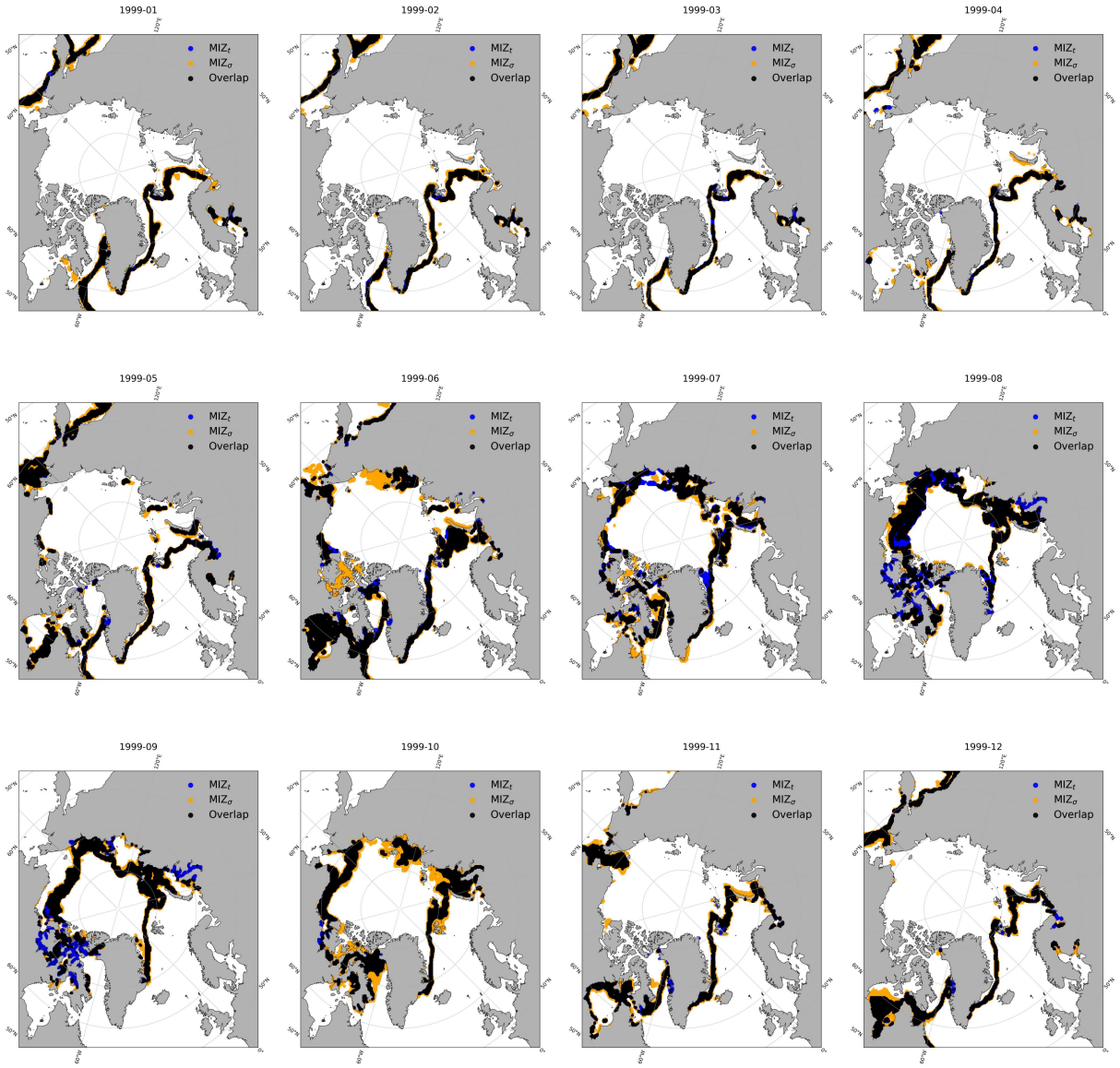

Figure 17: MIZ$_t$ and MIZ$_\sigma$ spatial map for all months in 1999. The MIZ$_t$ grid cells are defined using the criterion of $0.15 \leq \text{SIC} < 0.80$. The MIZ$_\sigma$ grid cells are defined using the criterion of $\sigma^a > 0.11$. The land is shown in grey.

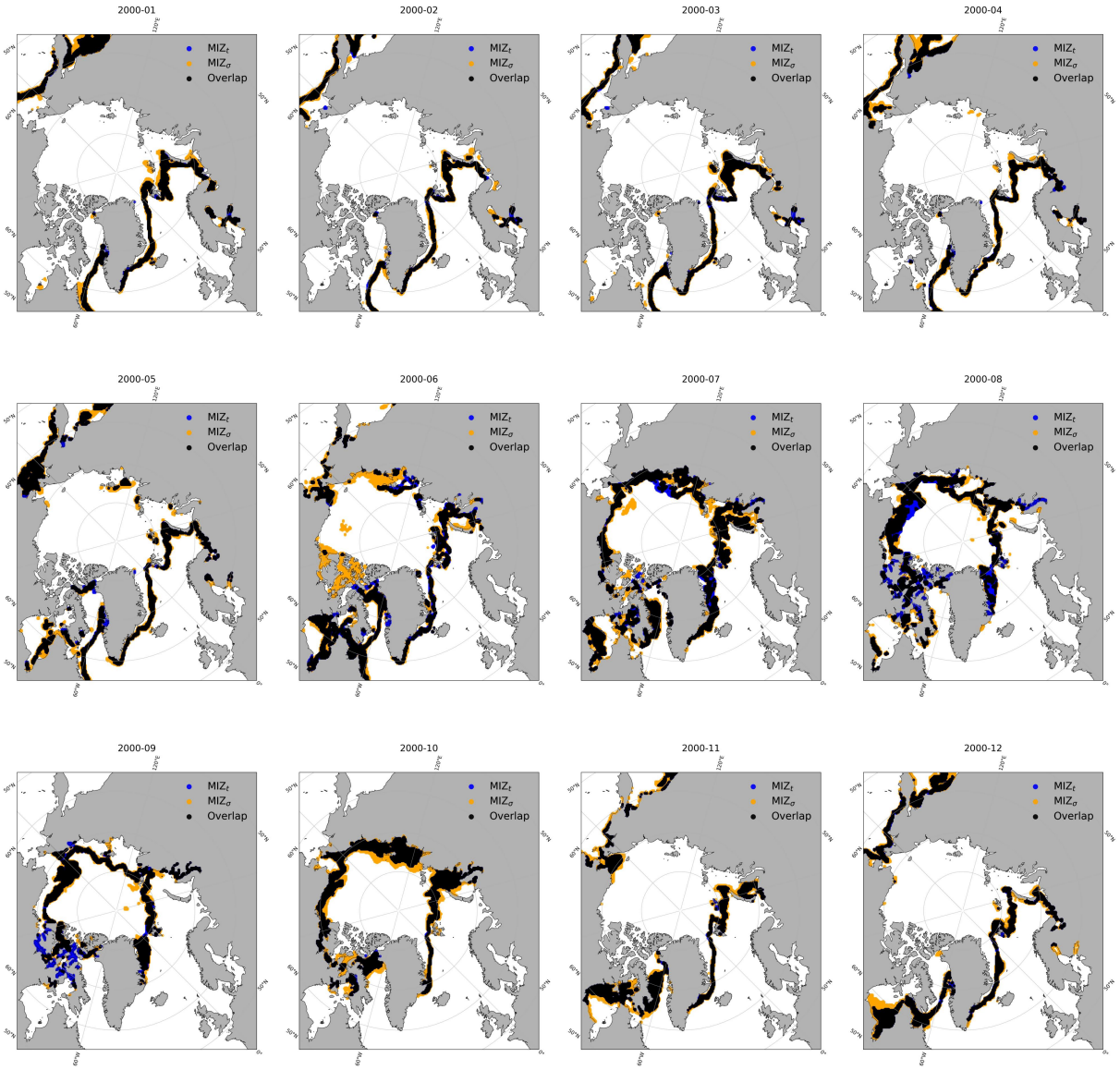

Figure 18: MIZ$_t$ and MIZ$_\sigma$ spatial map for all months in 2000. The MIZ$_t$ grid cells are defined using the criterion of $0.15 \leq \text{SIC} < 0.80$. The MIZ$_\sigma$ grid cells are defined using the criterion of $\sigma^a > 0.11$. The land is shown in grey.

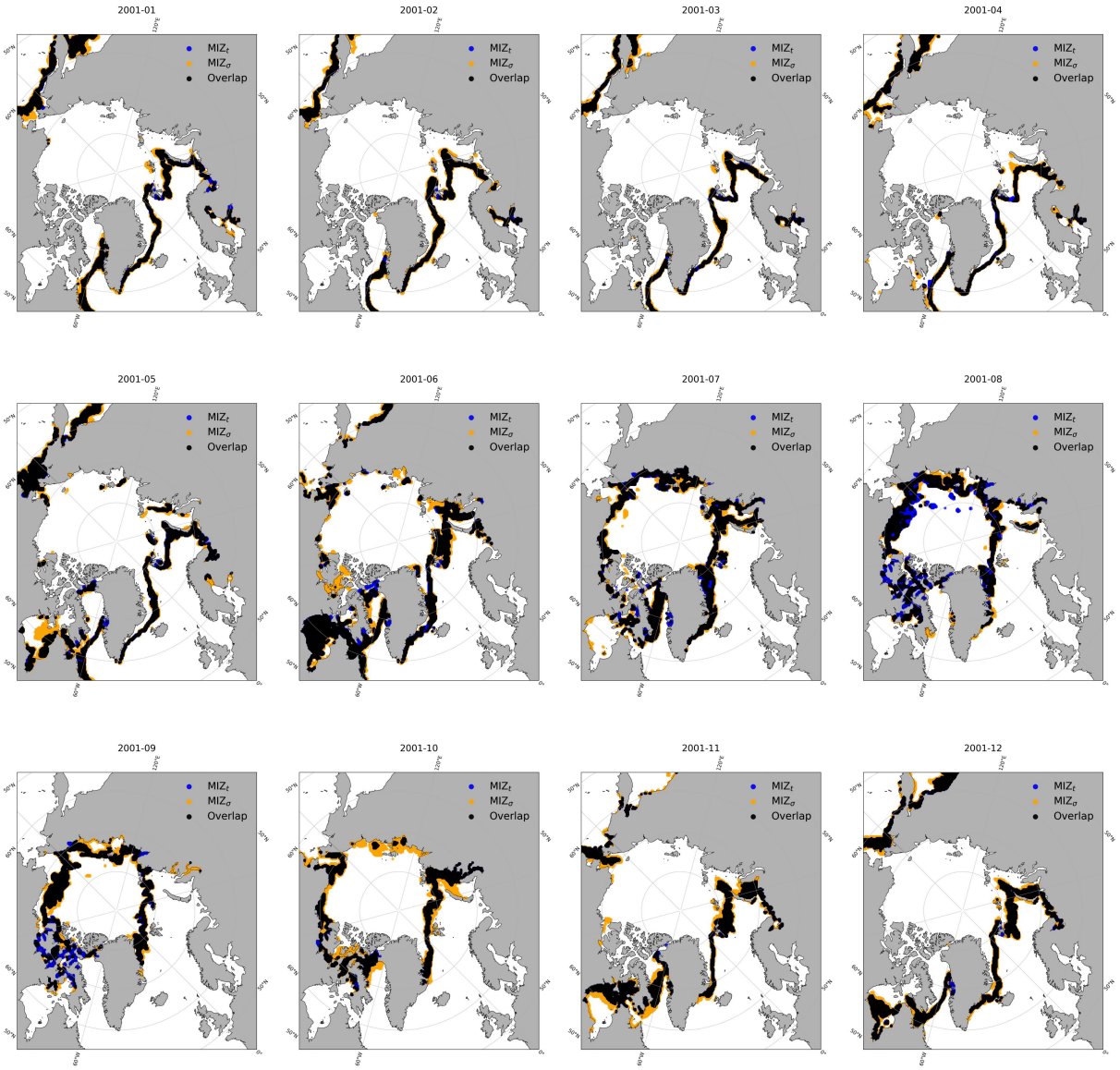

Figure 19: MIZ$_t$ and MIZ$_\sigma$ spatial map for all months in 2001. The MIZ$_t$ grid cells are defined using the criterion of $0.15 \leq \text{SIC} < 0.80$. The MIZ$_\sigma$ grid cells are defined using the criterion of $\sigma^a > 0.11$. The land is shown in grey.

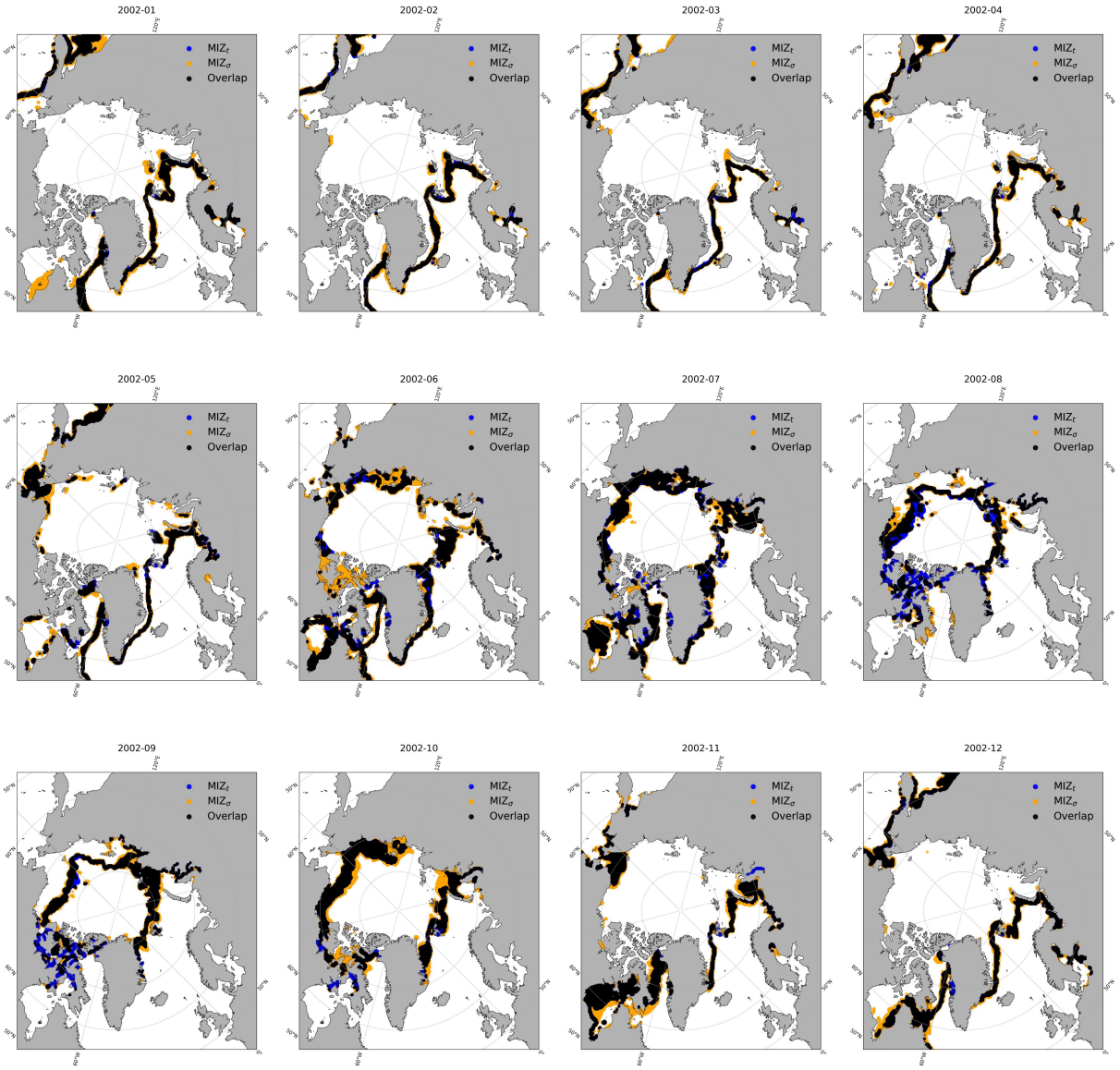

Figure 20: MIZ$_t$ and MIZ$_\sigma$ spatial map for all months in 2002. The MIZ$_t$ grid cells are defined using the criterion of $0.15 \leq \text{SIC} < 0.80$. The MIZ$_\sigma$ grid cells are defined using the criterion of $\sigma^a > 0.11$. The land is shown in grey.

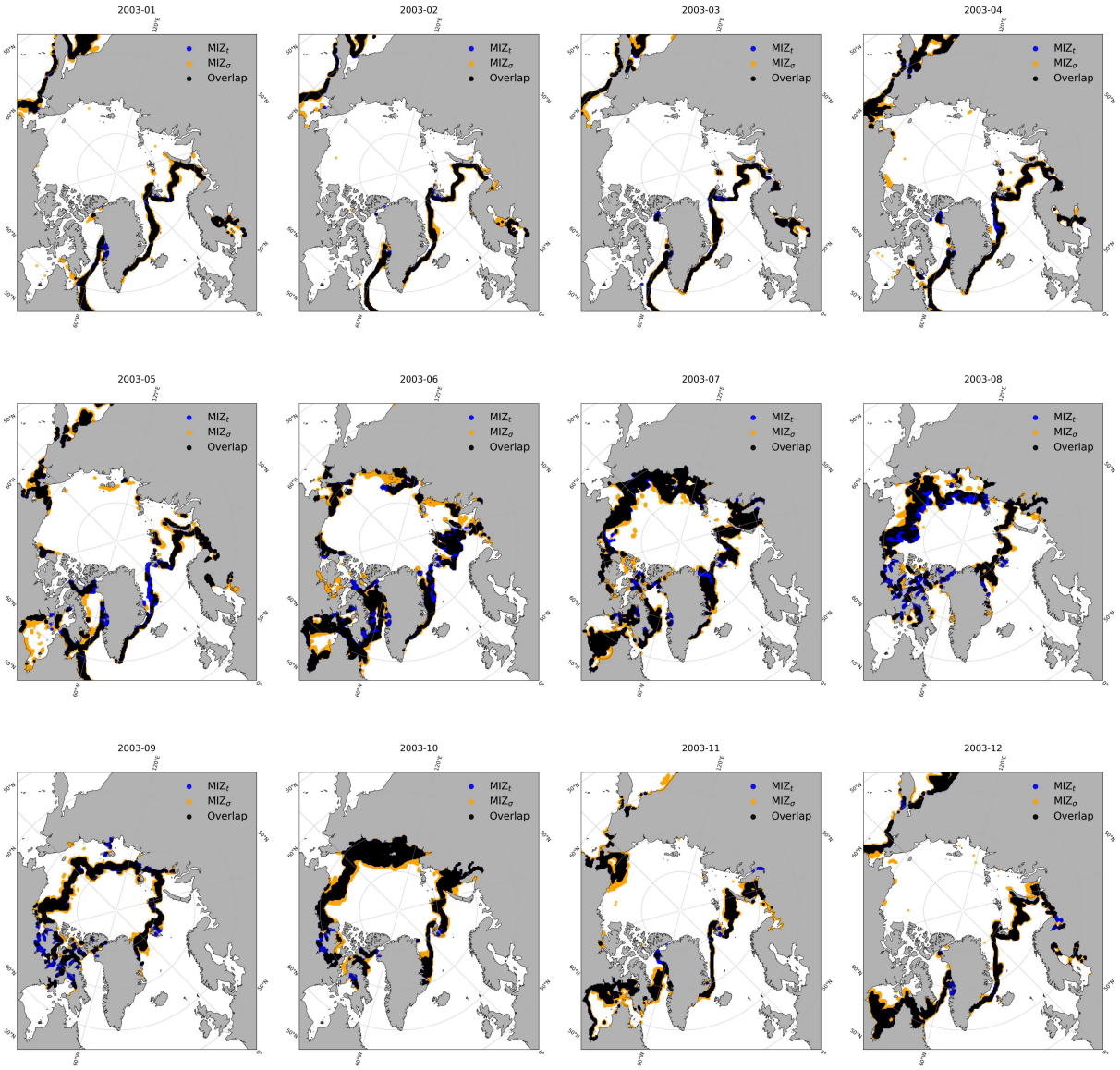

Figure 21: MIZ$_t$ and MIZ$_\sigma$ spatial map for all months in 2003. The MIZ$_t$ grid cells are defined using the criterion of $0.15 \leq \text{SIC} < 0.80$. The MIZ$_\sigma$ grid cells are defined using the criterion of $\sigma^a > 0.11$. The land is shown in grey.

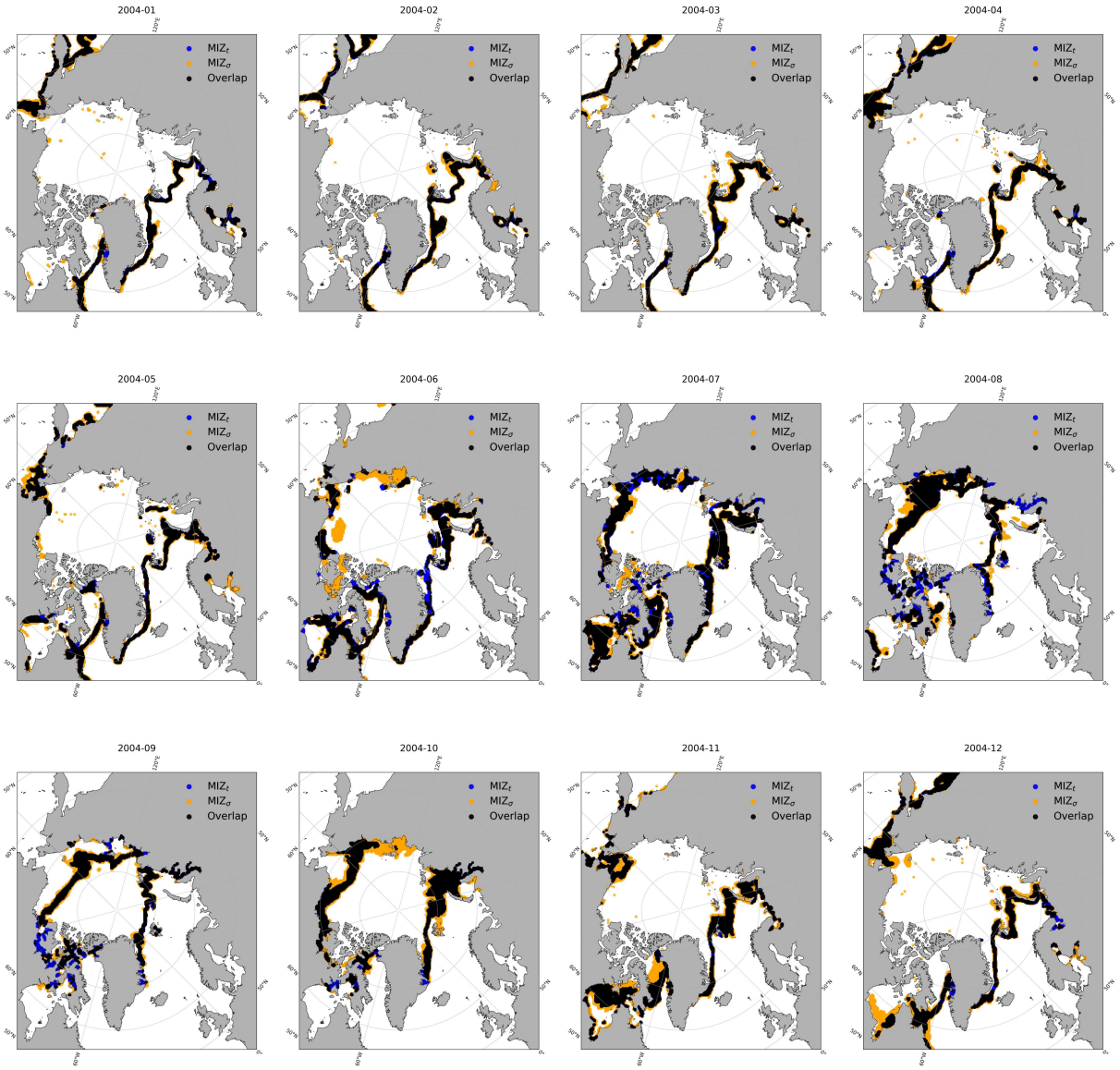

Figure 22: MIZ$_t$ and MIZ$_\sigma$ spatial map for all months in 2004. The MIZ$_t$ grid cells are defined using the criterion of $0.15 \leq \text{SIC} < 0.80$. The MIZ$_\sigma$ grid cells are defined using the criterion of $\sigma^a > 0.11$. The land is shown in grey.

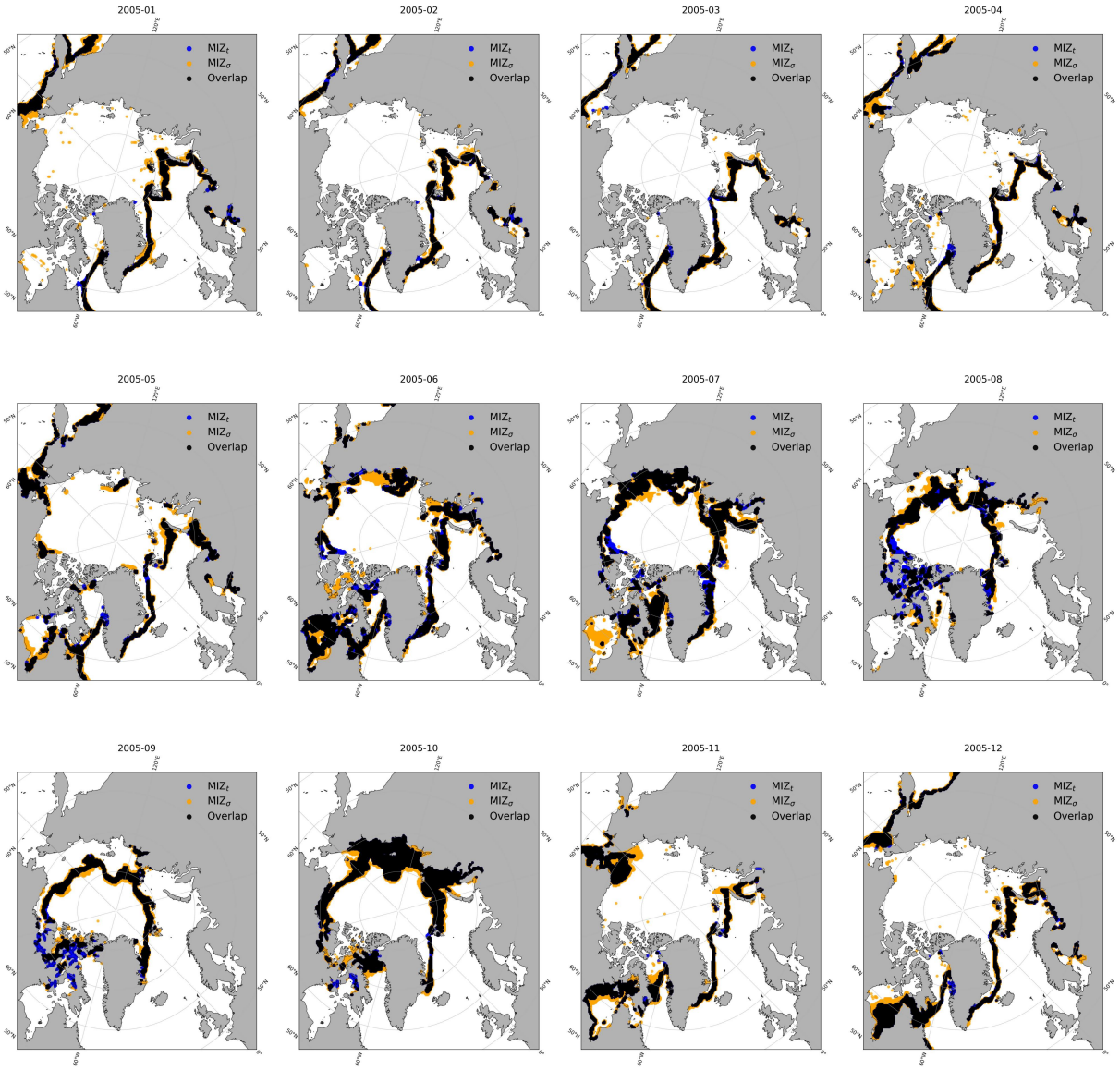

Figure 23: MIZ$_t$ and MIZ$_\sigma$ spatial map for all months in 2005. The MIZ$_t$ grid cells are defined using the criterion of $0.15 \leq \text{SIC} < 0.80$. The MIZ$_\sigma$ grid cells are defined using the criterion of $\sigma^a > 0.11$. The land is shown in grey.

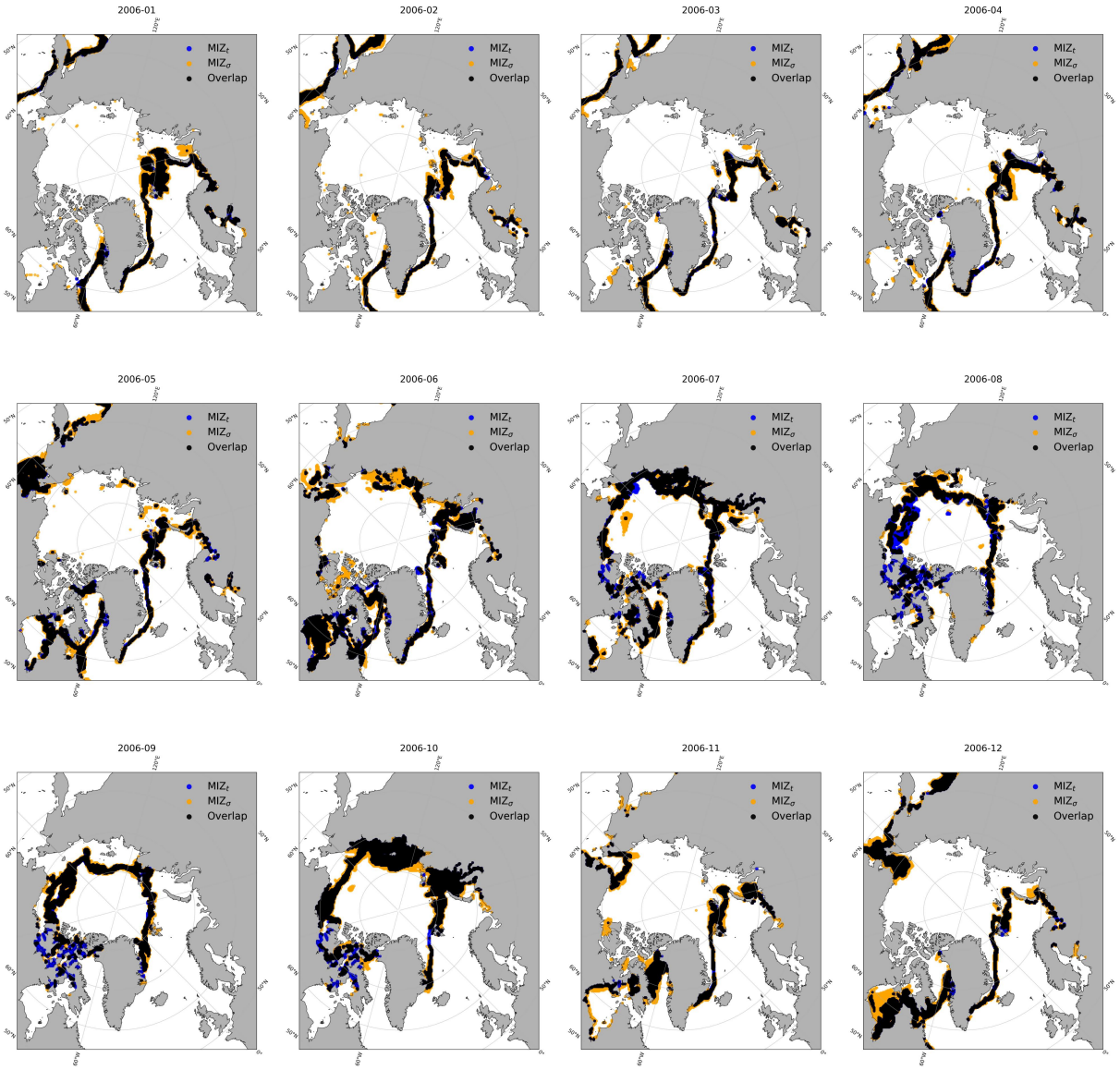

Figure 24: MIZ$_t$ and MIZ$_\sigma$ spatial map for all months in 2006. The MIZ$_t$ grid cells are defined using the criterion of $0.15 \leq \text{SIC} < 0.80$. The MIZ$_\sigma$ grid cells are defined using the criterion of $\sigma^a > 0.11$. The land is shown in grey.

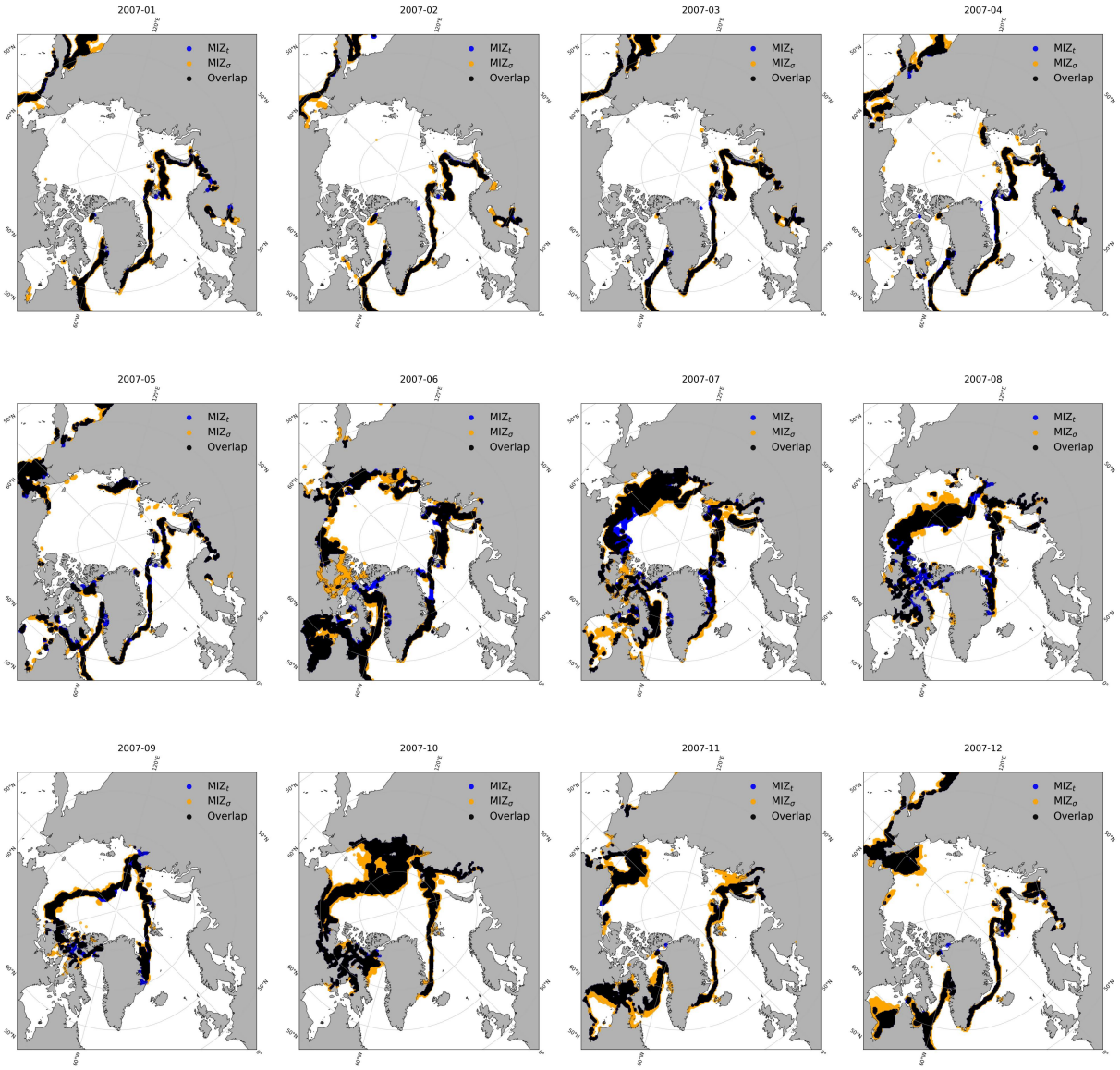

Figure 25: MIZ$_t$ and MIZ$_\sigma$ spatial map for all months in 2007. The MIZ$_t$ grid cells are defined using the criterion of $0.15 \leq \text{SIC} < 0.80$. The MIZ$_\sigma$ grid cells are defined using the criterion of $\sigma^a > 0.11$. The land is shown in grey.

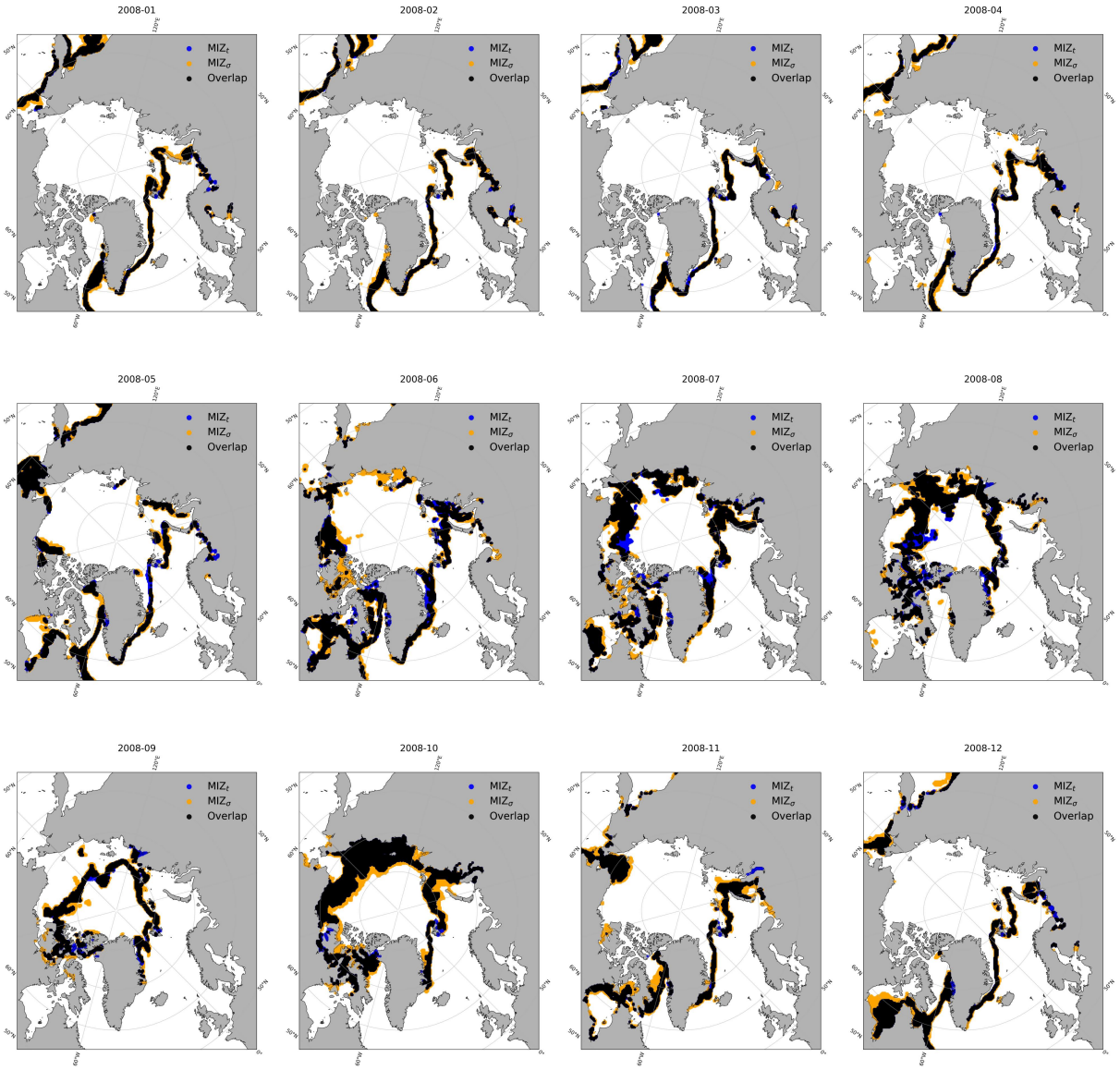

Figure 26: MIZ$_t$ and MIZ$_\sigma$ spatial map for all months in 2008. The MIZ$_t$ grid cells are defined using the criterion of $0.15 \leq \text{SIC} < 0.80$. The MIZ$_\sigma$ grid cells are defined using the criterion of $\sigma^a > 0.11$. The land is shown in grey.

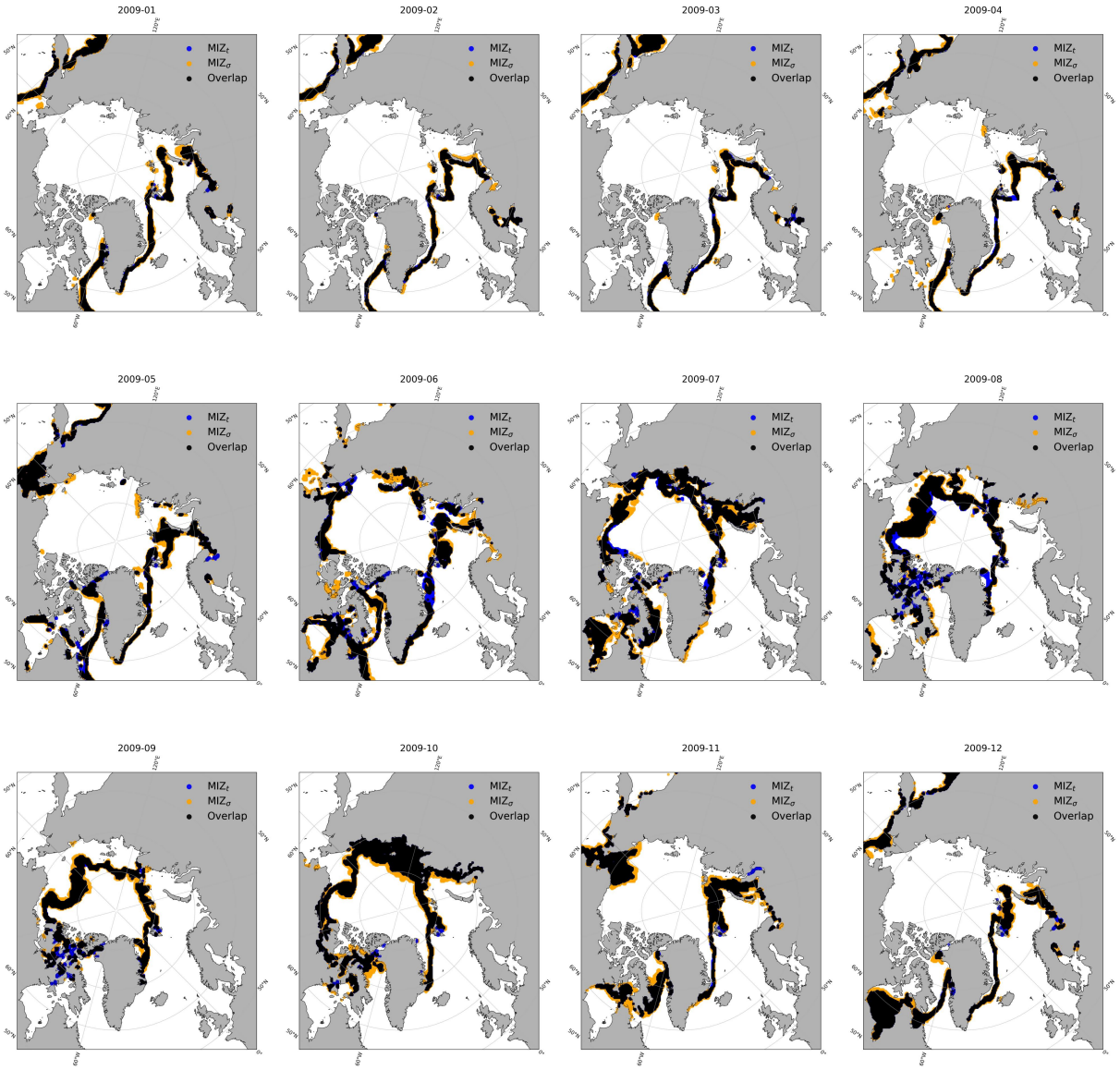

Figure 27: MIZ$_t$ and MIZ$_\sigma$ spatial map for all months in 2009. The MIZ$_t$ grid cells are defined using the criterion of $0.15 \leq \text{SIC} < 0.80$. The MIZ$_\sigma$ grid cells are defined using the criterion of $\sigma^a > 0.11$. The land is shown in grey.

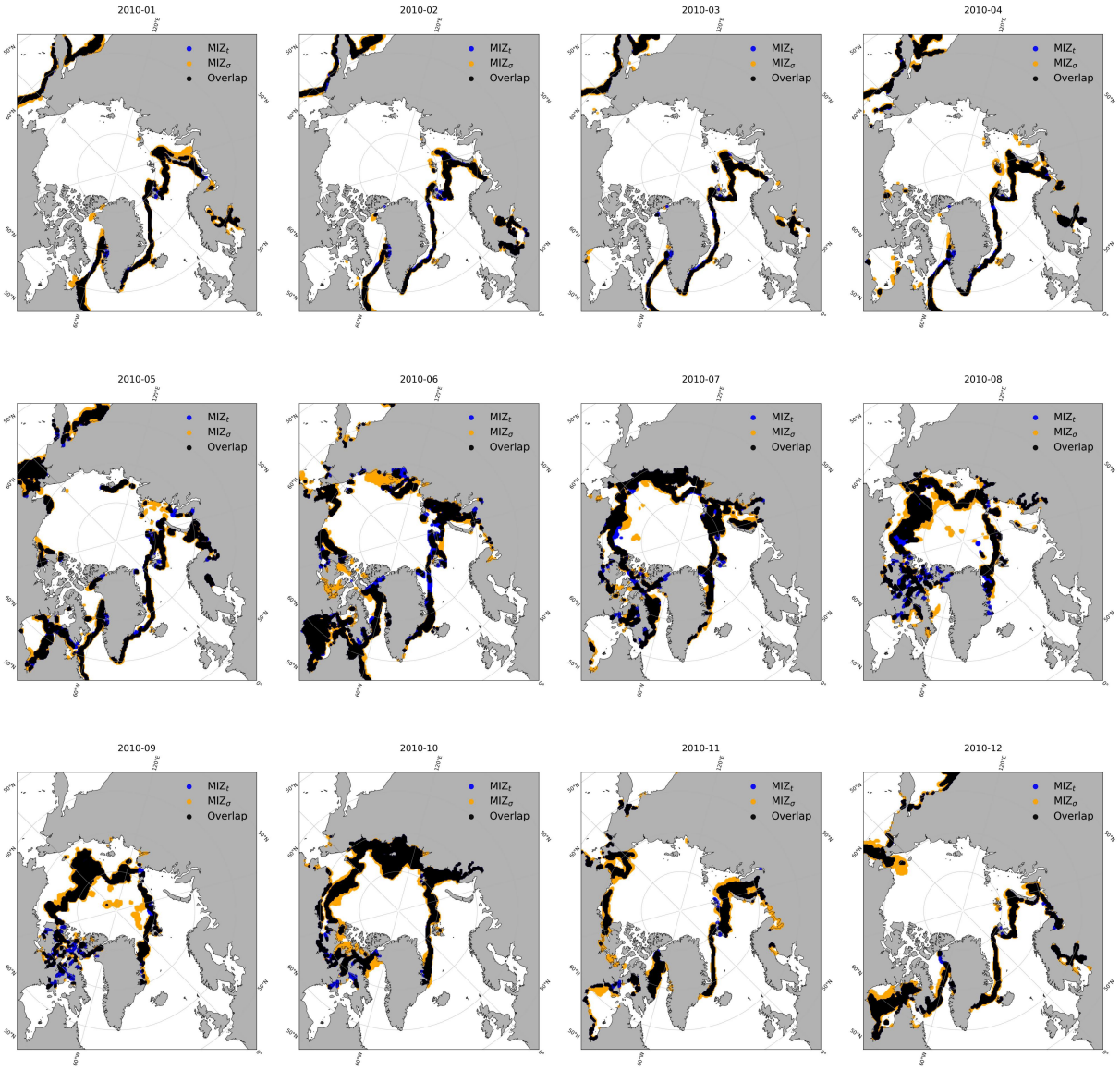

Figure 28: MIZ$_t$ and MIZ$_\sigma$ spatial map for all months in 2010. The MIZ$_t$ grid cells are defined using the criterion of $0.15 \leq \text{SIC} < 0.80$. The MIZ$_\sigma$ grid cells are defined using the criterion of $\sigma^a > 0.11$. The land is shown in grey.

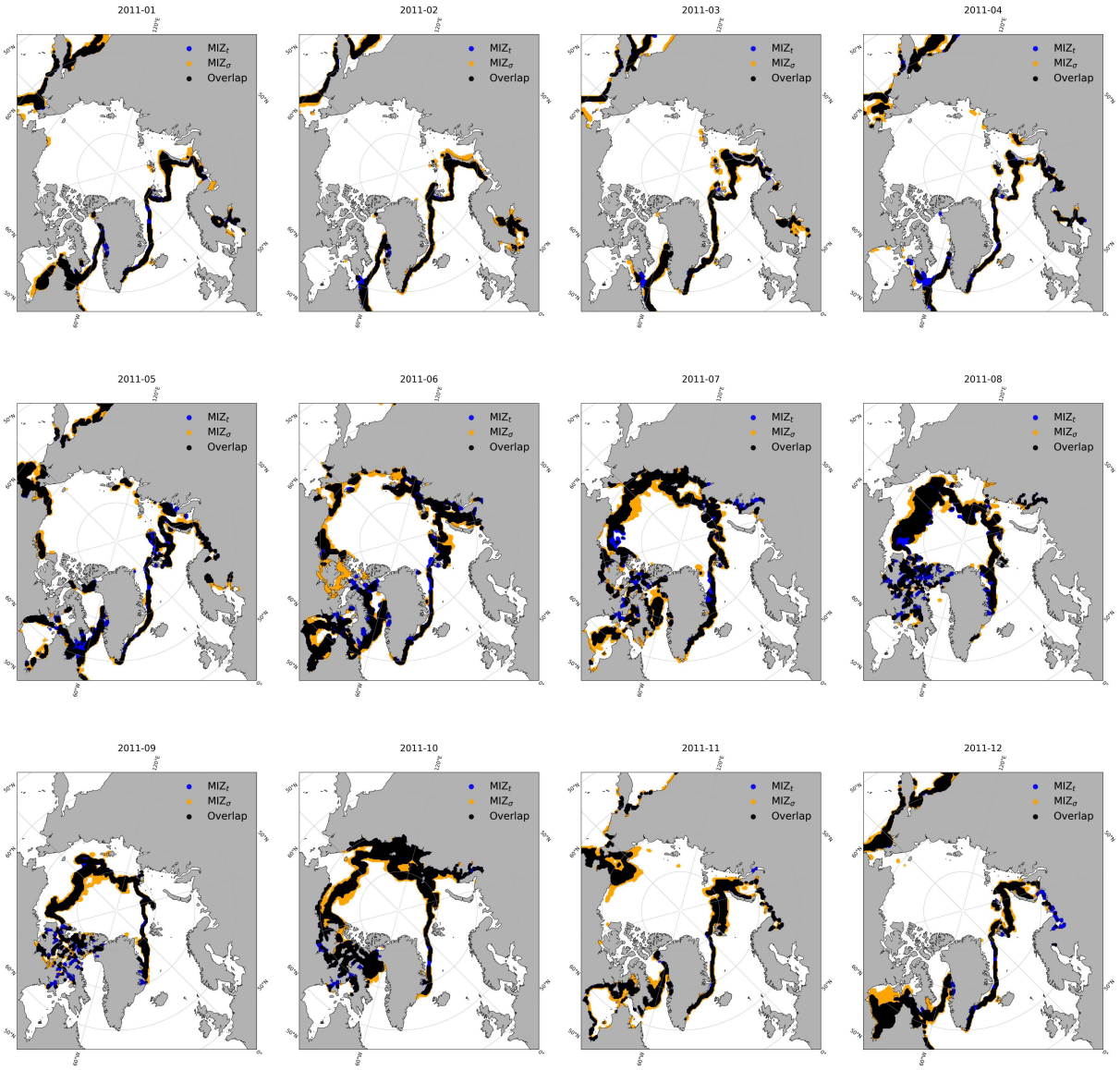

Figure 29: MIZ$_t$ and MIZ$_\sigma$ spatial map for all months in 2011. The MIZ$_t$ grid cells are defined using the criterion of $0.15 \leq \text{SIC} < 0.80$. The MIZ$_\sigma$ grid cells are defined using the criterion of $\sigma^a > 0.11$. The land is shown in grey.

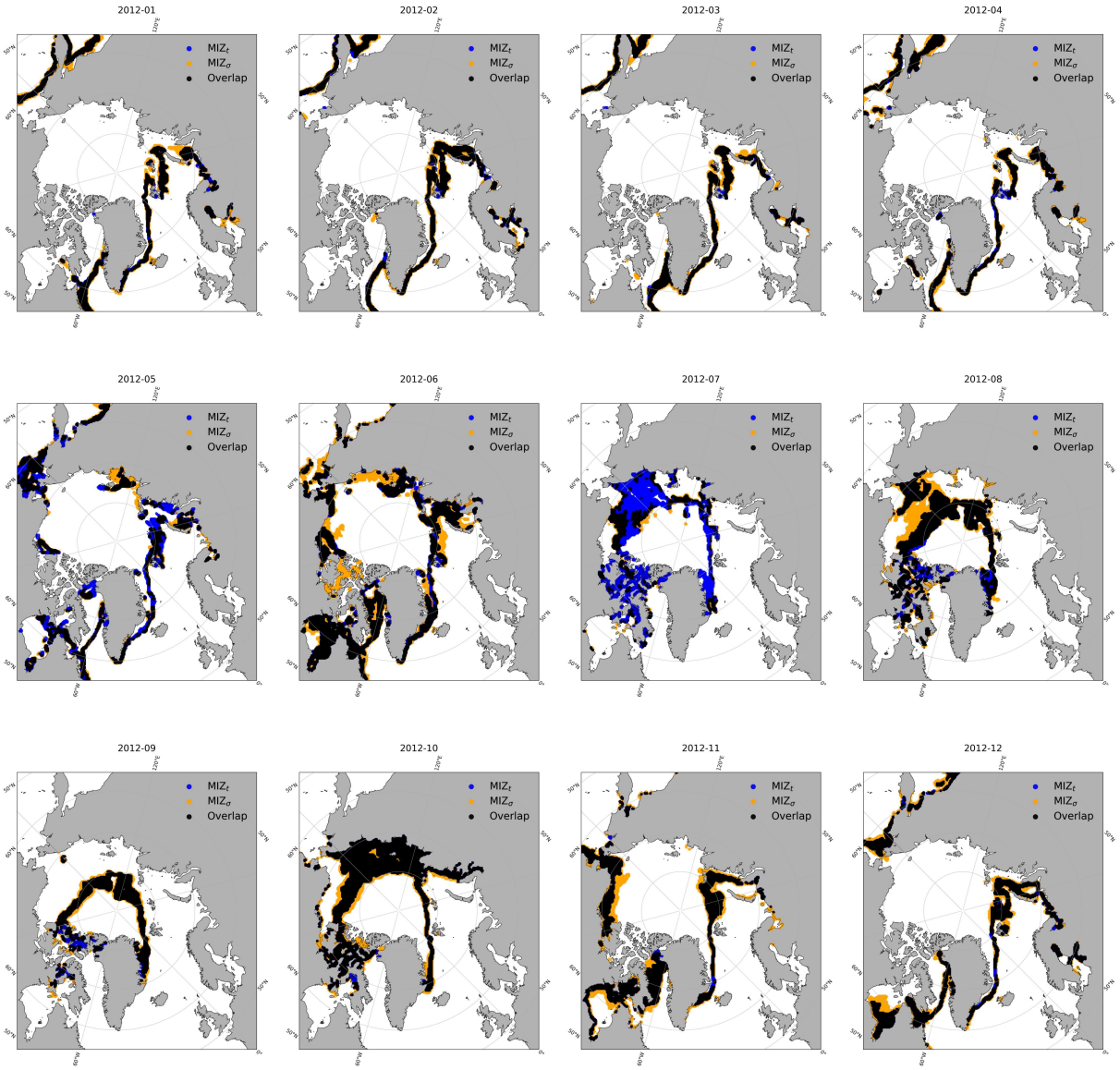

Figure 30: MIZ$_t$ and MIZ$_\sigma$ spatial map for all months in 2012. The MIZ$_t$ grid cells are defined using the criterion of $0.15 \leq \text{SIC} < 0.80$. The MIZ$_\sigma$ grid cells are defined using the criterion of $\sigma^a > 0.11$. The land is shown in grey.

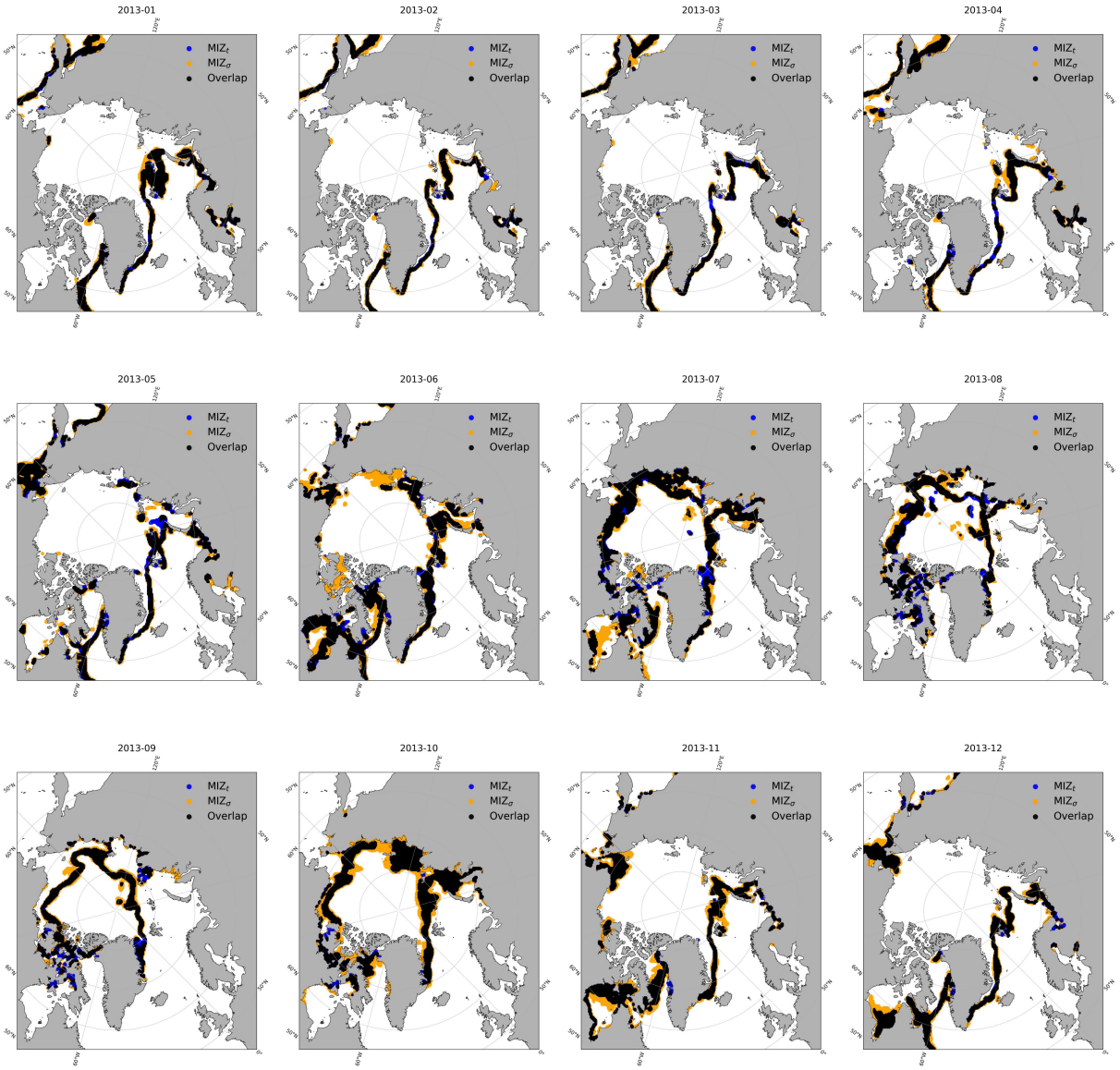

Figure 31: MIZ$_t$ and MIZ$_\sigma$ spatial map for all months in 2013. The MIZ$_t$ grid cells are defined using the criterion of $0.15 \leq \text{SIC} < 0.80$. The MIZ$_\sigma$ grid cells are defined using the criterion of $\sigma^a > 0.11$. The land is shown in grey.

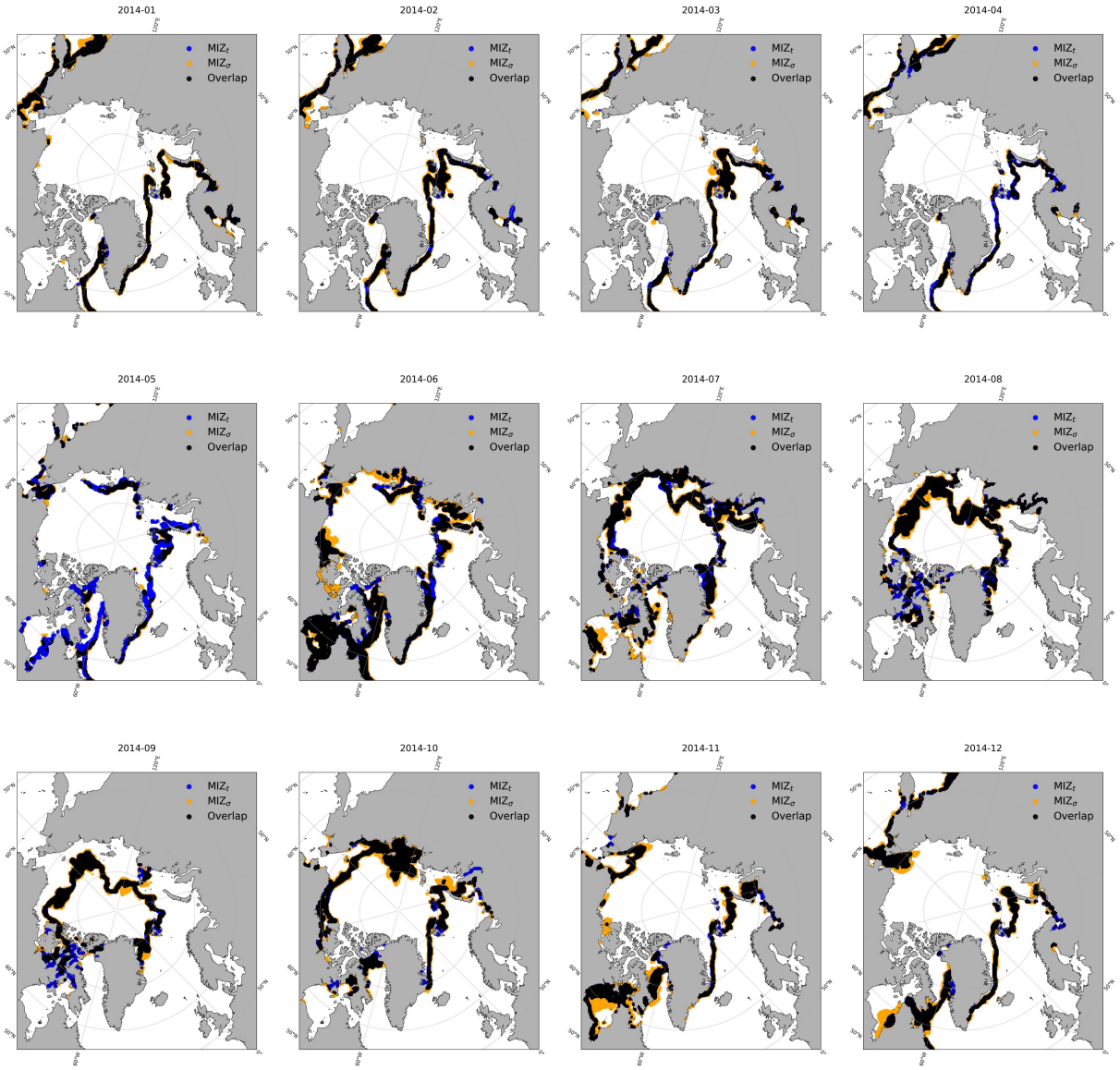

Figure 32: MIZ$_t$ and MIZ$_\sigma$ spatial map for all months in 2014. The MIZ$_t$ grid cells are defined using the criterion of $0.15 \leq \text{SIC} < 0.80$. The MIZ$_\sigma$ grid cells are defined using the criterion of $\sigma^a > 0.11$. The land is shown in grey.

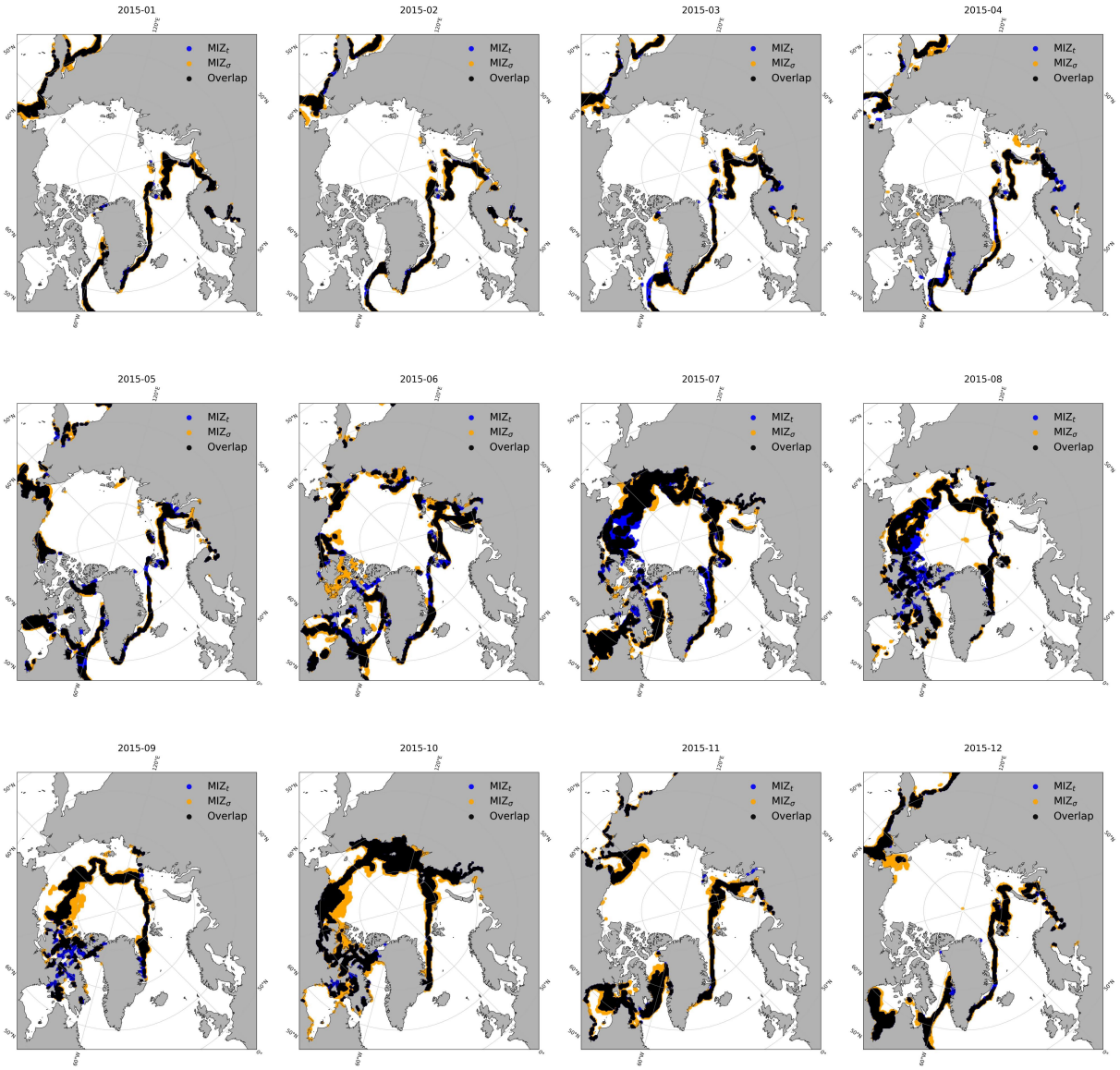

Figure 33: MIZ$_t$ and MIZ$_\sigma$ spatial map for all months in 2015. The MIZ$_t$ grid cells are defined using the criterion of $0.15 \leq \text{SIC} < 0.80$. The MIZ$_\sigma$ grid cells are defined using the criterion of $\sigma^a > 0.11$. The land is shown in grey.

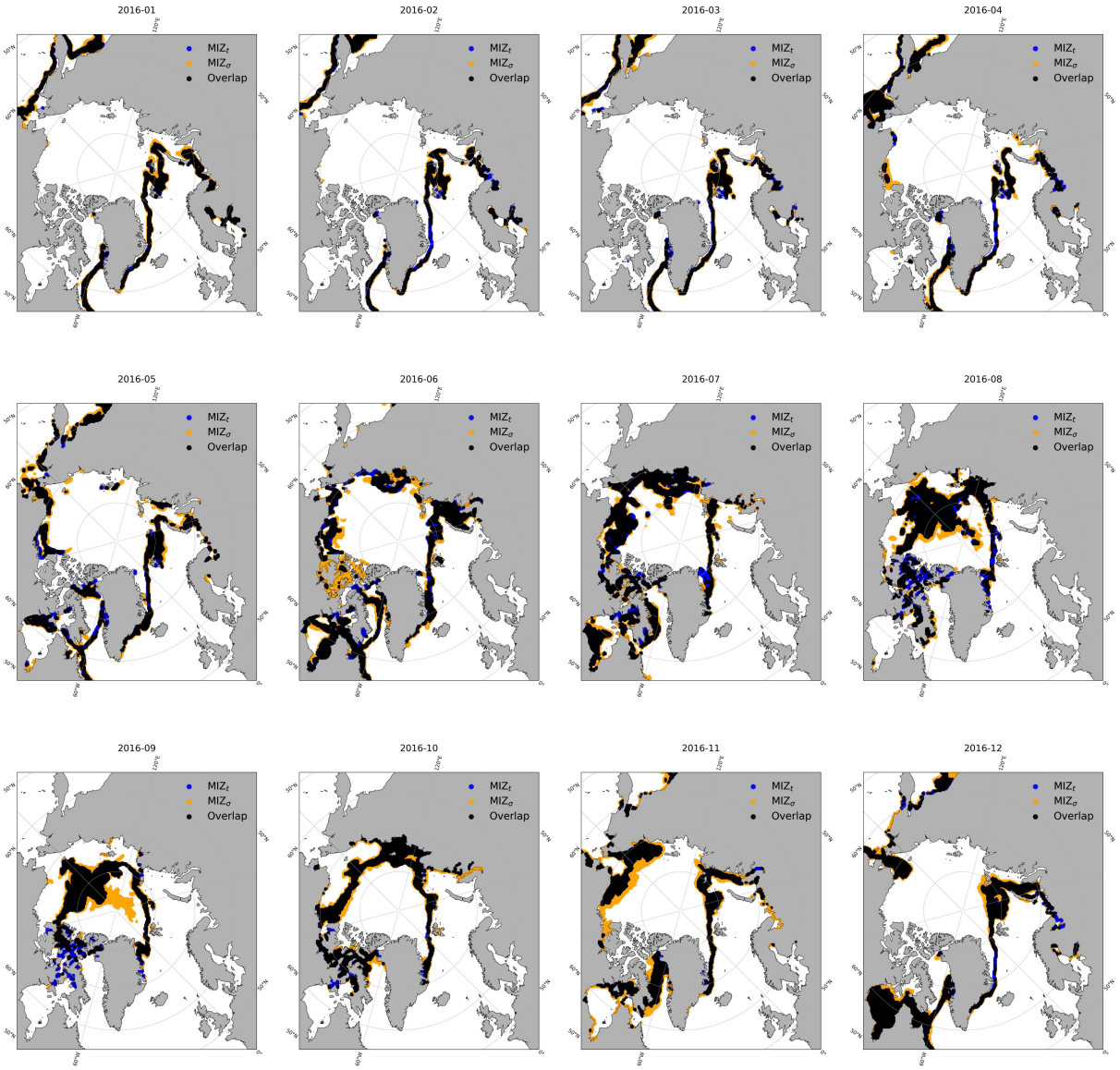

Figure 34: MIZ$_t$ and MIZ$_\sigma$ spatial map for all months in 2016. The MIZ$_t$ grid cells are defined using the criterion of $0.15 \leq \text{SIC} < 0.80$. The MIZ$_\sigma$ grid cells are defined using the criterion of $\sigma^a > 0.11$. The land is shown in grey.

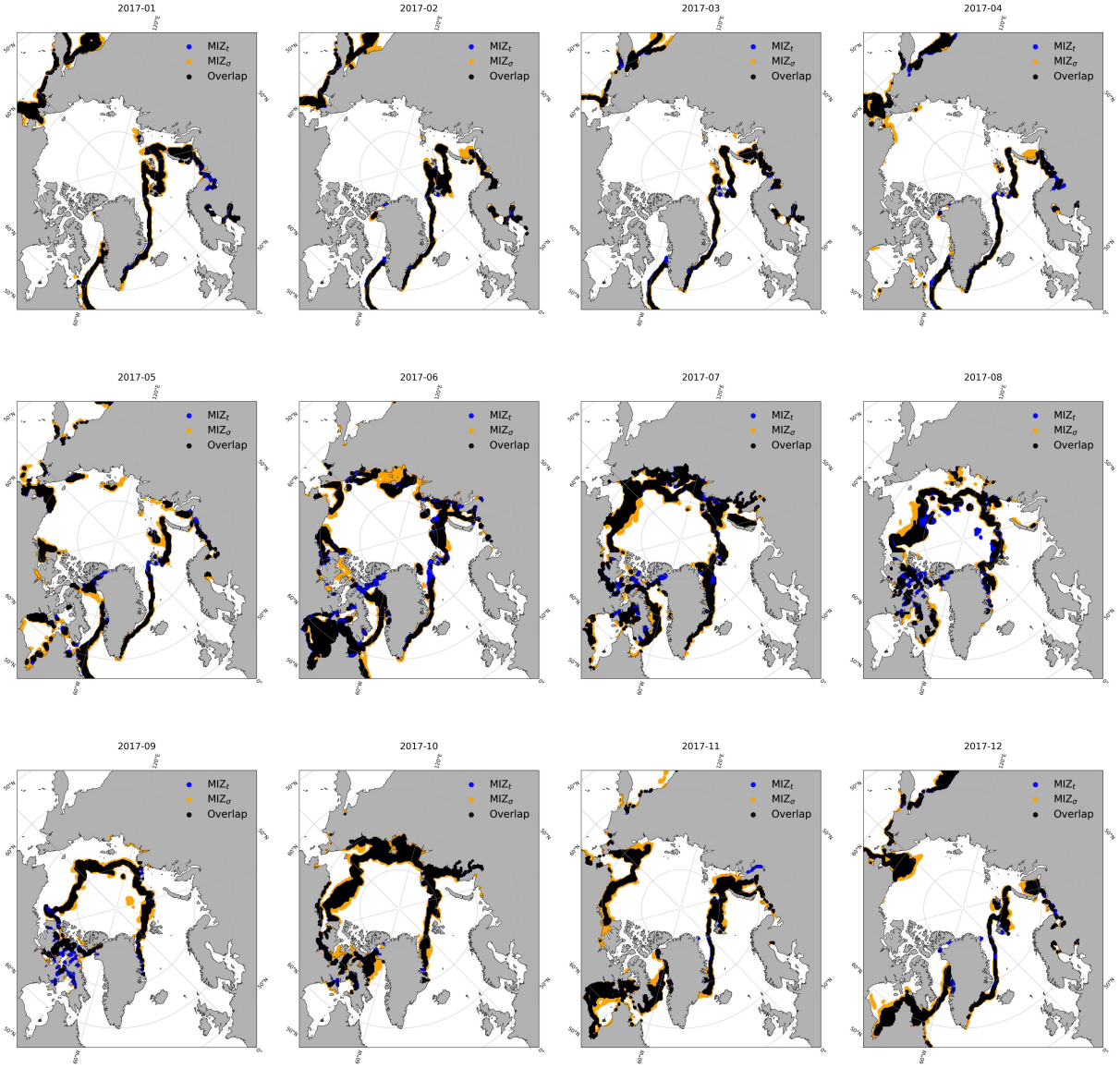

Figure 35: MIZ$_t$ and MIZ$_\sigma$ spatial map for all months in 2017. The MIZ$_t$ grid cells are defined using the criterion of $0.15 \leq \text{SIC} < 0.80$. The MIZ$_\sigma$ grid cells are defined using the criterion of $\sigma^a > 0.11$. The land is shown in grey.

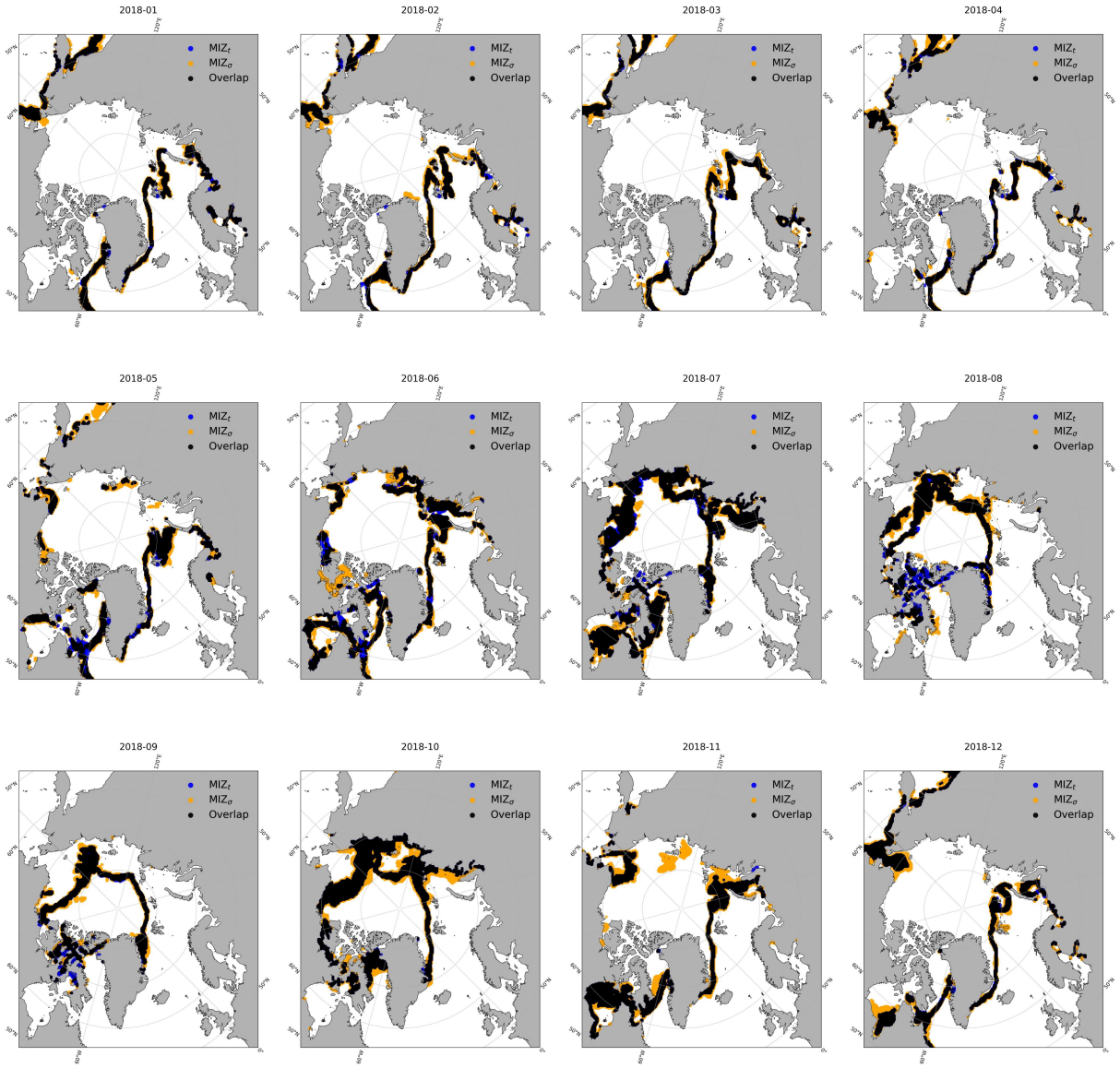

Figure 36: MIZ$_t$ and MIZ$_\sigma$ spatial map for all months in 2018. The MIZ$_t$ grid cells are defined using the criterion of $0.15 \leq \text{SIC} < 0.80$. The MIZ$_\sigma$ grid cells are defined using the criterion of $\sigma^a > 0.11$. The land is shown in grey.

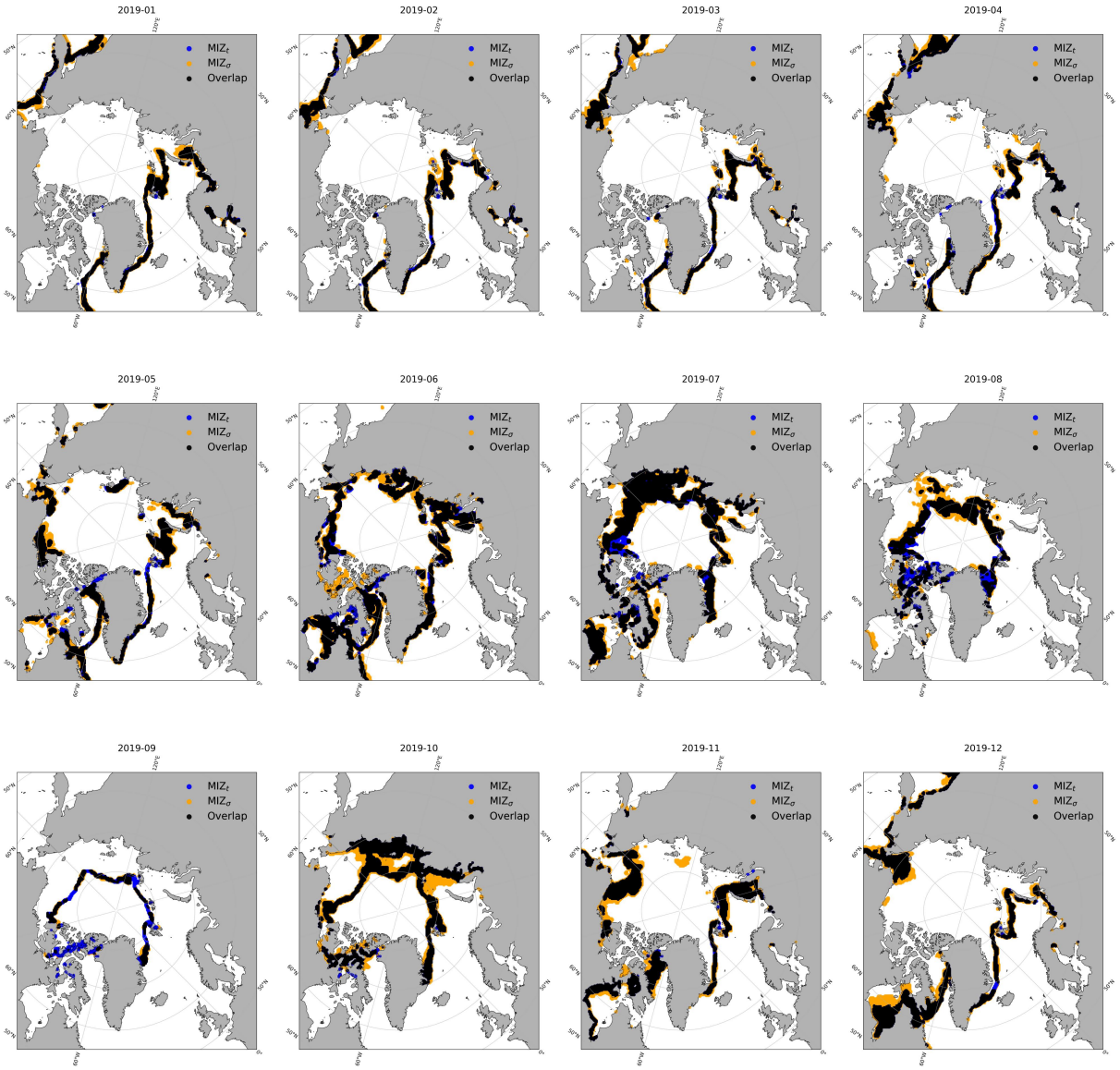

Figure 37: MIZ$_t$ and MIZ$_\sigma$ spatial map for all months in 2019. The MIZ$_t$ grid cells are defined using the criterion of $0.15 \leq \text{SIC} < 0.80$. The MIZ$_\sigma$ grid cells are defined using the criterion of $\sigma^a > 0.11$. The land is shown in grey.

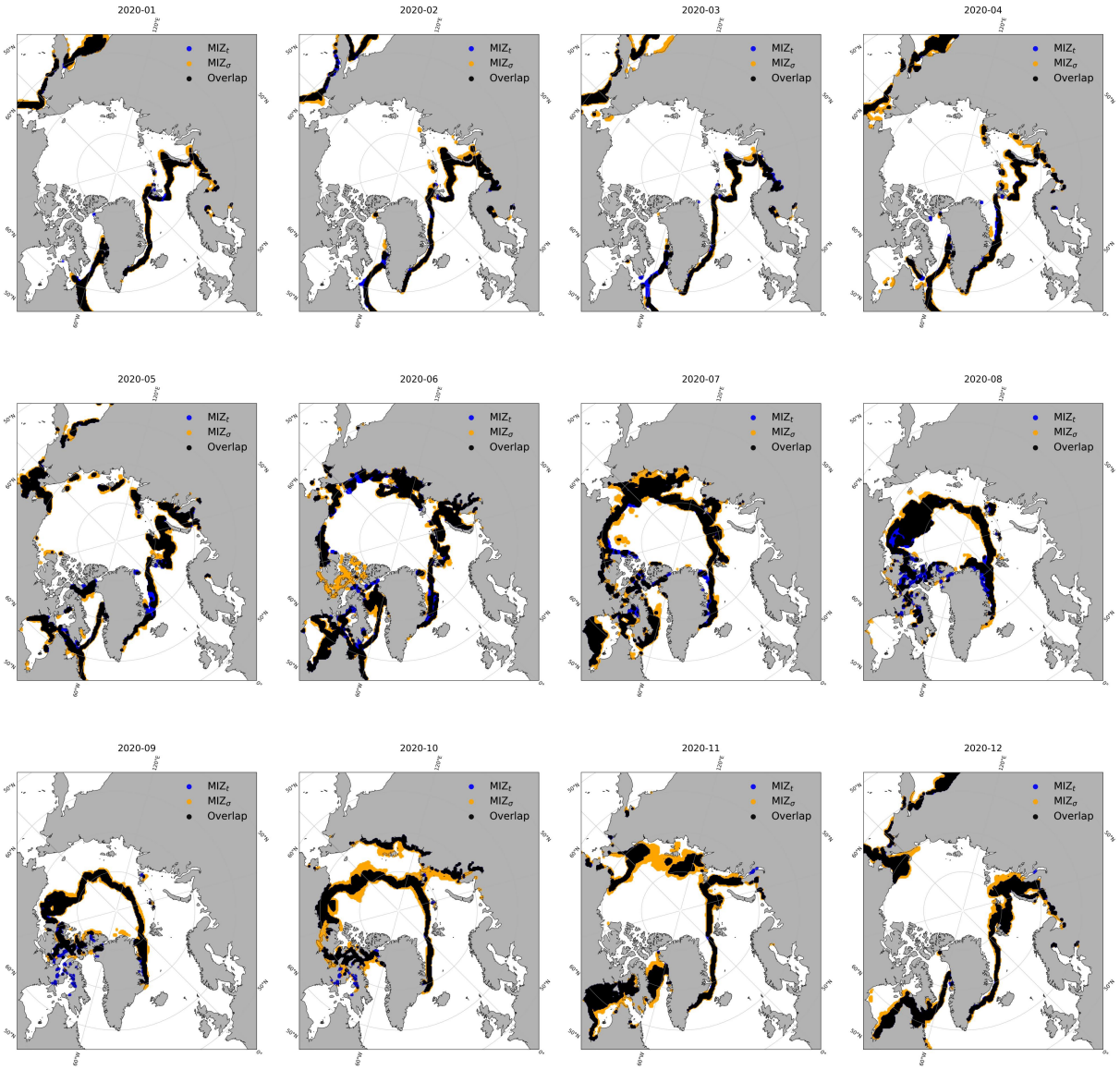

Figure 38: MIZ$_t$ and MIZ$_\sigma$ spatial map for all months in 2020. The MIZ$_t$ grid cells are defined using the criterion of $0.15 \leq \text{SIC} < 0.80$. The MIZ$_\sigma$ grid cells are defined using the criterion of $\sigma^a > 0.11$. The land is shown in grey.

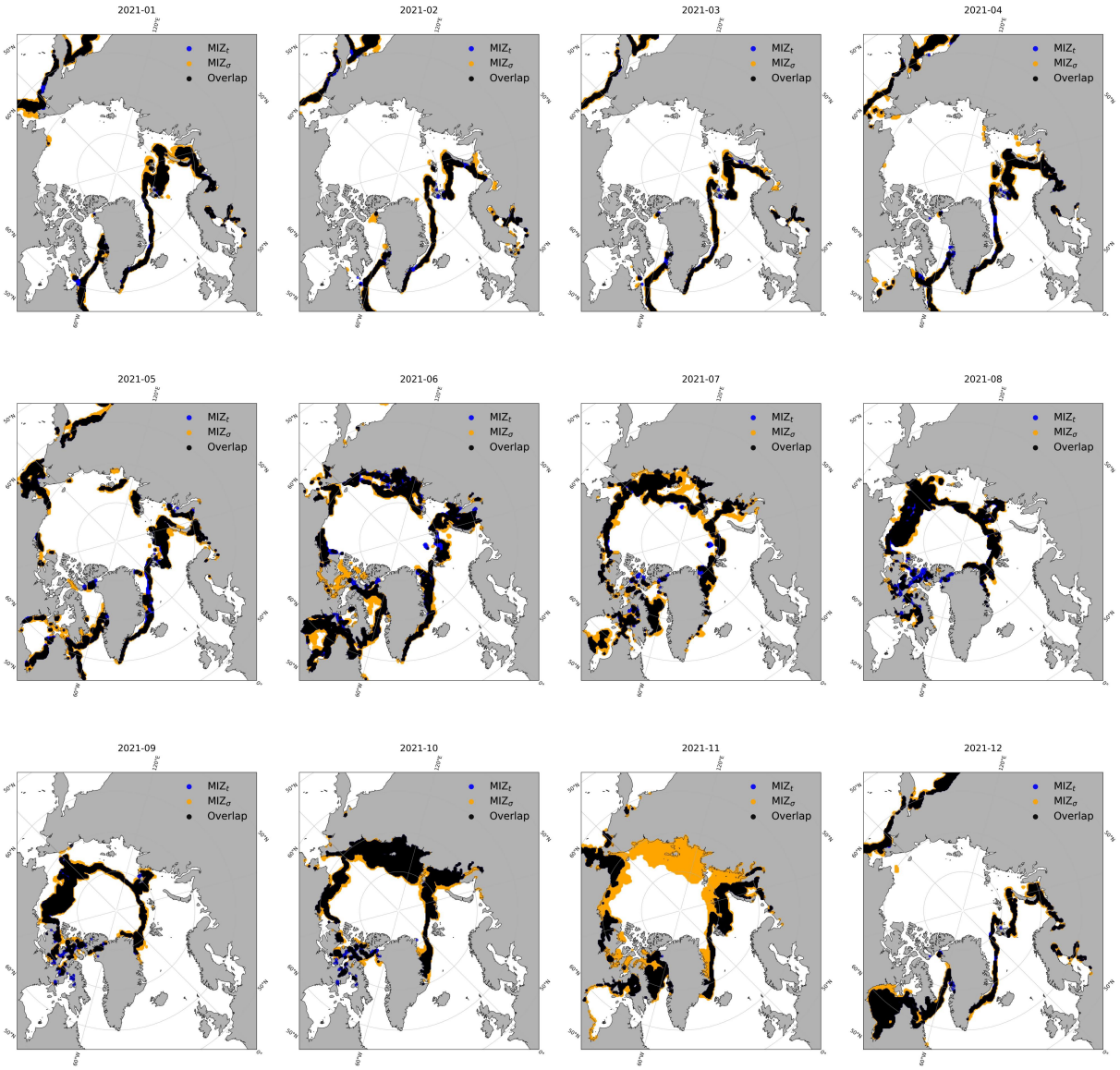

Figure 39: MIZ$_t$ and MIZ$_\sigma$ spatial map for all months in 2021. The MIZ$_t$ grid cells are defined using the criterion of $0.15 \leq \text{SIC} < 0.80$. The MIZ$_\sigma$ grid cells are defined using the criterion of $\sigma^a > 0.11$. The land is shown in grey.

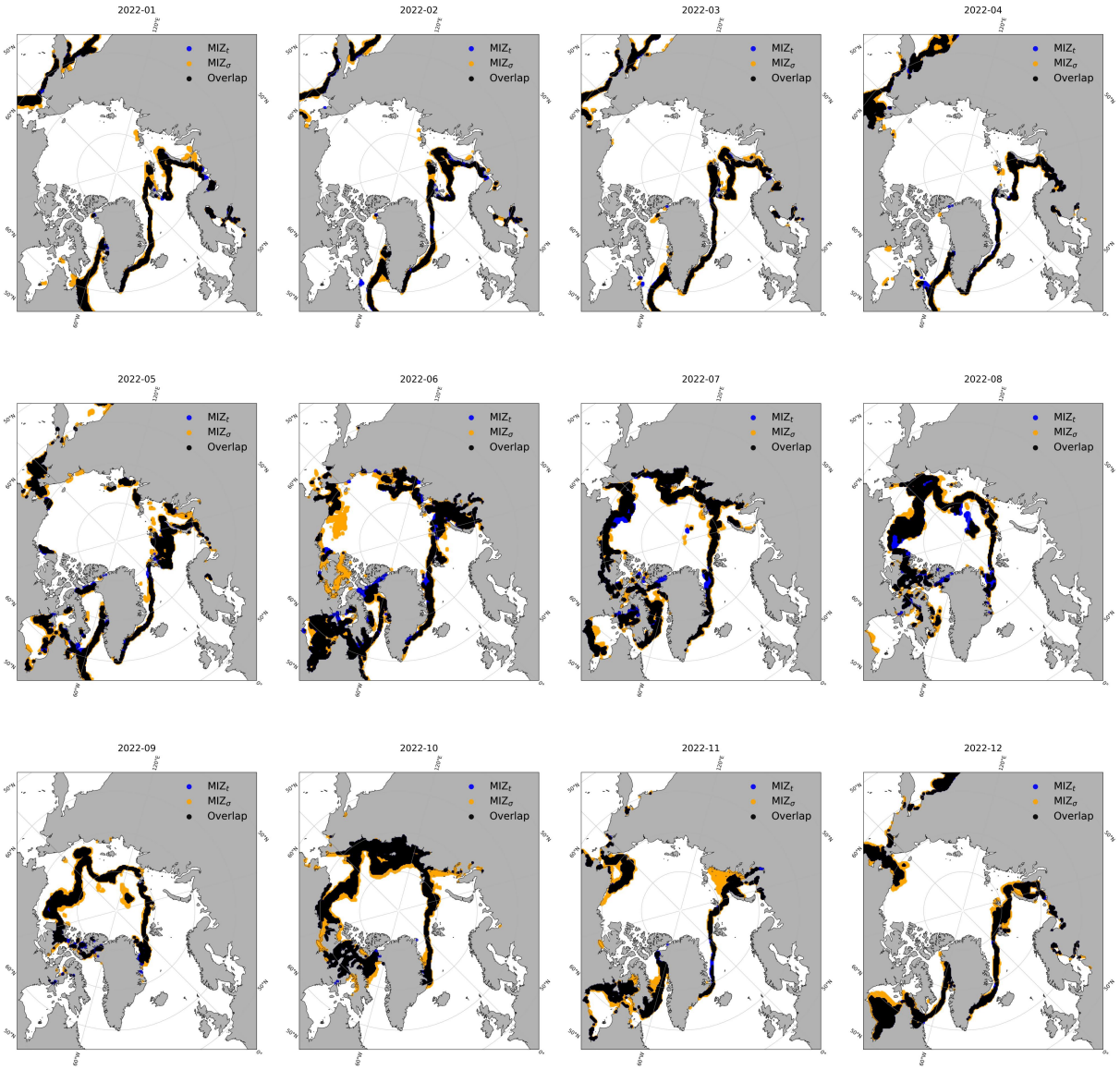

Figure 40: MIZ$_t$ and MIZ$_\sigma$ spatial map for all months in 2022. The MIZ$_t$ grid cells are defined using the criterion of $0.15 \leq \text{SIC} < 0.80$. The MIZ$_\sigma$ grid cells are defined using the criterion of $\sigma^a > 0.11$. The land is shown in grey.